An Investigation of the Effect of Metal Nanoparticles on the Optical Properties of Silicon Nanocrystals

Khamael Mohammed Abualnaja

A thesis submitted for the degree of

Doctor of Philosophy in Chemical Engineering and Advanced Materials

Nanoscale Science and Nanotechnology Group

School of Chemical Engineering and Advanced Materials

Newcastle University

Newcastle Upon Tyne, UK

November 2014

Abstract

An Investigation of the Effect of Metal Nanoparticles on the Optical Properties of Silicon Nanocrystals

By

Khamael Mohammed Abualnaja

This thesis describes the characterization of two types of nanocrystalline material i.e. alkylated silicon nanocrystals (C_{11}-SiNCs) and commercial silicon nanocrystals (SiNCs). The research presented throughout this work also shows that the optical properties of silicon nanocrystals can be affected by erbium ions and metal nanoparticles. The main goal of this characterization is to observe the energy transfer from the excited state of SiNCs to the erbium for optical fiber technology applications. Also, SiNCs have applications in biology as fluorescent labels.

Porous silicon was prepared successfully by galvanostatic etching of p-Si(100) wafers followed by a thermal hydrosilation reaction of 1-undecene in refluxing toluene in order to extract the C_{11}-SiNCs from porous silicon. The chemical characterization of C_{11}-SiNCs was carried out using X-ray photoemission spectroscopy (XPS); they are known to be crystalline and of diameter about 5 nm from previous work. The commercial SiNCs have been characterized using scanning electron microscopy (SEM), transmission electron microscopy (TEM), high resolution transmission electron microscopy (HRTEM), Atomic force microscopy (AFM), X-ray diffraction (XRD), XPS and Fourier transform infrared spectroscopy (FTIR). It was found that the average diameter of commercial SiNCs is 65 nm and are crystalline with an FCC lattice.

Erbium trichloride was added to both types of SiNCs using a simple mixing chemical route. To the best of our knowledge, this is the first investigation on mixing SiNCs with erbium ions (III) by this chemical method. Both SiNCs either C_{11}-SiNCs or commercial SiNCs and their mixtures with Er^{3+} were investigated using Raman spectroscopy and photoluminescence (PL). The samples showed an orange PL emission

peak at around 595 nm which originates from Si. Er/SiNCs mixtures also exhibit a weak PL emission peak at 1536 nm which originates from the intra-4f transition in erbium ions (Er^{3+}). The PL peak of Si in Er/C_{11}-SiNCs and Er/Commercial SiNCs mixtures are increased in the intensity up to four and three times, respectively as compared to pure C_{11}-SiNCs and commercial SiNCs. The collected data suggest that this chemical mixing route leads instead to a transfer of energy from erbium ions to SiNCs.

Metal-enhanced luminescence has been studied for mixtures of SiNCs (either C_{11}-SiNCs or commercial SiNCs) with silver nanoparticles (AgNPs). AgNPs of two different sizes were synthesised using photochemical reduction of $AgNO_3$ with sodium dodecyl sulphate (SDS). The synthesized AgNPs (1:5) and (10:50) have a polycrystalline structure with an average particle diameter of 100 nm and 30 nm, respectively. A significant enhancement up to 10 and 4 times in the PL intensity was observed for AgNPs (1:5)/C_{11}-SiNCs and AgNPs (10:50)/C_{11}-SiNCs, respectively using an excitation source of 488 nm. A similar observation was also reported for AgNPs (1:5)/Commercial SiNCs and AgNPs (10:50)/Commercial SiNCs; where the intensity of the PL signal increased up to 9 and 3 times respectively, using 488 nm; whereas the intensity of the PL signal increased up to 7 and 2 times respectively, using 514.5 nm excitation source. The enhancement in SERS intensities occurs as a result of the coupling between the excitation laser light and the plasmon bands of AgNPs; thus this intense field at AgNPs surface couples strongly to SiNCs. The results show that the closer wavelength of the laser excitation source to the surface plasmon resonance absorption bands of silver nanoparticles the greater the emission intensity. Our study also suggests that the larger AgNPs (1:5) caused an optimum enhancement in PL intensity of both types of SiNCs.

Under continuous wave (CW) irradiation at 488 nm in a confocal microscope, both types of SiNCs show reversible photoluminescence fading behaviour. This can be interpreted by the same model originally proposed to describe luminescence intermittency, i.e., 'blinking'. When single particles are studied, this leads to the well-known blinking phenomenon as particles ionize and later discharge by electron-hole recombination. In an ensemble, the result is a reversible photofading as the initial photoluminescence I_0 decays to a steady-state I_∞ controlled by the relative rates of photoionization k_a and recombination k_{eh}. Evidence for this interpretation comes

from two observations: (i) upon cessation of the irradiation, electron-hole recombination occurs in the dark and the photoluminescence is regained when irradiation recommences and (ii) the initial and steady-state spectra are identical except for a scale factor. The photofading data can be modelled as a simple first order decay with a lognormal distribution of rate constants and therefore characterized by three parameters; $\langle k \rangle$ the modal rate constant, γ which measurs the spread of activiation free energies in units of RT and I_o/I_∞.

C_{11}-SiNCs and commercial SiNCs show enhanced luminescence when drop cast as films on glass slides in mixtures with Ag or Au nanoparticles. Such metal-enhanced luminescence is generally explained in terms of the large electric field near the metal surface upon excitation of the plasmon resonance and an increase in the radiative decay rate owing to the effect of the plasmon on the optical density of states. In this work, we find evidence for a third effect: the metal nanoparticles can act as a source of electrons and increase the time integrated luminescence intensity by increasing the rate of electron-hole recombination. In the presence of Ag and Au nanoparticles with alkyl-capped SiNCs, the modal rate constants $\langle k \rangle$ increase by factors of up to 4-fold and the ratios I_o/I_∞ decrease by factors up to 5-fold; this is consistent with an increase in the rate of electron-hole recombination facilitated by the metal nanoparticles acting as a source of electrons. It is also should be noted that the presence of either Ag or Au NPs with commercial SiNCs are less effective at enhancing the PL than alkyl-capped SiNCs due to the larger average particle size of commercial SiNCs.

Dedication

Thanks to my parents

Mohammed & Salha

For their moral support throughout my education life

Acknowledgements

First of all, I would like to express my thanks to Allah (God) for providing me the blessings to complete this work.

After four years, thanks for everyone who helped me make this thesis possible. My deepest thanks to my supervisor, Dr. Lidija Šiller (Reader in Nanoscale Science, School of Chemical Engineering and Advanced Materials, Newcastle University, United Kingdom) for her help, motivation and encouragement during the whole period of my research. I also offer my sincerest gratitude to my co-supervisor, Dr Benjamin Horrocks (Senior Lecturer, School of Chemistry, Newcastle University, United Kingdom), who has helped me realize the power of the critical thinking and whose valuable scientific advice has been always freely given. Without the assistance, patience and guidance of both, I have never been able to complete the work.

Special thanks to all members of the Nanoscale Science & Nanotechnology group in Newcastle University for their help and support during the whole period of the study (Dr. Ross Little, Dr. Sunthon Piticharoenphun, Dr. Yayuk Astuti, Dr. Naglaa Nasrallah, Dr. Noor Harun, Dr. Mohammed Alamiry, Gaurav Bhaduri, Xiao Han, Jabian Wang, Wipapron Phatvej). I would also like to extend my deepest thanks to School of Chemical Engineering and Advanced Materials for their support and excellent service during my study. I offer my sincerest gratitude also to Newcastle University for outstanding learning atmosphere and good facilities.

It is my pleasure to thank the Ministry of Higher Education, Saudi Arabia and Taif University for their funding on the PhD programme and the opportunity to pursue this degree in Newcastle University. I also thank all the staff in Saudi Cultural Bureau in London for their excellent service on documentary issues.

Lastly, I offer my great thanks to my parents Mohammed and Salha, My lovely husband Nawaf, My little princesses (Rawnaa, Layan and Rose), My brother Abbas, My sisters (Dr. Khadija, Dr. Kholod, Khawla, Abeer, Dr. Matokah, Alaa , Fatimah) and to my friends for their unconditional love, support and encouragement throughout my journey.

List of Publication

1- K. Abualnaja, B. Horrocks and L. Šiller, Metal-enhanced luminescence of silicon quantum dots: effects of nanoparticles and molecular electron donors & acceptors on the photofading kinetics, Journal of Nanotechnology, accepted, NANO-105257.

2- K. Abualnaja, B. Horrocks and L. Šiller, Silver nanoparticles-enhanced luminescence spectra of silicon nanocrystals, International journal of chemical, nuclear, metallurgical, and materials engineering, World academy of science engineering and technology, Vol 8, No 11, 2014, International Science Index.

3- K. Abualnaja, B. Horrocks and L. Šiller, Photoluminescence study of erbium-mixed alkylated silicon nanocrystals, International journal of chemical, nuclear, metallurgical, and materials engineering, World academy of science engineering and technology, Vol 9, No 2, 2015, International Science Index.

Contents

List of Figures

List of Tables

Glossary

AFM	Atomic force microscopy
AgNPs 1:5	Silver nanoparticles prepared photochemically using 1 mM $AgNO_3$ with mean particle diameter ≃ 30 nm
AgNPs 10:50	Silver nanoparticles prepared photochemically using 10 mM $AgNO_3$ with mean particle diameter ≃ 100 nm
AuNPs	Gold nanoparticles prepared by citrate reduction of gold (III) chloride
BE	Backscattered electrons
BF	Bright field
CCD	Charge-couple device
CDS	Chemical database service
CHA	Concentric hemispherical analyser
CW	Continuous wave
DCM	Dichloromethane
DF	Dark filed
DTGS	Deuterated triglycine sulphate
EELS	Electron energy loss spectroscopy
eV	Electron volt
FCC	Face centred cubic
FFT	Fast Fourier transform
FRET	Fluorescence resonance energy transfer
FTIR	Fourier transform infrared spectroscopy
FWHM	Full width half maximum
HAADF	High-angle annular dark-field
HOMO	Highest occupied molecular orbital
HRTEM	High resolution transmission electron microscopy
KE	Kinetic energy
LEDs	Light emitting devices
LSPR	Localized surface plasmon resonance
LUMO	Lowest unoccupied molecular orbital
NIR	Near infrared

NPs	Nanoparticles
PL	Photoluminescence
PMMA	Polymethyl methacrylate
PMT	Photomultiplier tubes
QDs	Quantum dots
SDS	Sodium dodecyl sulphate
SE	Secondary electron
SED	Secondary electron detector
SEM	Scanning electron microscopy
SERS	Surface enhanced Raman spectroscopy
SiNCs	Silicon nanocrystals
SiNPs	Silicon nanoparticles
SPR	Surface plasmon resonance
TEM	Transmission electron microscopy
THF	Tetrahydrofuran
TM	Tapping mode
tmhd	2,2,6,6-tetramethyl1-3,5-heptanedionato
UHV	Ultra high vacuum
XPS	X-ray photoemission spectroscopy
XRD	X-ray diffraction

Chapter 1

Introduction

In this introductory chapter, a brief review of semiconductor nanocrystals quantum dots is presented. Furthermore, the synthesis and the optical properties of silicon nanocrystals (SiNCs) are described. Metal enhanced luminescence of SiNCs is also highlighted. Additionally, enhancing the optical properties of SiNCs by erbium ions is investigated. Next, the motivations and the objectives of this thesis are provided. Finally, a brief summary of each chapter in the thesis is given.

1.1 Semiconductor nanocrystals quantum dots

Nanostructured materials have unique optical and electrical properties which are considerably different from the bulk materials. There are two main factors that influence the properties of nanoscale and bulk materials.[1] The first main reason is that the surface area of nanoscale materials is larger than the same mass of the materials in bulk form. Consequently, the chemical reactivity and electrical properties of nanomaterials will growth compared to that of bulk materials because the catalytic chemical reactions and functionalization processes mainly occur on the surface. The second principle factor is the quantum confinement effect. This effect plays an important role in the behaviour of nanoscale materials which have typically dimensions in the range between 1 and 10 nanometres. As a result of the quantum confinement effect, the optical properties and electronic structures of nanomaterials differ significantly from that of bulk counterparts.

Recently, there has been an increased interest on semiconductor nanocrystals which are known also as quantum dots (QDs) from the researchers due to their useful and interesting photophysical and electrical properties.[2-6] Thus, these particles are considered to be promising candidates in various application such as electronic, photonic devices and biological applications.[2-6] These quantum dots have also exhibited unique characteristics which related to their size that present enormous a big difference with their corresponding materials in the bulk form. However, the quantum dots (QDs) are defined as zero dimensional confined semiconductor nanocrystals and their sizes are typically 10 nm or less.[7] Additionally, their properties

are hybrid between the bulk solid and the molecules.[8] CdSe, PbS, GaAs and Si are different examples of the QDs from the periodic table.[9] Lawson *et al*[10] in 1960 was the first group to prepare lead telluride (PbTe) quantum dots; even though they didn't suggest this word but the size of these nanoparticles were around 0.03 µm. The term quantum dot was used in 1974 by the group of Efros[11]. In 1981 and 1983, the properties of QDs were reported by Ekimov *et al*[12] and Kuczynski *et al*[13]. The first synthesis of monodisperse crystalline CdSe QDs was achieved by Murray *et al*.[14] The work which given by Bruchez *et al*[15] and Chan *et al*[16] in 1998 was the initial publication work which disperse the QDs in the water; which making them promising species to use in biological applications.

Depending on the band gap energy (E_g) between the valence and conduction bands, the materials are classified into three groups i.e. insulators, semiconductors and metals.[17] At room temperature, the highest electronic energy level which is occupied with electrons and the lowest unoccupied electronic energy level are known as the valence band and the conduction band edges, respectively. These two bands are separated by the energetically forbidden zone known as the band gap. Thus, the difference between the top of the valence band and the bottom of the conduction band in the energy is referred to as the band gap. In order to generate an exciton (electron-hole pair), an electron must be promote from the valence band to conduction band, which clearly depends on the band gap energy.[7] Consequently, the generated positive hole in the valence band behaves as a charge carrier.

As mentioned previously, the interesting optical properties of semiconductor nanocrystals are found to be dependent on their quantum confinement effect. Thus, the quantum confinement affects the electrons in the quantum dots by restricting the movement of holes and electrons in all three dimensions.[18,19] Figure 1.1 presents the electronic structure of the quantum dots which is intermediate between the bulk solid semiconductor and molecules.[20] It is known that the molecules have discrete energy levels; while these bands are continuous in the solids. The electronic and optical properties in quantum dots are variable between the solid and molecule; thus the characteristics of QDs are greatly dependent on their size. The quantum confinement effect emerges when the radius of QDs is less than the critical quantum measurement called Bohr exciton radius as presented in figure 1.2.[8] The Bohr exciton radius varies

from 1 nm to 10 nm depending on the material[3]; for example, in the case of Si and CdSe, the quantum confinement effect appears when the radii of those particles are around 5 nm.[21] The Bohr exciton can be pictured as the lowest excited state in the solid which has an electron in the conduction band orbiting a hole in the valence band as in H atom where the electron orbits a proton.[8]

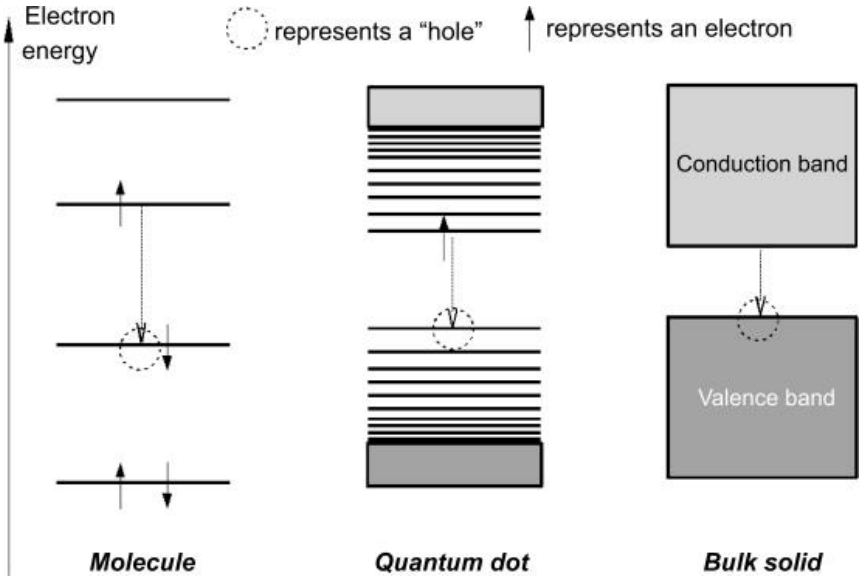

Figure 1.1: Schematic diagram presenting the energy levels of molecular dyes (left), quantum dots (centre) and bulk solid semiconductor (right).[8]

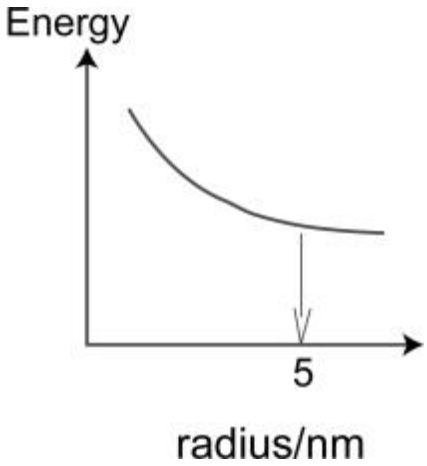

Figure 1.2: Diagram illustrating the difference of the energy which absorbed in semiconductor regarding to the radius of the nanoparticles.[8]

In quantum mechanics, the particle in a box model was used to describe the confined movements of the electrons in QDs in a small space.[22] Thus, the exciton (the electron-hole pair) in QDs which is generated as a result of the excited an electron

from the ground state valence band to the vacant conduction band by energy absorption can be pictured as a spherical box.[18] With decreasing the size of QDs, the quantum confinement effect increases the separation of energy levels which strongly impact the optical properties as the band gap increased which require more energy to generate an exciton.[3] Subsequently, the emission of photons (radiative recombination) shift to shorter wavelength and high energies. This unique property of the QDs is to produce the possibility to tune the emission wavelength to match the wavelengths in different regions such as IR, UV and visible spectrum by modifying their sizes.[7] The spectroscopic studies of crystalline CdS nanocrystals synthesised in silicate glasses were a first experimental evidence of quantum confinement effect.[23] This work by Ekimov *et al*[23] presented a blue shift up to 0.1 eV in the absorption spectrum of these clusters relative to their bulk. Corcoran[24] observed also that the absorption spectrum of CdS clusters shifts (blue shift) by 1 eV or more as the particles size are decreased. Furthermore, the characterization of luminescing semiconductors nanocrystals QDs such as CdS[25], CdSe[26], ZnSe[26] and Si[27] has obtained a great attention in last decade due to facile synthesis procedures, and size tunable excitation which making them useful in biological application and light emitting devices (LEDs).[28]

1.2 Silicon nanocrystals (SiNCs) synthesis

Silicon is one of the major materials whose various applications affect the world. This element is also dominant in the microelectronics industry and greatly influences our lives.[29] Silicon nanocrystals (SiNCs) can be synthesised using variety of methods which can be classified into two categories i.e. physical and chemical methods.[8] The former employ vacuum deposition techniques and/or high temperatures.[30, 31] The physical methods allow greater control over the nanoparticles size; although at the expense overall yield tend to produce small amounts of the nanoparticles which can be suitable for physical and electronic application. The latter typically produce great yields of the nanoparticles. The chemical composition of these particles most likely to be less well defined and the particle sizes are less controlled.[8] The resulted particles from the chemical routes are useful in the biological applications.[8]

Common SiNCs preparation methods are: laser ablation[32], reactive sputtering[33], sol-gel techniques[34], thermal vaporization[35], decomposition of silanes[36] and solution

synthesis[37]. Silicon nanocrystals that were investigated in this thesis were produced by electrochemical etching[27] of bulk silicon; thus the electrochemical etching method was reported below in more detail.

Porous silicon is considered to be a common starting point in the electrochemical etching and some chemical routes to produce SiNCs. In 1956, porous silicon was discovered by Uhlir[38] group at Bell labs in USA, where their research focused on the developing a technique for electro polishing and shaping the surfaces of Si and Ge in HF based solutions. They produced porous silicon by anodic etching of silicon wafer in fluoride media. Under certain conditions, Uhlir observed that the surfaces exhibit dark red-brown stains; at that time, this finding was not taken further. Typically, porous silicon luminesces due to quantum confinement effect and it is frequently defined as a nanocrystalline film. Individual Si nanoparticles can be extracted from the porous silicon by an ultrasound method. Thus, this route is the simplest way to produce Si nanoparticles which demand just a power supply (3 A, 30 V) to etch the silicon wafer and an electronic horn.[39]

Canham[40] observed that these porous silicon emits visible photoluminescence (PL) at room temperature. This red photoluminescence which is generated as a consequence of etching silicon wafers was considered to result from the small width of the pores which are $\sim$ 20 – 500 Å.[40] As the dimension of the pore walls is reduced to a few nanometres, the quantum confinement effect arises which increases the gap between the top of the valence band and the lowest conduction band. The produced emission has energy i.e. 2 to 3 eV which is higher than the band gap of bulk Si (1.12 eV). Typically, highly porous silicon exhibits a massive surface area which can be modified by chemical reactions as there is a wide range of literature on its surface chemistry.[8, 41] In general, the main limitation of porous silicon is its chemical instability and sensitivity to oxidation which reflects the presence of reactive Si-H bonds on the surface of porous silicon.[42] This drawback of porous silicon limits its use in applications. Thus, the surface modification of porous silicon is required.

Wolkin *et al*[43] synthesised porous Si quantum dots. In their research, the Si wafer was electrochemically etched at current densities of 5 – 80 mA cm^{-2} and the photo-assisted stain etching was performed by utilizing 10% - 25% HF: ethanol solution.

Ethanol (C_2H_5OH) is often added to HF in order to reduce the H_2 bubbles which form on the surface of the silicon wafer through the anodization and also to increase the wettability of the Si surface, which helps the pore penetration process, thus the homogeneity and the uniformity of porous layer can be improved.[44] Therefore, ethanol increases the porous layer uniformity. Furthermore, a halogen lamp (500 W) was used as illumination source to complete the stain etching and to raise the porosity. This group observed that as the size of Si quantum dots that existing in porous silicon changed, their PL tuned from near infrared (NIR) to the ultraviolet (UV) region. Additionally, a red shift (around 1 eV) in the photoluminescence measurements was observed when the Si quantum dots were exposed to O_2. Their wok shows that the electronic states of these quantum dots are influenced by both surface passivation and the quantum confinement effect. This experimental results were in a good agreement with the theoretical results which found that a new electronic state is formed when a Si=O is present on smaller Si quantum dots ($d < 3$ nm). Additionally, they suggested that the particles with smaller size emitted PL at higher wavelengths than expected due to presence of oxides which limits the observed photoluminescence energy to $\sim$ 2.1 eV.

Sweryda-Krawiec *et al*[45] prepared SiNCs colloidal solutions by sonication the porous Si wafers for 60 to 90 minutes in closed vials which contain degassed toluene (5 mL). This suspension of toluene turned into pale yellow during the sonication as porous Si broken up to individual SiNCs. Using alcohols, they modified the surfaces of SiNCs. The addition of 1-octanol, 1,12-dodecanediol, 1-hexadecanol and 1-undecanol at room temperature quenched the PL of SiNCs completely. Heating the SiNCs with those four additives resulted in formation of alcohol capped SiNCs with diameter range from 1 to 10 nm and with partially restored PL. AFM and TEM images showed that the formation of diol connected to 100 – 800 nm diameter of SiNCs agglomerates.[45]

Belomoin *et al*[46] prepared a group of individual sizes of hydrogen capped silicon (Si_nH_x) by electrochemical etching; where $n > 20$. These sizes are 1 nm for (Si_{29}) and 1.67, 2.15, 2.9 and 3.7 nm for (Si_{123}). Optical excitation and emission spectroscopy and direct electron imaging were used to characterize the particles. The emission bands and the band gaps of those particles were measured. From the smallest four luminescent particles, four ultra-bright colours were observed i.e. blue, green, yellow

and red. Belomoin *et al*[46] produced the blue particles by crumpling the silicon wafer in ultrasonic bath into colloidal suspension of ultra-small blue particles. The authors found that the formation of individual sizes and distinct emission in visible range make them useful for biomedical targeting.

Lie *et al*[27] obtained alkyl capped SiNCs by refluxing porous silicon which produced at high current densities in a dry toluene solution of alkenes. During the refluxing, the porous Si layer breaks up and the hydrosilation reaction of the alkene occur on the particle surface in order to produce a hydrocarbon monolayer. This monolayer served as a protection layer on the surface of SiNCs. Additionally, the alkyl chain is bound to the silicon by covalent bonds. They found that the alkyl monolayer on the surface of SiNCs rendered the aqueous hydrophobic but is nevertheless colloid lyophilic stable versus the flocculation over two weeks. Thus, this alkyl monolayer is a good candidate for surface modification of SiNCs as this monolayer is chemically robust and stable against the oxidation and hydrolysis except under intense X- ray irradiation.[47] 1-octene, 1-undecne, 1,9-decadiene and dimethoxytrityl-protected undecenol were used to produce luminescent SiNCs.[27] The dry yellow Si powder can be re-suspended in organic solvents such as dichloromethane and trichloromethane which are also stable against flocculation.[27] These particles emit bright red orange luminescence colour under UV lamp (λ = 365 nm) as presented in figure 1.3a.[27] Alkylated SiNCs display red-orange emission peak at around 670 nm; under UV excitation, which remains constant using different light wavelengths range from 280 to 370 nm (figure 1.3b).[27] These particles are small in the size as their Si core about 2.5 nm in diameter and the total particle diameter with undecyl monolayer is approximately 5 nm.[48] Figure 1.4 presents the ideal model of the alkylated SiNCs.[48] The alkylated SiNCs studied in this work were prepared at Newcastle University by this method reported in more details in chapter 2. It is worth to note that this process provides a cheap and simple route of a stable suspension of colloidal SiNCs comparing to many SiNCs production methods which comprise expensive techniques with relatively small volumes.

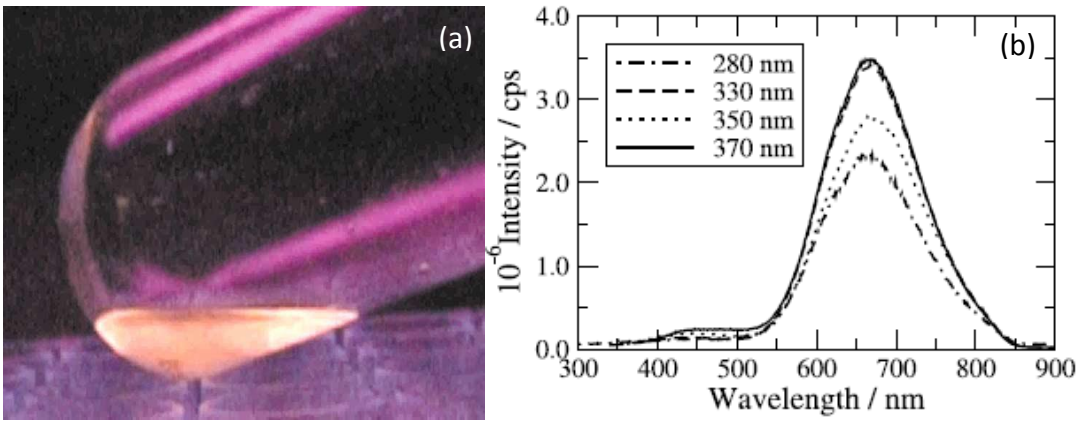

Figure 1.3: (a) Silicon nanocrystals capped with 1- undecene studied in this work dispersed in toluene, fluorescing orange colour under UV lamp (λ = 365 nm). The purple colour appears as a consequence of reflected light from the surface of the flask on the camera that used. (b) Emission spectra of silicon nanocrystals dispersed in trichloromethane (uncorrected). The corresponding excitation wavelengths are marked in nm.[27]

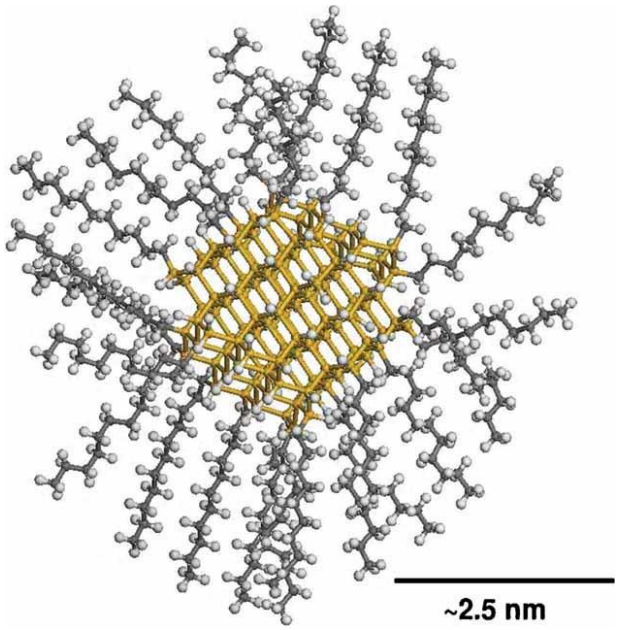

Figure 1.4: Schematic model of silicon nanocrystals capped with 1-undecene. The core diameter is around 2.5 nm and the total particle diameter with undecyl monolayer is approximately 5 nm.[48]

Sham *et al*[49] prepared white-light-emitting silicon nanoparticles (SiNPs) passivated with butyl groups by utilizing focused ultrasound. The authors observed that controlling the size of these particles leads to emission of white light from SiNPs. It was estimated that the average particle size of white-light-emitting SiNPs is about 2.7

nm with a wide size distribution from 1 to 5 nm. The sizes of these particles were small enough to display the quantum confinement effect of the silicon. The PL spectra of these particles covered a broad range from 320 nm to 700 nm.

Valenta *et al*[50] produced colloidal suspensions of SiNCs from light emitting porous silicon grains. They prepared the SiNCs by mechanical pulverization of electrochemically etched layers. The green PL peak which appeared at around 530 nm can be explained as a consequence of radiative recombination of electron-hole pairs inside SiNCs which have diameter of 2 nm. The authors used the single-molecule spectroscopy to study the photoluminescence of single grains of silicon nanoparticles. For this spectroscopic measurement, SiNCs were prepared by a drop-cast technique from highly diluted solutions. Furthermore, these concentrated colloidal suspensions of SiNCs enable the authors to fabricate the bulk Si with embedded Si nanoparticles and to synthesize self-organized nanostructures on the surfaces.

Kanoun *et al*[51] reported a low cost procedure to produce a monolayer of organized SiNCs located on a Si wafer. Using plasma etching and electron beam lithography led to form ordered arrays of nanoholes in a silicon nitride. A single SiNCs per each nanohole was performed using a short electrochemical etching current pulse. The average particle size of SiNCs is $\sim$ 10 nm. It also should be noted that the main advantage of this approach is controlling the location of SiNCs, the distance between them and their orientation. Thus, this process can be utilized in fabricating the electron devices.

Wang *et al*[52] are the first group to prepare Si nanoparticles using a green approach. They synthesized water-dispersible SiNPs using one-step reaction. This simple and quick reaction involves using mild reagents (3- aminopropyl) and ascorbate sodium without any treatments or any special equipment and at room temperature. The average diameter of those SiNPs is 2 nm and emits PL at 530 nm. They obtained that the lifetime of prepared SiNPs is longer than that of fluorophores which located in living cells. Thus, they suggested that these SiNPs is promising candidate in the living cells imaging.

1.3 Optical properties of silicon nanocrystals (SiNCs)

The alkylated silicon nanocrystals that were studied in this work and prepared by electrochemical etching of porous silicon[27] show orange-red luminescence when excited by a range of wavelengths. Taking into account the quantum confinement effect in these nanocrystals, their optical properties can be explained on the base of the band structure of bulk silicon.[29]

A diagram of electron energy (E) versus the electron wavenumber (k) for bulk silicon is presented in figure 1.5a. The bulk Si is presented by two bands i.e. valence band and conduction band. The former one is filled with electrons (occupied level) whereas the latter band is completely empty (unoccupied level). The gap between these two bands is called the band gap. In general, this gap can be either direct band gap or indirect band gap, depending heavily on the detailed of the band structure. In the direct band gap, the conduction band minimum directly lies up the valence band maximum (figure 1.5b); while in the indirect band gap there is a shift relative to the top of the valence band (figure 1.5a). Absorption of light by solid excites the electron from occupied level to unoccupied level. This absorption of light considered to produce only a vertical transition from valence band to conduction band due to the tiny momentum of these photons compared to crystal momentum of the electrons (ħk).

The band gap in bulk silicon at 1.1 eV is considered to be indirect and is not vertical transition due to the absorption of phonon (lattice vibration), where extra momentum is needed to change the crystal momentum of the electron (yellow horizontal arrow in figure 1.5a); where the transition in the direct band gap materials e.g. CdSe is vertical which reflects only the absorption of photons in these materials (figure 1.5b).[53] Therefore, the main consequence of the indirect gap in bulk Si is weak absorption emission. Silicon has also a direct band gap in which the electron can be promoted across this gap directly from the valence band to the conduction band but at higher energy (3.4 eV).

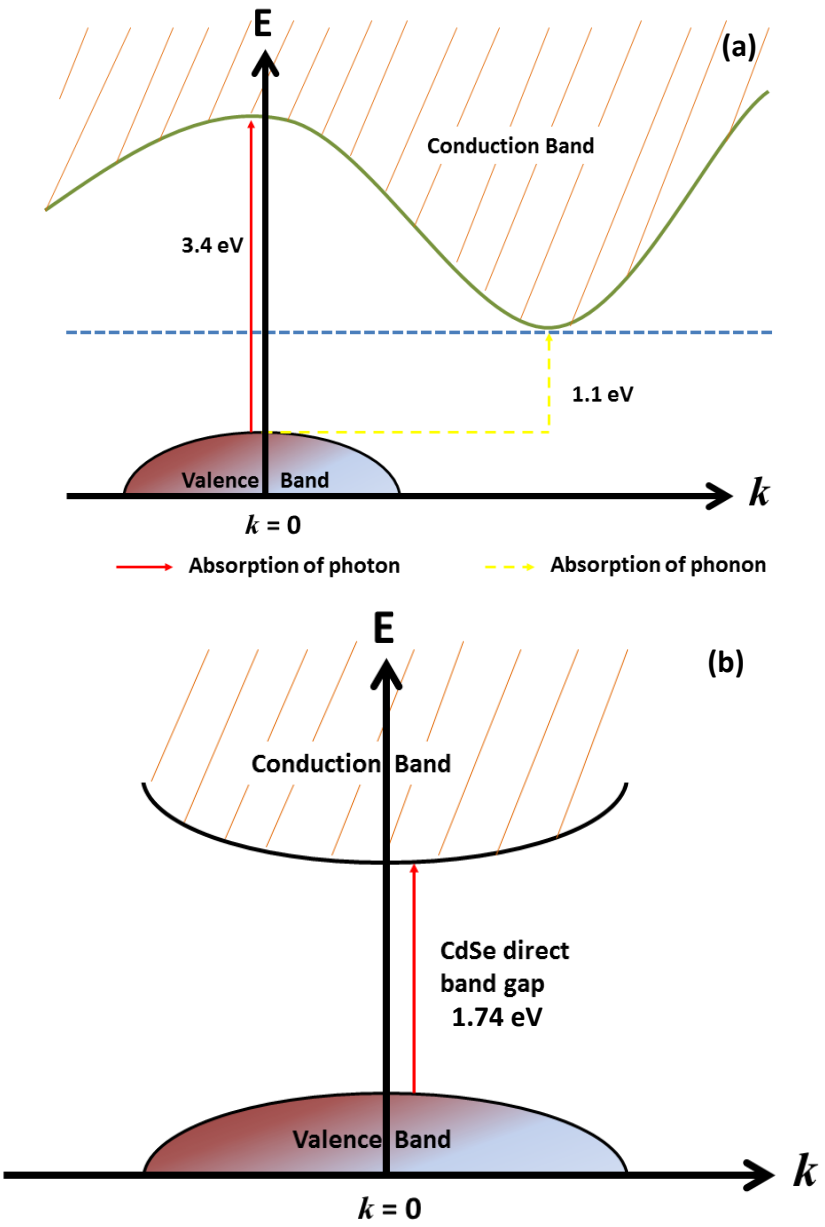

Figure 1.5: Electron energy (E) vs. the electron wavenumber (k) for a bulk Si (a) and bulk CdSe (b) showing the differences between the indirect band gap structure in silicon and direct band gap structure in cadmium selenide.

This electronic structure of the band gap is changed as the particles size of silicon is decreased.[29] Depending on the selection rule, the transition in low dimensional system of Si tends to be quasi direct.[29] However, in Si nanoparticles the size of the indirect band gap is increased due to quantum confinement effect. This leads to increase the indirect band gap size until approach the visible region at about 2.1 eV as observed for our prepared alkylated SiNCs in the Nanoscience lab at Newcastle University.[27] In contrast, the size of the direct band gap does not change considerably with the reduction of the particle size of Si because the maximum of the

conduction band located above the maximum of the valence band at k = 0.[29] It also should be noted that in the direct band gap materials such as GaAs and CdSe, the minimum of the conduction band located above the maximum of the valence band. Figure 1.6 presents the absorption spectrum of SiNCs which exhibits a weak and strong absorption for indirect and direct band gap, respectively. As mentioned above that the indirect band gap size of SiNCs is around 2.1 eV, thus the emission spectrum of Si nanoparticles appear at the wavelength correspond to this energy (600 nm).

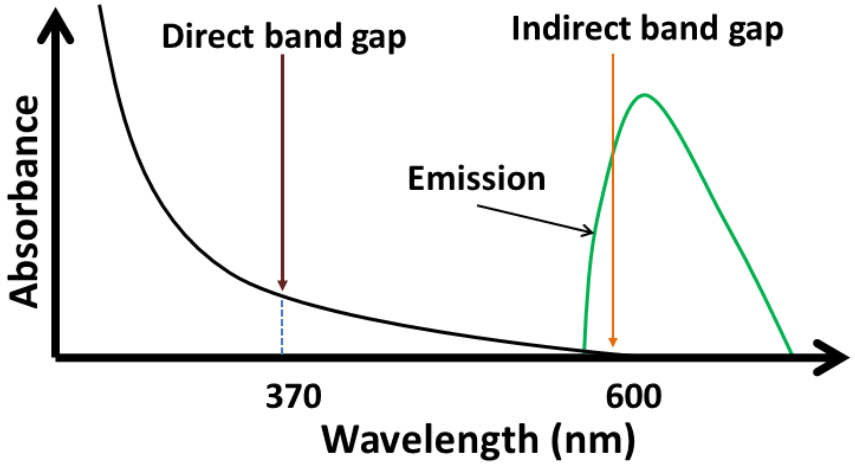

Figure 1.6: The absorption spectrum of silicon nanoparticles presenting the direct band gap and indirect band gap.

The origin of the photoluminescence which emit from silicon nanocrystals is still less understood compared to the direct band gap materials.[8, 54, 55] This is due to the fact that the preparation methods of direct band gap materials (e.g. CdSe) (i.e. precipitation reaction between the metal ions and hydrogen sulfide or hydrogen selenide) are highly developed compared to the chemical methods that are used to prepare SiNCs.[8] However, several models have been proposed to explain the origin of the photoluminescence in Si nanoparticles. For example, quantum confinement model in an indirect band gap of Si, interface state between the SiNCs and the surrounding environment and luminescent defect states.[56-60] Godefroo *et al*[60] indicates that the origin of the PL was due to defect related states. After removing the defects by modifying the surface with H_2 atoms, it was found that the quantum confinement effect was the dominant source for the PL.[60]

Beside the extensive research to find out the transition which is responsible for the photoluminescence, both theoretical and experimental investigations have claimed that the quantum confinement and the chemistry at the interface greatly influence the optical properties of Si nanocrystals.[61, 62] This means the PL process dominated by two mechanisms of the radiative recombination in SiNCs. Therefore, the electron-hole pair radiative recombination can occur inside the SiNCs due to quantum confinement effect or outside the nanocrystals due to interface state. Furthermore, their particular efficiency as a function of the size of SiNCs is not yet clear and their relative contribution in the PL process is not known.[55, 63-66]

The observation of the PL is mostly explained on the base of two major factors i.e. the quantum confinement effect and the interface state.[67] It is known that the indirect band gap (1.1 eV) in bulk Si is size dependent while it is not expected in direct band gap (3.4 eV) to be size dependent.[68] Thus, the size dependent photoluminescence studies have been important. Ledoux *et al*[69] provided convincing evidence that PL of SiNCs originates from quantum confinement model which is size dependent. In their study, the Si nanoparticles were synthesised by pyrolysis SiH_4 using a pulsed CO_2 laser in a gas flow reactor. Silicon nanoparticles were separated depend on their size ranging from 3 – 8 nm by applying fast spinning molecular beam chopper. The authors found that the PL blue shifted with reducing the particle size as their experimental results match well with the theoretical calculations. In addition, the spectroscopic studies which measured by Brus *et al*[53] and Sychugov *et al*[70] proved that the luminescence of SiNCs subject to quantum confinement model. Calcott *et al*[71] and Canham *et al*[40] found also that the radiative transition in highly porous silicon resulted from quantum confinement effect.

As the size of SiNCs plays a major factor in the transition process in PL process, also the surface chemistry of SiNCs is crucial. Si nanoparticles are quit common to be susceptible to oxidation from H_2O and the air.[72] Therefore, the role of the O_2 becomes important to assign the PL in SiNCs as the ratio of the surface to bulk increases which influence the nature of the luminescence.[8] There are two factors can considerably change the electronic behaviour of highest occupied molecular orbital (HOMO) and lowest unoccupied molecular orbital (LUMO). The first factor is presence of traces of oxides which affect the nature of the PL. The second effect is modulating the complete

surface with oxygen atoms. Traces of oxide has been studied by Wolkin *et al*[43], where silicon particles emitted red colour after exposure to O_2 due to presence of Si=O bonds which offer a new electronic state. They observed that this oxygen related electronic state minimized the maximum photoluminescence energy to around 2.1 eV, even though the diameter of Si less than 3 nm. In their study, the nature of the emission is not influenced by quantum confinement effect. The latter effect has been investigated theoretically by using density functional calculations for SiNCs range in diameter between 1.1 nm and 1.4 nm.[43] Zhou *et al*[73] investigated the properties of HOMO and LUMO of SiNCs as function of surface passivation. In particular, they compared OH terminated SiNCs with those having hydrogen atoms on the surface. Red emission was calculated for OH termination particles which reflected the dramatic decrease in the band gap; while blue colour was observed for H terminated Si nanoparticles.

However, the dominant source of the PL in SiNCs remains not clear as the experimental studies present some examples of blue PL which generated from oxidized SiNCs.[74, 75] In addition, some researchers[47, 72, 75, 76] expected that the oxidation of SiNCs shifted the luminescence from red to blue. This therefore can be explained as a result of decreasing the particle size with increasing the oxidation rate on the surface of SiNCs. The calculations of Zhou *et al*[73] also can be used in this situation to assign the blue PL peak to silicon oxides. Sham *et al*[49] and our group[47, 72] used X- ray and vacuum ultraviolet-excited PL in order to investigate the optical luminescence of silicon nanowires and alkylated SiNCs as these tools provide important information about the electronic states of Si nanoparticles. Our alkylated silicon nanocrystals that were prepared by electrochemical etching were subsequently oxidized. Thus, these SiNCs show two PL emission bands i.e. orange emission and blue emission.[72] It was estimated that the orange band associated to radiative recombination of the exciton inside the SiNCs due to quantum confinement effect; whereas the blue band attributed to silicon oxides on the surface of Si nanoparticles.[72] Figure 1.7 exhibits two intense PL bands of alkylated SiNCs illustrating the orange luminescence band at 600 nm and the blue luminescence band at 430 nm at 9 K.[72] It can be concluded that it is necessary to carry out comprehensive photophysical spectroscopic investigation on each new preparation method of SiNCs; as the surface chemistry of Si nanoparticles and the colour of their luminescence are not enough to reveal the nature of the PL.

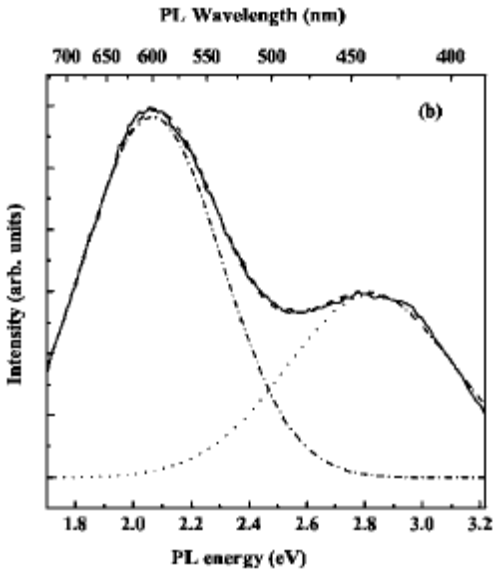

Figure 1.7: Photoluminescence spectrum of alkylated SiNCs at 9 K. The excitation energy = 21.2 eV.[72]

Semiconductor nanocrystals quantum dots (e.g. SiNCs) display also a luminescence intermittency by which the light emitted by a single nanocrystals because of continuous wave (CW) irradiation.[2, 77] The semiconductor nanocrystal switches between states of on and off in a random form as shown in Figure 1.8. It is worth mentioning that this universal property of semiconductor nanocrystals which has been termed as blinking became as highly important subject less than two decades ago, as this phenomenon gained the attention of Nirmal *et al*[78] and Efros *et al*[77]. The blinking happens because of photoionization of the excited particles to create a charged nanocrystals core that does not emit light. This occurs due to efficient energy transfer from photoexcited electron-hole pairs to the mobile charge carriers (most likely electrons).[2] The major restriction for the usage of semiconductor nanocrystals in different applications including biolabeling and optoelectronic devices is the long off period (dark state)[79-81], thus, semiconductor nanocrystals with non-blinking or reduced blinking characteristics would be beneficial to use the luminescence properties efficiently.[82] This blinking will be explained in further detail below.[2, 77]

When the nanocrystal is ionized along with luminescence is quenched by Auger non-radiative recombination, the model shows off periods (dark state). Whereas the bright state is concerned, this depends upon ionization rate of the nanocrystals through Auger autoionization.

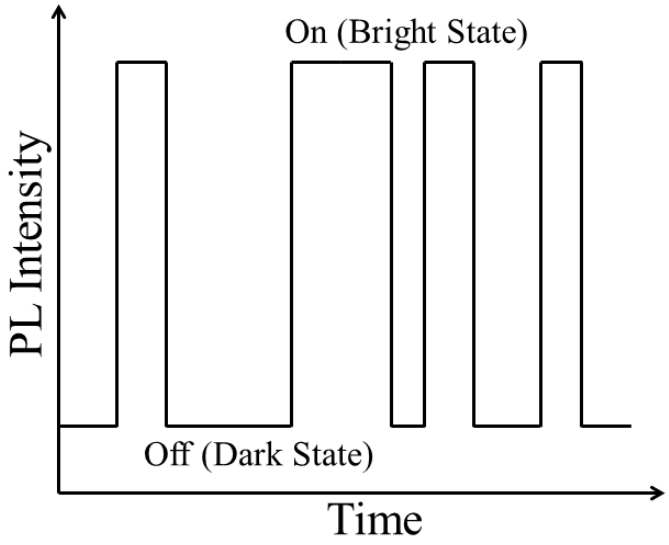

Figure 1.8: A graph presents the blinking effect of semiconductor nanocrystals in which the luminescence switches between on and off in a random manner under CW irradiation.

A single electron-hole pair has been produced as a consequence of promotion of an electron from the valence band to the conduction band by a nanocrystal which absorbs photon. Then, the electron returns to the valence band because of the recombination of the electron and hole. Where the nanocrystal is undergoing continuous wave excitation, it is likely to generate a second electron-hole pair before the first electron-hole pair recombines. This is to keep in mind that the excitation of a second electron-hole pair is not limited in silicon due to (high density of excited states that is continuous spectrum far from the band edge and the possibility of phonon assisted excitation of states which are out of resonance).[2, 77] The two pair phenomenon is very efficient in ionizing the nanocrystals as the energy released from recombination of the first electron-hole pair which transfers non-radiatively to second electron-hole pair. [2,72] This then ejects the electron from the nanocrystal. [2,72] It is important to recognise that the nanocrystal then has a positive charge. While in the charged nanocrystals, all Auger processes quench luminescence by interaction with the hole. Finally, the ejected electron returns to the nanocrystals and the PL recovers.

The intermittent light emission from silicon nanocrystals is similar to that in the direct band gap materials even though silicon had an indirect band gap and this is confirmed by Credo *et al*[83] and Cichos *et al*[84]. Cichos *et al*[84] observed that the emission intermittency in SiNCs (on and off times) was influenced by power law statistics. Their

research found that the dark state (off period) explained the photoionization in terms of Auger process and was intensity-dependent. In addition, they noticed that both blinking and emission recovery related to each other directly. Recently, Rostron *et al*[2] have investigated the emission intermittency of alkyl capped SiNCs which prepared by our method[27] at Newcastle University. They have subjected a film of SiNCs to CW excitation using two different excitation sources i.e. 488 nm and 633 nm for five minutes. They have described the intermittency of the luminescence (charging/discharging the silicon nanoparticles) of alkylated SiNCs as a reversible process. They have also suggested that off and on times can be due to an electron transfer process rather than any chemical reaction. They have interpreted the blinking and the recovery process of alkylated SiNCs based on Efros and Rosen[77] model, which considers three consecutive steps namely: photoabsorption, autoionization and electron-hole recombination.

The blinking of QDs is suppressed with the oligo ligands or thiol groups.[81, 85-88] The passivation of surface traps is created by ligand groups, and hence this causes suppression. Also, the enhancement of the photoluminescence and reduction of blinking of QDs have been reported which were deposited on the surface of metallic nanoparticles.[79, 89-91] The blinking of CdSe was reduced where there appears the covalent bonding with silver nanoparticles as observed by Fu *et al*[80]. This is due to the plasmon interaction which alters the energy gap between the exciton hole and trapped hole.[80] This then decreases the hole-trapping process leading to a suppression of the frequency of the blinking.

In this project, we treat the photofading of the luminescence under CW irradiation as a first order process, but with distributed kinetics. Each SiNCs particle may be either bright or dark according to whether it has undergoing photoionization [2] and the concentration of bright particles is proportional to the intensity of the luminescence (I).

1.4 Metal enhanced luminescence of silicon nanocrystals (SiNCs)

Semiconductor quantum dots are inorganic fluorophores that acquire distinctive photophysical properties which are valuable in an assorted array of applications.[80, 92-94] In order to expand the array of applications of inorganic nanoparticles, the combination of dissimilar nanoparticles having dissimilar functions within a complex nanoparticles are used. Multi component composite nanoparticles can show the way towards improvements and enhancements in the luminescence properties of individual inorganic nanoparticles.[94]

Silicon nanocrystals (SiNCs) are being intensively studied because of their potential as luminescent labels.[95] In particular, they may have advantages over the current technology (CdSe quantum dots) in applications due to their lack of cytotoxicity and smaller overall size as important factors.[48] Furthermore, a great attention has been focused into Si nanostructures since porous Si exhibit intense visible photoluminescence at room temperature.[40, 96] From this point of view, worldwide literatures have been investigated significantly silicon nanocrystals as light sources. Therefore, the unique optical properties of zero dimensional SiNCs which are different from the bulk silicon open the door to use them in biological sensors and light emitting devices.[2, 20, 32, 47, 72, 97] Subsequently, the bulk Si presents weak emission; while SiNCs with diameter less than 5 nm emit efficient visible PL at room temperature.[27] It is known that the luminescence characteristics of SiNCs depend upon their size and surface termination as discussed previously in 1.3. This helps to tune their emission frequency via part of the visible (Vis) and near infrared (NIR) spectrum by changing the size of SiNCs or their surface chemistry. This visible intense room temperature luminescence from SiNCs is associated to radiative recombination of quantum confined excitons.[98] However, Si nanocrystals suffer from the low radiative emission rates because of the indirect band gap of Si which limits the overall brightness of Si nanocrystals.[98-100] The indirect nature of the bulk Si band gap and the relatively long (of order 10 μs) radiative lifetimes observed in some preparations has been considered a disadvantage in applications where the PL of each particle is observed for only a short length of time.

There have been several attempts to improve the brightness of SiNCs by the technique of metal enhanced luminescence in which SiNCs are placed in close proximity to metal nanostructures (Ag, Au) which have a strong surface plasmon resonance in the visible spectrum.[94, 101, 102] Metal-enhancement of molecular fluorophores[103-106] and quantum dots[80, 89-91], including SiNCs[94, 98-100, 102, 107] has been observed. The mechanism of the effect is discussed as follow. The metallic nanoparticles exhibit interesting plasmonics properties which are associated with the interaction between the metal and the incident light which is commonly known as localised surface plasmon resonance (LSPR).[108] This phenomenon only occurs at the boundary between the metal nanostructures and their surrounding environment. The mechanism of this effect is attributed to coupling of the intense local electrical field of the surface plasmon resonance of the metal to the absorption and emission transitions. The surface plasmon resonance of silver and gold nanoparticles give rise to very large absorption coefficients and this alone can increase the brightness of the emitter through an increase in the rate of absorption.[99, 101, 109] This coupling has been found to be stronger when the wavelength of the incident radiation is near to the plasmon resonance of the metal; thus the enhancement of the emission from SiNCs can be observed.[110, 111] Therefore, this phenomenon can be resulted in several optical signal enhancements, such as surface enhanced Raman scattering (SERS), surface enhanced infrared absorption and surface enhanced fluorescence.[94, 108, 112-115]

The noble metal nanoparticles display unique and beneficial optical, magnetic, catalytic and electronic properties.[108, 116] Those properties are considerably different from their bulk form. In addition, the interesting properties of LSPR of metallic nanostructures make them attractive in different applications such as biological field, medicine, electronics, photonics, catalysis and sensing.[108, 117] Silver nanoparticles (AgNPs) and gold nanoparticles (AuNPs) are examples of metallic nanoparticles which first synthesised by Turkevich *et al*[118] method in 1951 and Lea *et al* in 1889.[119] Also, their solutions exhibit intense colours which are not appear in their bulk counterparts.[120] The properties of metallic nanoparticles are size dependent. For example, the bulk silver is grey while the colour of AgNPs which have diameter range from 35 nm to 50 nm is yellow.[121] This colour can be turned to dark yellow, violet and grey as the particle size of Ag nanoparticles increase.[121] Furthermore, the absorption

spectra of AgNPs and AuNPs exhibit a broad absorption bands in the visible region.[67] This change in the absorbance is due to LSPR of the metal nanoparticles and is size dependent.[108] Recently, Rycenga *et al*[108] have found that varying the dimension of AgNPs will influence the scattering and the absorption peak of LSPR. They have suggested that when AgNPs have diameter about 30 nm the absorption dominates scattering. However, AgNPs with a size range from 40 nm to 140 nm had a significantly higher scattering intensity compared to the absorption.[108]

LSPR can be defined as the collective oscillation of the free electrons of metallic nanoparticles under the influence of the wavelength of the incident light corresponding to the particle size as observed in figure 1.9.[108] This figure presents the LSPR of AgNPs as their particle size is much smaller than the wavelength of the applied electromagnetic field.[108] It is important to note that the strong electromagnetic field enhancements which lead to surface enhanced Raman scattering (SERS) is resulted mainly from LSPR of the metal nanoparticles.[67]

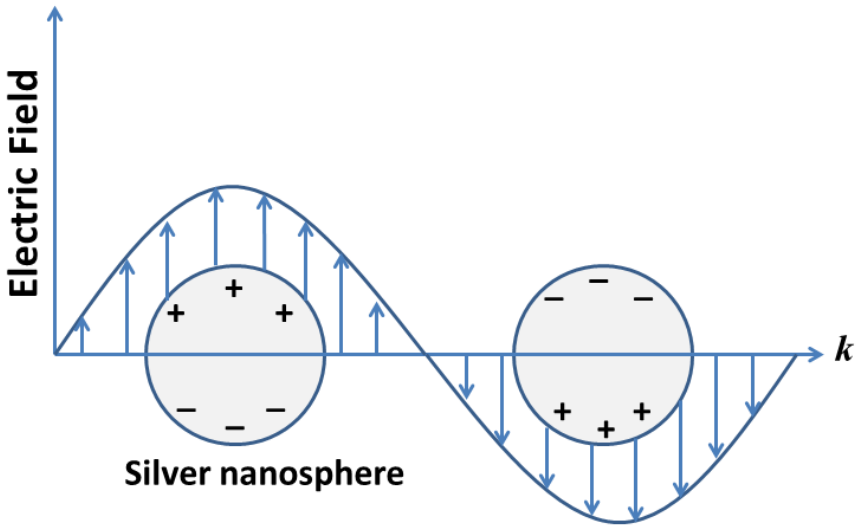

Figure 1.9: Schematic illustration of collective oscillation of the free electrons of silver nanoparticles that are excited by electric field incident light with wavevector (k). The size of AgNPs is less than the wavelength of the incident light and the electrons are in resonance with the light. This phenomenon is commonly known as localized surface plasmon resonance (LSPR) adapted from Rycenga *et al*[108]

It is known that the strong enhancement in Raman scattering which is known as SERS performed when the molecules adsorbed on rough noble metal surfaces.[122] In

1974, Fleischmann *et al*[76] discovered the effect of surface enhanced Raman scattering (SERS) from pyridine which adsorbed on rough silver electrode. They demonstrated that the magnitude of Raman scattering signal from the adsorbed molecules greatly enhanced up to 10^6. In 1977, Jeanmaire and Van Duyne[123] observed also a considerable enhancement in Raman scattering when the molecules located near or at silver substrate. Since the discovery of SERS, there is a debate between the researchers about the mechanism behind the Raman scattering enhancement; thus it remains an active research subject.[124-126]

There are two mechanisms that are responsible for the enhancement of Raman scattering i.e. the chemical enhancement and electromagnetic enhancement.[122] The first is a result of the interaction between the molecule and metallic nanoparticles which leads to changes in the electronic states of the molecule. In accordance with this change, a charge transfer state is formed between the adsorbed molecule and the metal nanoparticles. In this mechanism, Raman transition increases by providing a pathway for resonant excitation via the charge transfer state. The chemical enhancement can only be observed when the molecule is adsorbed directly on the surface of roughened metallic nanoparticles.[122] The second, and most important, mechanism is called electromagnetic enhancement, which is thought to arise from LSPR modes in the metals nanoparticles. LSPR are excited by incident light; subsequently a strong electromagnetic field is produced near the metallic nanoparticles. This results in increasing the inelastic Raman scattering of the molecules. It is believed that the electromagnetic enhancement contributes the most of the enhancement in Raman scattering signal (10^5 - 10^8) while the chemical enhancement introduce much less contribution (10 - 10^3).[108] In addition, Maitani *et al*[125] suggests that the electromagnetic effect enhances the Raman signal above 100 times compared to the chemical effect.

However, when the metal nanoparticles and semiconductor nanostructures are located near from each other and the surface plasmon is resonant with the incident radiation, the metal enhanced fluorescence is achieved.[94, 108, 112-115] From that perspective, it is necessary to choose a metal that provide a strong LSPR at the desired resonance wavelength.[127] Particularly, silver nanoparticles (AgNPs) are considered to be the most interesting metal in plasmonics amongst the noble metal

nanoparticles.[117, 128] This is because AgNPs support narrow LSPR in both visible and near infrared regions i.e. from 300 nm to 1200 nm.[129, 130] Furthermore, AgNPs offer intense SERS enhancements.[108, 117] Taking into accounts the advantages of AgNPs, Ag nanoparticles have been widely used in various applications such as SERS, optics, electronics and photography.[108, 131] However, there is another requirement in order to achieve efficient luminescence enhancement i.e. the incident light should be in resonance with absorption transition of the semiconductor fluorophore. Taking into account this requirement, SiNCs are ideal as their absorption spectrum presents an absorbance which increases gradually above the indirect band gap to reach around 2 eV as observed in alkylated SiNCs[27] that prepared at Newcastle University; subsequently only matching the wavelength of the excitation source with the plasmon mode of the metal is required.

Glass and co-workers[132] introduced the first experimental evidence of metal enhanced emission from the dyes Nile blue and rhodamine B that were adsorbed on AgNPs. They reported that the absorption spectrum of the dye was profoundly enhanced as a result of the coupling to Ag nanoparticles. Furthermore, the absorbance of the dye was still enhanced even the dye was separated from the metal by a 3 nm polymethyl methacrylate (PMMA); but the enhancement is less than the previous one. Glass and co-workers observed that the intensities of the luminescence from each dye reached their maximum when the resonance of AgNPs matches the absorption wavelength of each dye. Recently, metal enhanced luminescence i.e. AgNPs and AuNPs is not restricted to the emission of dyes but this enhancement has also exhibited in the emission intestines and radiative decay rates of semiconductor quantum dots.[79, 80, 89-91, 94, 107] Kulakovich *et al*[89] investigated distance-dependent photoluminescence enhancement from CdSe/ZnS nanocrystals which coupled to gold nanoparticles. Okamoto *et al*[90] reported also an enhancement in PL in CdSe quantum dots coupled to gold films. The PL intensities and PL decay rates of CdSe quantum dots were enhanced up to 23-fold and two-fold, respectively.

To-date investigations of metal-enhanced PL at SiNCs have focused on the steady-state spectra of single particles or ensembles and on measurements of the radiative lifetime. Biteen *et al*[99] presented the first evidence of metal enhanced luminesce of SiNCs. They observed that the local-field-enhanced light emission from

SiNCs near to film of nanoporous gold. They detected that the intensity of the luminescence from SiNCs enhanced up to four times; as the distance between the nanoporous gold and SiNCs varied from 0 to 20 nm. They interpreted this enhancement as a result of increasing the coupling between the SiNCs and gold. Because of the increasing in the SiNCs emission, they claimed that SiNCs are able to be competitive with the direct band gap materials emitters in light emitting devices (LEDs). Biteen *et al*[98] then examined metal enhanced luminesce of Si quantum dots using silver island arrays. They determined an enhancement up to seven times in the photoluminescence intensity of SiNCs. This enhancement is attributed to coupling Si quantum dots to AgNPs which fabricated by electron beam lithography. The emission frequencies of silicon are corresponding to collective dipole plasmon resonance frequency of the nanoscale Ag array. Subsequently, they outlined that the observed enhancement in PL intensity of Si quantum dots is produced as a result of increasing the radiative decay rate of the Si quantum dots. Mertens *et al*[102] later observed a polarization-selective photoluminescence intensity enhancement when Si quantum dots coupled to elongated AgNPs. They found that the observed polarization dependence gives direct evidence that the photoluminescence enhancement is attributed to coupling of SiNCs with Ag nanoparticles. From this behaviour, they suggested the ability to engineer the plasmonics metal nanostructure in order to tune and improve the performance of light sources via optimizing the absorption and emission rates.

Mochiznki *et al*[133] studied the effect of Ag nanotriangles and Au nanovoids array that are both prepared by nanosphere lithography on the PL properties of SiNCs. They observed that the PL intensity of SiNCs enhanced in both types of metal nanoparticles. In particular, the samples that contain Ag nanotriangles have been reported the largest PL enhancement up to 3-fold. This is because the incident excitation wavelength matches well with the wavelength of LSPR of Ag. Whereas, for the samples that contain Au nanovoids array, the origin of PL enhancement is mainly associated to radiative decay rates of SiNCs by sufficient excitation for SiNCs which then scattered effectively from SPR of Au. The effect of rough gold films that placed near from SiNCs on the enhancement of the PL of SiNCs is also studied by Ishikura *et al*.[110] In this work, different roughness of Au films were synthesised by electroless gold plating. The

photoluminescence intensity and the decay rate of SiNCs have been increased as the roughness of Au films increased. The largest enhancement has been achieved when the wavelength of the excitation source corresponds to that of SPR of gold films. Recently, our group have observed large enhancement 15-fold for SiNCs encapsulated with Au nanoparticles in polymer lattices.[94] This enhancement is occurred because the excitation light coupled to the plasmon band of the AuNPs and in turn the intense field at the AuNPs surface couples strongly to the SiNCs. In the absence of AuNPs, they have noticed weak absorption of the SiNCs at the laser wavelength (488) nm and scattering by only the polymer which produces a low PL intensity.

1.5 Enhancing the optical properties of silicon nanocrystals (SiNCs) using erbium ions (Er^{3+})

Use of materials for optical and electronic technology is an emerging field of research. Over the last two decades there has been a lot of literature that has been dedicated to development of this technology reviewed by Polman[134], Kenyon[135, 136] and Ray *et al*[137]. The optical communication allows data information transfer and processing at rates that are orders of magnitude higher than the current electronic systems.[137] The electronic systems, in this context, are the circuit systems that are used in modern computer technology (computer processors). It is expected that by using light to transfer data rates between logic devices has a higher rate than that of the electrical interconnects, bottle necking one of the major limitations in data transfer processes in traditional electronic systems. For example, a 1.5 μm optical signal has a corresponding optical frequency bandwidth of 10^{12} Hz that can be used to develop a new generation of optical communication networks.[138]

The major component in microelectronic and optical communication system is silicon. There are three limitations that are associated with silicon related to their use in optical communication system i.e. Si is an indirect band gap, strong non radiative recombination pathways resulting in a very short non radiative lifetime and there is a mismatch between the band edge luminescence at 1.1 μm (1.1 eV) and the wavelength of 1.55 μm (0.8 eV) that is a requirement for compatibility with optical communication system.[137] This number of factors makes this element a poor light emitter.

The limitation of the spectral mismatch is overcome by incorporating silicon with rare earth ions such as Er, Yb, Nd and Tm. Rare earth ions emission has been widely investigated in silicon last two decades.[134, 136, 137] Erbium ions especially have played a crucial role in the improvement of optical communication system, due to its luminescence band being at 1.54 μm which is the requirement in this technology. Erbium is 11th element in the series of rare earth elements which located in the sixth row of the periodic table and the electronic configuration of Er is [Xe]4f^{12}6s^{2}. It is known that Er presents intense narrow luminescence bands in both visible and near infrared regions.[139] The erbium has two oxidation states i.e. Er^{2+} and Er^{3+}, out of which the former one is very commonly seen in semiconductors; due to its radiative transition at around 1.54 μm which corresponds to the most interesting wavelength in photonics community. Losing one electron of 4f orbital and both of 6s orbital produces the trivalent erbium (Er^{3+}); thus in this ion the incomplete 4f orbital is shielded by 5s and 5p orbitals resulting in luminescence dependent host. The radiative transition of Er^{3+} in solid hosts looks like the free ion but with some changes due to Stark splitting.[140]

The labels of the energy levels in rare earth ions e.g. $^{4}I_{13/2}$ or $^{4}S_{3/2}$ correspond to their angular momentum and spin quantum numbers.[140] The letters here are attributed to the total orbital angular momentum of the ion. The total orbital angular momentum is resulted by adding the orbital angular momenta of the individual electrons in the ion following the Clebsch-Gordan series.[141] Thus, the letter S indicates the orbital angular momentum (*L*) of 0, P of 1, D of 2, F of 3 and etc. Therefore, the letter I presents an *L* of 6. The superscript number 4 denotes the possible orientation of the total spin angular momentum of the ion, which is given as 2*S*+1, where *S* is attributed to quantum numbers of spin. While the subscript presents the total angular momentum of the ion. Consequently, in rare earth ions, it should be considered that each discrete energy level is attributed to $^{2S+1}L_{J}$.[140]

Figure 1.10 presents the stark splitting of 4f^{11} of the electronic energy levels of triply charged erbium ion (Er^{3+}), showing the effect of the electric field in the host. This schematic presents the splitting of the ground state ^{4}I to 9/2, 11/2, 13/2 and 15/2 due to the crystal field of the host material.[134] The responsible transition of the strong emission band at about 1550 nm from trivalent erbium is corresponded to the

transition from $^4I_{13/2}$ to the ground state $^4I_{15/2}$. Furthermore, there are transitions in near infrared and visible regions; for example, the absorption peaks at around 980 nm, 800 nm and 545 nm associated to the transition from the ground state to $^4I_{11/2}$, $^4I_{9/2}$ and $^4S_{3/2}$, respectively.[142] However, these transitions are restricted in silicon and have a small value in the optical communication technology.[143]

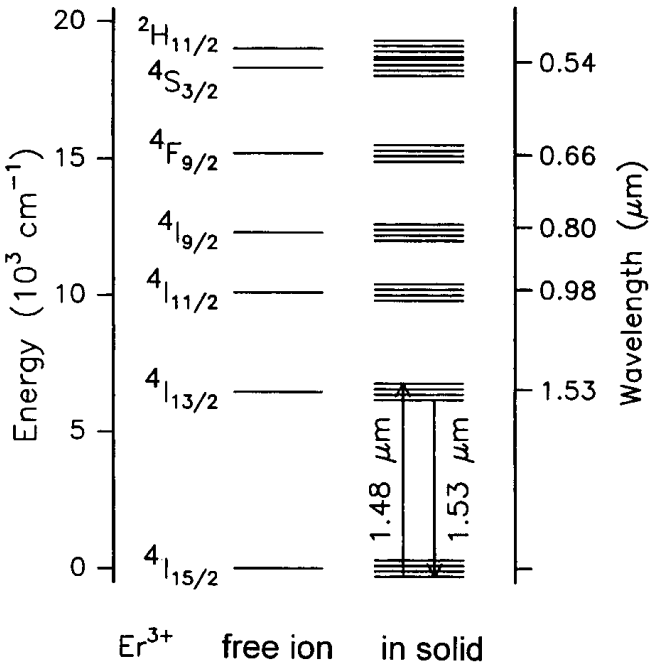

Figure 1.10: Diagram showing the energy levels of trivalent erbium. In the Er^{3+} free ion (left) the energy levels are sharp while the energy levels of Er^{3+} in a solid (right) are split due to the Stark effect.[134]

Commonly, the shapes of the energy levels of the rare earth ions affect the spectral line shapes as influenced by Stark splitting.[140] The Stark splitting of rare earth ions is formed as a result of the Stark effect. This effect is explained by the splitting and the changing of spectral lines which are caused by external electric field. Particularly, the energy levels of rare earth ions which are embedded in host solids split due to the crystal field of the host materials. Depending on the number of the electrons of the ion and the quantum number of the total angular momentum *J* of the energy level, the possible number of the Stark levels in the rare earth ions can be determined.[144] For example, the ground state $^4I_{15/2}$ of erbium ion (Er^{3+}) splits into a maximum of eight Stark levels depending on the intensity and the symmetry of the crystal field of the host materials.[116]

As mentioned previously, the emission from trivalent erbium at 1554 nm (due to $^4I_{13/2} \rightarrow {}^4I_{15/2}$ transition in erbium) is a standard wavelength in the optical telecommunication system; thus it is important to achieve maximum enhancement in Er emission intensity i.e. long luminescent lifetime and high active concentration of erbium.[145] Recently, the investigation on enhancing the optical activity of erbium ions has been extensively reported.[20, 137, 143] The erbium emission can be increased by i) adding clusters which act as sensitizers for erbium excitation, ii) increasing the fraction of trivalent erbium by changing the local atomic environment and iii) optimizing the rate of erbium excitation by applying local field enhancement in presence of metallic particles.[143] The sensitization effect has recently become attractive subject because of the successful enhancement in erbium emission via range of sensitizers (host materials) including SiNCs, SiO_2 and Yb ions.[20, 145-147]

Among the host materials, Si has received particular interest since the discovery of 1.54 µm light emission in erbium doped silicon at 20 K in 1983 by Ennen and co-workers[148] and later they observed electroluminescence at 77 K in 1985.[149] In their work, molecular beam epitaxy was used to grow erbium in silicon. At that time, the emission from erbium doped silicon was not efficient at room temperature; therefore this domain stayed not active several years till the successful experiment that observed the erbium emission at room temperature by growth of erbium in SiO_2 using ion implantation technique.[150] This effective light emission from silicon based erbium (with sufficient high concentrations of Er) has led to a novel Si-based optoelectronics and light emitting diodes (LEDs).[151]

Taking into account the importance of 1.54 µm light emission from erbium doped silicon in optical telecommunication system, the mechanism of the energy transfer from Si to erbium has been explained as follow.[137] Generally, the mechanism of the erbium emission of erbium doped silicon is described as followed (see figure 1.11).[137] Firstly, exciton (electron-hole pair) is generated inside SiNCs by using an excitation source. Then, the exciton recombines radiatively which causes photon emission as the energy of the resulted photon depends on the size of Si nanocrystal. A part of radiative recombination energy of the exciton of SiNCs is transferred to 4f shell in trivalent erbium; thus exciting Er^{3+}. The emission of erbium at 1.54 µm then occurs as a result of the transition from $^4I_{13/2}$ to the ground sate $^4I_{15/2}$. It is also should be

noted that the amount of the energy transferred to Er^{3+} depends strongly on the concentration of erbium in the host material and the distance between Si nanocrystals and trivalent erbium as observed by Cerqueira *et al*[104, 105], Xu *et al*[20] and Garrido *et al*[103].

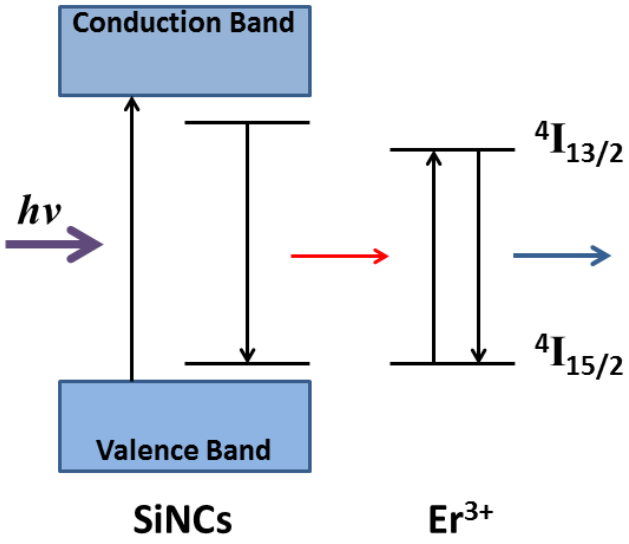

Figure 1.11: Schematic illustrating the energy transfer process from silicon nanocrystals to trivalent erbium. Adapted from Ray *et al*.[137]

There are several successful techniques that used to incorporate and to produce optically active erbium ions into SiNCs including molecular beam epitaxy[152], sputtering[105], chemical vapour deposition[104], thermal diffusion[153] and ion implantation[154]. It is known that the ion implantation is an effective method for the incorporation of Er^{3+} in the silicon film.[145] The main advantage of the method is that there is a great control over the position of the implanted material, but at the same time it introduces substantial damage to the matrix. High temperature annealing and molecular beam epitaxy are methods to overcome this limitation. The former method is rarely used as there are chances of erbium ions to aggregate within the matrix forming optically inactive clusters and silicides.[152] Thus, the latter is more used to overcome the damage introduced in the matrix during ion implantation, as it does not cause any damage to the implanted ions. In this present work, we use a new chemical route to mix SiNCs (either alkylated SiNCs or commercial SiNCs) with Er^{3+} by dispersing Si nanocrystals in tetrahydrofuoran (THF) and deionized water, respectively. Si nanocrystals then mixed with aqueous erbium tri chloride in order to observe any

change in the optical properties of SiNCs. To the best of our knowledge, there have been no reports on mixing SiNCs with erbium ions by this chemical route.

Fujii *et al*[155, 156] observed that Er-doped SiNCs films exhibit two emission bands i.e. 0.81 and 1.54 µm that associated to radiative recombination inside Si nanocrystals and to intra-4f transition ($^4I_{13/2} \rightarrow {}^4I_{15/2}$) in erbium ions, respectively. They studied the correlation between the intensities of the two luminescence bands as a function of erbium concentration. They found that the intensity of erbium emission band at 1.54 µm increased as the concentration of erbium increased, whereas the intensity of 0.81 µm decreased significantly. They suggested that the energy is transferred from Si nanocrystals to erbium ions. In contrast, Cerqueira *et al*[104, 105] found that the intensity of the emission peak of erbium increased with decreasing the erbium concentration. This provides also a clear evidence for the energy transfer from silicon to erbium. Also, they suggested that the intensity of this peak mainly depends on the chemical composition of the matrix where SiNCs are embedded in. However, Fujii *et al*[155, 156] and Cerqueira *et al*[104, 105] both observed that the PL peak of erbium ions was also more intense with small size of SiNCs embedded in silicon matrix.

John *et al*[157] and Ji *et al*[158] implanted Er^{3+} alongside SiNCs into SiO_2 films, where the SiNCs play as a sensitizer which absorb more photons efficiently. Thus, this leads to a significant improvement in the emission properties of Er ions as the erbium ions covalently bonded with SiNCs. In their work, Er-doped SiNCs samples exhibit NIR light emission which created by transfer energy from Si nanocrystal to erbium. John and co-workers[157] prepared erbium-doped SiNCs by the co-pyrolysis of disilane where $Er(tmhd)_3$ (tmhd = 2,2,6,6-tetramethyl1-3,5-heptanedionato) was used as a source of erbium ions. Transmission electron microscopy, selected area electron diffraction, photoluminescence and UV-Vis absorption spectroscopies have been used to characterize SiNCs. X-ray energy dispersive spectroscopy was used to confirm the presence of erbium. In addition, Ji *et al*[158] synthesised SiNCs by co-pyrolysis of disilane where erbium ions derived from erbium amidinate in a dilute He flow at 1000 °C. High resolution electron microscopy, selected area electron diffraction, energy dispersive X-ray and PL spectroscopy were used to characterize the samples. These two methods of preparation erbium-doped SiNCs provide high concentrations of erbium centred in given SiNCs, thus improvement in the light emission from Er^{3+} has been achieved.

Furthermore, they found that the structural and optical properties of SiNCs depend on the location of the erbium ions, where Er^{3+} directly excited by excitons if they dispersed over the Si nanocrystal.

Kik *et al*[111] produced SiNCs in silica using silicon ion implantation followed by high temperature annealing. Erbium ions then implanted into SiNCs doped SiO_2 layer. They found that the energy transfer from silicon to erbium ions by the mechanism of electron-hole pair radiative recombination inside SiNCs. In addition, they observed that electron-hole pairs excite erbium ions with efficiency larger than 55% and the maximum number of erbium ions around Si nanocrystals is near unity.

Kashtiban and co-workers[154] synthesised erbium-doped SiNCs in a silica matrix using ion implantation technique followed by high temperature annealing in N_2 atmosphere. The chemical composition and the distribution of implanted erbium have been investigated by high-angle annular dark-field (HAADF) imaging and electron energy loss spectroscopy (EELS). The sample shows intense PL emission band of Er^{3+} at 1.54 µm, as the Er in the film was found to be in an oxide form of Er_2O_3, surrounding Si nanocrystals. Xu *et al*[20] studied the structural and the opticl properties of erbium-doped silicon-rich silica containg different concentrations of Si. They obtained that the maximum optimization of the PL of Er^{3+} up to two times with the medium concentration of SiNCs.

1.6 The motivations and objectives

Due to the significant growing interest on silicon nanocrystals to be used in different applications including electronic, photonic devices and biological labels, it is desirable to synthesis these unique structures and investigate their own structural, chemical and optical properties. Furthermore, the previous studies attempted to enhance the emitted light from SiNCs by using metallic nanoparticles and rare earth ions. Thus, the motivation of this work is to use different methods to detect the enhancement in the light emission of Si nanocrystals.

The objectives of this work were as follow:

1- To synthesize alkylated SiNCs (C_{11}-SiNCs) by a galvanostatic anodization method followed by a thermal hydrosilation reaction.

2- To investigate the structure of commercial Si nanoparticles using different techniques.

3- To characterize the chemical composition and the optical properties of C_{11}-SiNCs and commercial SiNCs using different techniques.

4- To study the chemical change in C_{11}-SiNCs caused by erbium ions.

5- To detect the enhancement in the light emission of Er mixed SiNCs (both C_{11}-SiNCs and commercial SiNCs) using different techniques.

6- To study the metal-enhanced PL on both types of SiNCs caused by AgNPs.

7- To investigate the time dependence of photoluminescence of SiNCs over a period of time to determine if their photofading process is reversible.

8- To test the hypothesis that indicates the fading as well as recovery of the luminescence in SiNCs is caused by charging and photoemission the particles respectively rather than a chemical reaction.

9- To study the effect of the presence of metallic nanoparticles i.e. AgNPs and AuNPs, the electron donors i.e. ferrocene molecule ($FeC_{10}H_{10}$) and electron acceptors i.e. ferric chloride molecule ($FeCl_3$) on the photoluminescence fading of SiNCs over many minutes in terms of reducing the photofading and enhancing the luminescence.

10- To compare the kinetic measurements of SiNCs and their mixtures with metallic nanoparticles, electron donors and electron acceptors as well as to present comparison for C_{11}-SiNCs laboratory and commercial SiNCs. To the best our knowlege this work is the first demonstration of the effect of the electron donors and electron acceptors on the intermittency of light emission from C_{11}-SiNCs and commercial SiNCs under CW. Where many researchers have focused

on direct band gap semiconductors especially CdSe in the previous decade for making it usable in some applications for example in fluorescent labelling of biological specimen and optoelectronic devices.[80, 91, 159, 160]

1.7 Thesis overview

This thesis has 6 chapters; a short summary of each chapter is given as follow:

The first chapter consist of the background of semiconductor nanocrystals quantum dots. The synthesis and the optical properties of SiNCs are described. Metal enhanced luminescence of SiNCs and enhancing the optical properties of SiNCs by erbium ions are described.

The next chapter, chapter 2, presents the methods to prepare alkylated SiNCs, commercial SiNCs, AgNPs, AuNPs, $FeC_{10}H_{10}$ and $FeCl_3$. Furthermore, this chapter provides details of the experimental techniques that used throughout the thesis and the principles of their operation. This chapter also shows comprehensive details about the preparation methods of the investigated samples for all the spectroscopic measurements.

Chapter 3 presents the chemical characterization of synthesised C_{11}-SiNCs as well as the chemical composition of Er mixed C_{11}-SiNCs. Crystal structure, size distribution and the chemical characterization of commercial SiNCs are described. Furthermore, this chapter determines the structural and chemical characteristics of synthesised AgNPs.

In chapter 4, the optical properties of synthesised C_{11}-SiNCs, commercial SiNCs and their mixtures with aqueous $ErCl_3$ and AgNPs are presented. UV-Vis absorption measurements of C_{11}-SiNCs, commercial SiNCs and their mixtures with erbium ions and AgNPs are given. Photoluminescence (PL) measurements have been also investigated for C_{11}-SiNCs, commercial SiNCs and their mixtures with erbium ions. Furthermore, Raman and surface enhanced Raman spectroscopy (SERS) analyses have been studied for C_{11}-SiNCs, commercial SiNCs and their mixtures with $ErCl_3$ and AgNPs.

Chapter 5, presents the investigations of the enhanced PL observed in drop-cast films of SiNCs mixed with either noble metal nanoparticles (Ag, Au) or electron donor/acceptors (ferrocene/$FeCl_3$). This chapter test the hypothesis that electron injection into the SiNCs is responsible for diminution of the photofading and contributes to the overall PL enhancement.

In the final chapter 6, the overall conclusions of the project are highlighted from the previous three investigations followed by the potential future work.

References:

1. J. A. García-Calzón and M. E. Díaz-García, *TrAC Trends in Analytical Chemistry*, 2012, **35**, 27-38.
2. R. J. Rostron, Y. Chao, G. Roberts and B. R. Horrocks, *Journal of Physics Condensed Matter*, 2009, **21**, 235301.
3. A. M. Smith and S. Nie, *Accounts of Chemical Research*, 2010, **43**, 190-200.
4. M. Dasog, G. B. De Los Reyes, L. V. Titova, F. A. Hegmann and J. G. C. Veinot, *ACS nano*, 2014, **8**, 9636-9648.
5. H. C. Hao, W. Shi, J. R. Chen and M. Lu, *Mater. Lett.*, 2014, **133**, 80-82.
6. M. G. Panthani and B. A. Korgel, *Annu. Rev. Chem. Biomol. Eng.*, 2012, **3**, 287-311.
7. A. M. Smith, X. Gao and S. Nie, *Photochemistry and Photobiology*, 2004, **80**, 377-385.
8. N. O'Farrell, A. Houlton and B. R. Horrocks, *Int. J. Nanomed.*, 2006, **1**, 451-472.
9. F. Erogbogbo, C.-W. Chang, J. May, P. N. Prasad and M. T. Swihart, *Nanoscale*, 2012, **4**, 5163-5168.
10. F. A. S. a. A. S. Y. W. D. Lawson, *Journal of The Electrical Society,*, 1960, **107**, 206-210.
11. A. L. Éfros, *Advances in Physical Science,*, 1974, **16**, 789.
12. A. I. Ekimov and A. A. Onushchenko, *JETP Letters,*, 1981, **6**, 363-366.
13. J. P. Kuczynski, B. H. Milosavljevic and J. K. Thomas, *The Journal of Physical Chemistry*, 1983, **87**, 3368-3370.
14. C. B. Murray, D. J. Norris and M. G. Bawendi, *Journal of the American Chemical Society*, 1993, **115**, 8706-8715.
15. M. Bruchez, M. Moronne, P. Gin, S. Weiss and A. P. Alivisatos, *Science*, 1998, **281**, 2013-2016.
16. W. C. W. Chan and S. Nie, *Science*, 1998, **281**, 2016-2018.
17. C. Kittel, *Introduction to solid state physics*, Wiley, 1976.
18. A. P. Alivisatos, *Science*, 1996, **271**, 933-937.
19. D. Gammon, *Nature*, 2000, **405**, 899-900.
20. L. B. Xu, D. S. Li, L. Jin, L. L. Xiang, F. Wang, D. R. Yang and D. L. Que, *Nanoscale Res. Lett.*, 2014, **9**.
21. M. C. Beard, K. P. Knutsen, P. Yu, J. M. Luther, Q. Song, W. K. Metzger, R. J. Ellingson and A. J. Nozik, *Nano Letters*, 2007, **7**, 2506-2512.
22. A. P. Alivisatos, *The Journal of Physical Chemistry*, 1996, **100**, 13226-13239.
23. A. I. Ekimov, A. L. Efros and A. A. Onushchenko, *Solid State Commun.*, 1993, **88**, 947-950.
24. E. Corcoran, *Scientific American*, 1990, **263**, 03354.
25. J. Kakati and P. Datta, in *Transport and Optical Properties of Nanomaterials*, eds. M. R. Singh and R. H. Lipson, Amer Inst Physics, Melville, 2009, vol. 1147, pp. 316-322.
26. B. Bhattacharyya, P. K. Kalita and P. Datta, in *International Conference on Advanced Nanomaterials and Nanotechnology*, eds. P. K. Giri, D. K. Goswami, A. Perumal and A. Chattopadhyay, Amer Inst Physics, Melville, 2010, vol. 1276, pp. 124-130.
27. L. H. Lie, M. Duerdin, E. M. Tuite, A. Houlton and B. R. Horrocks, *Journal of Electroanalytical Chemistry*, 2002, **538–539**, 183-190.
28. D. J. Lockwood, *J. Mater. Sci.-Mater. Electron.*, 2009, **20**, 235-244.
29. L. Pavesi and R. Turan, *Silicon Nanocrystals: Fundamentals, Synthesis and Applications*, Wiley, 2010.
30. F. Priolo, T. Gregorkiewicz, M. Galli and T. F. Krauss, *Nat Nano*, 2014, **9**, 19-32.
31. A. M. Hartel, S. Gutsch, D. Hiller, C. Kübel, N. Zakharov, P. Werner and M. Zacharias, *Applied Physics Letters*, 2012, **101**, 193103.
32. K. Hata, S. Yoshida, M. Fujita, S. Yasuda, T. Makimura, K. Murakami and H. Shigekawa, *The Journal of Physical Chemistry B*, 2001, **105**, 10842-10846.
33. S. Furukawa and T. Miyasato, *Physical Review B*, 1988, **38**, 5726-5729.

34. D. Zhang, Z. Deng, J. Zhang and L. Chen, *Materials Chemistry and Physics*, 2006, **98**, 353-357.
35. L. N. Dinh, L. L. Chase, M. Balooch, W. J. Siekhaus and F. Wooten, *Physical Review B*, 1996, **54**, 5029-5037.
36. K. A. Littau, P. J. Szajowski, A. J. Muller, A. R. Kortan and L. E. Brus, *The Journal of Physical Chemistry*, 1993, **97**, 1224-1230.
37. R. A. Bley and S. M. Kauzlarich, *Journal of the American Chemical Society*, 1996, **118**, 12461-12462.
38. A. Uhlir, *Bell System Technical Journal*, 1956, **35**, 333-347.
39. J. L. Heinrich, C. L. Curtis, G. M. Credo, K. L. Kavanagh and M. J. Sailor, *Science*, 1992, **255**, 66-68.
40. L. T. Canham, *Applied Physics Letters*, 1990, **57**, 1046-1048.
41. Y. Masumoto and T. Takagahara, *Semiconductor Quantum Dots: Physics, Spectroscopy and Applications*, Springer, 2002.
42. D. P. Puzzo, E. J. Henderson, M. G. Helander, Z. Wang, G. A. Ozin and Z. Lu, *Nano Letters*, 2011, **11**, 1585-1590.
43. M. V. Wolkin, J. Jorne, P. M. Fauchet, G. Allan and C. Delerue, *Physical Review Letters*, 1999, **82**, 197-200.
44. K. Barla, G. Bomchil, R. Herino, J. C. Pfister and J. Baruchel, *Journal of Crystal Growth*, 1984, **68**, 721-726.
45. B. Sweryda-Krawiec, T. Cassagneau and J. H. Fendler, *The Journal of Physical Chemistry B*, 1999, **103**, 9524-9529.
46. G. Belomoin, J. Therrien, A. Smith, S. Rao, R. Twesten, S. Chaieb, M. H. Nayfeh, L. Wagner and L. Mitas, *Applied Physics Letters*, 2002, **80**, 841-843.
47. Y. Chao, S. Krishnamurthy, M. Montalti, L. H. Lie, A. Houlton, B. R. Horrocks, L. Kjeldgaard, V. R. Dhanak, M. R. C. Hunt and L. Šiller, *Journal of Applied Physics*, 2005, **98**, 044316.
48. N. H. Alsharif, C. E. M. Berger, S. S. Varanasi, Y. Chao, B. R. Horrocks and H. K. Datta, *Small*, 2009, **5**, 221-228.
49. T. K. Sham, S. J. Naftel, P. S. G. Kim, R. Sammynaiken, Y. H. Tang, I. Coulthard, A. Moewes, J. W. Freeland, Y. F. Hu and S. T. Lee, *Physical Review B*, 2004, **70**, 045313.
50. J. Valenta, P. Janda, K. Dohnalová, D. Nižňansky, F. Vácha and J. Linnros, *Optical Materials*, 2005, **27**, 1046-1049.
51. A. Ayari-Kanoun, D. Drouin, J. Beauvais, V. Lysenko, T. Nychyporuk and A. Souifi, *Applied Physics Letters*, 2009, **95**.
52. J. Wang, D. X. Ye, G. H. Liang, J. Chang, J. L. Kong and J. Y. Chen, *J. Mat. Chem. B*, 2014, **2**, 4338-4345.
53. L. Brus, *The Journal of Physical Chemistry*, 1994, **98**, 3575-3581.
54. M. J. Llansola Portolés, F. Rodriguez Nieto, D. B. Soria, J. I. Amalvy, P. J. Peruzzo, D. O. Mártire, M. Kotler, O. Holub and M. C. Gonzalez, *The Journal of Physical Chemistry C*, 2009, **113**, 13694-13702.
55. W. D. A. M. de Boer, TimmermanD, DohnalovaK, I. N. Yassievich, ZhangH, W. J. Buma and GregorkiewiczT, *Nat Nano*, 2010, **5**, 878-884.
56. E. G. Barbagiovanni, D. J. Lockwood, P. J. Simpson and L. V. Goncharova, *Journal of Applied Physics*, 2012, **111**.
57. G. Sahu, H. P. Lenka, D. P. Mahapatra, B. Rout and F. D. McDaniel, *J. Phys.-Condes. Matter*, 2010, **22**.
58. B. Rezgui, A. Sibai, T. Nychyporuk, M. Lemiti and G. Brémond, *Journal of Luminescence*, 2009, **129**, 1744-1746.
59. T. Schmidt, A. I. Chizhik, A. M. Chizhik, K. Potrick, A. J. Meixner and F. Huisken, *Physical Review B*, 2012, **86**, 125302.
60. S. Godefroo, M. Hayne, M. Jivanescu, A. Stesmans, M. Zacharias, O. I. Lebedev, G. Van Tendeloo and V. V. Moshchalkov, *Nat Nano*, 2008, **3**, 174-178.

61. J. Derr, K. Dunn, D. Riabinina, F. Martin, M. Chaker and F. Rosei, *Physica E: Low-dimensional Systems and Nanostructures*, 2009, **41**, 668-670.
62. R. Bardhan, N. K. Grady, J. R. Cole, A. Joshi and N. J. Halas, *ACS Nano*, 2009, **3**, 744-752.
63. W. Huang, W. Qian and M. A. El-Sayed, *Journal of the American Chemical Society*, 2006, **128**, 13330-13331.
64. A. Chaturvedi, M. P. Joshi, E. Rani, A. Ingale, A. K. Srivastava and L. M. Kukreja, *Journal of Luminescence*, 2014, **154**, 178-184.
65. L. M. Kukreja, A. Chaturvedi, B. N. Singh, A. P. Detty, V. P. M. Pillai, J. Sartor, H. Kalt and C. Klingshirn, *International Journal of Nanoscience*, 2011, **10**, 167-170.
66. S. Yang, W. Li, B. Cao, H. Zeng and W. Cai, *The Journal of Physical Chemistry C*, 2011, **115**, 21056-21062.
67. N. J. Halas, S. Lal, W.-S. Chang, S. Link and P. Nordlander, *Chemical Reviews*, 2011, **111**, 3913-3961.
68. Z. Ding, B. M. Quinn, S. K. Haram, L. E. Pell, B. A. Korgel and A. J. Bard, *Science*, 2002, **296**, 1293-1297.
69. G. Ledoux, J. Gong, F. Huisken, O. Guillois and C. Reynaud, *Applied Physics Letters*, 2002, **80**, 4834-4836.
70. I. Sychugov and K. högskolan., *Synthesis and Properties of Single Luminescent Silicon Quantum Dots*, Department of Microelectronics and Applied Physics, School of Information and Communication Technology, Royal Institute of Technology, 2006.
71. P. D. J. Calcott, K. J. Nash, L. T. Canham, M. J. Kane and D. Brumhead, *Journal of Physics: Condensed Matter*, 1993, **5**, L91.
72. Y. Chao, A. Houlton, B. R. Horrocks, M. R. C. Hunt, N. R. J. Poolton, J. Yang and L. Siller, *Applied Physics Letters*, 2006, **88**, 263119-263113.
73. Z. Zhou, L. Brus and R. Friesner, *Nano Letters*, 2003, **3**, 163-167.
74. D. C. Hannah, J. Yang, P. Podsiadlo, M. K. Y. Chan, A. Demortière, D. J. Gosztola, V. B. Prakapenka, G. C. Schatz, U. Kortshagen and R. D. Schaller, *Nano Letters*, 2012, **12**, 4200-4205.
75. L. Ondic, K. Kusova, M. Ziegler, L. Fekete, V. Gartnerova, V. Chab, V. Holy, O. Cibulka, K. Herynkova, M. Gallart, P. Gilliot, B. Honerlage and I. Pelant, *Nanoscale*, 2014, **6**, 3837-3845.
76. M. Fleischmann, P. J. Hendra and A. J. McQuillan, *Chemical Physics Letters*, 1974, **26**, 163-166.
77. A. L. Efros and M. Rosen, *Physical Review Letters*, 1997, **78**, 1110-1113.
78. M. Nirmal, B. O. Dabbousi, M. G. Bawendi, J. J. Macklin, J. K. Trautman, T. D. Harris and L. E. Brus, *Nature*, 1996, **383**, 802-804.
79. Y. Fu, J. Zhang and J. R. Lakowicz, *Chemical Physics Letters*, 2007, **447**, 96-100.
80. Y. Fu, J. Zhang and J. R. Lakowicz, *Chemical Communications*, 2009, 313-315.
81. S. Hohng and T. Ha, *Journal of the American Chemical Society*, 2004, **126**, 1324-1325.
82. Y. Matsumoto, R. Kanemoto, T. Itoh, S. Nakanishi, M. Ishikawa and V. Biju, *The Journal of Physical Chemistry C*, 2007, **112**, 1345-1350.
83. G. M. Credo, M. D. Mason and S. K. Buratto, *Applied Physics Letters*, 1999, **74**, 1978-1980.
84. F. Cichos, J. Martin and C. von Borczyskowski, *Physical Review B*, 2004, **70**, 115314.
85. K. T. Early, K. D. McCarthy, N. I. Hammer, M. Y. Odoi, R. Tangirala, T. Emrick and M. D. Barnes, *Nanotechnology*, 2007, **18**, 424027.
86. N. I. Hammer, K. T. Early, K. Sill, M. Y. Odoi, T. Emrick and M. D. Barnes, *The Journal of Physical Chemistry B*, 2006, **110**, 14167-14171.
87. M. Y. Odoi, N. I. Hammer, K. T. Early, K. D. McCarthy, R. Tangirala, T. Emrick and M. D. Barnes, *Nano Letters*, 2007, **7**, 2769-2773.
88. V. Fomenko and D. J. Nesbitt, *Nano Letters*, 2007, **8**, 287-293.
89. O. Kulakovich, N. Strekal, A. Yaroshevich, S. Maskevich, S. Gaponenko, I. Nabiev, U. Woggon and M. Artemyev, *Nano Letters*, 2002, **2**, 1449-1452.

90. K. Okamoto, S. Vyawahare and A. Scherer, *J. Opt. Soc. Am. B*, 2006, **23**, 1674-1678.
91. K. Ray, R. Badugu and J. R. Lakowicz, *Journal of the American Chemical Society*, 2006, **128**, 8998-8999.
92. T.-H. Chen, K.-W. Kuo, W.-T. Kuo, H.-Y. Huang and Y.-Y. Huang, *Journal of Bionanoscience*, 2008, **2**, 109-113.
93. R. Bakalova, Z. Zhelev, H. Ohba and Y. Baba, *Journal of the American Chemical Society*, 2005, **127**, 11328-11335.
94. N. A. Harun, M. J. Benning, B. R. Horrocks and D. A. Fulton, *Nanoscale*, 2013, **5**, 3817-3827.
95. F. Erogbogbo, K. T. Yong, I. Roy, G. X. Xu, P. N. Prasad and M. T. Swihart, *ACS Nano*, 2008, **2**, 873-878.
96. A. Cullis, L. T. Canham and P. Calcott, *Journal of Applied Physics*, 1997, **82**, 909-965.
97. S. Takeoka, M. Fujii and S. Hayashi, *Physical Review B*, 2000, **62**, 16820-16825.
98. J. S. Biteen, N. S. Lewis, H. A. Atwater, H. Mertens and A. Polman, *Applied Physics Letters*, 2006, **88**, 131103-131109.
99. J. S. Biteen, D. Pacifici, N. S. Lewis and H. A. Atwater, *Nano Letters*, 2005, **5**, 1768-1773.
100. J. S. Biteen, L. A. Sweatlock, H. Mertens, N. S. Lewis, A. Polman and H. A. Atwater, *The Journal of Physical Chemistry C*, 2007, **111**, 13372-13377.
101. D. M. Schaadt, B. Feng and E. T. Yu, *Applied Physics Letters*, 2005, **86**, 063106.
102. H. Mertens, J. S. Biteen, H. A. Atwater and A. Polman, *Nano Letters*, 2006, **6**, 2622-2625.
103. B. Garrido, C. García, P. Pellegrino, D. Navarro-Urrios, N. Daldosso, L. Pavesi, F. Gourbilleau and R. Rizk, *Applied Physics Letters*, 2006, **89**, 163103.
104. M. F. Cerqueira, M. Losurdo, M. Stepikhova, P. Alpuim, G. Andres, A. Kozanecki, M. J. Soares and M. Peres, *Thin Solid Films*, 2009, **517**, 5808-5812.
105. M. F. Cerqueira, T. Monteiro, M. J. Soares, A. Kozanecki, P. Alpuim and E. Alves, *physica status solidi (c)*, 2010, **7**, 683-687.
106. H. Horiguchi, T. Kinone, R. Saito, T. Kimura and T. Ikoma, in *Rare Earth Doped Semiconductors Ii*, eds. S. Coffa, A. Polman and R. N. Schwartz, 1996, vol. 422, pp. 81-86.
107. J. Goffard, D. Gérard, P. Miska, A.-L. Baudrion, R. Deturche and J. Plain, *Sci. Rep.*, 2013, **3**.
108. M. Rycenga, C. M. Cobley, J. Zeng, W. Li, C. H. Moran, Q. Zhang, D. Qin and Y. Xia, *Chemical Reviews*, 2011, **111**, 3669-3712.
109. C. Geddes and J. Lakowicz, *Journal of Fluorescence*, 2002, **12**, 121-129.
110. N. Ishikura, M. Fujii, M. Inui and S. Hayashi, *Photoluminescence properties of Si nanocrystals near rough Au films*, Materials Research Society Japan-Mrs-J, Tokyo, 2008.
111. P. G. Kik, M. L. Brongersma and A. Polman, *Applied Physics Letters*, 2000, **76**, 2325-2327.
112. B. Wiley, Y. Sun, B. Mayers and Y. Xia, *Chemistry – A European Journal*, 2005, **11**, 454-463.
113. A. M. Schwartzberg and J. Z. Zhang, *The Journal of Physical Chemistry C*, 2008, **112**, 10323-10337.
114. W. L. Barnes, A. Dereux and T. W. Ebbesen, *Nature*, 2003, **424**, 824-830.
115. W. A. Murray and W. L. Barnes, *Advanced Materials*, 2007, **19**, 3771-3782.
116. H. Przybylinska, W. Jantsch, Y. Suprun-Belevitch, M. Stepikhova, L. Palmetshofer, G. Hendorfer, A. Kozanecki, R. J. Wilson and B. J. Sealy, *Physical Review B*, 1996, **54**, 2532-2547.
117. I. Abdulhalim, *Small*, 2014, **10**, 3499-3514.
118. J. Turkevich, P. C. Stevenson and J. Hillier, *Discussions of the Faraday Society*, 1951, **11**, 55-75.
119. M. C. Lea, *American Journal of Science*, 1889, **Series 3 Vol. 37**, 476-491.

120. S. Link, M. B. Mohamed and M. A. El-Sayed, *The Journal of Physical Chemistry B*, 1999, **103**, 3073-3077.
121. M. C. Edmundson, M. Capeness and L. Horsfall, *New Biotech.*, 2014, **31**, 572-578.
122. C. L. Haynes, A. D. McFarland and R. P. Van Duyne, *Anal. Chem.*, 2005, **77**, 338A-346A.
123. D. L. V. D. Jeanmaire, R. P. , *J. Electroanal. Chem.*, 1977, **84**, 1-20.
124. A. Campion and P. Kambhampati, *Chemical Society Reviews*, 1998, **27**, 241-250.
125. M. M. Maitani, D. A. A. Ohlberg, Z. Li, D. L. Allara, D. R. Stewart and R. S. Williams, *Journal of the American Chemical Society*, 2009, **131**, 6310-6311.
126. J. A. Guicheteau, M. E. Farrell, S. D. Christesen, A. W. Fountain, P. M. Pellegrino, E. D. Emmons, A. Tripathi, P. Wilcox and D. Emge, *Appl. Spectrosc.*, 2013, **67**, 396-403.
127. S. Lal, S. Link and N. J. Halas, *Nat Photon*, 2007, **1**, 641-648.
128. H. K. Subramanian, 2013.
129. E. L. Ru and P. Etchegoin, *Principles of Surface-Enhanced Raman Spectroscopy: and related plasmonic effects*, Elsevier Science, 2008.
130. B. Wiley, Y. Sun and Y. Xia, *Accounts of Chemical Research*, 2007, **40**, 1067-1076.
131. G. A. Bhaduri, R. Little, R. B. Khomane, S. U. Lokhande, B. D. Kulkarni, B. G. Mendis and L. Šiller, *Journal of Photochemistry and Photobiology A: Chemistry*, 2013, **258**, 1-9.
132. A. M. Glass, P. F. Liao, J. G. Bergman and D. H. Olson, *Opt. Lett.*, 1980, **5**, 368-370.
133. Y. Mochizuki, M. Fujii, S. Hayashi, T. Tsuruoka and K. Akamatsu, *Journal of Applied Physics*, 2009, **106**, 013517.
134. A. Polman, *Journal of Applied Physics*, 1997, **82**, 1-39.
135. A. J. Kenyon, *Progress in Quantum Electronics*, 2002, **26**, 225-284.
136. A. J. Kenyon, *Semicond. Sci. Technol.*, 2005, **20**, R65-R84.
137. S. K. Ray, S. Maikap, W. Banerjee and S. Das, *J. Phys. D-Appl. Phys.*, 2013, **46**.
138. X. Z. Huang, J. Wu and J. L. Coffer, *Journal of Luminescence*, 2012, **132**, 3141-3147.
139. O. Savchyn, P. G. Kik, R. M. Todi and K. R. Coffey, *Physical Review B*, 2008, **77**, 205438.
140. H. Steinkemper, S. Fischer, M. Hermle and J. C. Goldschmidt, *New Journal of Physics*, 2013, **15**, 053033.
141. P. W. Atkins, V. Walters and J. De Paula, *Physical Chemistry*, Macmillan Higher Education, 2006.
142. S. V. J. Lakshman and C. K. Jayasankar, *Spectroc. Acta Pt. A-Molec. Biomolec. Spectr.*, 1984, **40**, 695-704.
143. L. B. Xu, L. Jin, D. S. Li and D. R. Yang, *Opt. Express*, 2014, **22**, 13022-13028.
144. G. H. Dieke and H. M. Crosswhite, *Appl. Opt.*, 1963, **2**, 675-686.
145. R. J. Kashtiban, U. Bangert, I. F. Crowe, M. Halsall, A. J. Harvey and M. Gass, in *Electron Microscopy and Analysis Group Conference 2009*, ed. R. T. Baker, Iop Publishing Ltd, Bristol, 2010, vol. 241.
146. D. S. Korolev, A. B. Kostyuk, A. I. Belov, A. N. Mikhaylov, Y. A. Dudin, A. I. Bobrov, N. V. Malekhonova, D. A. Pavlov and D. I. Tetelbaum, *Phys. Solid State*, 2013, **55**, 2361-2367.
147. F. Artizzu, F. Quochi, L. Marchio, E. Sessini, M. Saba, A. Serpe, A. Mura, M. L. Mercuri, G. Bongiovanni and P. Deplano, *J. Phys. Chem. Lett.*, 2013, **4**, 3062-3066.
148. H. Ennen, J. Schneider, G. Pomrenke and A. Axmann, *Applied Physics Letters*, 1983, **43**, 943-945.
149. H. Ennen, G. Pomrenke, A. Axmann, K. Eisele, W. Haydl and J. Schneider, *Applied Physics Letters*, 1985, **46**, 381-383.
150. P. M. Becker, A. A. Olsson and J. R. Simpson, *Erbium-Doped Fiber Amplifiers: Fundamentals and Technology*, Elsevier Science, 1999.
151. J. M. Ramirez, F. F. Lupi, Y. Berencen, A. Anopchenko, J. P. Colonna, O. Jambois, J. M. Fedeli, L. Pavesi, N. Prtljaga, P. Rivallin, A. Tengattini, D. Navarro-Urrios and B. Garrido, *Nanotechnology*, 2013, **24**.
152. S. A. Denisov, S. A. Matveev, V. Y. Chalkov, V. G. Shengurov, Y. N. Drozdov, M. V. Stepikhova, D. V. Shengurov and Z. F. Krasilnik, *Semiconductors*, 2014, **48**, 402-405.

153. H. Omar, N. K. Sabri, A. Radzi, M. Rusop, S. Abdullah and N. I. Ikhsan, in *Nanoscience, Nanotechnology and Nanoengineering*, eds. M. H. Mamat, Z. Khusaimi, S. A. Bakar, A. M. Nor, T. Soga and M. R. Mahmood, Trans Tech Publications Ltd, Stafa-Zurich, 2014, **vol**. 832, pp. 617-621.
154. R. J. Kashtiban, U. Bangert, I. F. Crowe, M. Halsall, A. J. Harvey and M. Gass, *Journal of Physics: Conference Series*, 2010, **241**, 012097.
155. M. Fujii, M. Yoshida, S. Hayashi and K. Yamamoto, *Journal of Applied Physics*, 1998, **84**, 4525-4531.
156. M. Fujii, M. Yoshida, Y. Kanzawa, S. Hayashi and K. Yamamoto, *Applied Physics Letters*, 1997, **71**, 1198-1200.
157. J. St. John, J. L. Coffer, Y. Chen and R. F. Pinizzotto, *Journal of the American Chemical Society*, 1999, **121**, 1888-1892.
158. J. Ji, R. A. Senter, L. R. Tessler, D. Back, C. H. Winter and J. L. Coffer, *Nanotechnology*, 2004, **15**, 643.
159. K. Zhang, H. Chang, A. Fu, A. P. Alivisatos and H. Yang, *Nano Letters*, 2006, **6**, 843-847.
160. A. K. Suresh, *Spectroc. Acta Pt. A-Molec. Biomolec. Spectr.*, 2014, **130**, 344-349.

Chapter 2

Experimental Methodology

In this chapter, the experimental techniques used throughout the thesis and the principles of their operation are described. Silicon nanocrystals prepared in the laboratory of the Chemical Nanoscience group at Newcastle University and Intrinsiq Ltd sample of silicon nanocrystals were characterized. Experiments to demonstrate different optical characteristics were carried out on both samples of silicon nanocrystals. The behaviour of silicon nanocrystals and their mixtures i.e. with erbium ions and metal nanoparticles under CW laser irradiation were studied as well as time-resolved luminescence fading characteristics. Structural characterization was performed using scanning electron microscopy (SEM), transmission electron microscopy (TEM), high resolution transmission electron microscopy (HRTEM), atomic force microscopy (AFM) and X-ray diffraction (XRD). Chemical characterization was performed also using X-ray photoemission spectroscopy (XPS) and Fourier Transform Infrared spectroscopy (FTIR). The optical characterization was performed using UV-Vis spectroscopy, Raman spectroscopy and photoluminescence (PL) spectroscopy.

2.1 Materials

Intrinsiq Ltd supplied SiNCs in the form of a crude powder. Erbium (III) chloride hexa-hydrate ($ErCl_3.6H_2O$), silver nitrate, sodium dodecyl sulphate (SDS), gold (III) chloride tri-hydrate ($HAuCl_4.3H_20$), sodium citrate, ferrocene and iron (III) chloride ($FeCl_3$) were purchased from Sigma Aldrich. All chemicals were analytical grade and used without further purification. Deionised water was used in all the experiments (nominal resistivity 18 MΩ cm, Nanopure™ purification system, Barnstead).

2.2 Preparation of samples

2.2.1 Preparation of alkyl SiNCs

A modified version of the method presented by Lie *et al*[1] was used to prepare alkyl-capped (11 carbon atoms) SiNCs. This method[2] forms C_{11}-SiNCs with the same optical characteristics with those explained in reference.[1] Porous silicon was formed by

anodic etching of silicon wafer in HF/EtOH. Alkylated silicon nanocrystals were extracted from the porous silicon by a thermal hydrosilation reaction in refluxing toluene.

A silicon chip 1×1 cm^2 was cut from a silicon wafer (boron-doped p-Si <100>, 10 Ω cm resistivity, Compart Technology, Peterborough, UK) using a diamond scribe. The silicon chip was then placed in electrochemical cell polytetrafluoroethylene (PTFE) with a diameter of 1 cm and using Viton™ O-ring at the base to seal against the silicon chip. Figure 2.1 shows the cell design that is used to etch the silicon chips.

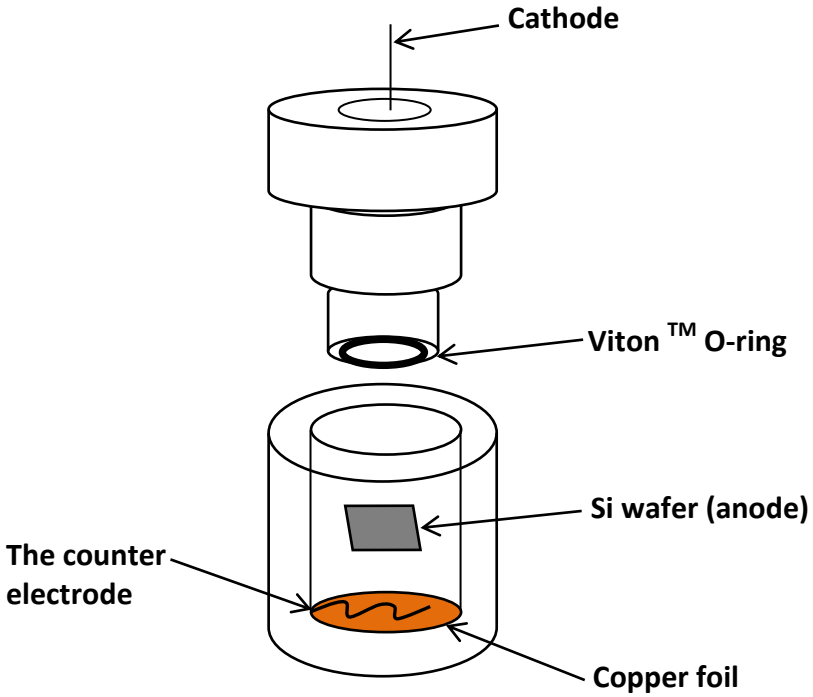

Figure 2.1: A diagram of the electrochemical cell that is used in etching the silicon chips.

In the cell, a total of 2 mL ethanol and hydrofluoric acid HF (1:1 V/V) solution was added. The electrochemical cell was linked to a power supply and control system (Keithley 2601 and Test Script Builder program) which were set at 400 mA for 5 minutes to etch the silicon and in order to improve the uniformity of the current distribution, a piece of tungsten wire coiled into a loop was used as a counter electrode.

After etching, a light orange colour was displayed at the surface of the porous silicon. The chip was cleaned with de-ionized water and dried with nitrogen gas as

shown in figure 2.2a. The dry porous silicon chips also luminesced orange under ultraviolet (UV) light (λ= 365 nm).

Four porous silicon chips were then refluxed in 25 mL of dry toluene solution (previously distilled over Na, Merck) which contained 0.4 mL of the alkene (1-undecene $C_{11}H_{22}$, 0.1 M, Merck) for four hours in a Schlenk flask (16 cm in length and 5 cm in diameter). The flask was placed on the magnetic stirrer hot plate linked to a refluxing condenser. During the refluxing time, a clear yellow liquid formed and a flow of nitrogen gas was present in order to keep air out of the Schlenk flask to avoid the oxidation of Si-H bond in Si chip. The boiling point of the solution was around 110 °C. Under the UV lamp (λ= 365 nm) an orange colour luminescence was emitted by the resulting suspension.

After the reflux, the solvent was decanted and transferred to another Schlenk flask. The flask then was placed on the hot plate at low temperature. The flask was also connected to vacuum pump at low pressure in order to evaporate the solvent and unreacted alkenes from this fluorescent solution. The remaining product after the evaporation process was silicon nanocrystals capped with a C_{11} alkyl chain, known as alkylated silicon nanocrystals. In order to dissolve the alkylated silicon nanocrystals from the surface of Schlenk flask, 10 mL of nonpolar solvents i.e. dichloromethane (CH_2Cl_2) was used. This solution was luminescent under UV lamp (λ = 365 nm) as presented in figure 2.2b. Per Si chip, It was estimated that 100 µg of alkyl SiNCs were typically formed.[3] Thus, the concentration of alkylated SiNCs used in the preparation is 0.04 g/L. This suspension of alkylated SiNCs in CH_2Cl_2 was kept in a vial before use.

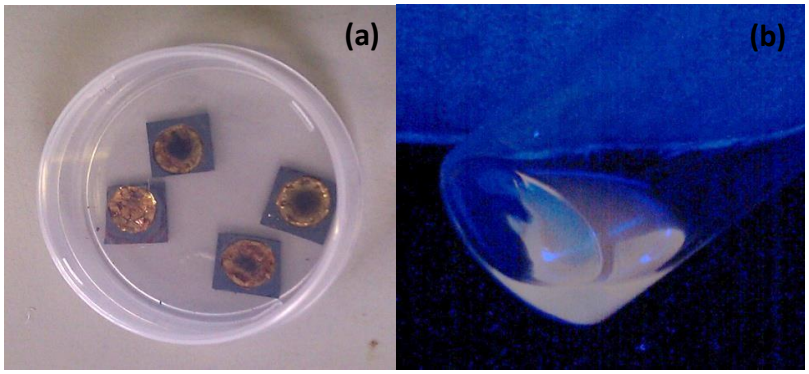

Figure 2.2: (a) A light orange colour was displayed by the surface of dry porous silicon after drying with nitrogen gas. (b) C_{11}-SiNCs in CH_2Cl_2 under UV lamp (365 nm). The blue colour appears as a consequence of reflected light from the walls of the flask on the camera.

2.2.2 Preparation of SiNCs suspension

To obtain well dispersed SiNCs, 3 mg of commercial SiNCs i.e. Intrinsiq Ltd was added to 10 mL of deionised water followed by sonication (Ultrasonic Processor Amplitude) for 10 minutes at 25% of maximum amplitude with a micro tip. Thus, the concentration of commercial SiNCs is 0.3 g/L.

2.2.3 Mixing with Erbium (III) chloride hexa-hydrate

Alkyl SiNCs were dissolved then in 200 µL of tetrahydrofuran (THF). Two beakers (each beaker was 15 mL. Fisher Scientific) were filled with 5 mL de-ionized water. (0.007 g, 4 mM, 10 mL) of $ErCl_3.6H_2O$ was added to first beaker and the second beaker was used for blank (i.e. without Er). 100 µL of C_{11}-SiNCs was added to each beaker. Thus, the concentration of C_{11}-SiNCs (0.08 g/L) kept constant during this study. These two beakers were placed on a magnetic stirrer plate for 2 minutes. Two glass vials then were utilized to keep the solutions. The same method has been used to prepare this mixture with commercial SiNCs. It also should be noted that the commercial SiNCs suspension was used immediately without dissolving it in THF. In addition, the concentration of commercial SiNCs (0.6 g/L) was kept constant during this project. The SiNCs/$ErCl_3$ mixture was dried in air on a glass slide coverslip for spectroscopic studies.

2.2.4 Preparation of silver nanoparticles

AgNPs were prepared according to the procedure described by Bhaduri *et al*.[4] AgNPs were synthesised using silver nitrate salt and sodium dodecyl sulphate (SDS) which were each dissolved in 100 mL of distilled water separately. The sealed sample vial that contains silver nitrate solution in added SDS solution (200 mL) was exposed to natural sunlight. The sunlight intensities which utilized in this experiment were ≈ 50.3 mW/cm^2 and the sunlight exposure time during the reaction was 1 hour. After around 10 minutes, a change in solution colour was noticed from transparent to light brown.

Throughout exposure to sunlight, the synthesis temperature of the vial was kept constant at 25 °C by using water bath (BS5, Fisher Scientist). The vials of synthesised silver nanoparticles were then kept in the dark. The concentration of $AgNO_3$ was 0.01 M and SDS was 0.05 M (SDS to $AgNO_3$ molar ratio 5:1) for all the experiments other than the one where the concentration of $AgNO_3$ and SDS was changed to 1 mM and 5 mM (SDS to $AgNO_3$ molar ratio 5:1).

2.2.5 Preparation of gold nanoparticles

The Turkevich method[5] was used for the synthesis of AuNPs. To obtain a yellow solution, $HAuCl_4.3H_2O$ (0.16 g, 0.41 mM) was added to boiling distilled water. The colour changed from light yellow to dark purple upon addition of 3.28 mM sodium citrate (34 mL) to the gold (III) chloride solution. To obtain a ruby-red colour aqueous dispersion of AuNPs, the resulting mixture was boiled for 30 minutes. The solution was allowed to cool and stored at room temperature. This protocol produces AuNPs with average diameter of about 20 nm.[5]

2.2.6 Preparation of ferrocene

1 mM of $FeC_{10}H_{10}$ solution was prepared by dissolving 0.002 g in 10 mL of CH_2Cl_2 .

2.2.7 Preparation of iron (III) chloride

In order to obtain 1 mM of the $FeCl_3$ solution, 0.002 g was dissolved in 10 mL of Nanopure water.

2.3 Principles of the techniques

This part describes the theory of the various characterization equipments that used in this project. The structural characterization comprises scanning electron microscopy (SEM), transmission electron microscopy (TEM), high resolution transmission electron microscopy (HRTEM), atomic force microscopy (AFM) and X-ray diffraction (XRD). While the chemical and optical characterization comprises X-ray photoemission spectroscopy (XPS), Fourier Transform Infrared spectroscopy (FTIR), UV-Vis spectroscopy, Raman spectroscopy and photoluminescence (PL) spectroscopy.

2.3.1 Scanning electron microscopy (SEM)

SEM was used to investigate the morphology and topography of the sample surfaces. In SEM, the information is obtained from secondary electrons (SE), backscattered electrons (BE), the X-rays as well as Auger electrons. The secondary signals occur due to the interaction between the electron incident beam and the sample as shown in figure 2.3.[6, 7] The electrons which are ejected from the surface of the specimen and have low energy are known as secondary electrons. The SE can reach the detector and SE was used to image the morphology and topography of the investigated sample. In contrast, the BE are electrons from the deeper region and contain high energy. The brightness of sample surface was also created by BE. In addition to SE and BE, X-rays are generated from the inelastic collision of the incident electron beam with inner shell electrons of the sample. Thus, the X-rays are utilized to determine the chemical composition of the sample.[7] In addition, X-rays may be used to measure the quantity of the elements that are present in the investigated samples.

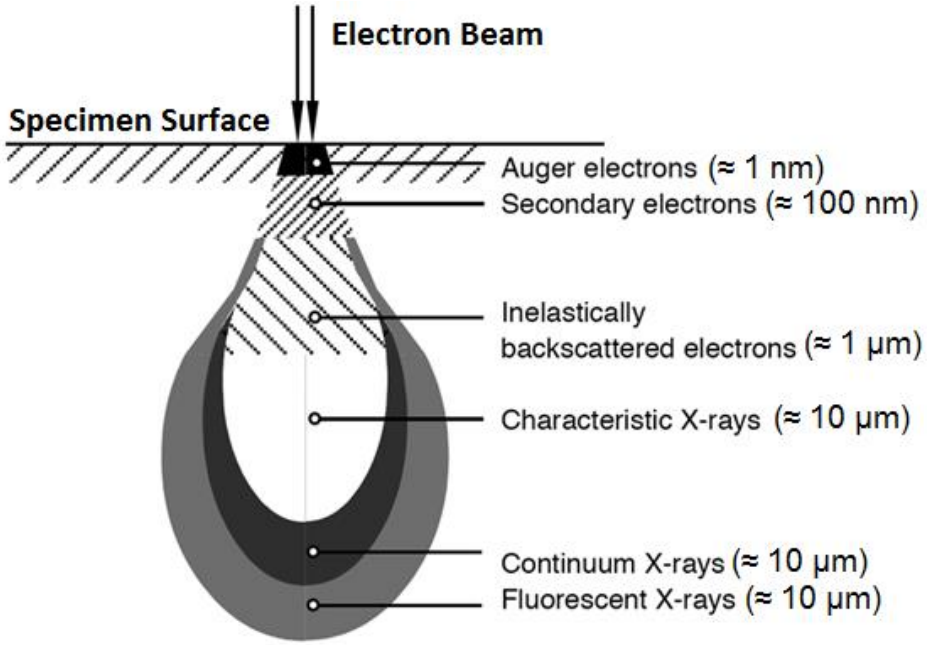

Figure 2.3: A diagram showing the secondary signals which are generated as a result of the interaction between the electron beam and the specimen (adapted from Reimer[6] and Dewar[8]).

It can be seen from figure 2.4 that SEM as an instrument comprises an electron gun, condenser lens, objective lens, scanning coils, a stage for the sample, detectors and display devices (computer).[9] The electrons are generated by using an electron gun under a high electric field. This gun which uses a sharp tip to generate electrons is known as a field emission electron gun.

In addition to the above, a spray pattern is produced by the electron gun, and the electrons must be focused on the investigated sample.[7] To achieve this, a set of condenser lenses and an objective lens are employed. The function of each lens differs; electrons are guided through the SEM column by the condenser lens, whereas the electrons are focused into the investigated sample using the objective lens. A raster scan pattern over the sample can be produced also by using scanning coils.[10]

As mentioned previously, the low energy SE which produced from the surface of the sample is occurring as a result of the interaction between the electron beam and sample. These electrons are used to produce signals which are recorded on a secondary electron detector (SED). The detector system of scintillator-photomultiplier amplifies the signals. The computer memory then stored this signal. These are actually numerical values that are converted into a digital image.[11]

In this project, SEM imaging was done using (FEI XL30-ESEM-FEG) at Newcastle University, United Kingdom which displayed in figure 2.5 to investigate the morphology and topography of commercial SiNCs. The sample was prepared by drop-casting 10 µL of SiNCs suspension in deionized water on aluminium support using a micropipette (Eppendorf) and left overnight to dry at room temperature. SiNCs were then coated with a thin layer of gold to prevent charging before the observation by scanning electron microscopy. The ImageJ program[12] was then used to measure the particle size of commercial SiNCs. The SEM images can be seen in chapter 3.

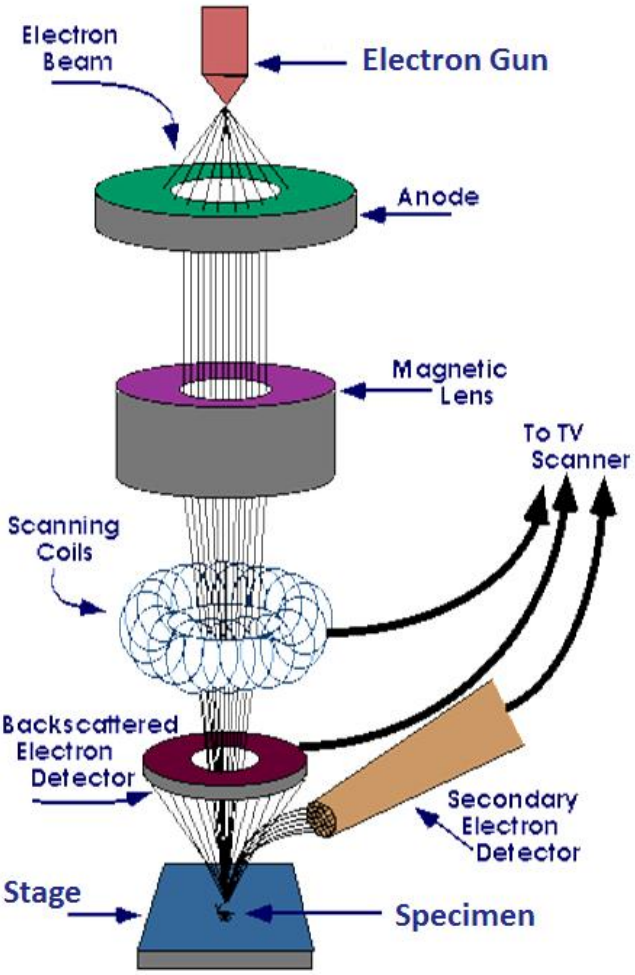

Figure 2.4: A diagram presenting the components of SEM equipment.[9]

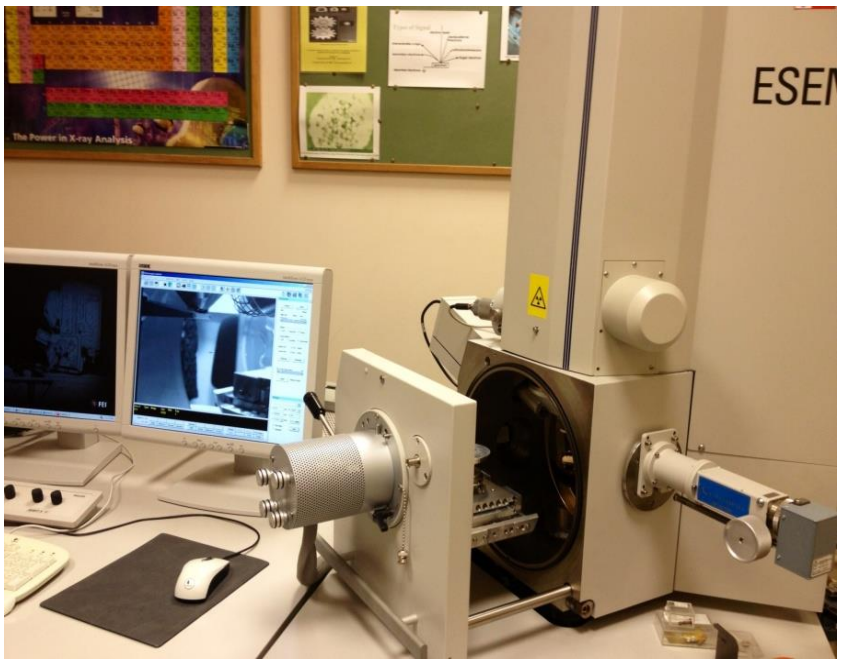

Figure 2.5: SEM instrument at Newcastle University.

2.3.2 Transmission electron microscopy (TEM)

The characterization of the materials in the nanometre range was carried out by TEM, which is a powerful technique.[13] The morphology, particle size and crystallographic structure can be determined by TEM. The sample must be thin to allow the incident electron beam to pass through; thick samples cannot be studied. Thus, there is a direct relationship between the thickness of the sample and the electron beam penetration. There are various forms of electron beam transmission including unscattered, inelastically and elastically scattered electrons. To produce the image, the elastically scattered electrons are detected.

In a typical TEM instrument there are four components : the illumination system, the sample holder, the objective lens and the TEM imaging detector.[7] Figure 2.6 shows the schematic arrangement of the TEM instrument.[7] Each of the components is described separately, where the illumination system consists of an electron gun and a condenser lens. The electron beam is generated by the electron gun. The beam is focused through a condenser lens and then onto the sample. The sample holder where the sample is located is the second compartment. The transmitted electrons can then be focused by an objective lens to produce high resolution images.

In TEM, the image projection and diffraction pattern projection are two types of the imaging modes which can be operated in the image formation. The purpose of these projections based on the aperture which utilized. The former is operated by occupying the objective aperture. The contrast of the image projection increased due to blocking the high angle diffracted electrons. While to operate the diffraction pattern projection, the selected area aperture is applied. The interaction between the electron beam and the arranged atoms of the sample produces periodic diffraction of electron in this mode of imaging.

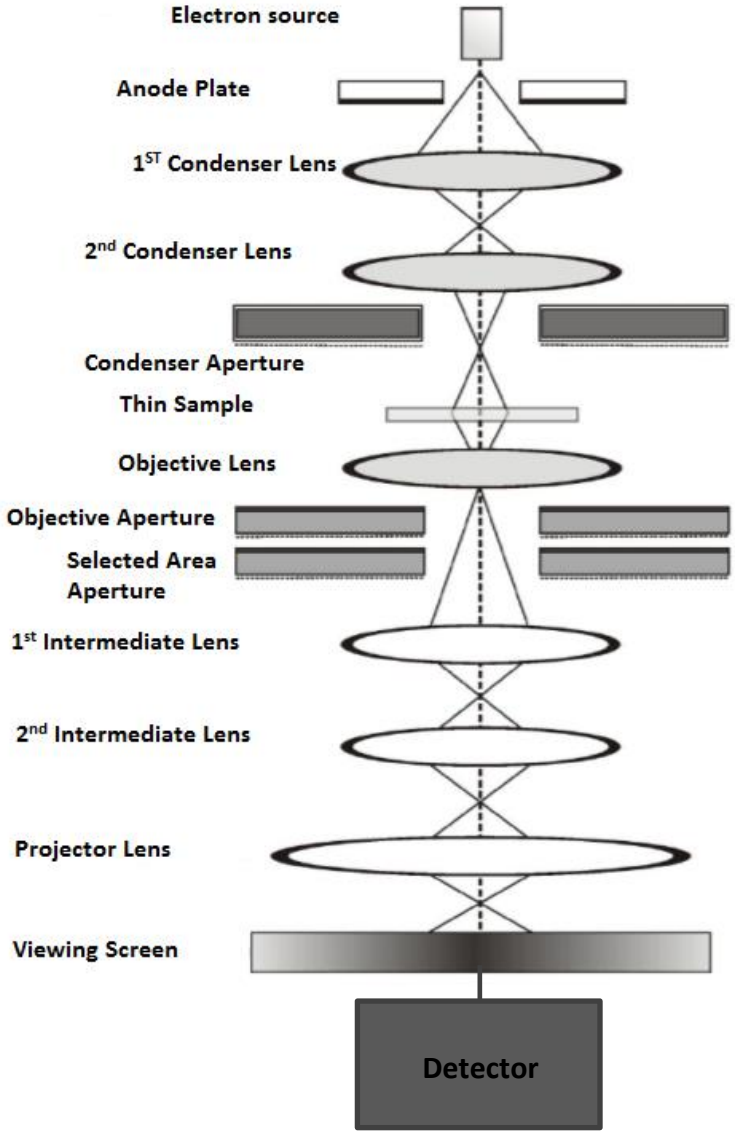

Figure 2.6: The schematic arrangement of the TEM instrument adapted from Chin *et al*.[7]

The TEM imaging system refers to the last compartment in this instrument. The image formed by the objective lens is projected and magnified using an intermediate lens and a projector lens on the viewing screen. The detector then converts these electrons to a visible light signal. Scintillator-photomultiplier systems and charge coupled devices (CCD) are used as detectors in TEM. The latter is now the detector of choice because of its low noise and high sensitivity.[14]

The imaging process in TEM instrument comprises three types i.e. mass thickness contrast, diffraction contrast and phase contrast.[15] These three types may produce different contrast in the image.

The mass thickness contrast is typically observed in the amorphous and crystalline samples.[15] In this phase, the enhancement of the contrast can be achieving when the diffracted beams from the objective lens contribute with transmitted beam to produce the image. This mechanism is occurs when setting the objective aperture of the objective lens on the optic axis. Thus, the investigated area that does not contain specimen will emerge bright. Therefore, this type of image is known as a bright field (BF) image.

The diffraction contrast can be applied for crystalline samples.[15] During this mechanism, the diffracted beam is the only permitted to travel via the objective aperture. Thus, this type of imaging contrast produces a dark field (DF) image. This type of the imaging also can be achieved when the objective aperture is not placed in the optic axis. Consequently, an investigated area which has only specimen will emerge bright.

In phase contrast, the transmitted electrons in various phases are used to create the image.[15] This mechanism can be achieved by removing the objective aperture or by providing a large objective aperture. Thus, the resulted beams either transmitted or diffracted easily travel through the objective aperture and the optical axis. This therefore detects the lattice fringes which assigned to the structure of the investigated samples.

Both SEM and TEM are two kinds of electron microscopy that use an electron beam to interrogate the sample.[15, 16] Thus, the electron gun, vacuum chamber,

condenser lenses and objective lenses are mainly used in those two instruments. As compared to scanning electron microscope, the transmission electron microscope gives information on the bulk of the sample rather than the surface of the sample. Around 2-40 keV is the required energy to accelerate the electrons in SEM instrument while about 80-200 keV in the TEM instrument.

In this project, TEM at Newcastle University, United Kingdom was used to investigate the microstructures of Intrinsiq Ltd commercial SiNCs. One drop of the SiNCs that dissolved in deionized water was dried onto a carbon-coated copper grid (Agar Scientific) and examined in a Philips CM100 transmission EM operated at 100 kV. Images were taken with an Optronics CCD camera 1824 x 1824 pixel with AMT40 version 5.42 image capture (Deben UK). The ImageJ program[12] was used to measure the particle size of commercial SiNCs. The images of TEM of commercial SiNCs can be seen in chapter 3.

2.3.3 High resolution transmission electron microscopy (HRTEM)

HRTEM technique is considered as another form of TEM. This technique can be utilized to determine the crystal structure of the crystalline samples. In HRTEM, the phase-contrast imaging mode is applied in order to obtain specimen images. The phase-contrast imaging mode as mentioned previously uses diffracted and non-diffracted beams to pass over the objective aperture and move along the optical axis in order to create interference which is used to develop the contrast in the image.[17] The finally constructed image could have the following shapes as parallel or crossing lines. These parallel and crossing lines also known as parallel fringes and crossing fringes respectively. The parallel lines are associated to maximal and minimal intensity while the spacing d between the lines correlated to lattice spacing of the crystallographic planes. The beams of diffracted and non- diffracted beams give rise to the crossing fringes in the objective aperture. The crossing fringes are attributed to maximal and minimal intensity of the pattern.

However, the orientation of crystal lattice planes is demonstrated by the crossing fringes. In order to measure d, the following equation is applied[16]:

$$r\,d = L\,\lambda \qquad 2.1$$

Where r is a characteristic for a particular specimen and obviously it is inversely proportional to the d lattice spacing of the specimen.[16] L is the camera length known as a camera constant and it can be altered for the microscope. λ is the wavelength of the electron beam. Using a chemical database service (CDS), the Miller indices of the investigated specimen can be explained depend on the d spacing values.

In this project, high resolution transmission electron microscopy was carried out at the Materials Science Centre at Manchester University, United Kingdom using a Tecnai F30 300 keV microscope. One drop of commercial SiNCs that dissolved in deionized water was added on the grids (Agar Scientific) using a micropipette (Eppendorf) and dried overnight in room temperature. To calculate d spacing from HRTEM images, the ImageJ program was used.[12] The Miller indices then were obtained from the chemical database service (CDS) at Daresbury.[18] The results of HRTEM studies of commercial SiNCs can be seen in chapter 3.

2.3.4 Atomic force microscopy (AFM)

To investigate the particles morphology and the particle size for organic, inorganic and biological materials, atomic force microscopy was employed. This is a type of scanning probe microscopy.[19]

The AFM instrument comprises a sharp tip cantilever, a piezoelectric scanner, a laser diode and a photodiode detector.[20] The schematic of the AFM instrumental technique is shown in Figure 2.7.[20] This cantilever is made from silicon or silicon nitride with a pyramidal tip with a radius of curvature on the order of a few nanometres.[21] This tip is located at the end of the cantilever and that allows the tip to touch the surface of the investigated sample. By applying a piezoelectric scanner, the tip moves on the sample surface in 3-dimensional movements in the x, y and z direction. The force of the interaction between the sample surface and the tip gives rise to deflection of the cantilever. This resulting deflection is then detected through a laser spot. This is available at the backside of the cantilever and then reflects towards a photodetector.[22] There are two photodiodes in the detector that function together in order to detect the alteration of the reflected beam from the cantilever deflection.[21] This helps to identify two different signals using the laser spot on the detector as well as the location of angular deflection of the cantilever. At the same time, the

interaction between the tip and the surface's sample is controlled at a fixed value using a feedback circuit. An image is produced by the feedback signals.[22]

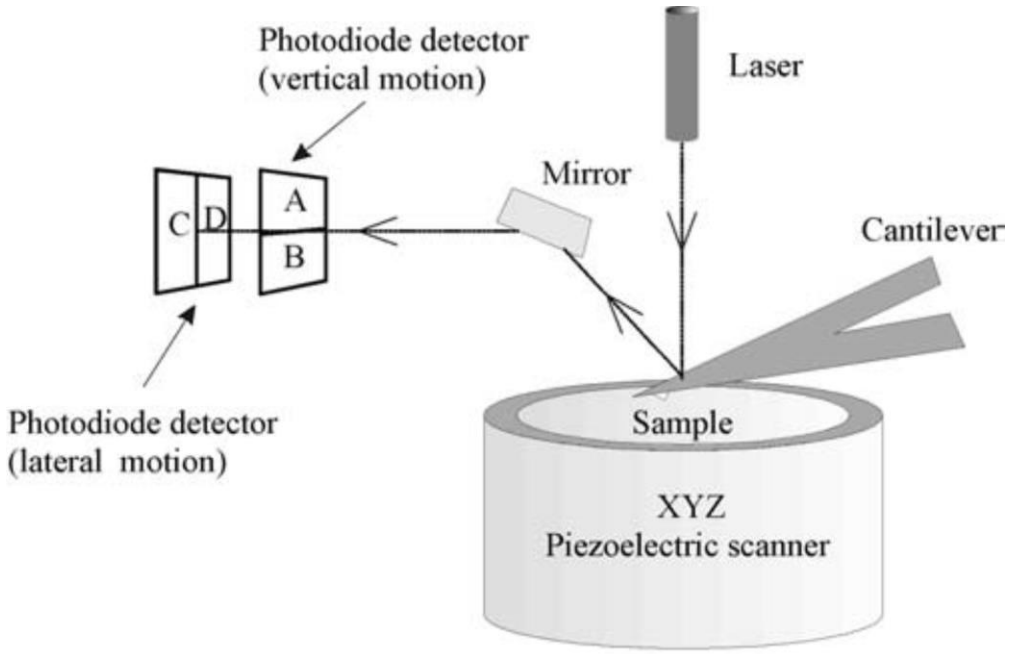

Figure 2.7: A schematic showing the general set up of AFM adapted from Kolasinski.[20]

The AFM works on three main imaging modes including contact mode, non-contact mode and tapping mode, that mainly depend on the nature of the tip motion and the interaction between the tip and sample surface.[22, 23] In contact mode imaging, the constant cantilever deflection is produced by the repulsive force between the tip and the surface sample due to interaction between them. Thus, it is important to keep the repulsive force constant in order to obtain better AFM images. To achieve this, feedback circuit is used so that the cantilever deflection stays constant. In the second mode of imaging, there is no contact between the tip and the sample surface. Van der Waals attractive force is generated in this type as a result of the location of the tip nearby the sample surface. Thus, this attractive force gives rise to a change in the frequency of cantilever's resonant frequency. As the contact mode images, the non-contact mode imaging maintain the frequency shift constant by controlling the oscillation amplitude of the cantilever. Most AFM imaging works on the final mode which is known as tapping mode (TM) when the tip taps on the sample surface. In the end of the tip, there is interaction between the tip and sample surface so that the

repulsive and attractive forces are produced on the tip. Then, the oscillation amplitude is conserved for having constant interaction between the tip and the sample surface.

In this project, the average particle size and the particle morphology of the commercial SiNCs were measured by atomic force microscopy (AFM) at Newcastle University, United Kingdom which presented in figure 2.8. The scanning probe of AFM was a Nanoscope IIIa/ Multimode system (Veeco Instruments Inc., Metrology Group, Santa Barbara) instrument. All AFM images were obtained in Tapping^{TM} mode. The tips which used in this measurement were TESPW (0.01–0.025 U cm antimony n-doped Si cantilevers, Veeco Instruments Inc., Metrology Group) with a spring constant of 20–80 N m^{-1} and a resonant frequency of 245–247 kHz. All the AFM images were taken on an air table (TMC) for vibration and noise isolation.

All AFM measurements were carried out at room temperature. A thin film of SiNCs was prepared by deposit approximately 10 µL of SiNCs suspension that dissolved in deionized water onto mica substrate using a micropipette (Eppendorf) and left overnight to dry in room temperature. The AFM images were exported using WSxM program.[24] The results of AFM images and their cross sections can be seen in chapter 3.

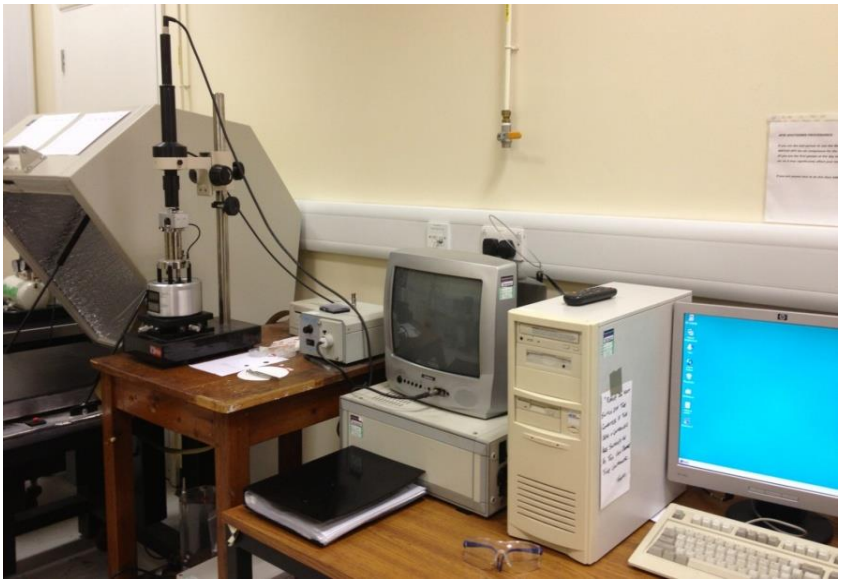

Figure 2.8: AFM instrument at Newcastle University.

2.3.5 X-ray diffraction (XRD)

X-ray diffraction is a technique that is utilized to detect the crystallographic phase of usually crystalline materials and may be used to determine the crystallite size of the investigated samples.[17] The diffraction patterns of the understudy samples take place due to the interaction between the X-ray and periodic planes of the atoms. Therefore, the diffraction patterns depend upon the structure of the materials. As each material has a specific diffraction pattern, it can be used as a fingerprint for the investigated samples. This is then used to determine the crystallographic phase.

There are number of interactions between X-rays and materials that can result such as reflection, absorption and diffraction.[17] The X-ray beam is reflected back by the investigated materials in the reflection. In addition, the direction of the beam might change as the photons passes through the investigated materials. If the materials absorb energy from X-ray radiation, excitation of the electrons from ground state to excited state results. The last diffraction is entirely different from reflection and absorption, takes place when the incident X- ray beam passes through the sample and the scattered beam is detected.

The XRD instrument consist of an X-ray tube, a sample stage and detector.[17] The electrons are produced and are accelerated towards the target material i.e. Cu, Fe, Mo and Co by heating a filament and applying a high voltage respectively in the X-ray tube. These electrons can eject electrons from the inner shells of the target materials. Consequently, the X-rays i.e. $\mathrm{K}\alpha$ and $\mathrm{K}\beta$ are generated. The resulting X-ray beam is then exposed to the sample. In practical use, rotation of the sample stage allows the detector to record the intensity of diffracted X-rays from the investigated sample as a function of scattering angle θ. After recording the signals by the detector, they are then converted into voltage pulses using photomultiplier tube (PMT) which are digitized and transmitted to the computer.

The X- rays are scattered when the periodic planes of the investigated atoms are irradiated with X- ray beam which has a wavelength λ.[17] This scattering of X- ray waves could be constructive or destructive interference. The former is only used to produce a diffracted beam. Thus, the constructive interference of diffracted beam is utilized in the XRD instrument, which employs the principle of Bragg's law[17]:

$$n\lambda = 2d\ sin\theta \qquad 2.2$$

Where n is an integer, λ is the wavelength of X-ray beam, d is the distance between the planes and this is where the diffraction is produced and θ refers to the angle of diffraction (Bragg's angle).

The following figure 2.9 presents the basics of Bragg's law.[25] When the incident beams of X-ray are exposed to the crystal planes of the material (ray 1 and ray 2), the X-ray will be diffracted and Bragg's angle θ is measured by the detector. The angle of the diffraction is the same as the angle of the incident beam. Obviously, ray 1 (the second plane) travels longer distance than that of the top plane, thus the desired constructive interference generates if the extra distance travelled by ray 1 is corresponding to integral number of the wavelength $(n\lambda)$. The constructive interference occurs when the wave of ray 1 and ray 2 are in phase meaning their crests and troughs coincide. Consequently, the waves will combine together in order to produce a strong diffracted beam.[25]

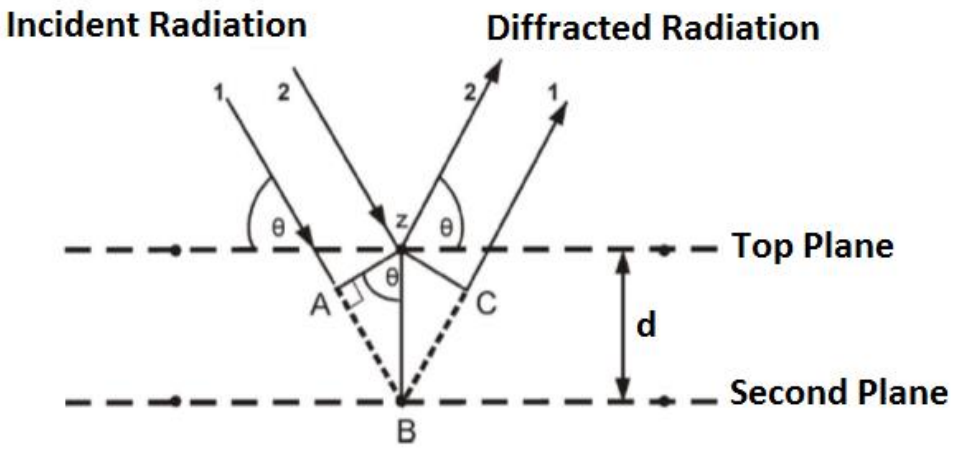

Figure 2.9: A graph showing the XRD in a crystal adapted from Cullity.[25]

XRD pattern is generated as a result of plotting reflected intensities of X-ray incident beam as Y axis and 2θ as X axis. The peak position, peak width and peak intensity of the materials are the main three ways to interpret the data.[7] The peak position is observed by 2θ. This 2θ correspond to d spacing between the planes as indicated in the Bragg's Law. Thus, the Miller indices of the lattice can be determined using this formula. The crystallographic phase of the samples and the particles size can

be identified by the peak width. Using Debye Scherrer formula, the crystallite sizes have been calculated[7]:

$$D = \frac{k\,\lambda}{\beta cos\theta} \qquad 2.3$$

Where D is the crystallite size (in nm units), k is the Scherrer constant = 0.94 for a sphere, β is the full width at half maximum (FWHM), ʎ is the wavelength of the X-ray (Cu-Kα), which widely used as X-ray with wavelength = 0.154 nm and θ is the angle of the diffraction peak.

However, the peak intensity identifies the total diffracted beam from each plane and it exhibits the different impurities in the material.[7] Thus, the structure of the samples and its composition can be determined from the peak intensity.

In this project, XRD at Newcastle University, United Kingdom which presented in figure 2.10 was used to confirm the crystalline nature of the Si core in commercial SiNCs and to measure the particle size. XRD patterns were reported from an investigated powder sample using Panalytical X'Pert Pro Multipurpose Diffractometer (MPD) with Cu-K_α X-ray radiation, which has a characteristic wavelength (λ) of 0.15418 nm. X-rays were produced from a Cu anode provided with a current of 40 mA and 40 kV. A scanning rate of 0.033 s^{-1} was used to report the pattern in the 2θ range of 20^o-120^o. The sample was prepared by placing 200 mg of the powder on a single crystal silicon wafer, the surface of the powder was levelled to the required height using a glass slide and then scanned. The results of XRD can be seen in chapter 3.

Figure 2.10: XRD instrument at Newcastle University.

2.3.6 X-ray photoemission spectroscopy (XPS)

XPS is a quantitative and qualitative technique which mainly used for surface characterization.[26] The elemental composition for all the elements can be observed by using XPS technique except for H and He. The molecular environment also can be determined such as the oxidation state of the materials and the existing of saturated and unsaturated transitions.[26]

After the sample placed into a vacuum chamber, it is irradiated with X-ray photons. Consequently, the emission of electrons (photoemission) is generated as a result of the interaction between the surface atoms and the X-ray photons considering that there is a total energy transfer from the photons to the electrons. Thus, the number of these electrons that ejected from the top of 1 nm to 10 nm of the investigated materials and their kinetic energy are analysed. The emitted electrons are separated on the basis of their kinetic energy. The number of emitted electrons is identifying the concentration of the emitting atoms that being irradiated on the surface. The kinetic energy of emitted electrons from the surface is recorded. Thus, their binding energy can be determined using Einstein equation [26]:

$$BE = h\upsilon - KE - \Delta\phi \qquad 2.4$$

Where BE is the binding energy of the emitted electron (eV), $h\upsilon$ is the photon energy of X-ray being applied (eV), KE is the kinetic energy of the emitted electron which is measured in the instrument (eV), $\Delta\phi$ is the spectrometer work function (eV).

Each element generates characteristic peak which has a specific value of the binding energy. These different values of the binding energy correspond to different elements that exist in or on the surface of the materials which have been irradiated. Thus, XPS can be utilized for elemental determination. Furthermore, the XPS peaks may be assigned to the electron configuration of the electrons in the atoms such as 1s, 2s, 2p etc.[26] It also should be noted that the number of recorded electrons for each XPS peak depend on the amount of elements which have been irradiated in the sample.

The general set up of XPS consist of ultrahigh vacuum chamber (UHV) , an X-ray source, an electron energy analyser and a detector.[26] A UHV chamber is used to maintain the chemical composition of the investigated sample during all the XPS experiments. The next reason to use UHV chamber is to prevent the collisions between the gas and the emitted electrons. X-ray source component also needs the UHV in order to stay working through the experiments. The pressure which used in the UHV chamber is order of 2 X 10^{-10} mbar.[26]

To generate X-ray beam, an energetic electron beam is directed to target materials i.e. Mg and Al, and these elements produce X-rays energy of 1253.6 eV and 1486.6 eV respectively. This high energy is enough to reach and eject the electrons from core levels. A concentric hemispherical analyser (CHA) is used to measure the energy of the emitted electrons. The CHA considered as the most popular energy analyser that used in XPS instrument.[26] This energy analyser contains inner hemisphere (with radius R1) and outer hemisphere (with radius R2). These two hemispheres are located concentrically as shown in figure 2.11.[27] The slit S allows the electron which has specific kinetic energy (KE) to enter through it. This electron then move across the median equipotential surface in trajectory and subsequently this electron will be reached the exit (slit F) as shown in figure 2.11. Regarding to this process, different electron with different values of KE will travel through the analyser after entering the slit S. it also should be noted that as the KE will be different for each electron,

different trajectory have been followed by these electrons. Consequently, these electrons cannot be focused to find a way out over the slit F. in order to figure out this issue, the potential V_1 and V_2 must be changed. Then the electrons with different kinetic energy are capable to select when they pass through the energy analyser.

Handbooks can be used to determine the chemical composition of the investigated sample by their binding energy values.[28] As the chemical environments affect the binding energy, there are chemical shifts that are noticed in the XPS spectrum,[26] where especially, the oxidation states of the atoms affects the binding energy. This can be understood from the following example; the binding energy of electrons in C atoms will be larger when they are bonded to an electronegative atoms such as O.[26] As the more O atoms are bonded to carbon atom, the binding energy of the carbon will increase as a result of increasing the positive charge on the carbon. Furthermore, the binding energy also affects by the final state effects of the electrons. Relaxation, spin orbital splitting and shake up satellites are three types of the final state effects of the electron. The first process is generated through the photoemission. When the electron ejects from the core level, another electron will fill the core hole to minimize the energy of the ionized atom. This will produce a new core hole by rearrangement of the electron. Thus, this energy which requires rearranging the electron is named as relaxation energy. This relaxation energy is the reason of decreasing the binding energy of the elements. It also should be noted that the chemical composition will affect the relaxation energy. As the relaxation energy depends on the both atoms that contain core hole and its surrounding atoms, the binding energy then will be changed. For example, the binding energy of cobalt element $2p_{3/2}$ is different when the binding energy measured in different other states of Co: Co^{2+} (780.5 eV) > Co^{3+} (779.6 eV) > Co° (778.2 eV).[26] The spin orbital splitting and shake up satellites considered to be other aspects that affect the final states of the electron and thus affect the binding energy.[26] The spin orbital splitting in the final state (after removal electron from the initial state) cause the electron energy spectrum (p, d, f) to be observed in closely spaced doublet rather than a single peak. While, the shakeup satellite occurs as a result of losing the photoelectron some of the kinetic energy through the excitation approach from valence electron to unoccupied electron i.e. π - π* transition.[26]

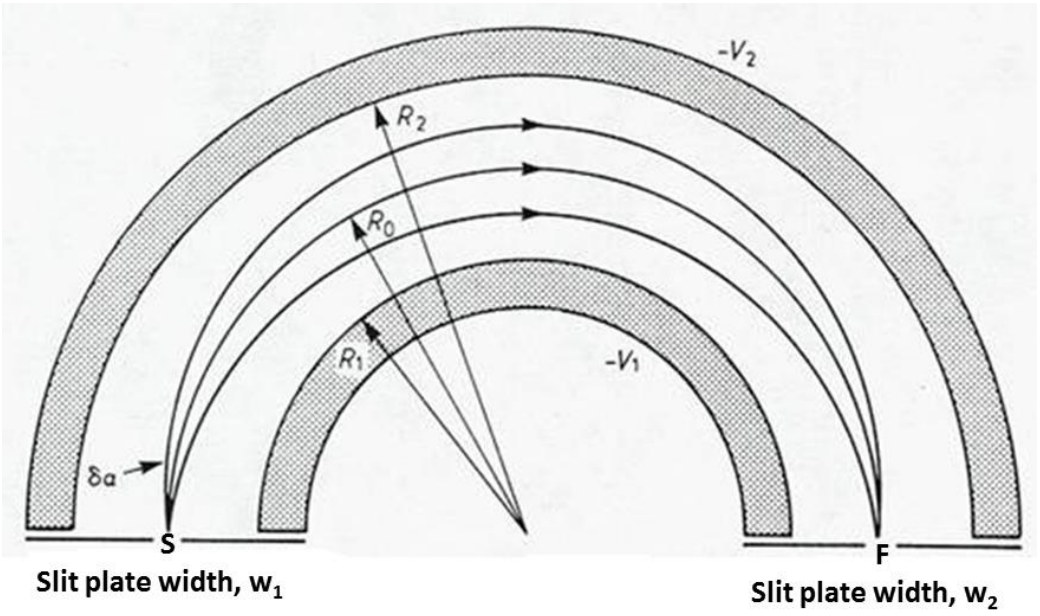

Figure 2.11: The schematic diagram of concentric hemispherical analyser (CHA) adapted from Briggs and Seah.[27]

The XPS spectrum is a plot of the intensity of the emitted electrons (counts per second) versus their binding energy (eV).[26] Each peak in an XPS spectrum might have several sub peaks and these may relate to the chemical oxidation states of the elements or final state effects.[26] This gives rises to attempt to fit the peak in order to increase the information obtained from the XPS spectrum. Different parameters are used to fit the curve, including peak position, secondary electron, peak height, peak width, background and line shapes such as Gaussian and Lorenzian. However, all these are constrained by chemical/physical principles.

In this project, X-ray photoelectron spectra measurements were used to characterize the chemical composition of alkyl SiNCs and their mixture with erbium ions and commercial SiNCs. All XPS measurements were carried out at Newcastle University, United Kingdom using (Kratos Axis Ultra 165 spectrometer) with a monochromatic Al K_α X-ray source (photon energy= 1486.6 eV). The pass energy was set at 20.0 eV for individual peaks region includes O*1s*, C*1s*, Si*2p* etc. and 80.0 eV for the survey spectrum. A thick film of the sample was prepared by a drop cast technique on a gold substrate using a micropipette (Eppendorf) and left overnight to dry in air at room temperature.

Peak fitting to XPS spectra was carried out using Winspec© software.[29] The binding energy scale of the spectra was calibrated with reference to the Au $4f_{7/2}$ at 84.0 eV.[30] The background was modelled by a Shirley background[31] and the peaks then were fitted using a mixed singlet function and mixed doublet as required. The results of XPS of alkyl SiNCs and their mixtures with erbium ion and Intrinsiq Ltd commercial SiNCs can be seen in chapter 3.

2.3.7 Fourier transform infrared spectroscopy (FTIR)

FTIR spectroscopy is a measurement technique that is used to identify the functional groups in molecules and material via their characteristic vibration frequencies. This instrument works on the basis of absorption of IR light. Infrared light has the appropriate frequency to interact with vibrations of chemical bonds.[32] As each molecule has different functional groups, a particular wavenumber of the infrared beam is absorbed by the molecule. Thus, the FTIR spectrum was be considered a fingerprint of the sample. Many types of vibration modes i.e. stretching and bending vibrations are observed in FTIR spectrum.[33] The stretching and the bending vibration modes involve a change in the bond length and the bond angle respectively. It also should be noted that the stretching vibration modes are classified as symmetric or asymmetric depend on the structure of the investigated sample and the symmetry of the vibration. While the bending vibration modes are categorised as scissoring, rocking, wagging or twisting based on the angle of molecular movement.

An FTIR instrument consists of an IR source, an interferometer, the sample holder and the detector.[33] Figure 2.12 shows the general set up of FTIR instrument.[33] However, the Michelson interferometer is the operator of FTIR instrument. It can be seen that the Michelson interferometer consists of the beam splitter, moving and fixed mirrors. When the infrared light hits the beam splitter, the IR light divided into two beams. One beam falls on a fixed mirror and the second beam travels to a moving mirror. The distance between a beam splitter and moving mirror could be measured precisely using a laser. The beams are then reflected back to the beam splitter after reflection in these two mirrors. Thus, both of the beams are recombined together before passing into the investigated sample and measured by the detector. As the distance varies between the beam splitter and the moving mirror, the distances that

travelled by the two beams before interference are changed. Depending on the position of the moving mirror, the same phase of two beams can be recombined to produce constructive interference (a maximum intensity) whilst the others does not have the same phase in order to produce destructive interference (a minimum intensity). This recombined beam is transmitted to the investigated sample. The resulting signal is then measured and plotted with the location of the moving mirror as an interferogram. The software working with a Fourier transform (FT) algorithm alters the interferogram to a spectrum in which the intensity (the absorbance or % transmittance) is plotted versus the wavenumber.

As motioned previously, the sample tends to absorb specific wavenumbers of light. Consequently, the detector converts the infrared intensities into signals in order to produce FTIR spectrum. Deuterated triglycine sulphate (DTGS) is typically utilized as a detector due to its high sensitivity in the infrared region that ranges from around 400 - 4000 cm^{-1}.

Practically, the background spectrum has been obtained first by measuring the interferogram without the investigated sample. The interferogram is then measured with the examined sample. After subtracting the background spectrum, the final spectrum of the sample is then observed.

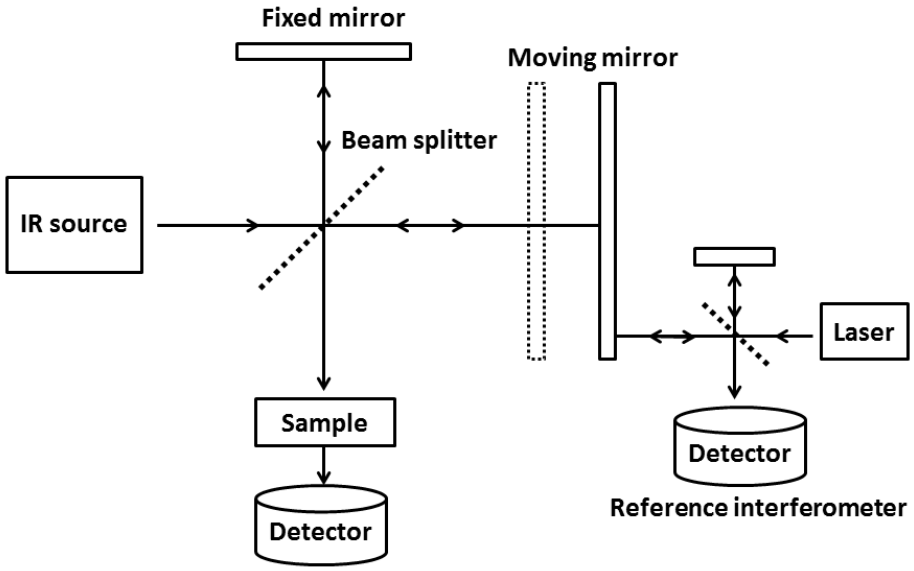

Figure 2.12: A diagram showing the general set up of FTIR instrument adapted from Long *et al*.[33]

In this project, FTIR spectroscopy is used to analyse the chemical composition of C_{11}-SiNCs that contain erbium ions and commercial SiNCs. FTIR measurements were carried out at Newcastle University, United Kingdom using a Varian 800 Scimitar Series FTIR over the range of 700 - 4000 cm^{-1}. A thick film of the C_{11}-SiNCs that contain erbium ions was prepared by a drop cast method on silicon substrate using a micropipette (Eppendorf) and left overnight to dry in air at room temperature while the commercial SiNCs was used as a solid. The results of FTIR can be seen in chapter 3.

2.3.8 UV-Vis spectroscopy (UV-Vis)

UV-Vis spectroscopy is an analytical technique that commonly used to interrogate the absorption bands of different species.[34] Qualitative and quantitative analysis can be obtained from UV-Vis equipment because each molecule absorbs particular wavelength and the absorbance intensity depend upon the concentration of the molecules. In UV-Vis range also, the metal nanoparticles such as gold and silver show absorption peaks related to their surface plasmon resonances.[35] Furthermore, the absorption bands may be used to interpret different aspects such as size distribution and the chemical environment of metallic nanoparticles.[35]

There are two wavelength regions in UV-Vis spectroscopy; ultraviolet (UV) and visible light (blue to red). UV light has a wavelength range from 10 nm to 400 nm. While the visible light ranges from 400-750 nm. A deuterium arc lamp and tungsten lamp are utilized as an excitation source in the UV range and Vis range, respectively. It also should be noted that in commercial UV-Vis spectrometers, UV light source begins from 190-400 nm. A vacuum system and purging gas i.e. helium are used in UV-Vis spectroscopy for a wavelength less than 200 nm. Thus, water vapour, oxygen and other species in air cannot absorb the light and then the measurement in this low wavelength will not change.

In UV-Vis spectroscopy, electrons in the molecules absorb the light and are promoted to an excited state.[33] In molecules, there are three main types of electrons: (i) sigma electrons (σ), (ii) pi electrons (π) and (iii) nonbonding electrons (n). These three types of electrons are active during the electronic excitation in UV-Vis absorption. The absorption of UV light with wavelength less than 200 nm can be observed in electrons of σ bonds. As mentioned previously, the commercial UV-Vis

spectrometers do not usually provide wavelengths less than 190 nm. Thus, saturated compounds which absorb only wavelengths less than 200 nm such as alkanes are used as a transparent solvent. However, electrons in both π bonds and nonbonding electrons are excited by UV light with a wavelength larger than 200 nm and possibly also visible light.

UV/Vis spectroscopy can be applied to non-molecular samples but the nature of the excited state may be very different. The localized surface plasmon resonance (LSP) effect occurs when metal nanoparticles such as gold nanoparticles and silver nanoparticles are excited in the UV-Vis region. A collective electron oscillation which is confined in metal nanoparticles is a definition of LSP.[35] In principle, the existence of plenty of free electrons in the interface between two materials produces the surface plasmon.[36] Thus, one of the materials should be metal with a high density of free electrons at their surface and the other may be a dielectric material or air.[37] The excitation of localized surface plasmon resonance occurs when metallic nanoparticles are irradiated with the light (an electric field) at the resonant frequency. This process generates intense absorption bands and these bands are specific for each type of material and also depend on the shape. For instance, two absorption peaks of plasmon resonance of gold nanorods appear at two different wavelengths.[38] The peak at low wavelength is attributed to the length of nanorods. While the second peak at high wavelength assigned to electron oscillation across the diameter.

The commercial UV-Vis spectrometers consist of a deuterium arc lamp as an excitation source in the UV range while the xenon arc lamp is used as a visible lamp, wavelength selector (monochromator), sample holder (cuvette), detectors i.e. photomultiplier tubes (PMT) and data output device (computer).[39] As the sample which located in cuvette cell absorbs the particular wavelength, the intensity of beam decreases. UV-Vis spectrum generated as a result of plotting the absorbance as a function of the wavelength. It is important to define the transmittance and the absorbance for the quantitative analysis. It is known that, the intensity of the light decreases after the light passes over the sample that absorbs a specific wavelength. The following equation is used to define the transmittance (T) of the light[39]:

$$T = \frac{I}{I_0} \qquad 2.5$$

Where T is transmittance, I is defined as the light intensity after passing through the sample and I_0 is the light intensity before passing the sample. As the ratio of I / I_0 has not change even if I_0 alters, the transmittance (T) maintain constant. Thus, the absorbance (A) equation given as[39]:

$$A = log \frac{I_0}{I} = \log \frac{1}{\mathrm{T}} = -log\ T \qquad 2.6$$

In this project, UV-Vis spectroscopy is used in order to measure the optical characterizations of the samples i.e. C_{11}-SiNCs, commercial SiNCs, their mixtures with erbium ions and $ErCl_3$ solution (4 mM). It is utilised also to measure the surface plasmon resonance of synthesised AgNPs (i.e. 1 mM and 10 mM) and their mixtures with SiNCs. The UV-Vis analysis is carried out using UV-Vis spectroscopy (Varian, Cary 100 BIO) at Newcastle University, United Kingdom of the wavelength range between 200 to 800 nm using quartz cuvette of 1 cm path length. This instrument can be seen in figure 2.13. This measurement was carried out at room temperature. The sample was prepared by adding 4 mL of the investigated sample that dissolved in deionized water (i.e. C_{11}-SiNCs, commercial SiNCs and their mixtures with erbium trichloride) in the quartz cuvette. The mixtures of SiNCs with metal nanoparticles were prepared by mixing 2 mL of AgNPs with 2 mL of SiNCs in a vial. All of the solution was dissolved in deionized water. The mixture was then sonicated for 10 minutes (Hilsonic). 4 mL of the mixture was added to the quartz cuvette. The results of UV-Vis spectroscopy can be seen in chapter 3 and chapter 4.

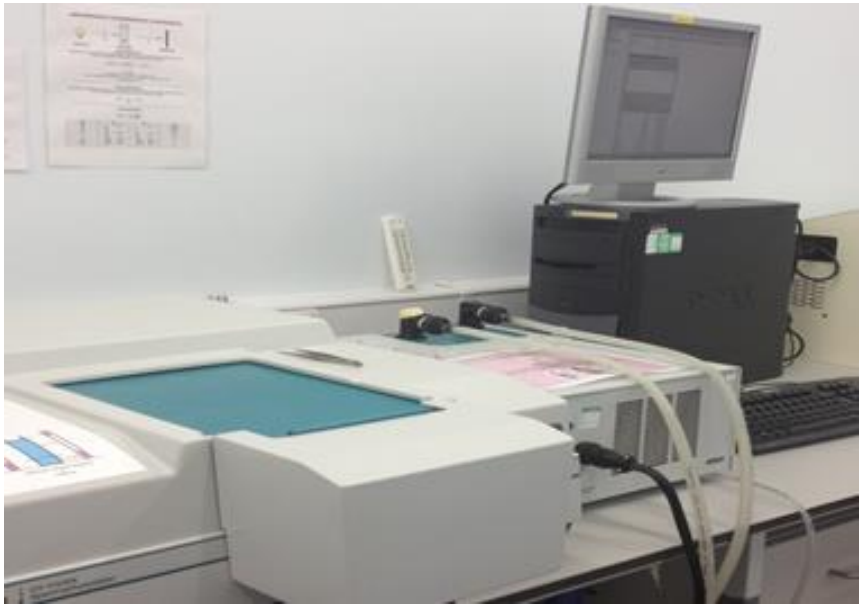

Figure 2.13: The UV-Vis spectroscopy at Newcastle University.

2.3.9 Raman spectroscopy

The complementary technique to FTIR spectroscopy is Raman spectroscopy, because this technique is also sensitive to the vibrational modes of the samples.[40] Raman spectroscopy is commonly used to characterize the chemical composition, crystallographic phase and the functional groups of the samples.

The principle of Raman spectroscopy is dependent on the interaction between the incident monochromatic light and the vibrational states of the samples.[40] Consequently, the light is scattered inelastically from the sample. The energy of the scattered light could be decrease or increase in the wavelength compared to the wavelength of the incident beam. This is therefore known as Raman shift. Raman shift is defined as the difference in wavenumber between incident and scattered light.

Stokes Raman scattering, anti-Stokes Raman scattering and Rayleigh scattering are three forms of light scattering. Stokes Raman scattering and anti-Stokes Raman scattering can be obtained when the energy of the scattered light shifts to higher and smaller wavelength than that of the incident beam. Rayleigh scattering occurs when there is no change in energy between the irradiated and scattered light. It also should be noted that the anti-Stokes Raman shift is not often utilized because the spectral features are less intense by a factor related to Boltzmann distribution.[40]

As Stokes scattered radiation is weak, a laser source is usually used. The laser source may be ultraviolet, visible or near infrared light.[41] The wavelength of the incident beam affects the intensity of Raman scattering of the investigated sample; there is inverse 4th power dependence (λ^{-4}).

The intensity of Raman scattered radiation can be enhanced using rough surfaces and metal particles, for instance silver and gold.[42] This technique is known as surface enhanced Raman spectroscopy (SERS). However, there is a debate between the researchers about the theories behind the Raman scattering enhancement.[43-45] There are two effects that play role on the enhancement of Raman scattering i.e. the chemical enhancement and electromagnetic enhancement.[43] The chemical enhancement occurs as a result of the interaction of the molecule with the metal surface, which changes the molecular electronic structure in a way that increases the Raman scattering. While the electromagnetic enhancement is a result of the interaction of light with the surface plasmon increases, which the electric field near the metal and this increases the Raman scattering. Thus, it is suggested that the chemical composition of the sample surface and the electromagnetic field intensity near metal surface are both able to enhance the Raman scattering. Recently, the consensus has arisen that the electromagnetic effect is the major part of the enhancement process.[45, 46] Maitani *et al* [44] suggests that the electromagnetic effect enhances the Raman signal above 100 times compared to the chemical effect .

The general set up of Raman spectroscopy is a laser source, microscope objective lens, a spectrophotometer and a detector as presented in figure 2.14.[47] To irradiate the sample, the laser source is used (typically ultraviolet, visible or near infrared). The microscope objective lens is used to focus the beam to the sample and to collect the scattered beam. Furthermore, the detectors are used to generate spectrographs by converting the optical signals to electrical signals. As a charge-coupled device (CDD) has low noise and high sensitivity, it is commonly used as detectors in Raman spectroscopy. The Raman spectrum is denoted as a plot of the scattered light intensity (counts per second) as a function of Raman shift (cm^{-1}).

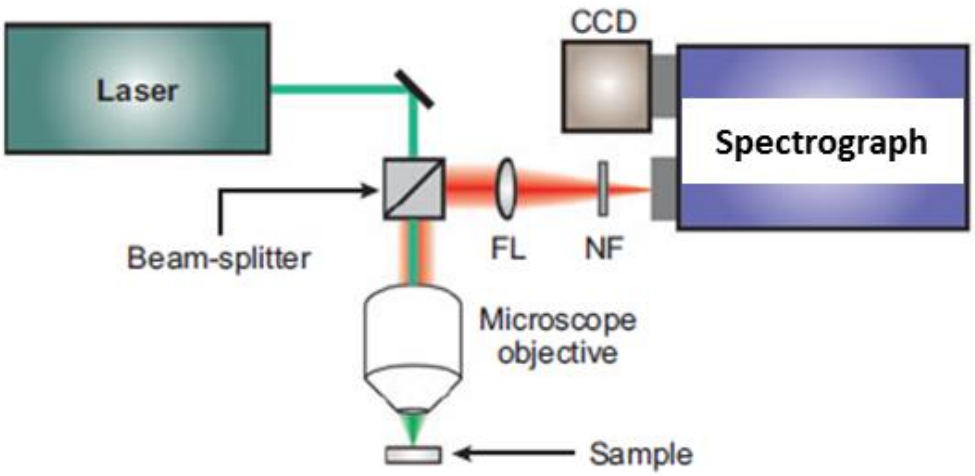

Figure 2.14: A graph showing the general set up of Raman spectroscopy adapted from Stiles *et al*.[47]

In this project, two types of Raman instruments were used: (i) a confocal microscope (WiTec Confocal Raman Microscope model CRM200, Ulm, Germany) at School of Chemistry at Newcastle University, United Kingdom as presented in figure 2.15 (ii) a Lab RAM HR800-9CCD at School of Electrical and Electronic Engineering at Newcastle University, United Kingdom as presented in figure 2.16. The confocal Raman microscope is used to capture Raman spectra and luminescence images of the following samples: C_{11}-SiNCs, commercial SiNCs and their mixtures with erbium ions (Er/SiNCs) and their mixtures with synthesised silver nanoparticles (AgNPs/SiNCs), $ErCl_3$ (4 mM) and AgNPs (1 mM). Whereas the Lab RAM is utilized to capture Raman spectra of commercial SiNCs and their mixtures with prepared AgNPs (AgNPs/Commercial SiNCs). The former instrument has a high intensity an Argon Ion laser (Melles-Griot) with output power 35 mW at a wavelength of 488 nm was utilized as the excitation source. The collected light was analysed by a spectrograph equipped with a CCD detector; a grating of 150 lines mm^{-1} was chosen in order to capture the full spectrum including all Raman and luminescence bands of interest. The scan size of all the experiments was 50 x 50 µm in 100 lines at 100 pixels per line with an integration time of 0.1 s/pixel. While the latter has Symphony Jobin Yvon detector and labspee 5.01 software with the 514.5 nm line from an Ar ion laser. A 100X objective lens with a numerical aperture of about 0.9 was used. Raman spectra were collected with low laser beam power at <10 mW in order to prevent destruction of the investigated

samples. It also should be noted that the WiTec instrument has better sensitivity and therefore it is faster while the Lab RAM has better resolution thus, it can detect small shifts in wavenumber.

Figure 2.15: Confocal Raman spectroscopy at School of Chemistry at Newcastle University. The excitation source = 488 nm.

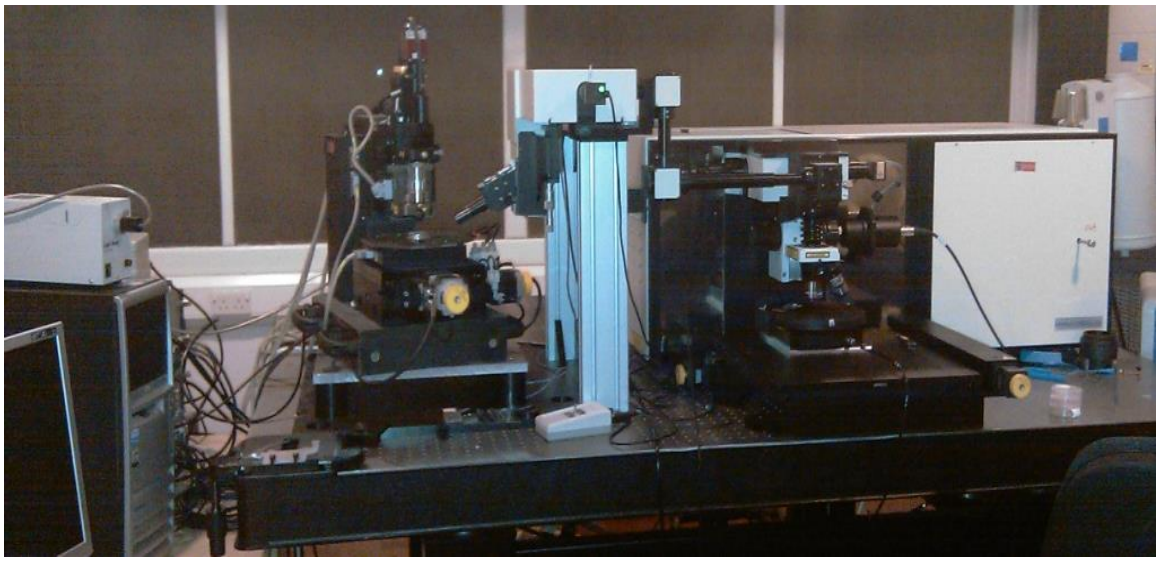

Figure 2.16: Raman spectroscopy at School of Electrical and Electronic Engineering at Newcastle University. The excitation source = 514.5 nm.

The samples for Raman spectroscopy were prepared by drop-coating 100 µL of alkylated SiNCs and commercial SiNCs suspension on a glass slide coverslip using a micropipette (Eppendorf). The samples were air dried over night at room temperature

and kept in sealed Petri-dishes to avoid contamination. Silver nanoparticles were mixed with SiNCs in order to enable surface enhanced Raman spectroscopy (SERS). These mixtures were prepared by mixing 100 µL of AgNPs solution with 100 µL of SiNCs suspension in centrifuge tube (1.5 mL, Eppendorf). The mixture was then sonicated for 10 minutes (Hilsonic). Then using a micropipette (Eppendorf), 100 µL of the mixture was then drop-coated on a glass slide coverslip. The samples were air dried overnight and kept in sealed Petri-dishes until further analysis.

Repeats were performed by moving the microscope onto another area of the samples. The main reason of repetition in this experiment is to cover more of the investigated sample because confocal Raman spectroscopy observes a small area of the sample (~ 300 nm dia.) which may not be representative of the whole sample. While Lab RAM instrument focused on 1 µm diameter of the sample. However, collected Raman spectra of the investigated samples can be seen in chapter 4.

2.3.10 Photoluminescence spectroscopy (PL)

The PL technique is commonly applied to measure the band gaps of solids and to investigate defects or impurities in the samples.[48] Generally, the luminescence process is the opposite to absorption.[49] Furthermore, there are different types of the luminescence depending on the excitation source as listed in table 2.1.[49] When the light is used as an excitation source and photons are emitted from the sample this is known as photoluminescence.

In PL, the material absorbs photons from the light excitation source. The valence electrons are excited from the ground state to an excited state in the conduction band. A relaxation process subsequently occurs when the electron returns back to the ground state with emission of photons. There may also be vibrational relaxation, leading to a Stokes shift with respect to the absorbed light. Thus, each material has characteristic luminescence bands that are assigned to the band gap defects or impurities of the investigated sample.[48]

Basically, the photoluminescence mechanism can be interpreted via three steps: absorption, vibrational relaxation and radiative recombination.[50] The features of this mechanism can be shown in figure 2.17.[48] In the first step, the valence electron is

excited to the excited state and this absorption process produces an electron-hole pair. In the next step, the electron relaxes to the bottom of the conduction band as they lose their excess energy to vibrational modes of the lattice. In the radiative recombination, the electron returns to the ground state by emitting a photon. It also should be noted that this energy which have been emitted has a lower energy than that of the excitation source (Stokes shift).

Types of Luminescence	**Excitation Source**
Photoluminescence	Light
Cathodoluminescence	Electrons
Thermoluminescence	Heating
Electroluminescence	Current or electric field
Chemiluminescence	Energy from chemical reaction
Bioluminescence	Energy from chemical reaction inside an organism

Table 2.1: Different types of luminescence adapted from Solé *et al*.[49]

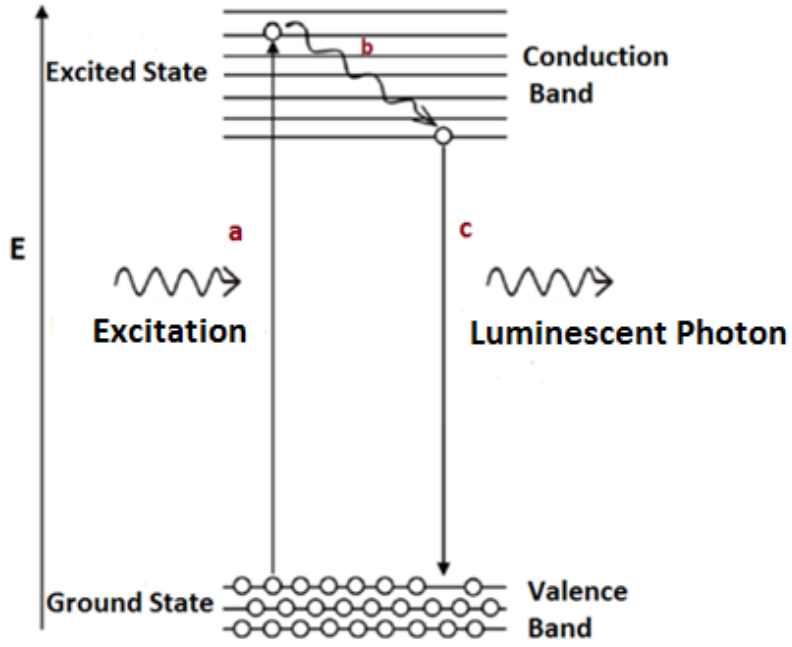

Figure 2.17: A diagram showing the PL mechanism: (a) Absorption. (b) Vibrational relaxation. (c) Radiative recombination. Adapted from Aoki.[48]

The general set up of a PL instrument consists of a light source, monochromator (wavelength selector), sample container, detectors and data output devices.[48] A Xe arc lamp is used as an excitation source which provides intense visible light. There are two monochromator; one is between the excitation source and the investigated sample while the second one is between the sample and the detector. They are assigned to an excitation spectrum and to the emission spectrum of the sample, respectively. Thus, the wavelength of the light source in the excitation spectrum remains constant via the monochromator. While the specific wavelength of the light that emitted from the investigated sample is measured in the emission spectrum. A charge coupled devices (CCD) detector or photomultiplier tube (PMT) are then used to detect the photon emission.

In this project, the photoluminescence properties of C_{11}- SiNCs, commercial SiNCs and their mixtures with erbium trichloride was carried out in Manchester University, United Kingdom using Fluorolog and cooled InGaAs by Horiba Jobyn Yvon. PL measurements were performed on a thin film of the sample which prepared by the following method. The investigated samples that dispersed in deionized water i.e. C_{11}-SiNCs, commercial SiNCs, Er/C_{11}-SiNCs and Er/commercial SiNCs were prepared by drop-coating 100 µL of each sample on a glass slide coverslip using a micropipette (Eppendorf). The samples were air dried over night at room temperature and kept in sealed Petri-dishes until further analysis.

Also, the WiTec (Confocal Raman Microscope model CRM200, Ulm, Germany) at School of Chemistry at Newcastle University, United Kingdom as presented in figure 2.15 was used also to report the temporal and spectral dependence of the intensity of photoluminescence emitted by the investigated samples under continues wave (CW) laser irradiation. An argon ion laser (Melles-Griot) with output power 35 mW at a wavelength of 488 nm was used as the excitation source. Emitted light was transmitted through a Raman edge filter to attenuate the elastically scattered component and collected by a multimode optical fiber which also served as the confocal pinhole. The light was then dispersed on a grating (150 lines mm^{-1}) and detected using a Peltier-cooled CCD camera. The intensity reported is the integral of the spectrum over the range of wavenumbers from 200 and 7000 cm^{-1} with respect to the excitation light. Spectra were collected very second upon opening the laser shutter

and recorded for periods up to 5 min. The photofading curves are plots of the integral of the spectrum against recording time. Replicate measurements were performed by moving the microscope onto another area of the sample in order to collect a representative dataset.

The samples were prepared by drop-cast 100 µL of alkylated SiNCs and commercial SiNCs onto glass coverslip from THF solution and deionised water, respectively using a micropipette (Eppendorf). The samples were air dried over night at room temperature and kept in sealed Petri-dishes to avoid contamination. Glass coverslips were chosen because they were observed to have no luminescence background and only very weak, broad Raman features themselves.

Mixtures of SiNCs and the respective additives (AgNPs 1 mM, AgNPs 10 mM, AuNPs 0.41 mM, $FeC_{10}H_{10}$ 1 mM and $FeCl_3$ 1 mM) was prepared by adding 100 µL of SiNCs suspension to 100 µL of the additive solution in centrifuge tube (1.5 mL, Eppendorf). The mixture was then sonicated for 10 minutes (Hilsonic). Then using a micropipette (Eppendorf), 100 µL of the mixture was then drop-coated on a glass slide coverslip. The samples were air dried overnight and kept in sealed Petri-dishes until further analysis. The coverslip is then placed under the microscope for the photoluminescence measurements. The recording of spectra was started at the same time the laser was switched on and the computer recorded spectra every 1.0 second. All the PL measurements were carried out at room temperature. The results of PL characterization and luminescence decay curves are presented in chapter 4 and chapter 5.

References:

1. L. H. Lie, M. Duerdin, E. M. Tuite, A. Houlton and B. R. Horrocks, *Journal of Electroanalytical Chemistry*, 2002, **538–539**, 183-190.
2. Y. Chao, L. Siller, S. Krishnamurthy, P. R. Coxon, U. Bangert, M. Gass, L. Kjeldgaard, S. N. Patole, L. H. Lie, N. O'Farrell, T. A. Alsop, A. Houlton and B. R. Horrocks, *Nat Nano*, 2007, **2**, 486-489.
3. F. M. Dickinson, T. A. Alsop, N. Al-Sharif, C. E. M. Berger, H. K. Datta, L. Šiller, Y. Chao, E. M. Tuite, A. Houlton and B. R. Horrocks, *Analyst*, 2008, **133**, 1573-1580.
4. G. A. Bhaduri, R. Little, R. B. Khomane, S. U. Lokhande, B. D. Kulkarni, B. G. Mendis and L. Šiller, *Journal of Photochemistry and Photobiology A: Chemistry*, 2013, **258**, 1-9.
5. J. Turkevich, P. C. Stevenson and J. Hillier, *Discussions of the Faraday Society*, 1951, **11**, 55-75.
6. L. Reimer, *Scanning electron microscopy: physics of image formation & microanalysis*, Springer-Verlag Berlin Heidelberg, Germany, 1998.
7. W. S. Chin, C. H. Sow and A. T. S. Wee, *Science at the nanoscale: an introductory textbook*, Singapore : Pan Stanford c2010.
8. M. P. Dewar, Master of Science, University of Alberta, 2013.
9. Radiological & Enviromental Mnagement, *Scanning Electron Microscope.*, http://www.purdue.edu/rem/rs/sem.htm, Accessed 18 March, 2014.
10. M. Wilson, K. Kannangara, G. Smith, M. Simmons and B. Raguse, *Nanotechnology: basic science and emerging technology*, 27 June 2002 edn., Boca Raton : Chapman & Hall/CRC 2002.
11. J. I. Goldstein, D. E. Newbury, P. Echlin and D. C. Joy, *scanning electron microscopy and x-ray microanalysis, a text for biologists, material scientists and geologists*, 2nd edn., Plenum Press, New York, USA, 1992.
12. M. Picquart, *The Journal of Physical Chemistry*, 1986, **90**, 243-250.
13. M. Kuno, *Introductory Nanoscience: Physical and Chemical Concepts* New York : Garland Science London 2012.
14. D. B. Williams and C. B. Carter, Springer, New York, US, 2nd ed. edn., 2009, p. 760 pages.
15. R. Kelsall, I. W. Hamley and M. Geoghegan, *Nanoscale Science and Technology*, Wiley, 2005.
16. P. J. Goodhew and F. J. Humphreys, *Electron Microscopy And Analysis*, Taylor & Francis, 1988.
17. E. J. Mittemeijer, *Analysis of the microstructure; Analysis of Lattice Imperfections: Light and eelctron microscopical and XRay diffraction methods. In Mittemeijer E. J. Fundamentals of materials Science: The microstructure-property relationship using metals as model systems*, Springer, Berlin, Germany, 2011.
18. CDS. Chemical Database Service, *Daresbury*, http://cds.dl.ac.uk/, Accessed 18 March, 2014.
19. S. Magonov, *Microscopy and Microanalysis*, 2004, **10**, 1080-1081.
20. K. W. Kolasinski, *Surface Science : Foundation of Catalysis & Nanoscience*, John Wiley & Sons, New York, USA, 2008.
21. D. R. Pier Carlo Braga, ed. D. R. Pier Carlo Braga, Humana Press Inc., Totowa, New Jersey, 2004.
22. A. Alessandrini and P. Facci, *Measurement Science and Technology*, 2005, **16**, R65-R92.
23. D. Ricci and P. C. Braga, eds. P. C. Braga and D. Ricci, Humana Press Inc., Totowa, New Jersey, 2004.
24. W. Program, *Nanotec Cervantes FullMode AFM* http://www.nanotec.es/products/wsxm/, Accessed 1 April, 2014.
25. B. D. Cullity, *Elements of X-Ray Diffraction*, Addison-Wesley, 1978.
26. J. C. Vickerman, *Surface analysis: the principal techniques*, John Wiley, 1997.

27. B. Rezgui, A. Sibai, T. Nychyporuk, M. Lemiti and G. Brémond, *Journal of Luminescence*, 2009, **129**, 1744-1746.
28. S. Hofmann, *Auger- and X-Ray Photoelectron Spectroscopy in Materials Science: A User-Oriented Guide*, Springer, 2012.
29. G. Faraci, S. Gibilisco, P. Russo, A. R. Pennisi and S. La Rosa, *Physical Review B*, 2006, **73**, 033307.
30. Y. Chao, S. Krishnamurthy, M. Montalti, L. H. Lie, A. Houlton, B. R. Horrocks, L. Kjeldgaard, V. R. Dhanak, M. R. C. Hunt and L. Šiller, *Journal of Applied Physics*, 2005, **98**, 044316.
31. D. A. Shirley, *Physical Review B*, 1972, **5**, 4709-4714.
32. B. C. Smith, *Fundamentals of Fourier Transform Infrared Spectroscopy*, Taylor & Francis, 1995.
33. D. A. Long, *Journal of Raman Spectroscopy*, 2005, **36**, 462-462.
34. D. A. Skoog, *Principles of instrumental analysis*, Saunders College Pub. ; Harcourt Brace College Publishers, Philadelphia; Orlando, Fla., 1998.
35. A. F. van Driel, I. S. Nikolaev, P. Vergeer, P. Lodahl, D. Vanmaekelbergh and W. L. Vos, *Physical Review B*, 2007, **75**, 035329.
36. C. Kittel, *Introduction to solid state physics*, Wiley, 1976.
37. T. Nychyporuk, Y. Zakharko, T. Serdiuk, O. Marty, M. Lemiti and V. Lysenko, *Nanoscale*, 2011, **3**, 2472-2475.
38. S. Vial, D. Nykypanchuk, F. L. Deepak, M. Prado and O. Gang, *Journal of colloid and interface science*, 2014, **433**, 34-42.
39. T. Owen, *Fundamentals of Modern UV-visible Spectroscopy: Primer*, Agilent Technologies, 2000.
40. D. A. Long, *Raman spectroscopy*, McGraw-Hill International Book Company, 1977.
41. J. M. Hollas and R. S. o. Chemistry, *Basic Atomic and Molecular Spectroscopy*, Royal Society of Chemistry, 2002.
42. L.-L. Bao, S. M. Mahurin, C.-D. Liang and S. Dai, *Journal of Raman Spectroscopy*, 2003, **34**, 394-398.
43. A. Campion and P. Kambhampati, *Chemical Society Reviews*, 1998, **27**, 241-250.
44. M. M. Maitani, D. A. A. Ohlberg, Z. Li, D. L. Allara, D. R. Stewart and R. S. Williams, *Journal of the American Chemical Society*, 2009, **131**, 6310-6311.
45. J. A. Guicheteau, M. E. Farrell, S. D. Christesen, A. W. Fountain, P. M. Pellegrino, E. D. Emmons, A. Tripathi, P. Wilcox and D. Emge, *Appl. Spectrosc.*, 2013, **67**, 396-403.
46. P. Etchegoin, L. F. Cohen, H. Hartigan, R. J. C. Brown, M. J. T. Milton and J. C. Gallop, *The Journal of Chemical Physics*, 2003, **119**, 5281-5289.
47. P. L. Stiles, J. A. Dieringer, N. C. Shah and R. P. Van Duyne, *Annual Review of Analytical Chemistry*, 2008, **1**, 601-626.
48. T. Aoki, in *Characterization of Materials*, John Wiley & Sons, Inc., 2002.
49. J. Solé, L. Bausa and D. Jaque, *An Introduction to the Optical Spectroscopy of Inorganic Solids*, Wiley, 2005.
50. P. Y. Yu and M. Cardona, *Fundamentals of Semiconductors: Physics And Materials Properties*, Springer, 2005.

Chapter 3

Structural and Chemical Characterization of Silicon Nanocrystals (SiNCs) and Silver Nanoparticles (AgNPs)

In this chapter, the properties of synthesised alkylated silicon nanocrystals (C_{11}-SiNCs) are presented, which include a brief review of the properties of synthesised C_{11}-SiNCs and the chemical characterization of C_{11}-SiNCs using X- ray photoemission spectroscopy (XPS). The chemical composition of erbium mixed alkylated silicon nanocrystals (Er/C_{11}-SiNCs) is also determined by XPS and Fourier transform infrared spectroscopy (FTIR) measurements. Crystal structure and size distribution of Intrinsiq Ltd commercial silicon nanocrystals (SiNCs) are obtained by scanning electron microscopy (SEM), transmission electron microscopy (TEM), high resolution transmission electron microscopy (HRTEM), atomic force microscopy (AFM) and X -ray diffraction (XRD). The chemical characterization of commercial SiNCs is performed also using XPS and FTIR measurements. The structural and chemical characteristics of synthesised silver nanoparticles (AgNPs) are also presented.

3.1 Characterization of synthesised alkylated silicon nanocrystals (C_{11}-SiNCs)

In this section, a review of the properties of C_{11}-SiNCs that were used in the experiments is presented. The chemical composition of C_{11}-SiNCs is obtained also using XPS and FTIR techniques. Alkylated SiNCs prepared by a modification method from Lie *et al*[1] as in Chao *et al*.[2] The size, structure and composition of alkylated silicon nanocrystals have been well investigated by our group (Nanoscale Science and Nanotechnology Research Group, Newcastle University, United Kingdom).[2-4] Thus, the properties of C_{11}-SiNCs which utilized in this project are shortly reviewed in this section. Porous silicon was formed by etching silicon wafer. C_{11}-SiNCs were then extracted from the porous silicon by thermal hydrosilation reaction.

After etching process, a light orange colour was seen on the surface of the porous silicon chips as shown in figure 2.2a (Chapter 2, section 2.2.1). The colour of porous silicon is dependent on the current density which is applied. Therefore, the colour of the porous silicon varies from red to orange as the current density is

increased.[1] The dry porous silicon chips also luminesced orange under ultraviolet (UV) light (λ = 365 nm). Alkylated silicon nanocrystals are obtained by refluxing the porous silicon chips in dry toluene with 0.1 M 1-undecene. Under the UV lamp (λ = 365 nm) an orange colour luminescence is emitted by the resulting suspension. Under reduced pressure, the solvent was removed and a waxy pale yellow product is observed. This remaining product is alkylated silicon nanocrystals whose surface is covered with a monolayer of Si-C bonded alkyl species produced by a thermal hydrosilation reaction. Alkylated silicon nanocrystals were then dissolved in dichloromethane (DCM) to present a luminescent orange colour under UV lamp (λ = 365 nm) as shown in figure 2.2b (Chapter 2, section 2.2.1). DCM was chosen as a solvent because the evaporation process of DCM (313 K) is easier than toluene (383 K).

Chao *et al*[2] reported that these alkylated silicon nanocrystals which refluxed in toluene solution in presence of 1-undecene have a diameter of 2.5 nm, which associate to the silicon core of the nanoparticles. Using fluorescence spectroscopy, alkylated silicon nanocrystals in trichloromethane present one emission peak at 670 nm using different excitation sources i.e. 280 nm, 330 nm, 350 nm and 370 nm.[1] This orange luminescence peak is typical for alkylated silicon nanocrystals and was assigned to the excitation of un-oxidized silicon atoms.[3, 5] X- ray diffraction shows that the alkylated silicon nanoparticles have a crystalline silicon core with a particle diameter of 2.5 nm as shown in figure 3.1.[2] XPS and FTIR measurements indicate that the particles consist of a Si core with a sub-monolayer amount of oxide and a capping alkyl monolayer. Figure 3.2 presents the FTIR spectra of 1-undecene and undecenyl SiNCs which deposited on a single crystalline Si wafer.[1] It can be seen that the two infrared peaks of alkylated silicon nanocrystals at 800 and 1259 cm^{-1} are attributed to minority silanol sites and Si-CH_2-R deformation, respectively.[1] As a result of gradual oxidation of alkylated silicon nanocrystals, two broad IR peaks appeared. The former peak at around 700-900 cm^{-1} region assigned to the bending vibration mode of SiO. The second IR peak at 1050 cm^{-1} is assigned to symmetric and antisymmetric stretching mode of Si-O-Si. The terminal CH_3 stretching mode is at around 2956 cm^{-1} and the methylene C-H stretching modes appear at 2854 cm^{-1} and 2926 cm^{-1}. These peaks emphasize the presence of long alkyl chains in the alkylated silicon nanocrystals. This long alkyl monolayer is bonded to the silicon core by covalent Si-C bonds not by the

oxide. Thus, the alkyl monolayer is chemically robust and stable against the oxidation and hydrolysis except under intense X- ray irradiation.[3, 6-8]

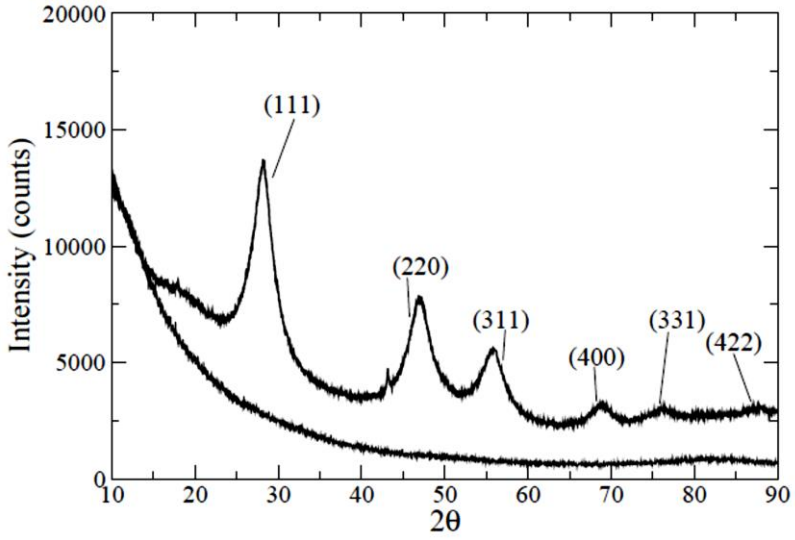

Figure 3.1: X- ray diffraction pattern of alkylated SiNCs. The peaks are attributed to the indicated lattice planes of crystalline Si. The lower spectrum is the scattering from the blank.[9]

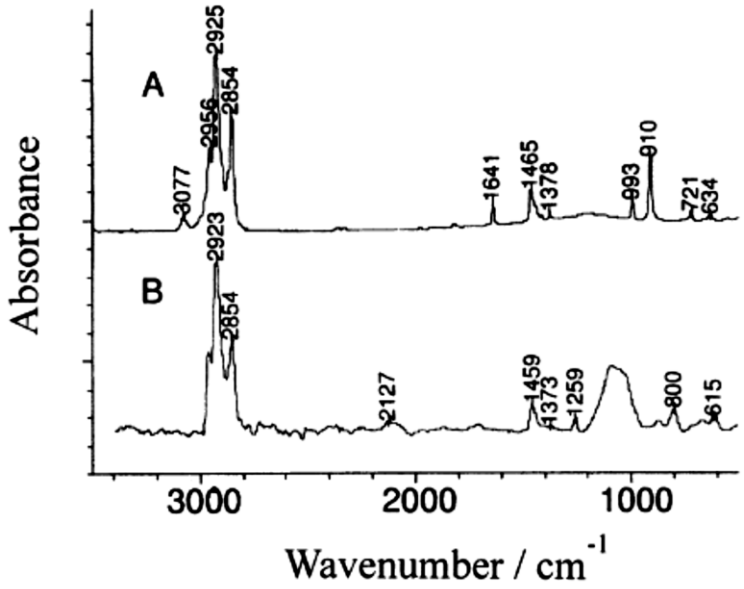

Figure 3.2: FTIR spectra of (a) 1-undecene on a single crystalline Si wafer (b) the undecenyl capped SiNCs dried on a single crystal Si wafer.[1]

In this work, X- ray photoemission spectroscopy (XPS) is used to determine the chemical composition of synthesised C_{11}-SiNCs. XPS measurement was carried out at

Newcastle University using (Kratos Axis Ultra 165 spectrometer) with monochromatic excitation photon energy of Al K_α at 1486.6 eV. In addition, the experimental details of this procedure are given in chapter 2. section 2.3.6.

Figure 3.3a shows the Si*2p* spectrum of C_{11}-SiNCs suspension in deionized water dried on gold substrate. The Si*2p* peak has been fitted with a mixed doublet. This figure presents a peak at a binding energy of 101.2 eV. This binding energy of Si*2p* at 101.2 eV is consistent for alkylated SiNCs.[2] This peak assigned to a multicomponent peak that contain different species i.e. bulk silicon, Si-C and Si-H.[3] The second peak at 101.8 eV is attributed to Si-O. As discussed previously, the IR spectrum of the C_{11}-SiNCs[1] confirms the presence of Si-C and Si-O (see figure 3.2). The Si*2p* spectra of alkylated SiNCs in this figure is similar to that observed by Chao *et al*.[2, 3] They determined a peak for alkylated silicon nanocrystals at 101.6 eV. Obviously, the difference between these two binding energies is 0.2 eV. This difference in the binding energy values are predictable because the thickness of the C_{11}-SiNCs film change in every deposition, thus would impact the degree of charging in the film. The charge effect arises from the long alkyl chain that passivates the surface of SiNCs. Also, the charge effect would likely to be due to the agglomeration of SiNCs as clusters rather than diffuse as individual particles as observed by Chao *et al*.[2, 3]

Figure 3.3b shows the O*1s* core level of C_{11}-SiNCs dried on gold substrate. This peak has been fitted using a mixed singlet. The binding energy at 532.0 eV and 532.6 eV are assigned to Si-O and Si-O_2, respectively.[10]

Figure 3.3c shows the C*1s* core line of alkyl capped SiNCs. The peak has been fitted with mixed singlet. This peak at 284.6 eV and 284.8 eV are attributed to adventitious carbon and Si-C, respectively.[9]

Figure 3.3d presents a survey spectrum of alkylated silicon nanocrystals. The core lines i.e. Si*2p*, Si*2s*, C*1s* and O*1s* are clearly visible in the survey spectrum which appears at 101.4 eV, 150.0 eV, 284.6 eV and 532.0 eV, respectively. Thus, in the film of the investigated sample silicon, carbon and oxygen are present. Some hydrogen atoms may be there in the film but X- ray photoemission spectroscopy cannot detect them.[3] This survey spectrum confirmed also the previous study of IR spectroscopy[1] which exhibits the existence of Si-C and Si-O bonds (see figure 3.2). The Si-C bonds are

anchoring the alkyl chains to dots by covalent bonds while the Si-O bonds arise from the oxidation of unalkyalted Si-H.[1] Altogether, the data suggest that the alkyl chains and sub oxides are present on the surface of silicon nanocrystals.

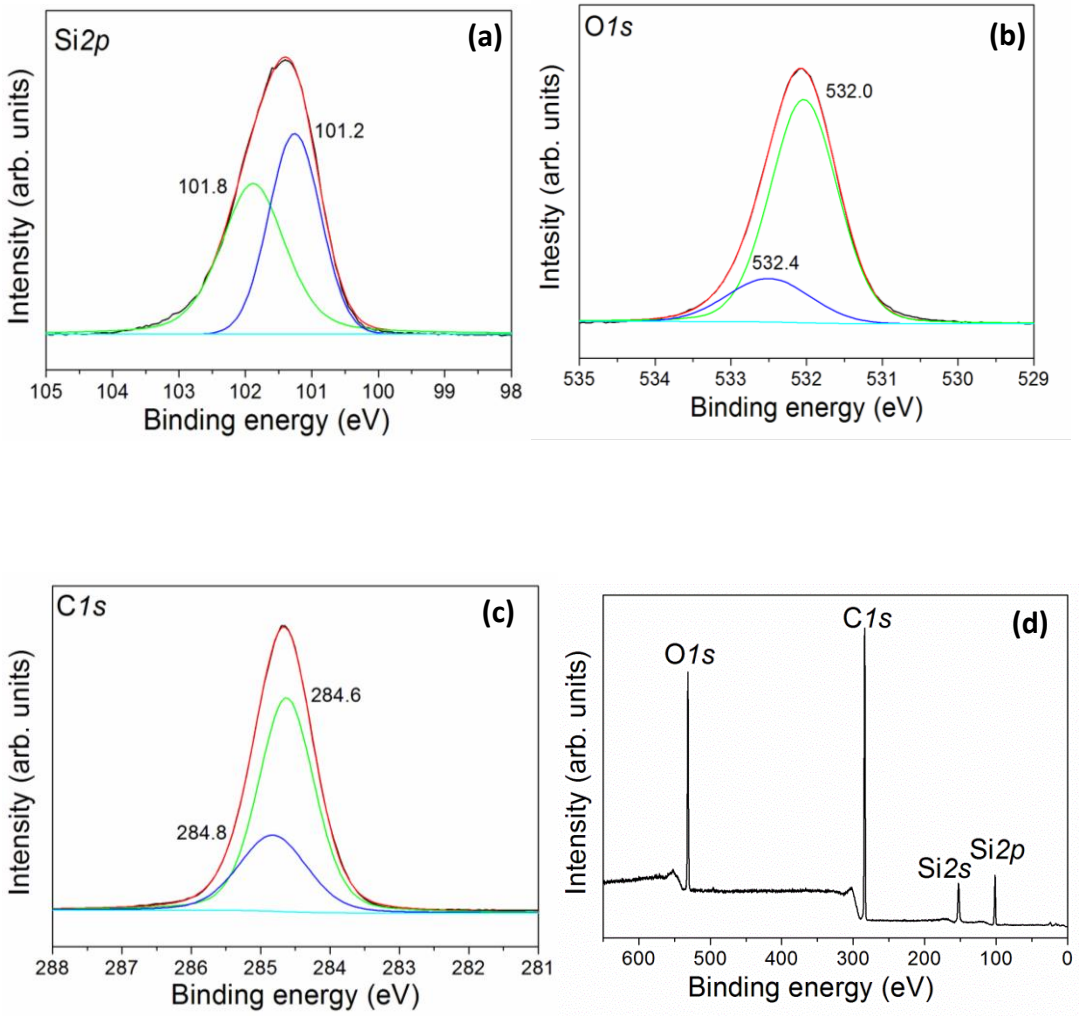

Figure 3.3: XPS spectra of C_{11}-SiNCs sample deposit on a gold substrate showing, (a) Si*2p*, (b) O*1s* (c) C*1s* and (d) survey scan.

3.2 Chemical characterization of erbium mixed alkylated silicon nanocrystals (Er/C_{11}-SiNCs), measured by Fourier transform infrared spectroscopy (FTIR) and X- ray photoemission spectroscopy (XPS)

In this section, the surface chemical composition of Er/C_{11}-SiNCs is investigated using two techniques i.e. FTIR and XPS in order to study the effect of erbium (III) on alkylated silicon nanocrystals. The setup of these two experiments is explained in more details in (Chapter 2, section 2.3.7 and 2.3.6), respectively.

Figure 3.4 presents the FTIR spectrum of Er/C_{11}-SiNCs. It can be seen that there are several IR bands of erbium mixed alkylated silicon nanocrystals sample. The IR peak at 2954 cm^{-1} corresponds to CH_3 stretching mode.[1] The IR peaks that appear at 2921 cm^{-1} and 2854 cm^{-1} are assigned to the methylene C-H asymmetric and symmetric stretching mode, respectively.[1] These three IR bands at 2954 cm^{-1}, 2921 cm^{-1} and 2854 cm^{-1} prove that the long alkyl chains are present in the film of Er/C_{11}-SiNCs. The band at 1459 cm^{-1} corresponds to Si-C bending mode.[1, 11] The two IR bands at 1259 cm^{-1} and 1220 cm^{-1} are corresponding to Si-CH_2-R bending mode.[1, 12] Broad IR peak occurs at 1053 cm^{-1} as a result of gradual oxidation of the investigated sample which correspond to Si-O-Si symmetric and asymmetric stretching modes.[1] In addition, SiO bending vibration modes appear at the region 700 – 900 cm^{-1}.[1] The IR peaks at 800 cm^{-1} and 615 cm^{-1} are attributed to silanol sites and unalkyalted Si-H bending vibration mode, respectively.[1]

The FTIR spectrum of Er/C_{11}-SiNCs in figure 3.4 is similar to that observed by Lie *et al*.[1] There is no considerable change in the vibration modes of Er/C_{11}-SiNCs when compared with that of C_{11}-SiNCs as presented in Table 3.1. Thus, these data suggest that the erbium ions (Er^{3+}) do not have effect on the surface of alkylated SiNCs. However, there is no peak determined for erbium trichloride by FTIR spectrum as the erbium does not vibrate in IR range.[13] Thus, XPS is used to determine the surface chemical composition of Er/C_{11}-SiNCs.

Functional group	Vibration modes	C_{11}-SiNCs (cm^{-1})	Er/C_{11}-SiNCs (cm^{-1})
CH_3	Stretching	2956	2954
CH	Stretching	2926	2921
CH	Stretching	2854	2854
SiC	Bending	1459	1459
$SiCH_2R$	Bending	1259	1259 & 1220
SiOSi	Stretching	1050	1053
SiO	Bending	700-900	700-900
$Si(CH_3)_3OH$	Bending	800	800
SiH	Bending	615	615

Table 3.1: IR vibrations bands that observed in FTIR spectra for pure C_{11}-SiNCs and Er/C_{11}- SiNCs.

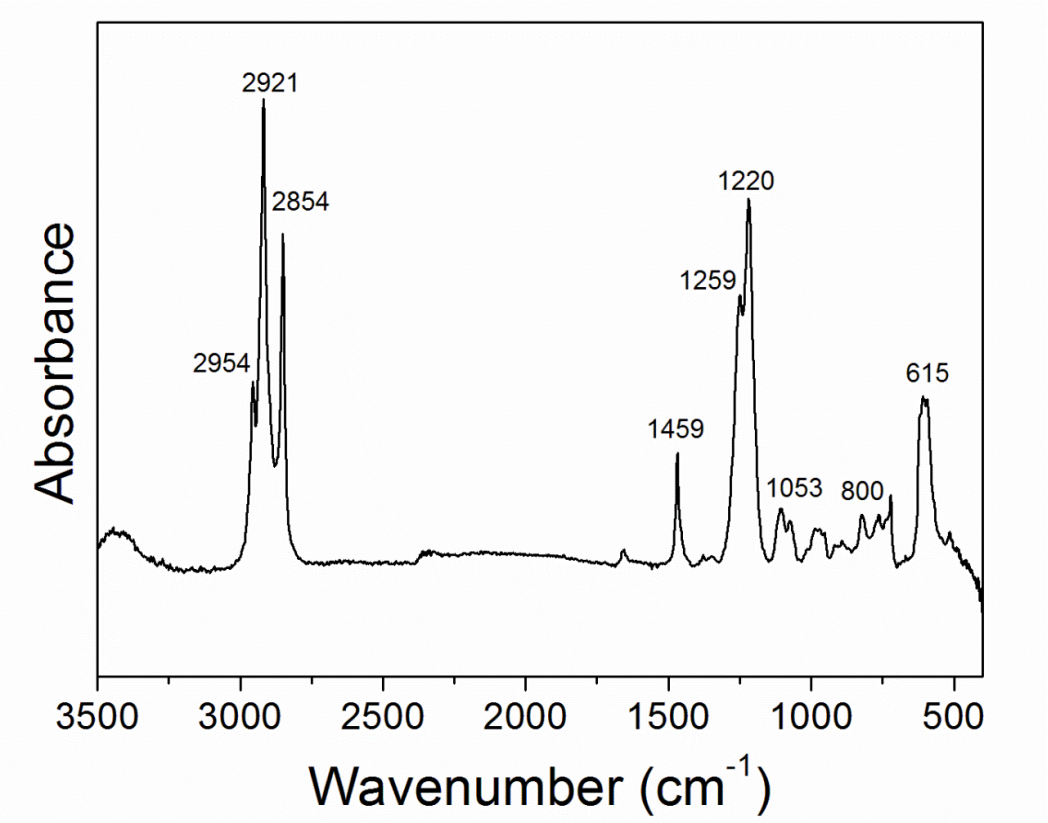

Figure 3.4: FTIR spectrum of Er mixed C_{11}-SiNCs deposited on a single crystal silicon wafer.

Figure 3.5a presents the XPS spectrum of Si*2p* of Er/C_{11}-SiNCs solution dried on gold substrate. This spectrum is similar to that observed by Chao *et al*.[2] This peak consists of broad peak with a tail to higher binding energy. This peak has been fitting using mixed doublet. This spectrum is fitted with three peaks with binding energies of 98.6 eV, 102.4 eV and 106.6 eV. They are assigned to different species of Si that are present in Er/C_{11}-SiNCs. The peak at 98.6 eV is assigned to Si.[10] While the peak at 102.4 eV can be attribute to SiO_2, Si_xC_y and Si_xO_y.[3, 14, 15] Furthermore, the higher binding energy component, at 106.6 eV can be associated to saturated peak of silicon i.e. SiO_2.[3]

Figure 3.5b presents the O*1s* core level spectrum of Er/C_{11}-SiNCs. This spectrum is fitted using mixed singlets into three components i.e. 530.8 eV, 532.6 eV and 533.4 eV. The binding energies at 530.8 eV assigned to Er_2O_3.[14-16] The binding energy at 532.6 eV corresponds to Si_xO_y while the binding energy at 533.4 eV corresponds to SiO_2. [14, 15]

Figure 3.5c shows the XPS spectrum of Er*4d* for Er/C_{11}-SiNCs. This peak has also been fitted used mixed doublet. The two peaks constitute a doublet with spin orbit splitting of 2 eV that is consistent with Shen *et al*.[16] The binding energy at 168.4 eV and 170.4 eV of Er*4d* assigned to $4d_{5/2}$ and $4d_{3/2}$ of Er_2O_3.[16]

Figure 3.5d presents the XPS spectrum of C*1s* for Er/C_{11}-SiNCs. The peak has also been fitted using mixed singlets. This spectrum consist of three peaks i.e. 284.6 eV, 285.8 eV and 288.9 eV which they are correspond to adventitious carbon[17], C-C[18] and Si-C[19] , respectively. The FTIR data confirm the presence of Si-C (see Table 3.1).

A survey spectrum of erbium mixed alkylated silicon nanocrystals is plotted in figure 3.5e. The core lines of Si*2p*, O*1s*, Er*4d*, and C*1s* are visible and clear which supports the FTIR study (see figure 3.4), that indicate the presence of both Si-O (originate from the oxidation of unalkyalted Si-H) and Si-C (bonded the alkyl chains to the dots). Thus, the XPS data confirm the presence of the components of Si-C and Si-O in binding energy at 102.4 eV. In addition, the data in figure 3.5e show that the silicon nanocrystals are surrounded with a combination of surface SiO_2, Er_2O_3 and alkyl chains.

Comparing the two investigated samples i.e. C_{11}-SiNCs and Er/C_{11}-SiNCs, it can be seen that the core level Si*2p* for alkylated SiNCs shows two multicomponent peak (see

figure 3.3a), while the core level Si*2p* for erbium mixed alkylated SiNCs presents three peaks (see figure 3.5a). It can be explained as result of presence of erbium sesquioxide on the surface of alkylated SiNCs which affect the oxidation states of SiNCs on the surface. Figure 3.5c shows the core level Er*4d* for Er/C_{11}-SiNCs, which confirm that the erbium trichloride hydrolysis to Er_2O_3 when mixed with alkylated SiNCs. Meanwhile, figure 3.5b presents O*1s* of Er/C_{11}-SiNCs that prove that Er_2O_3 is present on the surface of C_{11}-SiNCs. This observation can be also interpreted as a result of exposing C_{11}-SiNCs for oxygen and H_2O for long times which increase the amount of Si_xO_y species on the C_{11}-SiNCs surface. These data suggest that the main effect of erbium ions (III) is affecting the oxidation states of alkylated SiNCs.

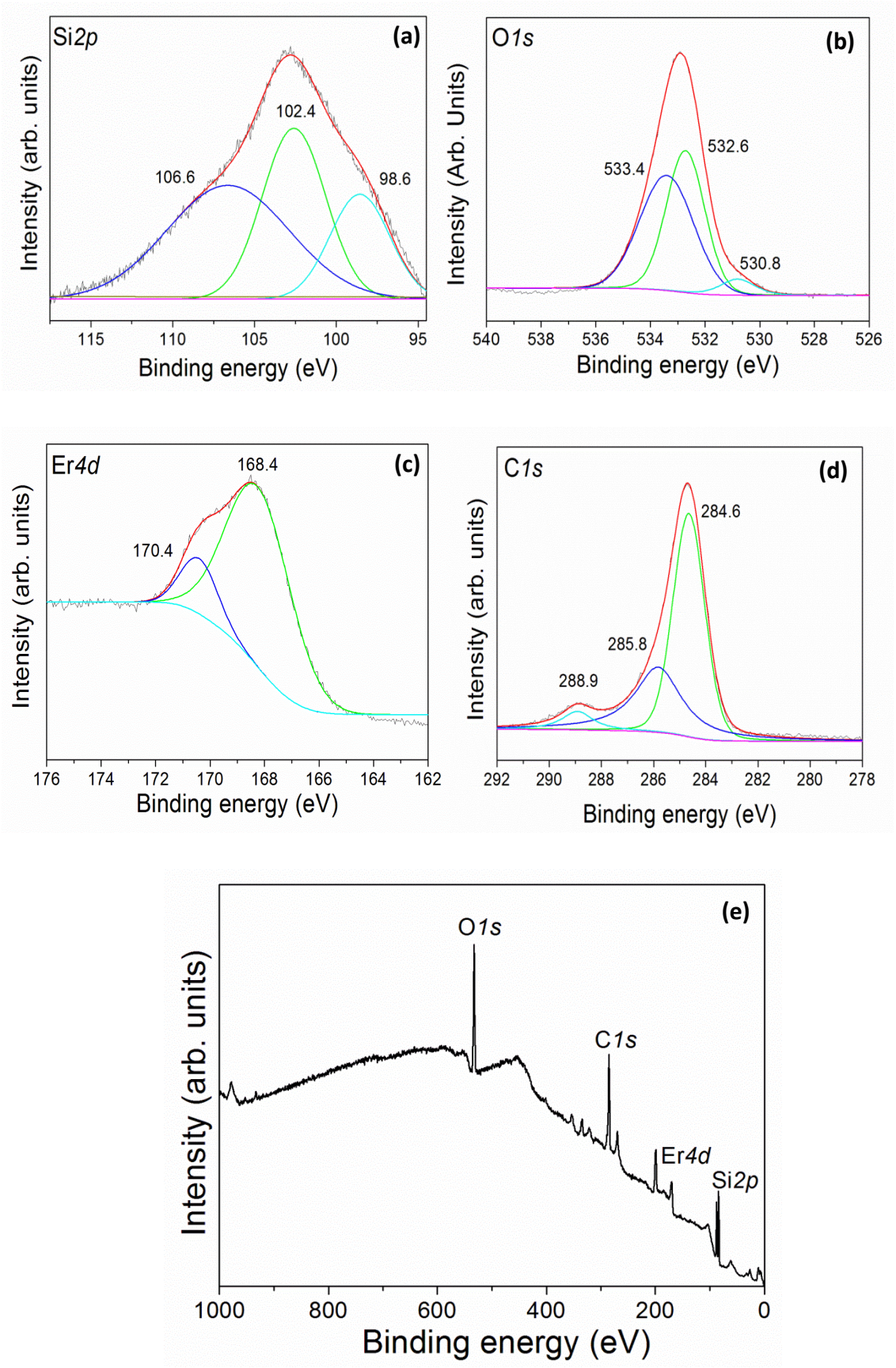

Figure 3.5: XPS spectra of Er/C_{11}-SiNCs deposited on gold substrate showing (a) Si*2p*, (b) O*1s*, (c) Er*4d,* (d) C*1s* and (e) survey scan.

3.3 Characterization of commercial silicon nanocrystals (SiNCs)

In this section, the crystal structure and size distribution of commercial silicon nanocrystals (SiNCs) are obtained by scanning electron microscopy (SEM), transmission electron microscopy (TEM), high resolution transmission electron microscopy (HRTEM), atomic force microscopy (AFM) and X -ray diffraction (XRD). The chemical characterization of Intrinsiq Ltd SiNCs is carried out also using X- ray photoemission spectroscopy (XPS) and Fourier transform infrared spectroscopy (FTIR) analysis.

3.3.1 Crystal planes and size distribution of commercial silicon nanocrystals (SiNCs), measured by scanning electron microscopy (SEM), transmission electron microscopy (TEM), high resolution transmission electron microscopy (HRTEM), atomic force microscopy (AFM) and X -ray diffraction (XRD)

The commercial silicon nanocrystals were characterized using scanning electron microscope (SEM), transmission electron microscopy (TEM), high resolution transmission electron microscopy (HRTEM), atomic force microscopy (AFM) and X-ray diffraction (XRD). The general setup of these experiments is explained in more details in (Chapter 2, sections 2.3.1, 2.3.2, 2.3.3, 2.3.4 and 2.3.5), respectively.

Scanning electron microscope images were obtained to investigate the morphology and size distribution of the commercial SiNCs. Figure 3.6 shows the SEM images of commercial SiNCs dried on an aluminium support. From figure 3.6 a-b, it can be revealed that the particles are spherical in shape and there are agglomerates of SiNCs. Figure 3.6c shows the particle size distribution of the commercial SiNCs. It can be noticed that there is a large size distribution in commercial SiNCs and the majority of the size of these particles are in range between 20 - 90 nm. The average particle size of commercial SiNCs is ≈ 65 ± 30 nm.[20]

TEM images of commercial SiNCs dried on carbon copper grid are shown in Figure 3.7. From TEM images (figure 3.7a), it can be seen that the commercial SiNCs have a spherical morphology. There are agglomerates of commercial SiNCs as seen in figure 3.7b. The particles size of commercial SiNCs are in range of 20 - 90 nm. In general, the TEM results are in agreement with the SEM observations.[20]

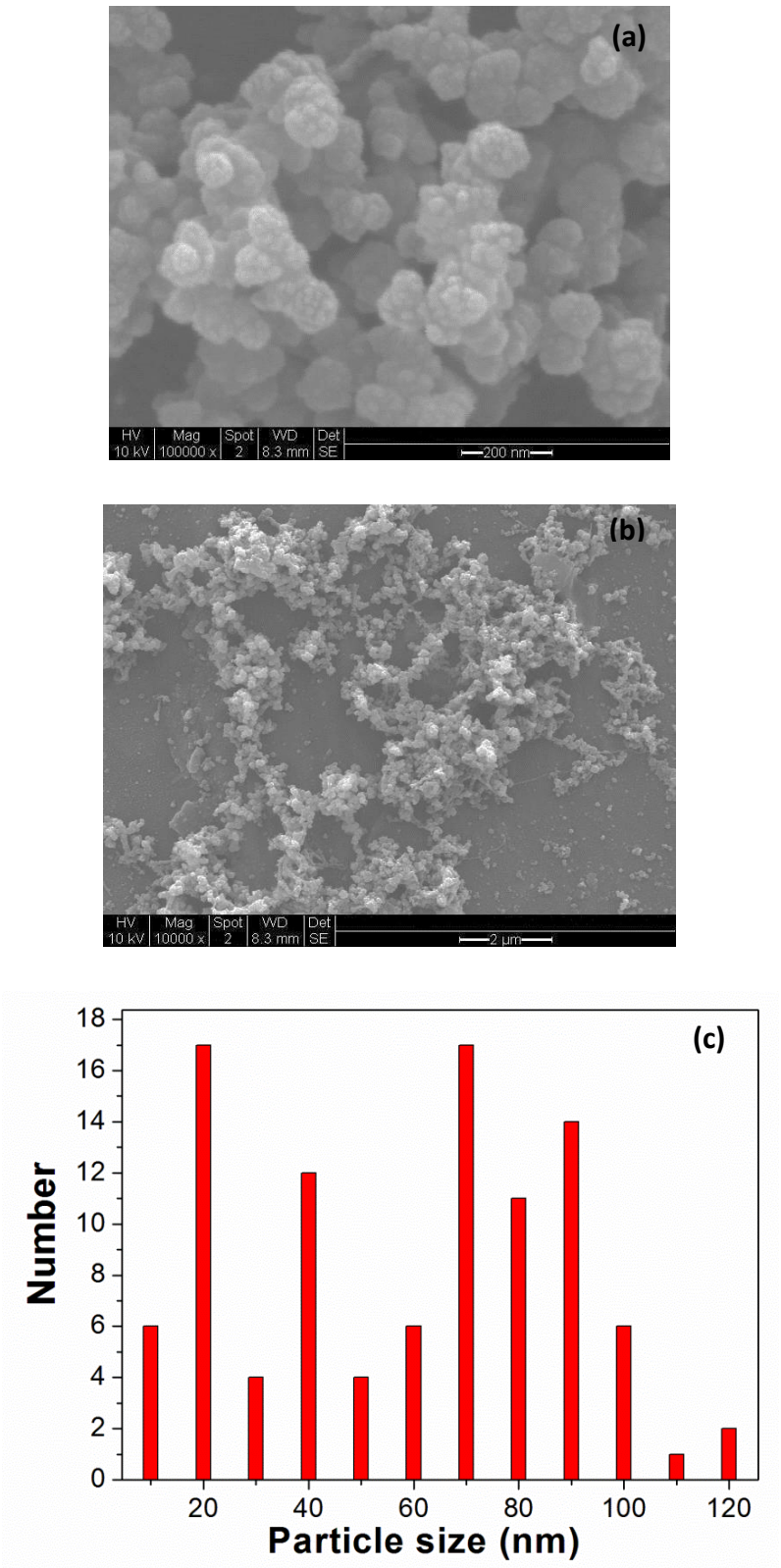

Figure 3.6: Scanning electron microscope images of commercial SiNCs dried on an aluminium support present (a) agglomerated SiNCs. The scale bar = 200 nm. (b) larger area indicating distribution of SiNCs. The scale bar = 2 µm. (c) a histogram of the particle size distribution obtained from 100 Si nanocrystals.[20]

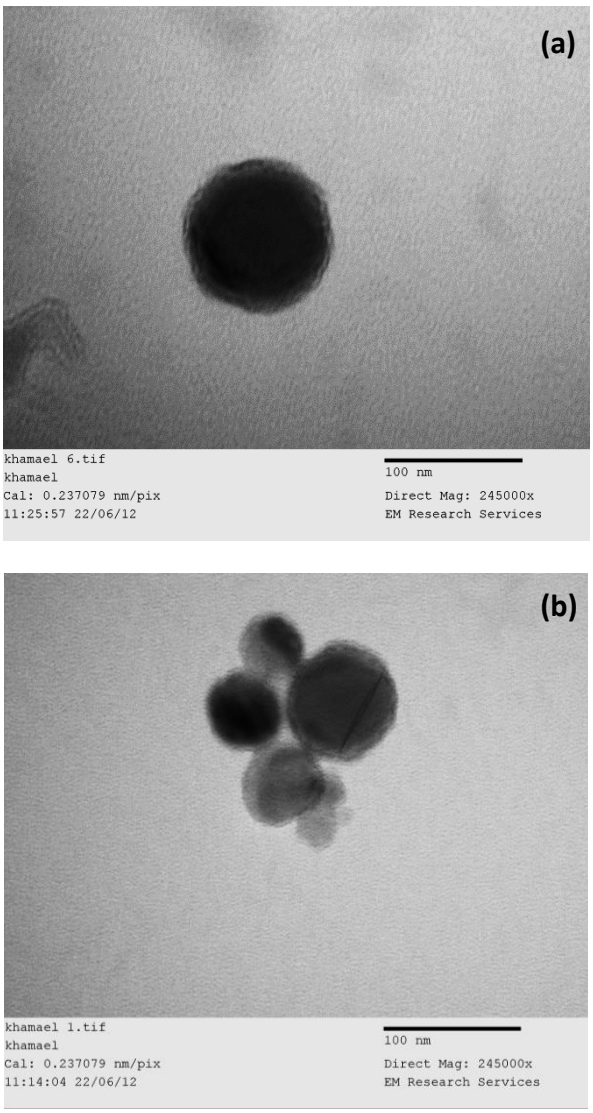

Figure 3.7: TEM images of commercial SiNCs dried on carbon copper grid. (a) typical spherical shape of SiNCs, (b) agglomerated SiNCs. The scale bar is 100 nm.

High resolution transmission electron microscopy was performed to determine the crystallographic phase of commercial SiNCs. Figure 3.8 presents the HRTEM images of commercial SiNCs dried on carbon copper grid. Figure 3.8a demonstrates that the commercial SiNCs are crystalline. The calculations of Fast Fourier transform (FFT) on the images of commercial SiNCs were carried out on different regions and showed the presence of the (111) crystal plane (Figure 3.8a inset).[20] This diffraction spot that is attributed to the (111) crystal plane corresponds to the face centred cubic (FCC) structure of SiNCs.[21] Agglomerates of SiNCs were detected in HRTEM image as shown in figure 3.8b as observed also by SEM and TEM results.

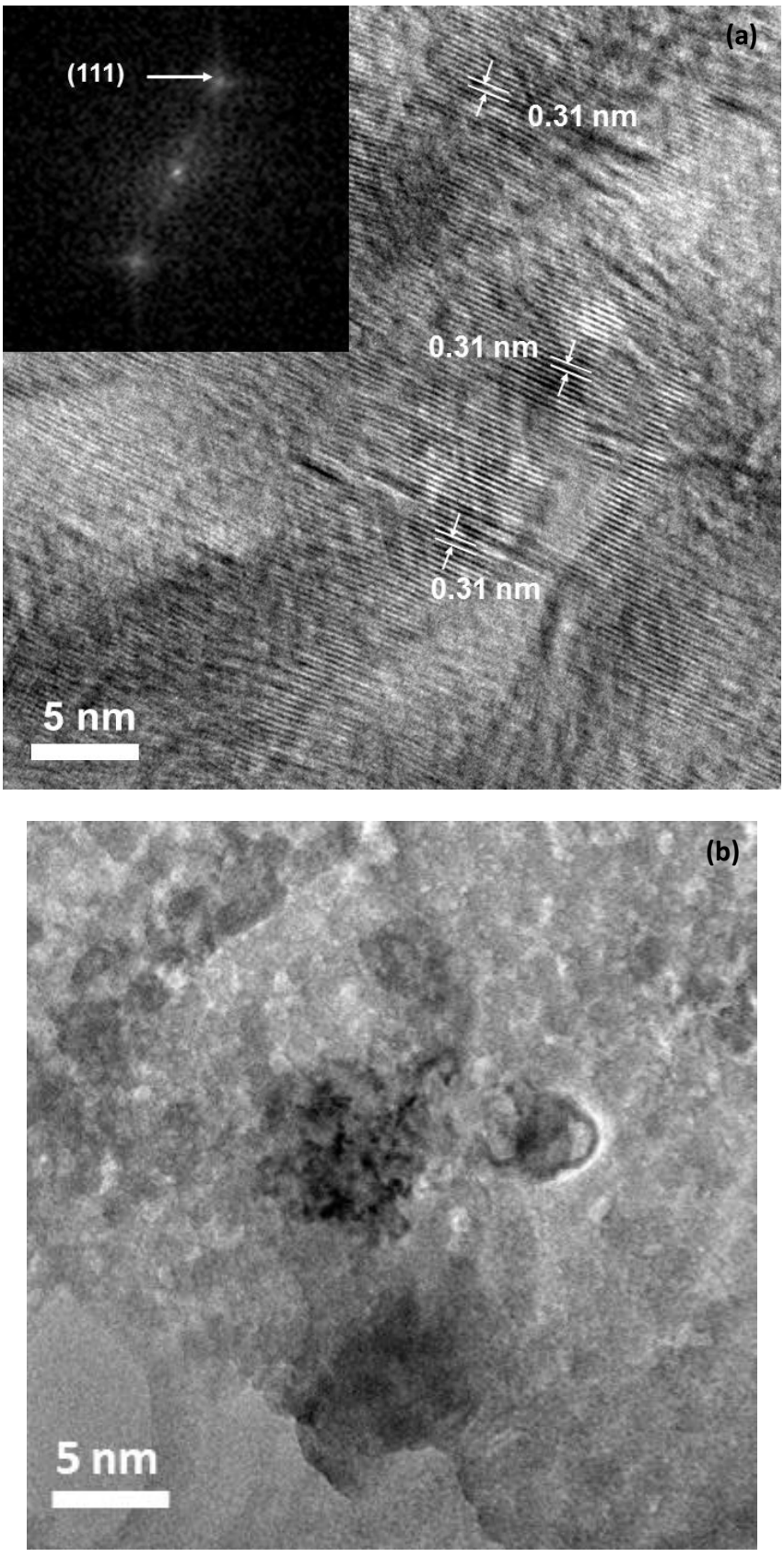

Figure 3.8: HRTEM images of commercial SiNCs dried on carbon copper grid showing (a) agglomerated SiNCs (the inset shows the diffraction pattern of SiNCs), (b) more agglomeration of SiNCs. The scale bar is 5 nm.[20]

The commercial SiNCs were also characterized by AFM to present more insight into their size and size distributions. Figure 3.9 presents the tapping mode AFM image and cross sections of different circles of commercial SiNCs sample dried on a mica substrate. AFM images of SiNCs indicate that the nanoparticles present as prolate spheroid, which is likely, a result of particle-surface interactions and could be from the tip which does not trace the topography completely. Figure 3.9a shows mainly single SiNCs without any aggregations due to using the mica as a substrate which does not allow SiNCs to move around and cluster into aggregates. The particle size of commercial SiNCs is also determined using AFM (performed on different circles as shown in figure 3.9). Figure 3.9b presents that the particles lie within the range of 20 - 90 nm.

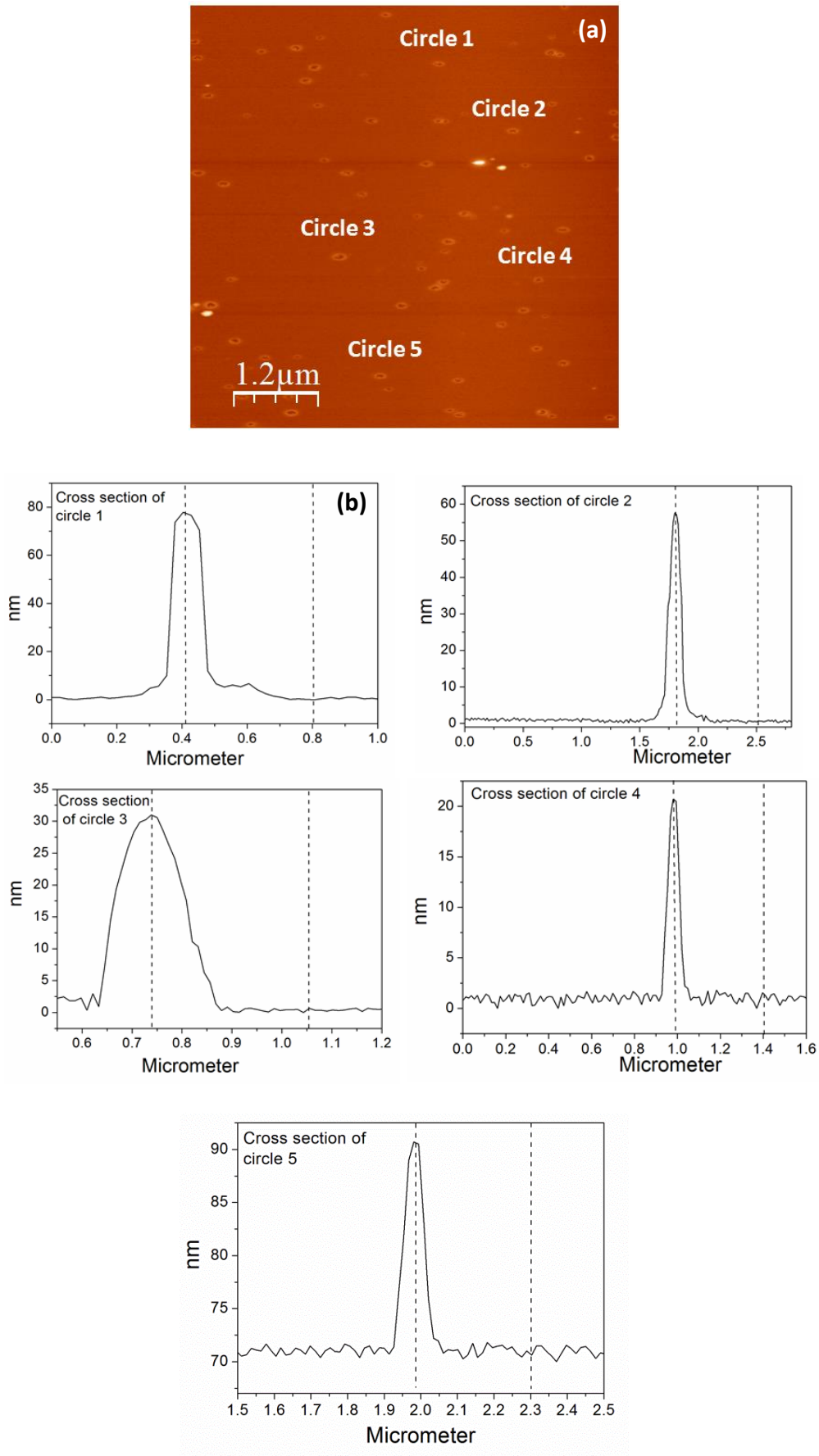

Figurer 3.9: a) Tapping mode AFM image of commercial SiNCs dried on mica substrate, b) cross sections of five different circles of SiNCs. Scan size =1.2 µm.

X -ray diffraction is carried out also to detect the crystallographic phase of commercial SiNCs and to determine the size of SiNCs. Figure 3.10 shows XRD pattern of the commercial SiNCs. Figure 3.10 presents well defined sharp peaks which reveal the high crystallinity of the commercial SiNCs. Thus, figure 3.10 exhibits the expected peaks that correspond to crystalline silicon and the crystal lattice of commercial SiNCs appears to exhibit ideal cubic symmetry. Table 3.2 presents the peak positions and intensities of investigated commercial SiNCs sample and bulk Silicon. The peak positions have been assigned by comparison of the spectrum with that of a bulk crystalline Si.[22] The feature at 2θ=28 degrees due to (111) planes has been fitted with a pseudo-Voigt function as shown in figure 3.11. Using Debye Scherrer formula (2.3. Chapter 2) and the peak width from the fit, the crystallite size D has been calculated.[23] It is found that the commercial Si particle diameter is 40 nm for (111) pattern. The value deduced from the feature at 47 and 56 degree were 43 and 44 nm, respectively (see table 3.3). However, from the table 3.3, it can be seen that the size of commercial SiNCs particles lie in the similar range as observed from SEM and TEM results.

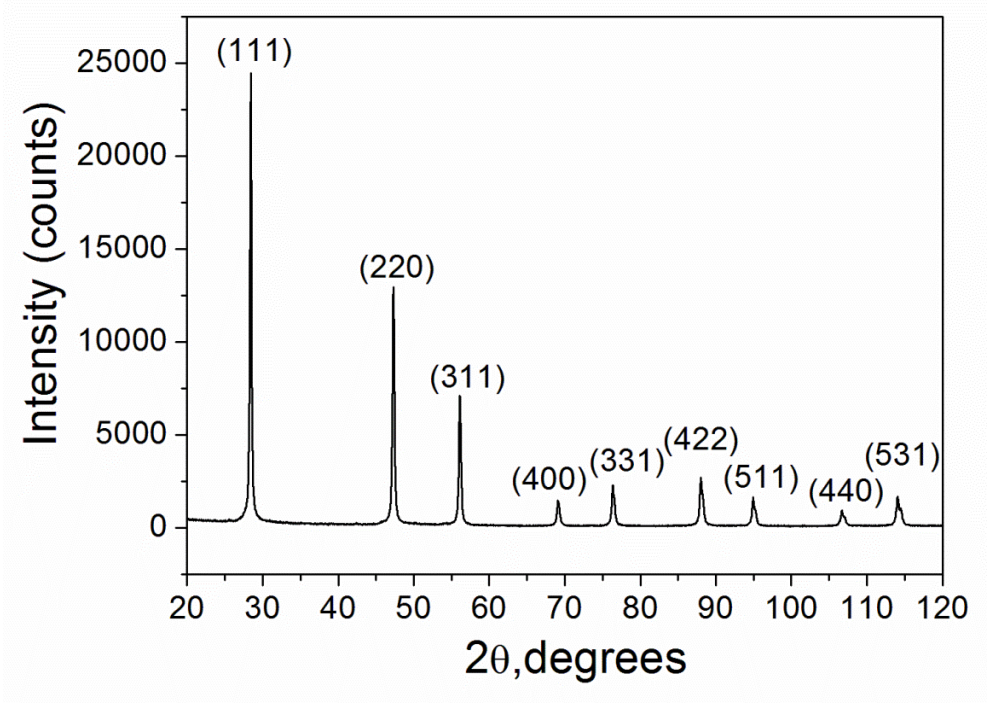

Figure 3.10: XRD pattern of commercial SiNCs. The peaks are attributed to the indicated lattice planes for crystalline silicon.

2θ Si bulk standard	2θ Commercial SiNCs	Intensity (% max) : Si bulk standard[24]	Intensity (% max) : Commercial SiNCs
28.443	28.47	100	100
47.304	47.16	55	52
56.122	56.01	30	28
69.132	69.20	6	5
76.380	76.56	11	9
88.029	88.06	12	10
94.951	94.99	6	5
106.719	106.6	3	3
114.092	114.11	7	5

Table 3.2: XRD peak positions and intensities for the commercial SiNCs and bulk Si standard.

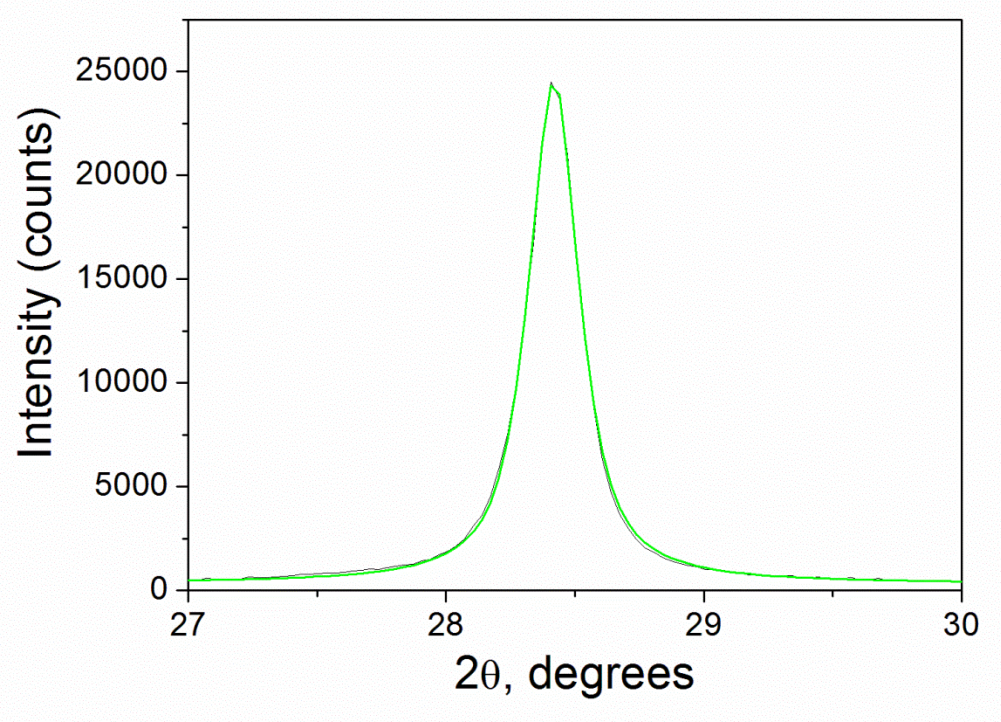

Figure 3.11: (111) peak of the XRD pattern for commercial SiNCs fitted to Pseudo-Voigt after subtraction of a linear baseline.

Diffraction pattern	2θ Commercial SiNCs	The particle size of commercial SiNCs (nm)
(111)	28.47	40
(220)	47.16	43
(311)	56.01	44

Table 3.3: XRD pattern and XRD positions and the particle diameter size of commercial SiNCs using Debye Scherrer formula.

3.3.2 Chemical characterization of commercial silicon nanocrystals (SiNCs), measured by Fourier transform infrared spectroscopy (FTIR) and X- ray photoemission spectroscopy (XPS)

In this part, the surface chemical composition investigation of commercial SiNCs is carried out by using FTIR and XPS. The experimental details can be shown in (Chapter 2, section 2.3.7 and 2.3.6), respectively.

An FTIR spectrum of the commercial SiNCs is presented in figure 3.12.[20] The Si-H_2 bending vibration mode of SiNCs is observed at 620 cm^{-1}.[25] The peak at 860 cm^{-1} attributed to bending vibration mode of Si-O.[1] The IR broad peak at 1080 cm^{-1} correspond to stretching vibration mode of Si-O-Si.[12, 25] The sharp peaks at 1379 cm^{-1} and 1459 cm^{-1} assigned to the bending vibration modes of C-H_2 in commercial SiNCs.[1, 12] The stretching vibration mode of C=O appeared at 1700 cm^{-1}.[26] The sharp IR peaks observed at 2080 cm^{-1} and 2250 cm^{-1} correspond to stretching vibration modes of Si-H and O_3-Si-H, respectively.[12] It can be seen that there are three IR bands of commercial SiNCs in the range 2854-2954 cm^{-1}. The peaks that appear at 2854 cm^{-1} and 2921 cm^{-1} are assigned to the methylene C-H symmetric and asymmetric stretching mode, respectively.[1] While the IR band at 2954 cm^{-1} corresponds to CH_3 stretching mode.[1]

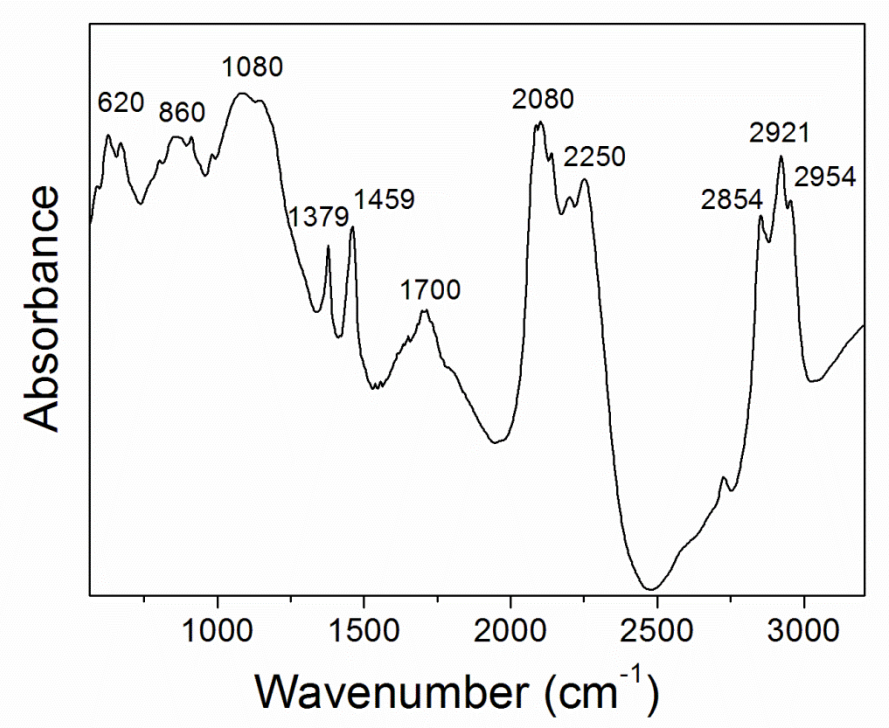

Figure 3.12: Fourier transform infrared spectrum of commercial SiNCs.[20]

XPS spectra for commercial SiNCs suspension in deionized water were dried on gold substrate are shown in figure 3.13.[20] Figure 3.13a shows the XPS spectra of Si2*p* core level for the commercial SiNCs. This peak has been fitted using mixed doublet. The peak at 101.8 eV can be assigned to the different species i.e. Si-Si, Si-H and Si-C, thus this peak is a multicomponent peak.[3] In addition, the peak at 102.6 eV is attributed to Si-O. As discussed previously, the IR spectrum of commercial SiNCs indicates the presence of Si-H, Si-C and Si-O. It is should be noted that this peak in this figure is similar to that reported by Chao *et al*.[2, 3] They determined a peak for alkylated silicon nanocrystals at 101.6 eV. Obviously, the difference between these two binding energies is 1.7 eV. This difference in the binding energy values is large. This difference can be explained as a result of using different methods in preparing Si nanocrystals. Thus, it would impact the binding energy values of silicon.

Corresponding to those peaks a similar peaks at 531.1 eV and 531.7 eV is observed in the O*1s* spectra (see figure 3.13b).[20] This peak has been fitted using mixed singlet. Those peaks can be attributed to the presence of SiO_x and SiO_2 in the film of commercial SiNCs.[20, 27] FTIR study of commercial silicon nanocrystals also confirms the presence of SiO_x in the sample (see figure 3.12). However, figure 3.13c presents a survey spectrum of the commercial SiNCs sample. This figure indicates the presence of

Au4f, Si2*p*, Si2s, O*1s* and C*1s* core lines which support the FTIR investigation and appear at 84.0 eV, 102.0 eV, 150.0 eV, 531.6 eV and 284.6 eV, respectively.

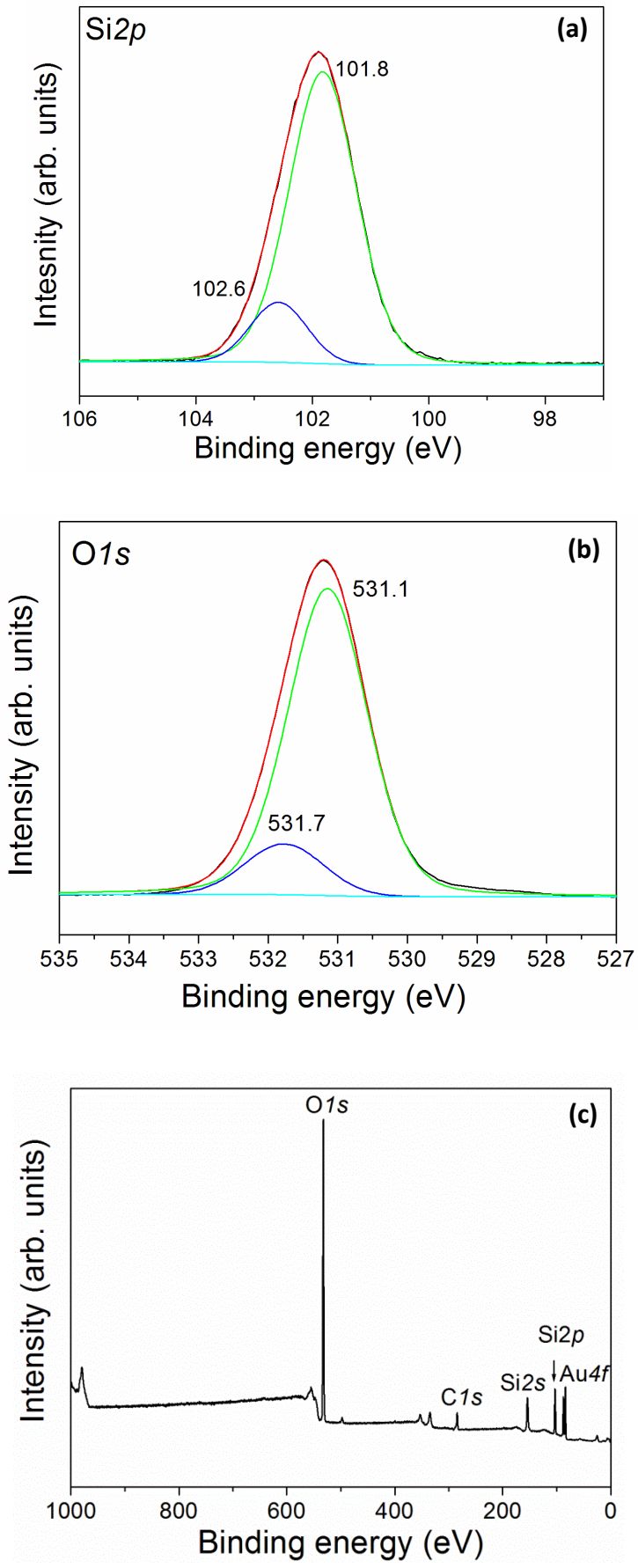

Figure 3.13: XPS spectra of commercial SiNCs deposited on gold substrate showing (a) Si*2p*, (b) O*1s* and (c) survey scan.[20]

3.4 Characterization of synthesised silver nanoparticles (AgNPs)

The properties of synthesised silver nanoparticles (AgNPs) have been presented in this section. Silver nanoparticles have been prepared by a green novel method from Bhaduri *et al*.[17] The resulting AgNPs also have been characterized using high resolution transmission electron microscope (HRTEM), scanning electron microscope (SEM), UV-Vis spectroscopy, X- ray photoemission spectroscopy (XPS) and Fourier transform infrared spectroscopy (FTIR).[17] Therefore, the properties of AgNPs which used in this work are briefly reviewed, while the experimental details were given in (Chapter 2 section 2.2.4 and 2.3.8).

AgNPs were formed at room temperature in presence of sunlight and an anionic surfactant i.e. sodium dodecyl sulphate (SDS) without utilizing a reducing agent. Thus, the sunlight and SDS play an important role for this reaction.[17] Concentrations of AgNPs i.e. 1 mM $AgNO_3$ and 10 mM $AgNO_3$ were exposed to sunlight for one hour, thus the colour of their solution changes from colourless to faint brown and brown, respectively as shown in figure 3.14a-b, respectively. Throughout exposure to sunlight, the synthesis temperature of the two concentrations was kept constant at 25 °C. However, the colour was changed after 5 minutes from the starting time of the reaction.

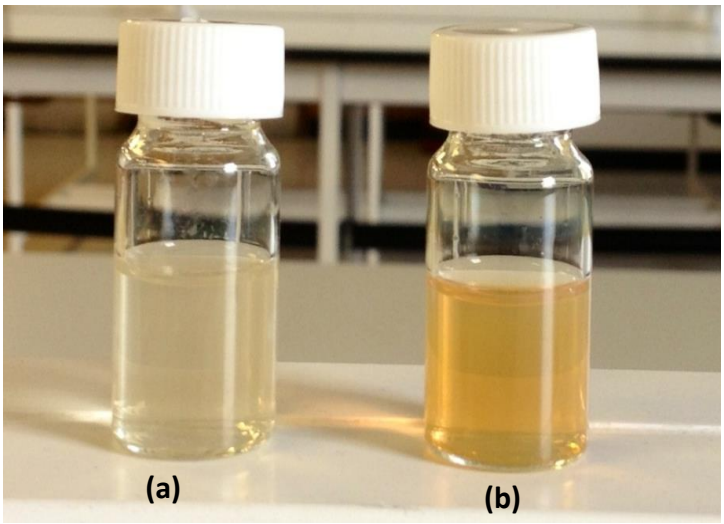

Figure 3.14: Silver nanoparticles (AgNPs) solution prepared under sunlight at 25 °C (a) Reactant concentrations (1 mM $AgNO_3$ and 5 mM SDS) after exposure to sun for one hour, and (b) Reactant concentrations (10 mM $AgNO_3$ and 50 mM SDS) after exposure to sun for one hour.

Bhaduri *et al*[17] obtained that AgNPs in two different concentration (1 mM $AgNO_3$ and 10 mM $AgNO_3$) have an average diameter of 100 nm and 30 nm, respectively by using SEM. HRTEM results shows that AgNPs are crystalline with a face centred cubic (FCC) lattice and AgNPs are surrounding with a layer of the surfactant. Bhaduri *et al*[17] suggested a mechanism of the reaction on the basis of XPS and FTIR results. Figure 3.15 presents this mechanism; silver dodecyl sulphate forms in solution initially. Then a photon is been absorbed by silver dodecyl sulphate, resulting in metallic silver and DS free radical. This free radical rearranges the S-O-C and S-O bonding of SO_4 of the SD molecule. This arrangement makes the radical more stable.

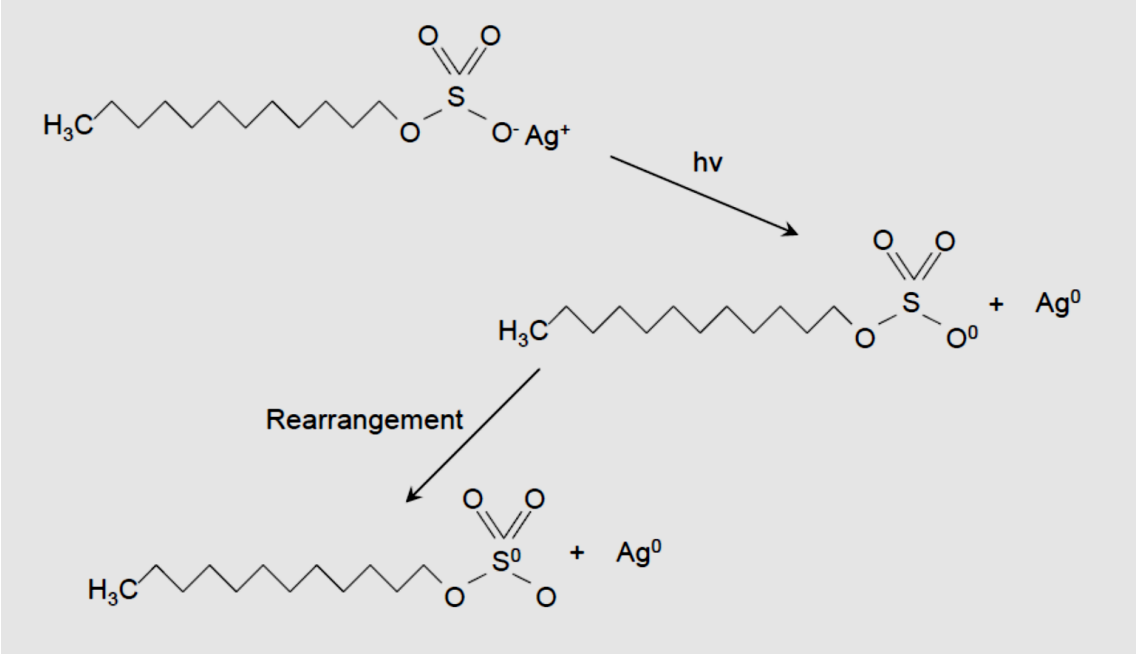

Figure 3.15: The schematic of the photochemical reaction of AgNPs from reactants i.e. $AgNO_3$ with SDS.[17]

The optical properties of AgNPs were studied in this work using UV-Vis spectroscopy. Figure 3.16 shows UV-Vis absorption spectra of both concentrations of synthesised AgNPs after exposure to sunlight for one hour. From the figure 3.16a-b, it was found that there are two characteristic plasmon absorption peaks which observed in different wavelengths i.e. 398 nm and 425 nm, respectively. This is due to surface plasmon resonance of AgNPs which relies on the particle size and dipole/multipole resonance.[17] It should be pointed out that the absorption of light at different wavelengths by silver nanoparticles gives an evidence of particle size, while the broadening of these peaks indicates the particle size distribution.[17] Consequently, the

width of these two peaks is different. When the concentration of $AgNO_3$ is higher, the narrowest particle size distribution is produced (see figure 3.16a-b). Thus comparing the broadening peak at 425 nm and 398 nm may be result of different average particle size distribution as confirmed by SEM results.[17] Figure 3.16a-b presents a peak at 398 nm and 425 nm which assigned to plasmons in AgNPs. There is a hump also in the figure 3.16a-b observes at 350 nm this is due to multi-pole surface plasmon which generates from larger AgNPs as observed by Bhaduri *et al*.[17] The intraband transition of metallic silver is observed also at 320 nm in figure 3.16a-b.[17] It can be seen that the UV-Vis absorption peak of AgNPs (10 mM) which have an average particle size of 100 nm is appeared at shorter wavelength (398 nm vs 425 nm) comparing with AgNPs (1 mM) which have an average particle size of 30 nm. This is can be explained as a result of the further agglomeration of AgNPs with higher concentration as observed by SEM images of AgNPs.[17] This agglomeration will cause a lack of the absorption wavelength of AgNPs (10 mM) as seen in figure 3.16b.

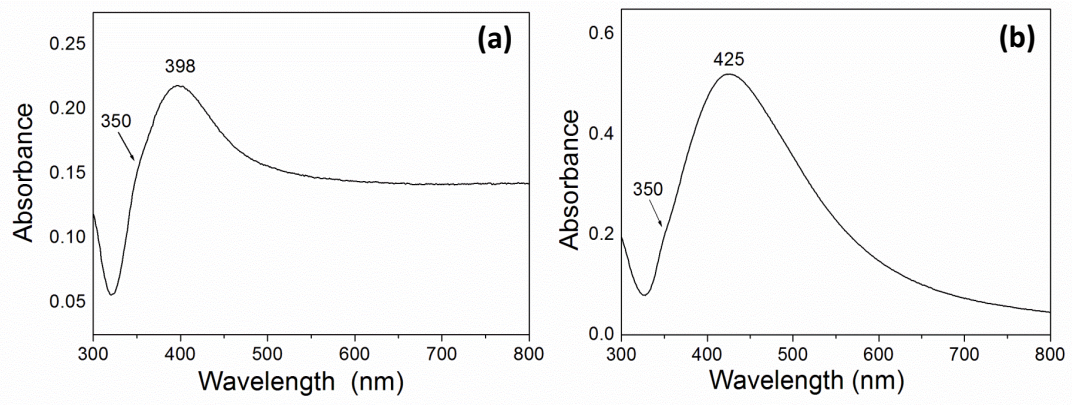

Figure 3.16: UV-Vis spectra of synthesised AgNPs (a) $AgNO_3$ concentration of 1 mM after exposure to sun for one hour, and (b) $AgNO_3$ concentration of 10 mM after exposure to sun for one hour.

3.5 Summary

To summarize, porous silicon have been prepared successfully by a galvanostatic etching method of p-Si(100) wafers followed by a thermal hydrosilation reaction of 1-undecene in refluxing toluene in order to extract the C_{11}-SiNCs from porous silicon. XPS measurement with photon energy of 1486.6 eV indicates that the estimation of the Si*2p* core level of the alkylated SiNCs and the other core lines i.e. C*1s* and O*1s* were observed in survey spectrum of alkylated silicon nanocrystals.

Erbium trichloride was added to C_{11}-SiNCs using a simple mixing chemical route. To the best of our knowledge, this is a first investigation on mixing C_{11}-SiNCs with erbium ions (III) by this chemical method. The erbium trichloride hydrolysis to erbium sesquioxide (Er_2O_3) in Er/C_{11}-SiNCs film which coat the surface of alkylated SiNCs. The presence of Er_2O_3 on the surface of C_{11}-SiNCs affects the oxidation state of alkylated SiNCs on the surface as observed by XPS measurement of Er/C_{11}-SiNCs. We can conclude that, the mixing chemical route which used in this project using Er^{3+} affect the oxidation state of alkylated SiNCs.

Commercial SiNCs have been characterized by SEM, HRTEM, AFM, XRD and XPS. It is found that the SiNCs are crystalline with an average diameter of 65 nm and FCC lattice. Infrared spectrum of commercial SiNCs presents characteristic vibrations bands of SiH_2, SiO, SiOSi, CH_2, SiH, CH and CH_3. It has been monitored the evolution of Si*2p* core level of the commercial SiNCs by using XPS.

Silver nanoparticles have been synthesized using sunlight and an anionic surfactant (SDS). Both sunlight and SDS play in an important role for this reaction to completed. With changing the concentration of the surfactant, it determined that the higher concentration of AgNPs (i.e. 10 mM $AgNO_3$ and 50 mM SDS) gives narrower particle size distribution. It is seen from UV-Vis measurements of silver nanoparticles, a presence of surface plasmon which makes silver nanoparticles convenient in different applications such as photovoltaic, plasmonics and photonics.

References:

1. L. H. Lie, M. Duerdin, E. M. Tuite, A. Houlton and B. R. Horrocks, *Journal of Electroanalytical Chemistry*, 2002, **538–539**, 183-190.
2. Y. Chao, L. Šiller, S. Krishnamurthy, P. R. Coxon, U. Bangert, M. Gass, L. Kjeldgaard, S. N. Patole, L. H. Lie, N. O'Farrell, T. A. Alsop, A. Houlton and B. R. Horrocks, *Nat Nano*, 2007, **2**, 486-489.
3. Y. Chao, S. Krishnamurthy, M. Montalti, L. H. Lie, A. Houlton, B. R. Horrocks, L. Kjeldgaard, V. R. Dhanak, M. R. C. Hunt and L. Šiller, *Journal of Applied Physics*, 2005, **98**, 044316.
4. L. Šiller, S. Krishnamurthy, L. Kjeldgaard, B. R. Horrocks, Y. Chao, A. Houlton, A. K. Chakraborty and M. R. C. Hunt, *Journal of Physics: Condensed Matter*, 2009, **21**, 095005.
5. Y. Chao, A. Houlton, B. R. Horrocks, M. R. C. Hunt, N. R. J. Poolton, J. Yang and L. Siller, *Applied Physics Letters*, 2006, **88**, 263119-263113.
6. M. R. Linford and C. E. D. Chidsey, *Journal of the American Chemical Society*, 1993, **115**, 12631-12632.
7. M. R. Linford, P. Fenter, P. M. Eisenberger and C. E. D. Chidsey, *Journal of the American Chemical Society*, 1995, **117**, 3145-3155.
8. G. F. Cerofolini, C. Galati, S. Reina, L. Renna, N. Spinella and G. G. Condorelli, *Physical Review B*, 2006, **74**, 235407.
9. Y. Chao, L. Siller, S. Krishnamurthy, P. R. Coxon, U. Bangert, M. Gass, L. Kjeldgaard, S. N. Patole, L. H. Lie, N. O'Farrell, T. A. Alsop, A. Houlton and B. R. Horrocks, *Nat Nano*, 2007, **2**, 486-489.
10. Y. Hijikata, H. Yaguchi, M. Yoshikawa and S. Yoshida, *Applied Surface Science*, 2001, **184**, 161-166.
11. T. J. Pinnavaia and A. Sayari, *Nanoporous Materials II*, Elsevier Science, 2000.
12. L. J. Bellamy, *The Infra-red Spectra of Complex Molecules*, Chapman and Hall, 1975.
13. B. C. Smith, *Fundamentals of Fourier Transform Infrared Spectroscopy*, Taylor & Francis, 1995.
14. M. Losurdo, M. M. Giangregorio, G. Bruno, D. Yang, E. A. Irene, A. A. Suvorova and M. Saunders, *Applied Physics Letters*, 2007, **91**, 091914.
15. M. Losurdo, M. M. Giangregorio, P. Capezzuto, G. Bruno, G. Malandrino, I. L. Fragalà, L. Armelao, D. Barreca and E. Tondello, *J. Electrochem. Soc.*, 2008, **155**, G44-G50.
16. H. H. Shen, S. M. Peng, X. G. Long, X. S. Zhou, L. Yang and X. T. Zu, *Vacuum*, 2012, **86**, 1097-1101.
17. G. A. Bhaduri, R. Little, R. B. Khomane, S. U. Lokhande, B. D. Kulkarni, B. G. Mendis and L. Šiller, *Journal of Photochemistry and Photobiology A: Chemistry*, 2013, **258**, 1-9.
18. S. K. Mishra, A. S. Bhattacharyya, P. K. P. Rupa and L. C. Pathak, *Nanosci. Nanotechnol. Lett.*, 2012, **4**, 352-357.
19. Y. S. Gu, Y. P. Zhang, X. R. Chang, Z. Z. Tian, N. X. Chen, D. X. Shi, X. F. Zhang and L. Yuan, *Sci. China Ser. A-Math. Phys. Astron.*, 2000, **43**, 185-198.
20. K. Abualnaja, L. Šiller and B. Horrocks, *World Academy of Science, Engineering and Technology, International Science Index, Biotechnology and Bioengineering* 2014, **2**, 1078-1086.
21. K. Yvon, W. Jeitschko and E. Parthe, *Journal of Applied Crystallography*, 1977, **10**, 73-74.
22. H. F. McMurdie, M. C. Morris, E. H. Evans, B. Paretzkin, W. Wong-Ng and C. R. Hubbard, *Powder Diffraction*, 1986, **1**, 265-275.
23. C. W. Shong, C. H. Sow and A. T. S. Wee, *Science at the Nanoscale: An Introductory Textbook*, Pan Stanford, 2009.
24. N. B. Monograph, *National Bureau of Standards Monograph of U.S.*, 1976, 13-35.

25. P. Schmuki, E. S. C. Division, E. S. Luminescence, D. M. Division and E. S. Meeting, *Pits and Pores II: Formation, Properties, and Significance for Advanced Materials : Proceedings of the International Symposium*, Electrochemical Society, 2001.
26. B. H. Stuart, *Infrared Spectroscopy: Fundamentals and Applications*, Wiley, 2004.
27. *NIST X-ray Photoelectron Spectroscopy Database, Nist Standard Reference Database*, http://srdata.nist.gov/xps/EngElmSrchQuery.aspx?EType=PE&CSOpt=Retri_ex_dat&Elm=Si, 2014.

Chapter 4

The Optical Characterization of Silicon Nanocrystals (SiNCs) and their Mixtures with Erbium trichloride ($ErCl_3$) and Silver Nanoparticles (AgNPs)

In this chapter, the optical properties of synthesised alkylated silicon nanocrystals (C_{11}-SiNCs), commercial SiNCs and their mixtures with erbium trichloride ($ErCl_3$) and silver nanoparticles (AgNPs) are presented. UV-Vis absorption measurements of C_{11}-SiNCs, commercial SiNCs and their mixtures with erbium ions and AgNPs in two different concentrations i.e. 1 mM $AgNO_3$: 5 mM SDS (1:5) and 10 mM $AgNO_3$: 50 mM SDS (10:50) are also carried out. Photoluminescence (PL) measurements have been also investigated for C_{11}-SiNCs, commercial SiNCs and their mixtures with erbium ions. Raman and surface enhanced Raman spectroscopy (SERS) analyses have been studied for C_{11}-SiNCs, commercial SiNCs and their mixtures with $ErCl_3$ and AgNPs.

4.1 UV-Vis absorption measurements of synthesised alkylated silicon nanocrystals (C_{11}-SiNCs), commercial silicon nanocrystals (SiNCs) and their mixtures with erbium trichloride ($ErCl_3$) and silver nanoparticles (AgNPs)

In this work, a UV-Vis spectrometer was used to determine the optical absorption spectra of silicon nanocrystals i.e. alkylated SiNCs and commercial SiNCs. Silicon nanocrystals were studied on their own and in mixtures with erbium trichloride and silver nanoparticles. These mixtures are Er/C_{11}-SiNCs, Er/Commercial SiNCs, AgNPs (1:5)/C_{11}-SiNCs, AgNPs (10:50)/C_{11}-SiNCs, AgNPs (1:5)/Commercial SiNCs and AgNPs (10:50)/Commercial SiNCs. The results from this analysis are reported and discussed below. The experimental details for this part are shown in Chapter 2 section 2.3.8.

Figure 4.1 shows the absorption spectra of alkylated SiNCs dispersed in THF and commercial SiNCs dispersed in deionized water in the wavelength range from 250 nm to 800 nm. It can be seen that both absorption spectra of SiNCs (alkyl capped SiNCs and commercial SiNCs) present a broad absorption tail with a steep rise feature at around 350 nm which can be assigned to the direct band gap transition (ca. 3.4 eV in

bulk silicon). It is known that bulk silicon exhibits direct band gap of 3.4 eV and an indirect band gap of 1.1 eV.[1] Therefore, there is a rapid increase in the absorbance with decreasing the wavelength from the wavelength of 600 nm (2.06 eV) which presents the absorption band edge of the indirect band gap of SiNCs.[1-3] However, in order to excite an electron in SiNCs from the highest level of the valence band to the lowest level of the conduction band a higher energy is required than in bulk silicon due to quantum confinement effect. The result shows the absorption increases as the direct gap is approached as observed by Lie *et al*.[1]

It is known that the band gap in bulk silicon at 1.1 eV is considered to be indirect and is not vertical transition due to the absorption of phonon (lattice vibration), where extra momentum is needed to change the crystal momentum of the electron (yellow horizontal arrow in figure 1.5a); where the transition in the direct band gap materials e.g. CdSe is vertical which reflects only the absorption of photons in these materials (figure 1.5b).[4] Therefore, the main consequence of the indirect gap in bulk Si is weak absorption emission (see figure 1.6). Silicon has also a direct band gap in which the electron can be promoted across this gap directly from the valence band to the conduction band but at higher energy (3.4 eV). However, in Si nanoparticles the size of the indirect band gap is increased due to quantum confinement effect. This leads to increase the indirect band gap size until approach the visible region at about 2.1 eV (600 nm) as observed for our prepared alkylated SiNCs and commercial SiNCs. In contrast, the size of the direct band gap does not change considerably with the reduction of the particle size of Si because the maximum of the conduction band located above the maximum of the valence band at k = 0 (see figure 1.5a).

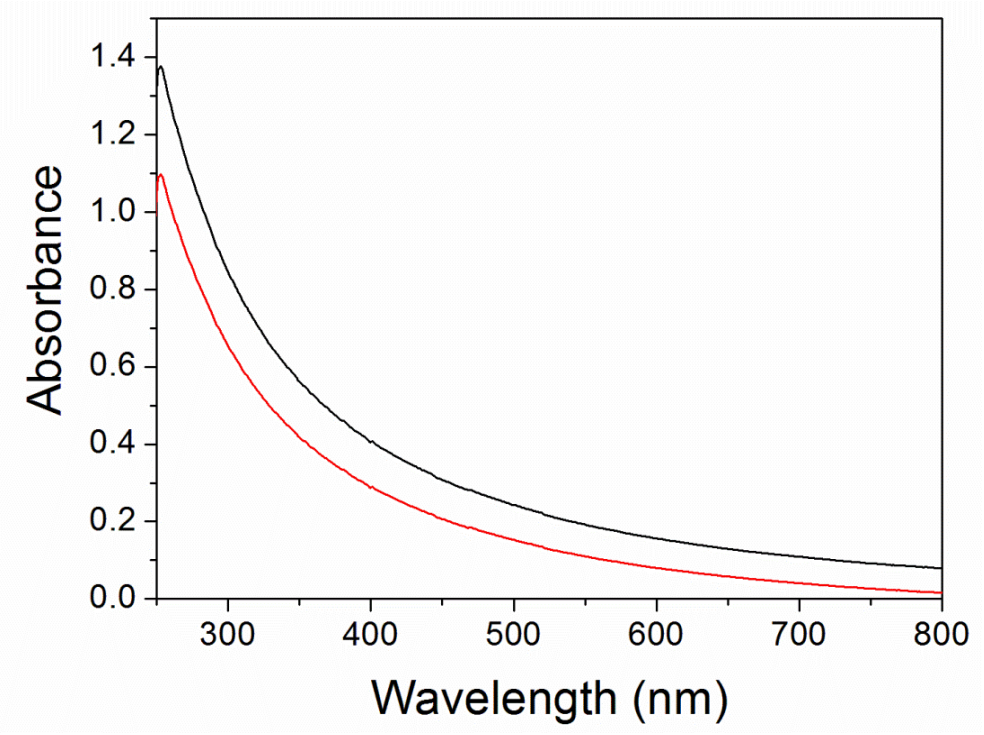

Figure 4.1: UV-Vis absorption spectra of alkylated SiNCs (0.08 g/L) dispersed in THF (black line) and commercial SiNCs (0.6 g/L) dispersed in deionized water (red line).

To study the optical properties of erbium mixed silicon nanocrystals, the UV-Vis investigation was also carried out. Figure 4.2 displays the absorption spectra of erbium mixed C_{11}-SiNCs which dispersed in deionized water and erbium mixed commercial SiNCs that also dispersed in deionized water. It can be indicated that the presence of erbium ions with both types of silicon nanocrystals i.e. C_{11}-SiNCs and commercial SiNCs does not change the absorption spectra of silicon nanocrystals. These absorption spectra of erbium mixed silicon nanocrystals are similar to those observed by John *et al*[5] as this manner is constant for silicon nanocrystals due to indirect band gap.

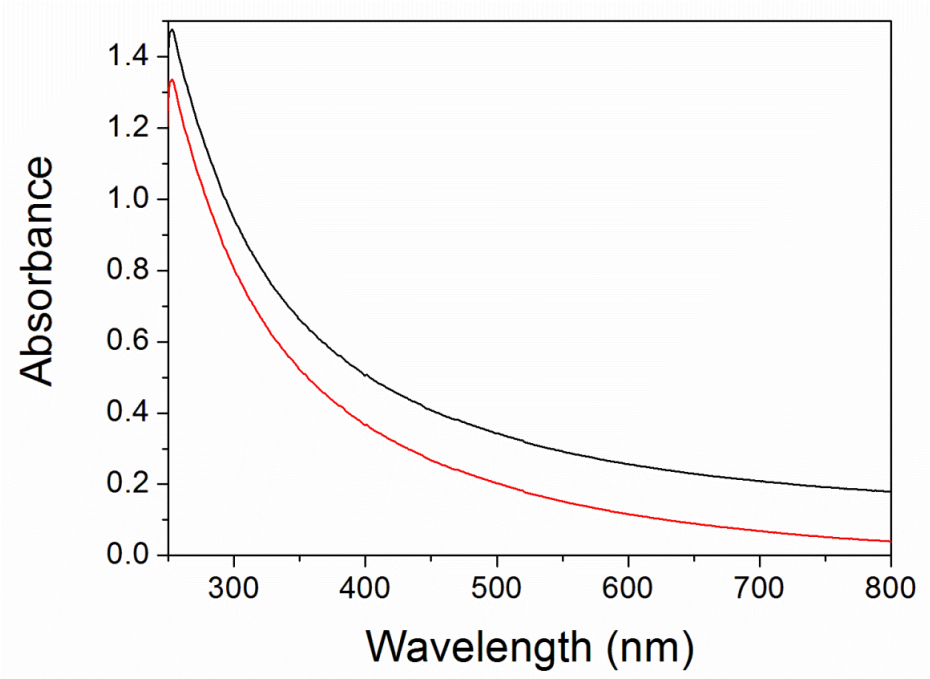

Figure 4.2: UV-Vis absorption spectra of Er/C_{11}-SiNCs dispersed in deionized water (black line) and Er/Commercial SiNCs dispersed in deionized water (red line).

Figure 4.3 and figure 4.4 indicate the absorption bands of alkylated SiNCs and commercial SiNCs, respectively mixed with two different concentrations i.e. (1:5) and (10:50) of silver nanoparticles. It is clear that there is a change in the absorption bands of SiNCs either C_{11}-SiNCs or commercial SiNCs in the presence of AgNPs. The characteristic absorption bands of SiNCs mixed with AgNPs (1:5) and (10:50) appear at 394 nm and 423 nm, respectively (see figure 4.3 and figure 4.4). These two peaks are assigned to surface plasmon resonance (SPR) of AgNPs which relies on the particle size of AgNPs and dipole/multipole resonance.[6] The intraband transitions of metallic silver is observed also in AgNPs (1:5) and (10:5) mixed with SiNCs at 324 nm and 326 nm, respectively.[6] It can be seen that in figure 4.3 there is no considerable change in SPR positions of AgNPs when they mixed with alkylated SiNCs compared to AgNPs without Si nanoparticles. Furthermore, this phenomenon is constant for AgNPs when they mixed also with commercial SiNCs as shown in figure 4.4. Thus, the presences of Si nanoparticles do not affect the plasmons of silver nanoparticles.

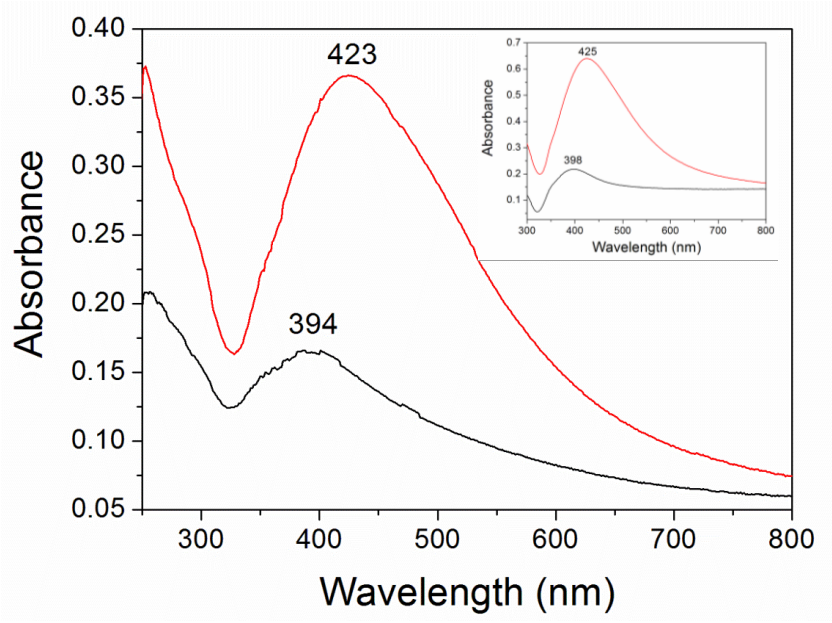

Figure 4.3: UV-Vis absorption spectra of C_{11}-SiNCs mixed with AgNPs (1:5) dispersed in deionized water (black line) and mixed with AgNPs (10:50) dispersed in deionized water (red line). The inset shows the UV-Vis absorption spectra of AgNPs (1:5) dispersed in deionized water (black line) and AgNPs (10:50) dispersed in deionized water (red line).

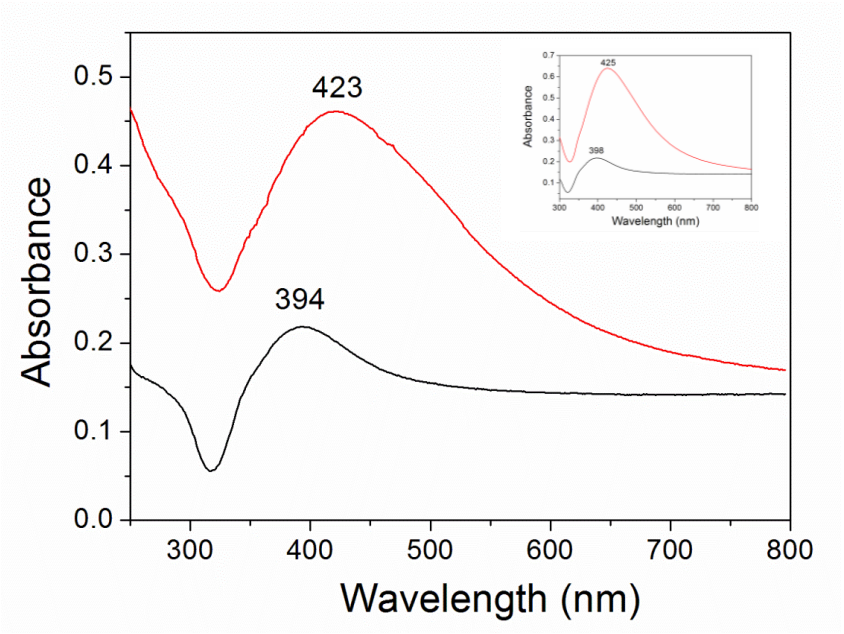

Figure 4.4: UV-Vis absorption spectra of commercial SiNCs mixed with AgNPs (1:5) dispersed in deionized water (black line) and mixed with AgNPs (10:50) dispersed in deionized water (red line). The inset shows the UV-Vis absorption spectra of AgNPs (1:5) dispersed in deionized water (black line) and AgNPs (10:50) dispersed in deionized water (red line).

4.2 Photoluminescence (PL) of synthesised alkylated silicon nanocrystals (C_{11}-SiNCs), commercial silicon nanocrystals (SiNCs) and their mixtures with erbium trichloride ($ErCl_3$), measured by PL spectroscopy

In this work, alkylated silicon nanocrystals (C_{11}-SiNCs), commercial silicon nanocrystals (SiNCs) and their mixtures with erbium trichloride ($ErCl_3$) were prepared and their photoluminescence (PL) properties were investigated. The general set up of this experiment is explained in more detail in (Chapter 2 section 2.3.10). Two different excitation wavelengths have been used i.e. 400 nm and 520 nm in order to excite SiNCs and Er mixed SiNCs, respectively. This is because the instrument which used in PL measurement provides two different excitation wavelengths.

The PL emission spectrum of alkylated silicon nanocrystals (C_{11}-SiNCs) drop coated from deionized water onto glass coverslip is presented in figure 4.5 (the excitation wavelength = 400 nm). The sample reveals an orange emission peak at 595 nm (2.1 eV). This peak can be attributed to the band gap transition of alkyl capped SiNCs which is assigned to radiative recombination of excitons inside alkyl capped SiNCs.[7] It is known that the higher energy is required to generate the exciton luminescence in SiNCs which is higher than the band gap energy of bulk silicon due to quantum confinement.[8]

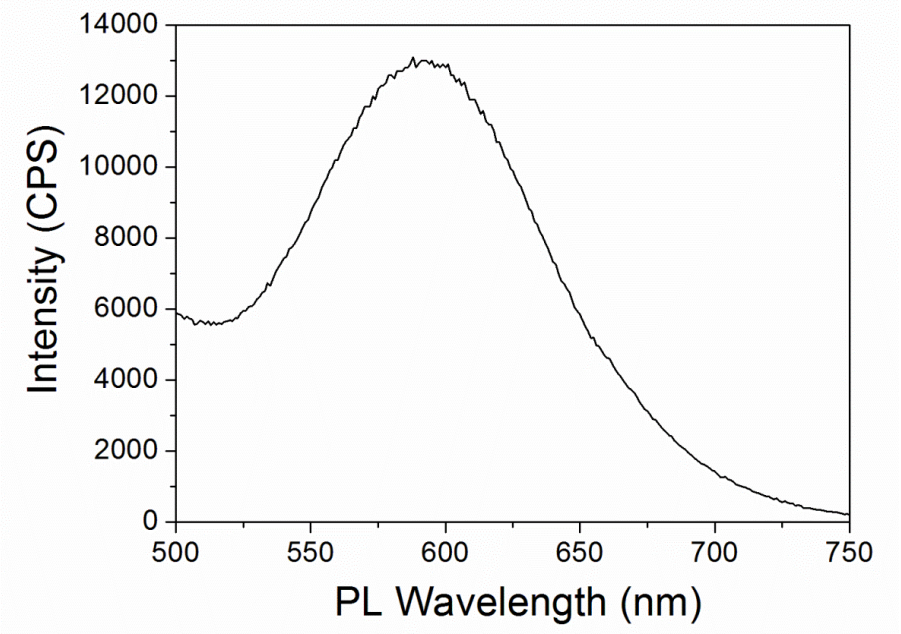

Figure 4.5: PL emission spectrum of alkylated SiNCs drop coated from deionized water onto glass coverslip. The excitation wavelength = 400 nm.

Figure 4.6 indicates the PL emission spectra of erbium mixed alkylated SiNCs which drop coated from deionized water onto glass coverslip. This sample also exhibits the characteristic C_{11}-SiNCs PL band at 595 nm in the region between 500 and 750 nm as seen in figure 4.6a (the excitation wavelength was 400 nm).[7] The position of this Si peak (595 nm) does not change in the presence of erbium ions; while the intensity of this PL band is considerably higher than the PL intensity band of C_{11}-SiNCs as presented in figure 4.7; where the concentrations of C_{11}-SiNCs are equal in both samples i.e. 0.08 g/L (see chapter 2 section 2.2.3). Figure 4.6a presents also PL bands at 545 nm and 652 nm which assigned to $4S_{3/2}$ and $4F_{9/2}$ of Er ion.[9]

It can be seen that the peak at 595 nm of erbium mixed alkyl capped SiNCs shows a fourfold increase in the PL emission intensity. This enhancement in the intensity can be explained as a result of the presence of erbium ions on the surface of alkyl capped SiNCs which influence the luminescence intensity of Er/C_{11}-SiNCs. Therefore, the typical absorption spectrum of erbium trichloride is carried out in order to interpret this significant improvement in the intensity of the PL peak of Er/C_{11}-SiNCs as shown in figure 4.8. This optical absorption spectrum of erbium trichloride solution shows various bands that correspond to different absorption transitions of erbium ions.[9, 10] These electronic transitions bands are listed in table 4.1. There is an electronic transition peak at around 405 nm which is assigned to $2H_{9/2}$.[9] This band is very close to the laser wavelength at 400 nm that used to excite the Er/C_{11}-SiNCs. Hence, it is quite possible that erbium absorbing laser light in this transition band and the energy transferred to the C_{11}-SiNCs from the erbium ion causing a significant enhancement in the intensity of the PL emission band of SiNCs when they mixed with erbium ions.

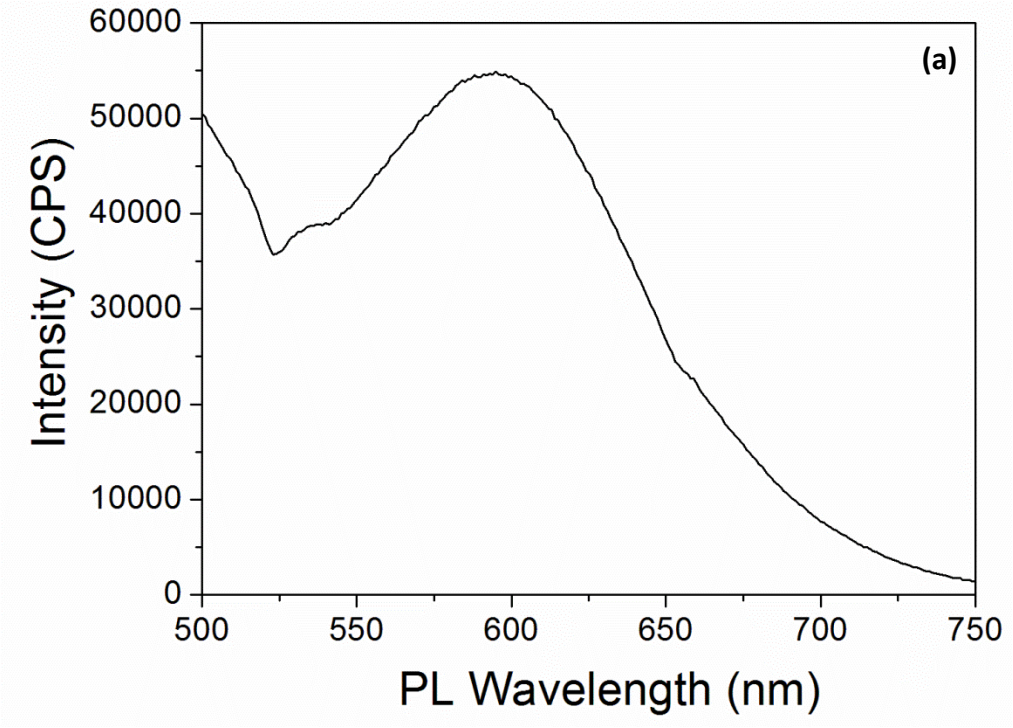

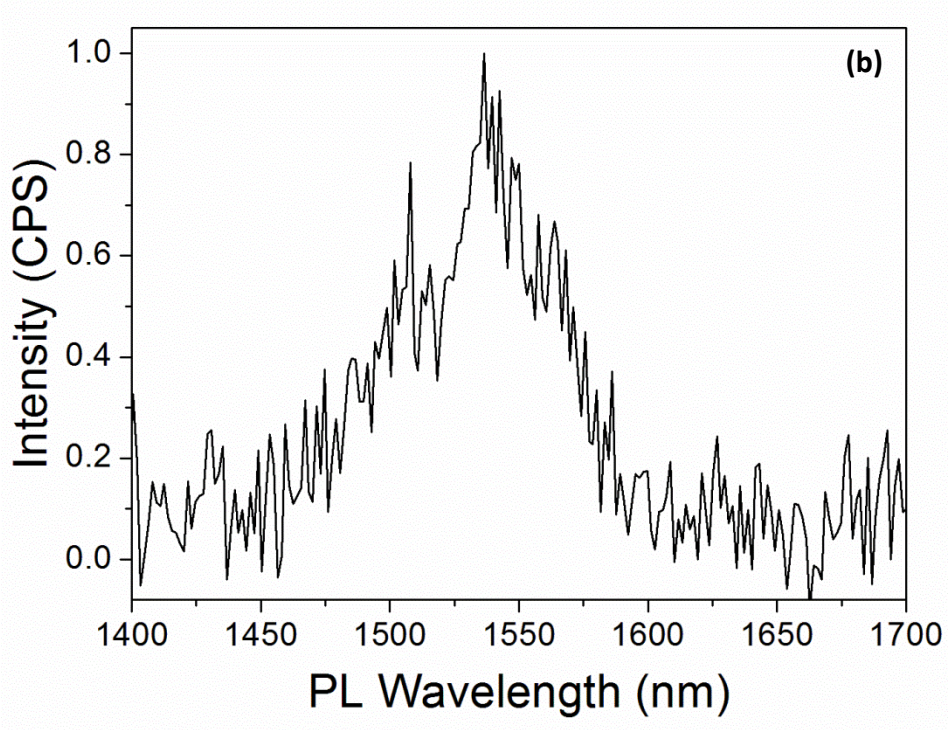

Figure 4.6: PL emission spectra of erbium mixed alkylated SiNCs drop coated from deionized water onto glass coverslip showing two different regions (a) 500 – 750 nm and the excitation wavelength was 400 nm (b) 1400 – 1700 nm and the excitation wavelength was 520 nm.

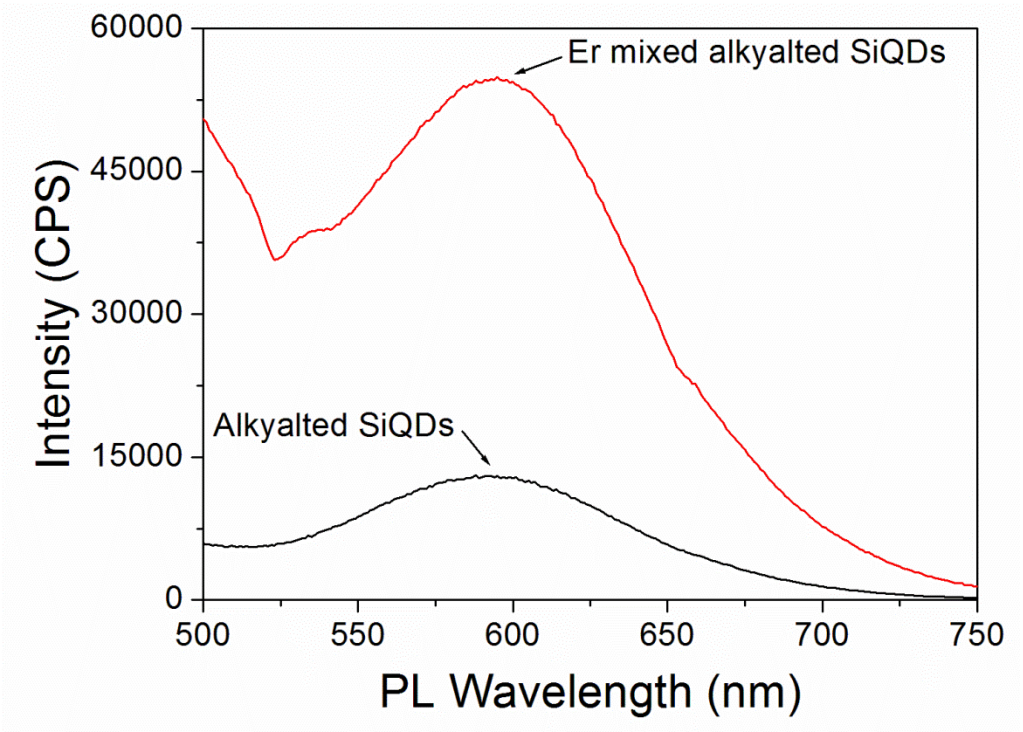

Figure 4.7: Comparison PL spectra of alkylated SiNCs drop coated from deionized water onto glass coverslip (black line) and Er mixed with alkylated SiNCs drop coated from deionized water onto glass coverslip (red line). The excitation wavelength = 400 nm.

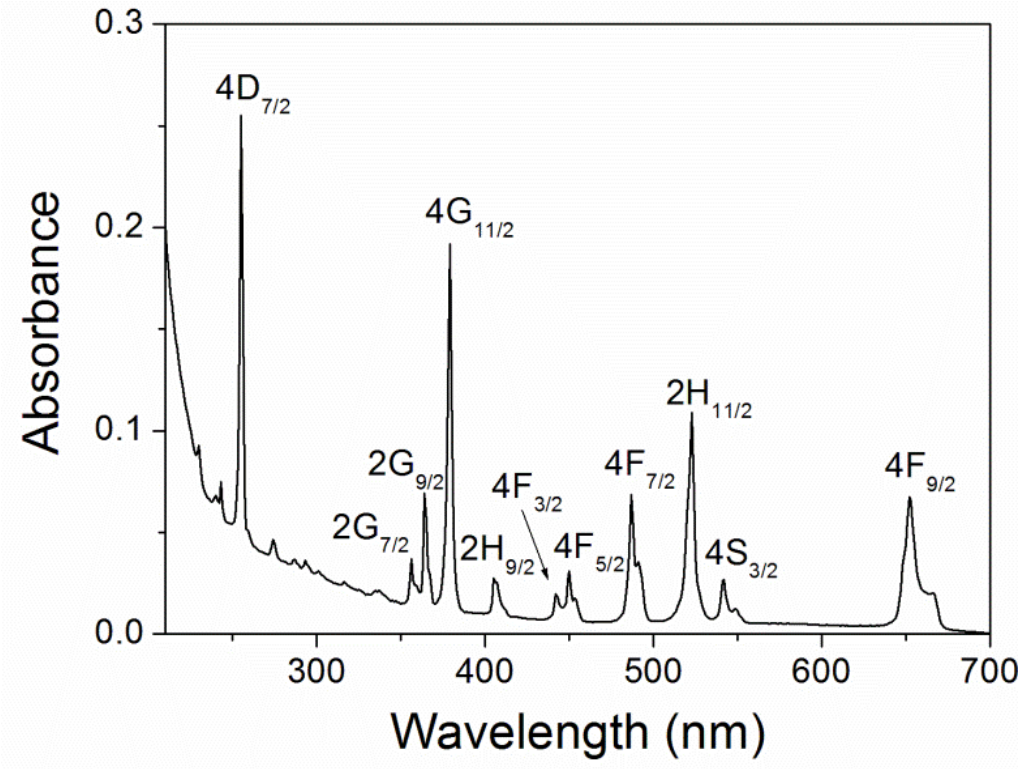

Figure 4.8: Absorption spectrum of erbium trichloride dispersed in deionized water.

Energy level	λ_{peak} (nm)
$4F_{9/2}$	652
$4S_{3/2}$	545
$2H_{11/2}$	521
$4F_{7/2}$	488
$4F_{5/2}$	449
$4F_{3/2}$	442
$2H_{9/2}$	405
$4G_{11/2}$	379
$2G_{9/2}$	364
$2G_{7/2}$	356
$4D_{7/2}$	255

Table 4.1: The experimental absorption peaks of Er^{3+} energy level.

The PL infrared emission peak at around ≈ 1536 nm in the region between 1400 nm and 1700 nm (figure 4.6b) attributed to the intra-4*f* transition of trivalent erbium (intra-atomic $^4I_{13/2} \rightarrow {}^4I_{15/2}$ transitions of Er^{3+})[11] and the excitation wavelength was 520 nm. It is known that erbium has an important role in optical fiber technology due to its luminescence at around 1535 nm.[12] In addition, the main goal of mixing SiNCs with erbium is to observe the energy transferred from the excited state of Si to the erbium. Thus, figure 4.6a-b demonstrated that Er/C_{11}-SiNCs sample exhibits simultaneously two PL emission bands corresponding to radiative recombination of electron-hole pairs in alkylated SiNCs (595 nm) and the intra-4*f* transition in Er^{3+} (1536 nm). The latter peak is very weak and the intensity at 1536 nm is around a factor of 1 which determines very low PL emission intensity from erbium ions. While, the Si PL peak becomes high in the intensity as the erbium trichloride exists.

The lack of the PL Er^{3+} intensity band (1536 nm) can be due to the mixing method that used in this project which does not growth the PL intensity of erbium in Er/C_{11}-SiNCs mixture but it causes a significant enhancement in the PL peak of Si nanoparticles. Thus, there is no energy transfer from excited alkylated SiNCs to Er^{3+} as we expected[13, 14] while the energy transfer from erbium ions to alkylated SiNCs. In order to transfer energy from SiNCs to erbium ions, the enhancement of 1536 nm PL

emission band should be achieved. Assuming that the energy transferred from alkylated SiNCs to erbium ions (Er^{3+}), figure 4.6 should be interpreted as follow. Basically, the photons are absorbed by alkylated SiNCs and then excitons are generated in the SiNCs.[15] Then, the exciton recombines radiatively which causes photon emission as the energy of the resulted photon depends on the size of Si nanocrystal (see figure 1.11). A part of radiative recombination energy of the exciton of SiNCs is transferred to 4f shell in trivalent erbium; thus exciting Er^{3+}. The emission of erbium at 1.54 μm then occurs as a result of the transition from $^4I_{13/2}$ to the ground sate $^4I_{15/2}$. It is also should be noted that the amount of the energy transferred to Er^{3+} depends strongly on the concentration of erbium in the host material and the distance between Si nanocrystals and trivalent erbium. This generates enhancement in the PL intensity peak of erbium (1536 nm) and quenching in the PL intensity peak of Si (595 nm).This phenomenon known as fluorescence resonance energy transfer (FRET). While, the results from this chemical mixing method which present in figure 4.6a-b shows growth in the 595 nm PL peak of Si and quenching in the 1536 nm PL band of Er^{3+} which provides a clear evidence that the energy does not transfer from alkylated SiNCs to Er^{3+} as the concentration of SiNCs kept constant in both cases. This can be explained as a result of presence of the erbium in an oxide form i.e.Er_2O_3 as confirmed from XPS results of Er mixed alkylated SiNCs. Thus, the presence of oxides between the erbium and silicon core forbids this energy transfer. Kik *et al*[16] and Ji *et al*[17] observed that the efficient enhancement in the PL band of erbium at ~ 1530 nm occur when the Er^{3+} are spaced closely enough to SiNCs in order to allow the energy transfer process.

Figure 4.9 presents the PL emission spectrum of commercial SiNCs drop coated from deionized water onto glass coverslip and the excitation wavelength was 400 nm. The PL orange emission shouldering appears at 595 nm can be attributed to radiative recombination of electron-hole pairs inside SiNCs.[7] It is surprisingly that the luminescence of commercial SiNCs behaves in the same manner as alkylated SiNCs regarding to the size of commercial SiNCs which have a diameter of 65 nm. This can be due to (i) the presence of small fraction of small particles size (their radius > Bohr radius) of commercial SiNCs which SEM, TEM, HRTEM, AFM and XRD techniques cannot detect them and (ii) the presence of small grains which are responsible for the luminescence of Si nanoparticles. The second reason should be ruled out as there are

no grains observed in HRTEM image of commercial SiNCs. Thus, the first reason is most likely to be the main responsible of the luminescence in commercial SiNCs in this study.

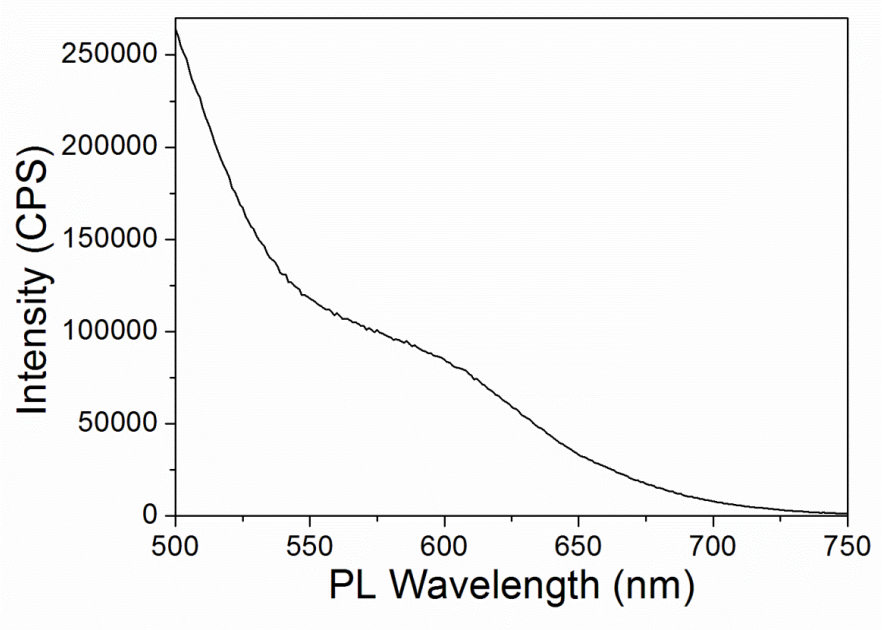

Figure 4.9: PL emission spectrum of commercial SiNCs drop coated from deionized water onto glass coverslip. The excitation wavelength = 400 nm.

Figure 4.10 shows the PL emission spectra of erbium mixed commercial SiNCs that drop coated from deionized water onto glass coverslip. The PL wavelength region between 500 nm and 750 nm indicates an orange emission band at 595 nm which is consistent for SiNCs[7] (the excitation wavelength = 400 nm). It can be seen that there is no any shift in this orange emission peak even in the presence of trivalent erbium. Therefore, the position of PL emission band from SiNCs (595 nm) is not affected by trivalent erbium and is considered to be consistent for both alkylated SiNCs and commercial SiNCs. Figure 4.10a presents also PL bands at 545 nm and 652 nm which assigned to $4S_{3/2}$ and $4F_{9/2}$ of Er ion.[9] Meanwhile, figure 4.11 compares the two intensities of the two PL Si peaks of commercial SiNCs and Er/commercial SiNCs as the concentrations of commercial SiNCs are equal in both samples i.e. 0.6 g/L. This figure presents that the intensity of this PL emission peak (595 nm) of erbium mixed commercial SiNCs is three times higher than that of the intensity of the PL emission band of commercial SiNCs. This significant enhancement in PL emission intensity provide a clear evidence that the chemical composition affect the PL emission

intensities of commercial SiNCs as has already been discussed in previous case of alkylated SiNCs and Er/C_{11}-SiNCs (see figure 4.7).

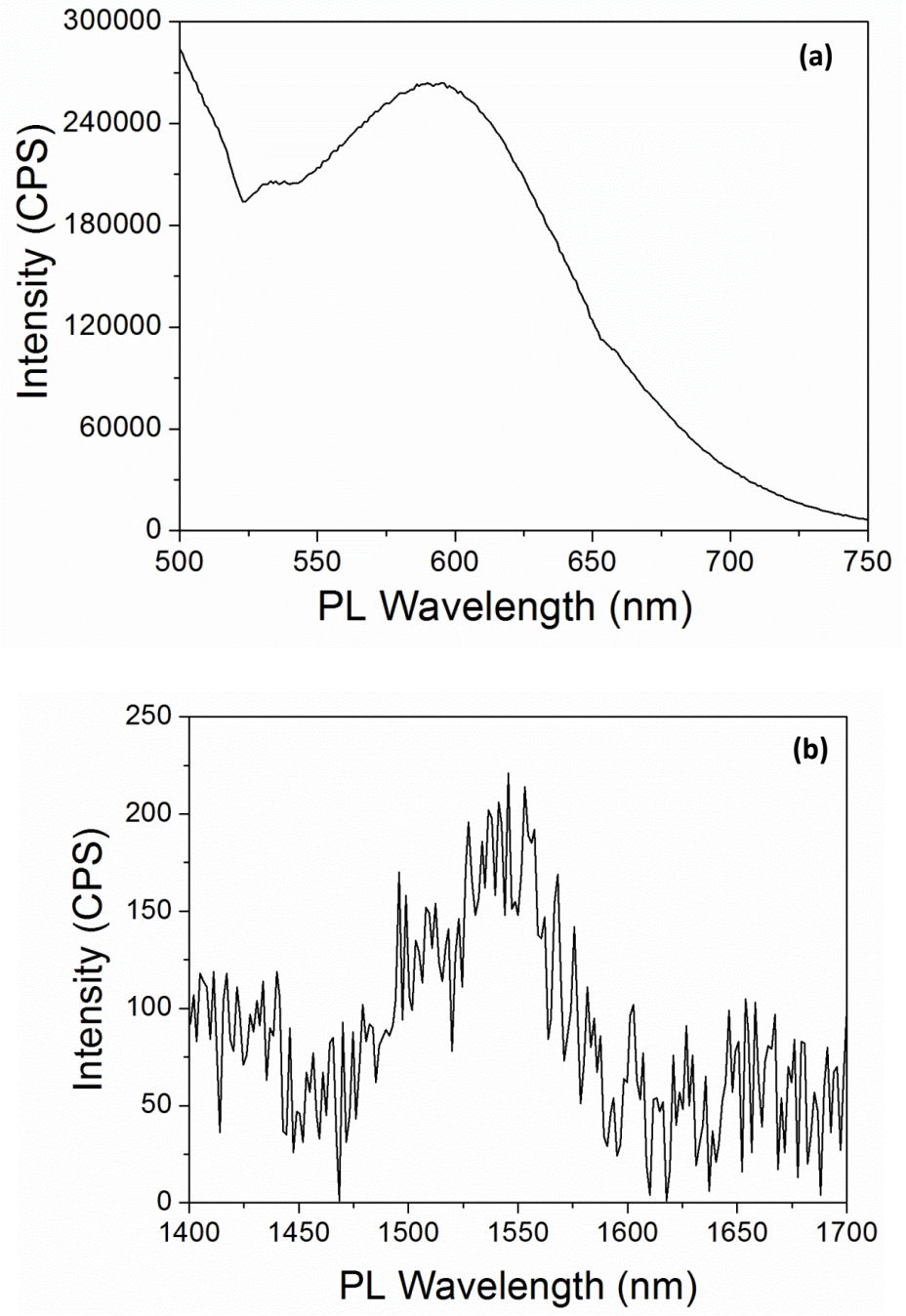

Figure 4.10: PL emission spectra of erbium mixed commercial SiNCs drop coated from deionized water onto glass coverslip showing two different regions (a) 500 – 750 nm and the excitation wavelength was 400 nm (b) 1400 – 1700 nm and the excitation wavelength was 520 nm.

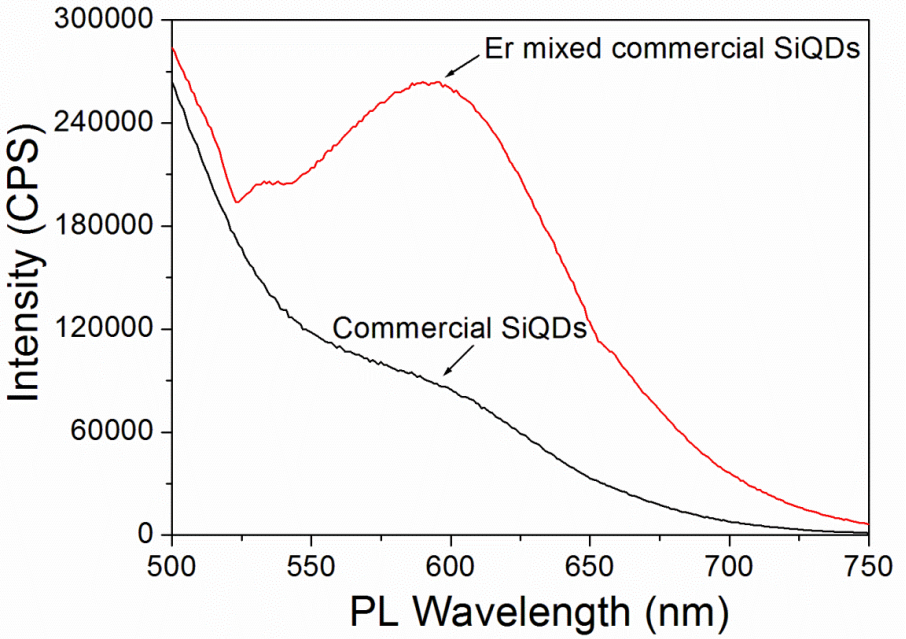

Figure 4.11: Comparison PL spectra of commercial SiNCs drop coated from deionized water onto glass coverslip (black line) and Er mixed with commercial SiNCs drop coated from deionized water onto glass coverslip (red line). The excitation wavelength = 400 nm.

For this sample that contain trivalent erbium, there is another peak at approximately 1536 nm in the range (1400 - 1700 nm) and the excitation wavelength was 520 nm as seen in figure 4.10b. This peak is corresponding to the intra-4*f* transition of Er^{3+}.[11] Therefore, figure 4.10a-b detected two different PL peaks at 595 nm and 1536 nm that are associated to band gap transitions of SiNCs and the ionic transition in trivalent erbium, respectively. The PL Er^{3+} band (1536 nm) is weak; whereas the intensity of this peak is about a factor of around 200. Meanwhile, the intensity of the PL peak of SiNCs becomes larger in Er/Commercial SiNCs as it has been already discussed in the case of Er/C_{11}-SiNCs. Furthermore, on the basis of energy transfer between Si and Er ions, figure 4.10 shows a significant enhancement in the 595 nm PL peak and quenching in the 1536 nm which provides clear evidence that the energy transfers from trivalent Er to commercial SiNCs as observed also in Er/C_{11}-SiNCs mixture.

However, the chemical mixing route which used in this work does not provide efficient PL from erbium ions when they mixed with SiNCs. It is noteworthy that erbium ions have an important emission wavelength centred at about 1535 nm

(characteristic for the intra-4*f* transition of Er^{3+}) which correspond to a standard optical telecommunication wavelength.[18] Thus, this project aims to achieve maximum emission intensity from trivalent erbium which generated as a result of the energy transfer from excited silicon nanocrystals to the nearby erbium ion. Regarding to these data for both Er/C_{11}-SiNCs and Er/commercial SiNCs, this simple chemical mixing of SiNCs and erbium ions leads to transferring energy from erbium ions to SiNCs not as we expected[13, 14] from excited SiNCs to Er^{3+}. Furthermore, this failure to observe optical active erbium may be due to the concentration of erbium that experimentally used which was not sufficient to get efficient Er emission from the samples but affects the photoluminescence of SiNCs considerably. In contrast, previous works[8, 11, 13, 19, 20] have been reported a significant increase in the intensity of the PL emission peak of erbium when the erbium doped silicon nanocrystals by different doping methods such as ion implantation method and sputtering procedure. It was observed that intensity of 1536 nm peak increased dramatically in the presence of silicon nanocrystals and the PL emission peak of silicon nanocrystals is quenched.

However, Fujii *et al*[13] and Cerqueira *et al*[19, 20] found that the size of silicon nanocrystals, the chemical environment of erbium doped silicon nanocrystals films and different concentration of erbium ions inside the silicon nanocrystals film affect the PL emission intensities of Si and Er^{3+}. Fujii *et al*[13] and Cerqueira *et al*[19, 20] found that the intensity of PL peak of erbium ions (1545 nm) increased rapidly with decreasing the size of SiNCs from 3.8 nm to 2.7 nm and from 8 nm to 3 nm, respectively. In addition, they found that the PL intensity of erbium ions increases as the concentration of erbium decreased within the SiNCs. Thus, different intensities of the PL emission bands can be observed depending on the above factors. Thus, it is apparent that the chemical mixing method, chemical environment of the erbium mixed SiNCs and the concentration of erbium trichloride that practically utilized (4 mM) does not transfer energy from SiNCs to Er ion. It is also exert an insignificant effect on the PL efficiency of erbium ions but there is a large effect on the luminescence of SiNCs.

4.3 Confocal Raman measurements of synthesised alkylated silicon nanocrystals (C_{11}-SiNCs), commercial silicon nanocrystals (SiNCs) and their mixtures with erbium trichloride ($ErCl_3$)

The optical characterization and chemical composition of both alkylated silicon nanocrystals (C_{11}-SiNCs) and commercial silicon nanocrystals (SiNCs) and Er/SiNCs mixtures have been investigated by confocal Raman spectroscopy. The investigated samples were drop-cast on glass coverslips for confocal Raman spectroscopic measurements. The samples were investigated at an excitation wavelength of 488 nm provided by an Argon ion laser and the scattered/emitted light was dispersed on a grating of 150 lines mm^{-1} to collect a broad spectral range (200 cm^{-1} to 7000 cm^{-1}) including both Raman and luminescence bands of interest. The procedures of preparing those samples are given in details in (Chapter 2 section 2.3.9).

Figure 4.12a-b displays a reflected light image and luminescence image of alkylated SiNCs do not contain erbium trichloride drop cast on glass coverslip. The confocal luminescence images of dried C_{11}-SiNCs present bright features which are due to the aggregates of C_{11}-SiNCs as shown in figure 4.12b. Figure 4.12c-d presents a reflected light image and luminescence image of alkylated SiNCs do contain erbium ions drop cast on glass coverslip. The bright features confirm the presence of clusters of C_{11}-SiNCs which are associated to Er^{3+} (figure 4.12d). Mainly, the drying process during sample preparation for the microscopy is the original reason for these aggregates (clusters) which determined in figure 4.12b,d as these clusters were observed by previous works on confocal Raman spectroscopy.[21-23]

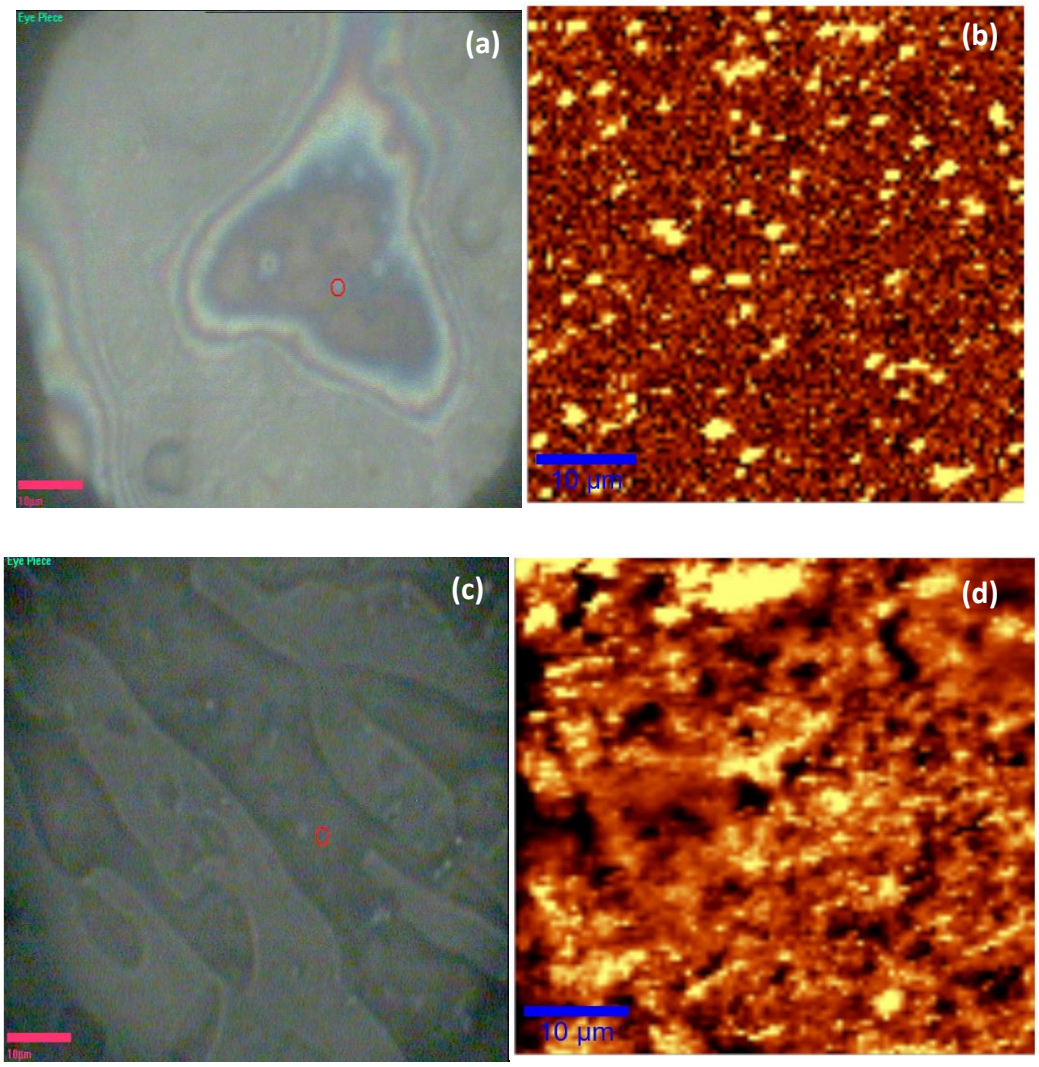

Figure 4.12: (a) Reflected light image of C_{11}-SiNCs collected before (b) confocal luminescence spectrum image of dried C_{11}-SiNCs deposited from dichloromethane on the glass coverslip. (c) reflected light image of Er/C_{11}-SiNCs collected prior to (d) confocal luminescence spectrum image of dried Er/C_{11}-SiNCs deposited from aqueous solution on the glass coverslip. The laser wavelength was 488 nm and the scale displays the scattered intensity integrated over the Stokes shift range from 200 cm^{-1} to 7000 cm^{-1}, which corresponds to a mixture of Raman signals and the luminescence. The scale bar of the reflected light images (a,c) is 10 µm and the scan size of the luminescence images (b,d) is 50 X 50 µm.

These bright regions of the confocal luminescence images were gathered together in order to provide complete average Raman luminescence spectra for C_{11}-SiNCs and Er/C_{11}-SiNCs as presented in figure 4.13. Figure 4.13a provides an average Raman spectrum of C_{11}-SiNCs which exhibit the consistent Raman bands of alkylated

SiNCs that prepared by this method. The Raman peak at 515 cm^{-1} is assigned to the first order of crystalline SiNCs as this peak constant for SiNCs.[23] This peak is less than the peak of bulk silicon (520 cm^{-1}) due to quantum confinement effect.[23] The feature at 960 cm^{-1} can be attributed to the second order of SiNCs.[24] There is also a broad and large peak with a maximum at 4915 cm^{-1} (642 nm) which attributed to the orange luminescence signal of alkylated SiNCs due to quantum confinement effect.[22-24] This orange luminescence peak is characteristic for C_{11}-SiNCs that synthesised by this method as observed by our research group several years ago.[1, 7, 24-26]

However, when the luminescence spectrum of alkylated SiNCs in figure 4.13a is compared to the luminescence spectrum of the alkylated SiNCs (figure 4.5); a clear blue shift is observed (642 nm versus 595 nm). A possible explanation for this observation is using different solvents for alkylated SiNCs i.e. dichloromethane and water for Raman and photoluminescence measurements, respectively. Consequently, using the water leads to a chemical change i.e. oxidation of the silicon nanocrystals which increase the amount of Si-O_x species on the alkylated SiNCs surface. However, it is known that the alkyl monolayer is chemically robust and stable against the oxidation except under intense X- ray irradiation.[27-30] Dickinson *et al*[24] found that the water penetrate the underlying silicon atoms via the monolayers on silicon nanocrystals which have some defects or are less ordered. In addition, the differences between the two luminescence spectra may be due to using different excitation source i.e. 400 nm in PL measurement and 488 nm in confocal Raman investigation. Thus, this blue shift of the luminescence wavelength is observed as a consequence of excited small particle sizes of alkylated SiNCs. This suggests that at PL measurement, the smaller particles which possess a larger quantum confinement effect,[31] exhibit luminescence in lower wavelength than that observed in Raman spectrum of alkylated SiNCs.

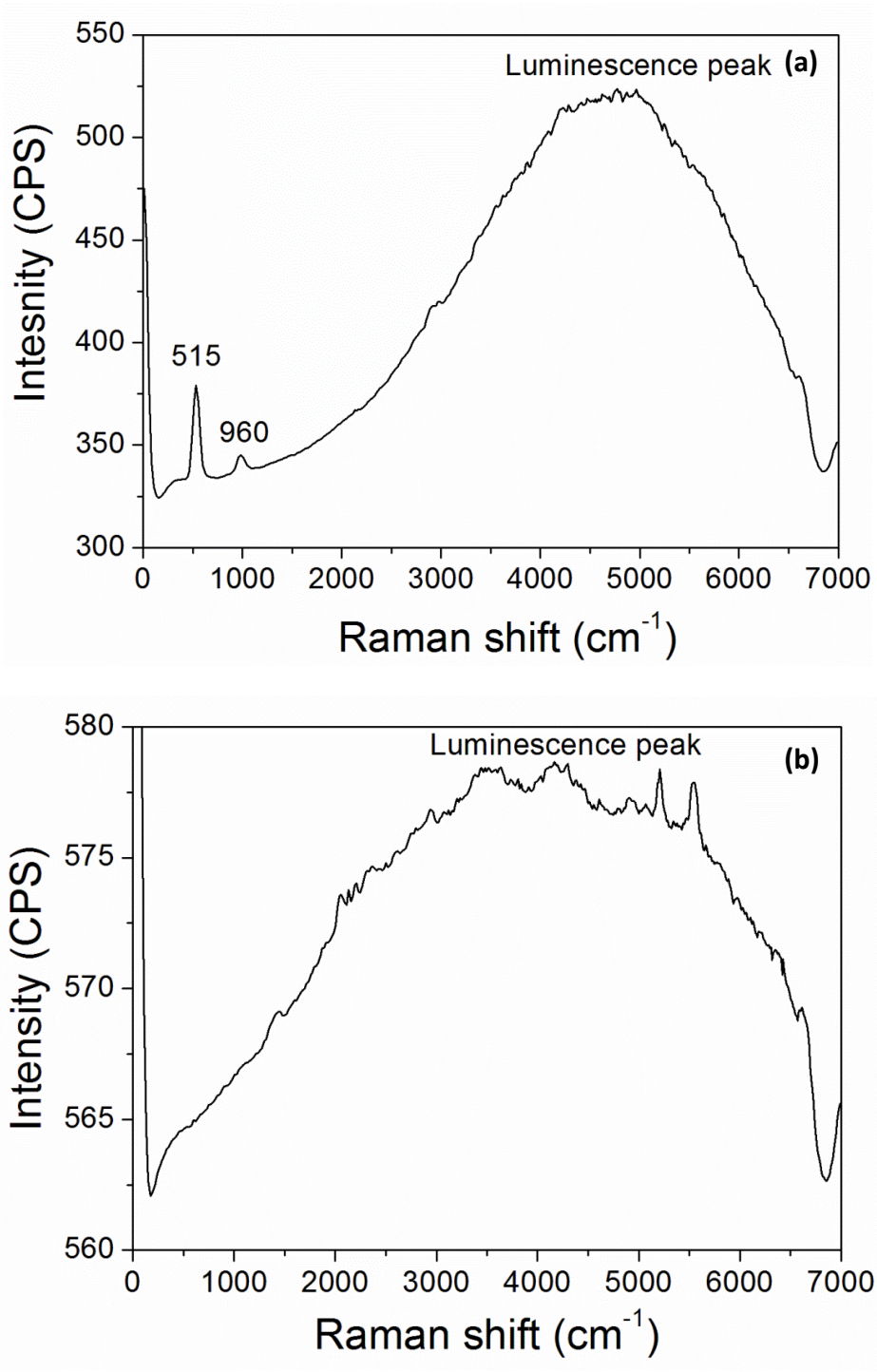

Figure 4.13: Average Raman and luminescence spectra of (a) C_{11}-SiNCs drop-coated from dichloromethane solution on glass coverslip. (b) Er/C_{11}-SiNCs drop-coated from aqueous solution on glass coverslip. The excitation wavelength = 488 nm line of an argon ion laser was used to excite the luminescence and the spectra was collected using a grating = 150 lines mm^{-1} which provides collection of both Raman and luminescence from alkylated silicon nanocrystals. These spectra are collected as averages from the particles that shown on figure 5.12(b,d). The elastically scattered laser light is observed as a higher intensity peak at 0 cm^{-1}.

XPS spectrum (figure 3.3), the absorbance spectrum (figure 4.1), the emission spectrum (figure 4.5a) and Raman spectrum (figure 4.13a) of alkyl capped SiNCs that studied in this work are identical with previous work which reported for alkylated SiNCs. Thus, these data indicate the successful synthesis of alkyl capped SiNCs.

Figure 4.13b shows the average Raman/luminescence spectrum that observed from erbium mixed alkylated SiNCs that drop coated from deionized water onto glass coverslip. The characteristic large and very broad Raman peak presented in this spectrum with a maximum intensity at around 3960 cm^{-1} (605 nm) can be referred to orange luminescence signals from C_{11}-SiNCs.[1, 22-24] It is also should be noted that this peak is a broader than that of alkylated SiNCs. In addition, the position of this peak shifts to a lower wavelength (blue shift) due to the oxidation of alkylated SiNCs in presence of erbium ions. As mentioned above, the position of the luminescence peak of C_{11}-SiNCs that prepared by the electrochemical method[1] most likely to be affected by the oxidation reaction between the SiNCs and the water. In addition, these oxidations states of alkylated SiNCs (SiO_x) are affected when they mixed with rare earth ion i.e. Er^{3+} as obtained from the core line Si*2p* in XPS spectrum of Er/C_{11}-SiNCs (see figure 3.5a). XPS spectrum shows that the Er/C_{11}-SiQDs have sub oxides on the surface of the nanoparticles. This gives evidence that the blue shift in the luminescence peak of SiNCs in Er/C_{11}-SiNCs arises from states that related with surface oxide. Thus, the surface chemical composition must play an important role in the blue shift of the luminescence of alkylated SiNCs when they mixed with erbium ions. It can be seen also that the typical peak of crystalline Si at 515 cm^{-1} does not appear in presence of erbium trichloride. This observation may be a result of overlap with the Si orange luminescence peak to become one broad peak. Furthermore, the sharp features at around 5145 cm^{-1} likely due to the electronic transitions from $^4F_{9/2}$ to the ground state $^4I_{15/2}$ in erbium ions.[10]

However, this orange luminescence peak (figure 4.13b) also is similar to that observed from PL emission of Si in Er/C_{11}-SiNCs mixture (figure 4.6). This suggests that the above hypothesis about the oxidation of the C_{11}-SiNCs in the water medium is confirmed when Er^{3+} exist. It also can be seen that the intensity of the scattered Raman light from the mixture is higher than that of pure alkylated SiNCs. The similar observation has been also obtained from PL measurements of C_{11}-SiNCs and Er/C_{11}-

SiNCs (figure 4.7) as discussed previously based on the energy transfer from erbium to silicon nanocrystals. From the typical absorption spectrum of erbium trichloride (figure 4.8), there is an electronic transition peak at 488 nm which attributed to $4F_{7/2}$.[9] This transition band is corresponding to the laser wavelength at 488 nm of Raman spectroscopy that used to excite the Er/C_{11}-SiNCs sample. Consequently, it is most likely that the laser light has been absorbed by Er^{3+} in this transition band and the energy transferred to the C_{11}-SiNCs which reflect the significant enhancement in the intensity of the luminescence band of SiNCs when they mixed with erbium ions (see figure 4.13) .

Moving to Raman measurements of commercial SiNCs and their mixture with erbium ions (Er/SiNCs), figure 4.14a-d shows a reflected light images and luminescence images of commercial SiNCs and Er/SiNCs mixture drop cast on glass coverslip. The confocal luminescence images of dried commercial SiNCs and Er/Commercial SiNCs exhibit bright spots (see figure 4.14b,d) due the presence of clusters of SiNCs and SiNCs which are associated to trivalent erbium, respectively. These observed aggregations (clusters) are a result of the drying method that used to prepare the samples. SEM images, TEM images and HRTEM images of commercial SiNCs present clear evidence that the Si nanoparticles after drying process are aggregated as a clusters.

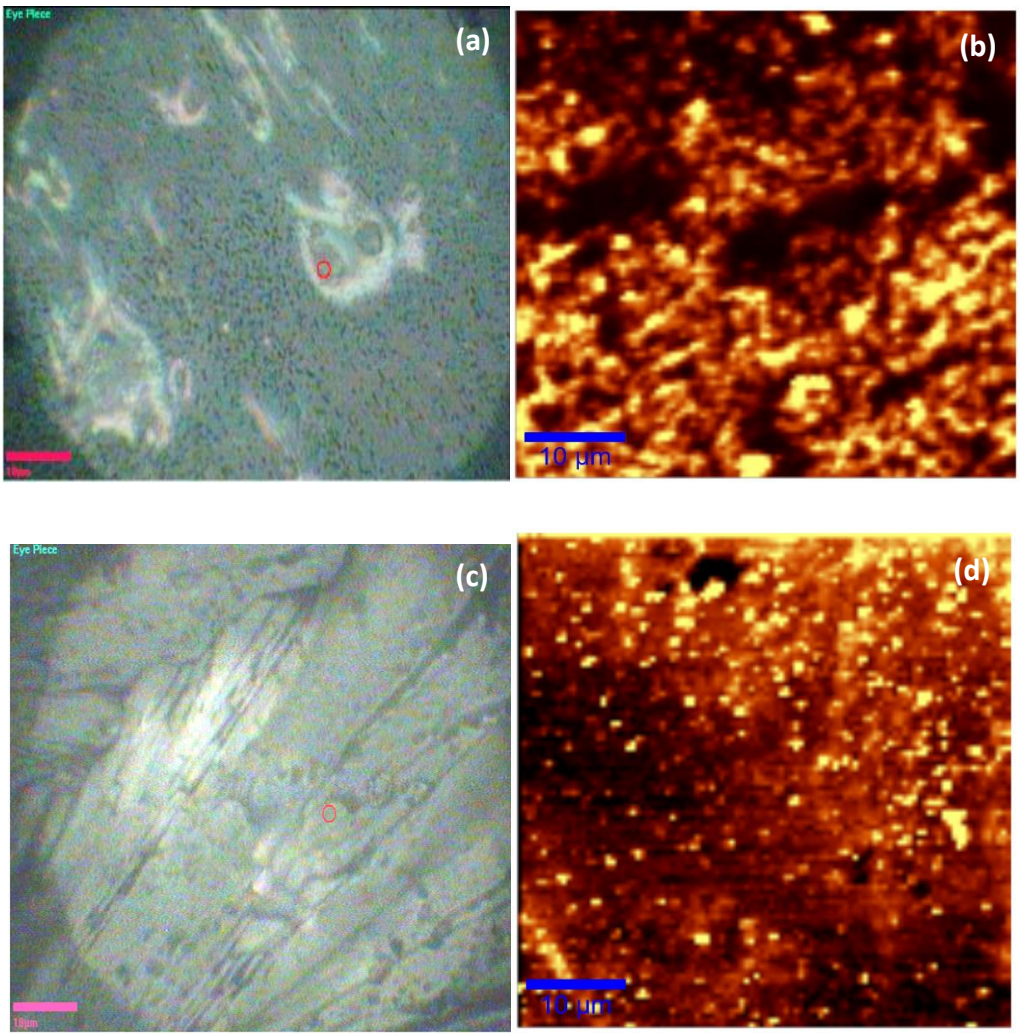

Figure 4.14: (a) Reflected light image of commercial SiNCs collected before (b) confocal luminescence spectrum image of dried commercial SiNCs deposited from deionized water on the glass coverslip. (c) reflected light image of Er/Commercial SiNCs collected prior to (d) confocal luminescence spectrum image of dried Er/Commercial SiNCs deposited from deionized water on the glass coverslip. The laser wavelength was 488 nm and the scale displays the scattered intensity integrated over the Stokes shift range from 200 cm^{-1} to 7000 cm^{-1}, which corresponds to a mixture of Raman signals and the luminescence. The scale bar of the reflected light images (a,c) is 10 µm and the scan size of the luminescence images (b,d) is 50 X 50 µm.

Figure 4.15 provides an average Raman and luminescence spectra of commercial SiNCs and Er/Commercial SiNCs which deposited on the glass coverslips. As the bright spots of the confocal luminescence images (figure 4.14b,d) were collected together, the complete average Raman and luminescence spectra of both commercial SiNCs and their mixture with erbium trichloride are obtained in figure 4.15.

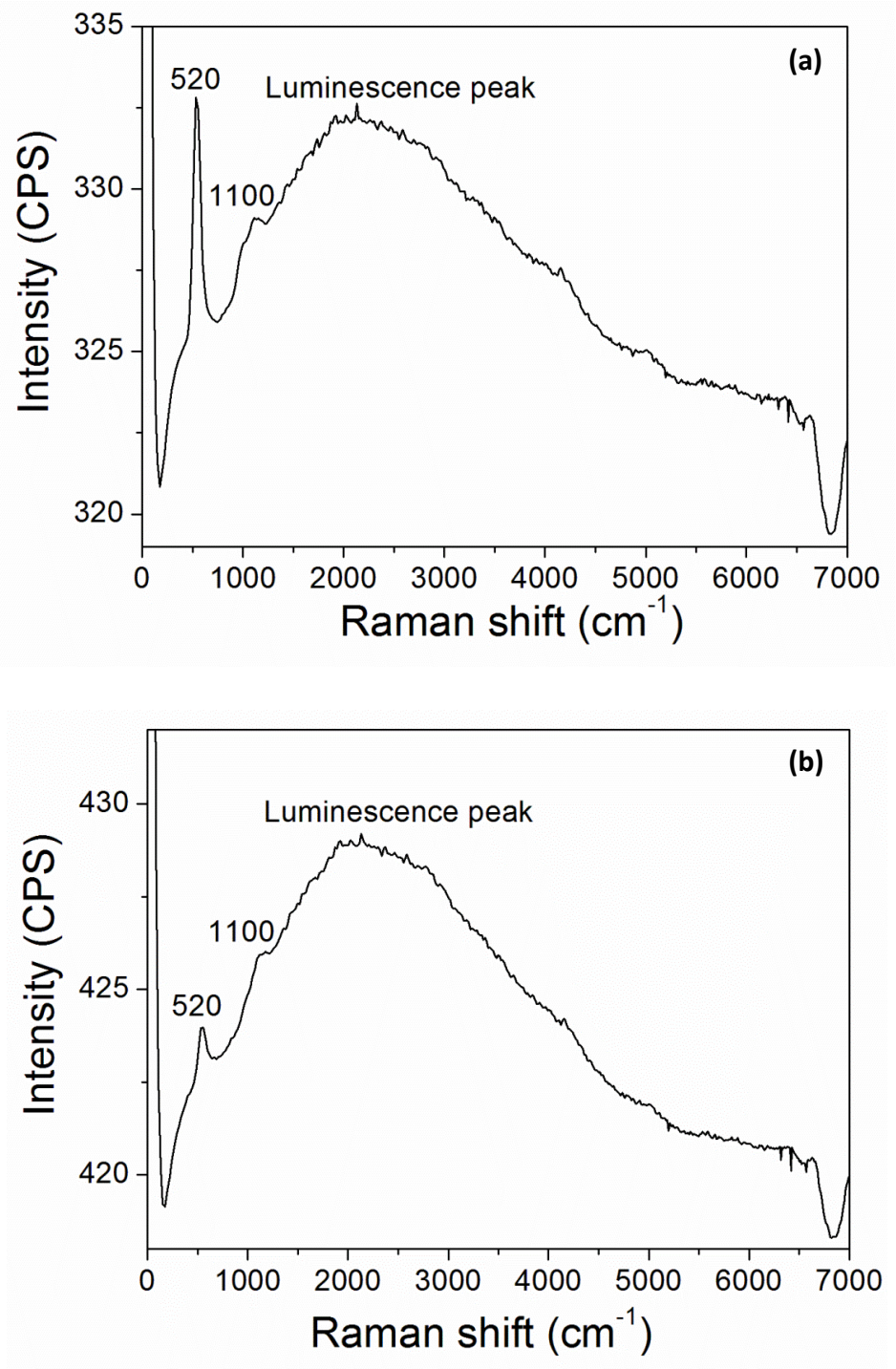

Figure 4.15: Average Raman and luminescence spectra of (a) commercial SiNCs drop-coated from aqueous solution on glass coverslip. (b) Er/Commercial SiNCs drop-coated from aqueous solution on glass coverslip. The excitation wavelength = 488 nm line of an argon ion laser was used to excite the luminescence and the spectra was collected using a grating = 150 lines mm^{-1} which provides collection of both Raman and luminescence from commercial silicon nanocrystals. These spectra are collected as averages from the particles that shown on figure 5.14(b,d). The elastically scattered laser light is observed as a higher intensity peak at 0 cm^{-1}.

The Raman spectrum of commercial SiNCs which drop coated from deionized water onto glass coverslip is presented in figure 4.15a. The characteristic Raman peak of crystalline Si appears at 520 cm^{-1}. This sharp peak has the same value as bulk crystalline silicon.[32, 33] Duan *et al*[33] have claimed that the quantum confinement effect is a dominant for Raman peak shift for crystalline SiNCs with particles size less than 6 nm. While for the particles larger than 6 nm, no considerable shift was observed in Raman peak and approached to the bulk value (520 cm^{-1}). They[33] have concluded that the different sizes of silicon nanoparticles that range from 2 nm to 100 nm influence the shifts in Raman spectra. Consequently, the crystalline silicon Raman peak of commercial SiNCs which have an average diameter of 65 nm emerged at 520 cm^{-1}, while this crystalline silicon peak sifts to 515 cm^{-1} in the case of synthesised alkylated SiNCs with a diameter of 2.5 nm (see figure 4.13a) due to the quantum confinement effect. The Raman feature at 1100 cm^{-1} can be assigned to Si-O vibration mode.[34] The presence of this vibration mode has been also determined in FTIR data of SiNCs (figure 3.12). In addition, this Raman peak can be also associated to second order of SiNCs.[24] The large and broad Raman peak which detected at 2330 cm^{-1} (550 nm) refers to the luminescence signals from SiNCs.

However, when the PL spectrum of commercial SiNCs (figure 4.9) is compared with the emission spectrum of the same silicon nanoparticles (figure 4.15a); a significant blue shift in the luminescence signal is detected (595 nm versus 550 nm). This blue shift can be due to (i) the oxidation of SiNCs, (ii) using different excitation sources i.e. 400 nm and 488 nm for PL investigation and Raman measurement, respectively. For the former reason, it is quite common that the nanoparticles are oxidized when they exposed to water and O_2.[24, 27, 35, 36] FTIR data (see figure 3.12) support this interpretation as the stretching peaks of SiO and O_nSiH_x are exist. In addition, the SiO Raman peak is presented in Raman spectrum of commercial SiNCs. These observations give strong evidence of the surface oxidation of commercial SiNCs. Thus, exposing the SiNCs to the water and the oxygen increase the oxidation states of the nanoparticles which result in blue shift. Therefore, the origin of this blue shift in the luminescence produces from the surface oxidation states of SiNCs. However, the oxidation effect on the luminescence (blue shift) of SiNCs has been already discussed in details in the case of alkylated SiNCs. The second possibility of this blue shift in the

luminescence is using different excitation sources in those two techniques. Thus, this shift of the luminescence wavelength is observed as a consequence of excited different sizes of SiNCs by using different excitation wavelength which confirmed the particle size distribution of commercial SiNCs as found from SEM, TEM, AFM and XRD data. This suggests that at Raman measurement, the smaller particles which possess a larger quantum confinement effect,[31] exhibit luminescence with lower excitation wavelength than that observed in PL emission spectrum of commercial SiNCs. This observation is somewhat similar to that observed by Lin *et al*[35] during the photoluminescence measurement of SiNCs in water medium using different excitation source range from 340 nm to 370 nm. The PL peak of SiNCs shifts to a lower wavelength as the wavelength of the excitation source increased. This phenomenon was explained in their investigation as a result of exciting different particles sizes with various excitation sources which reflect the particles size distribution of SiNCs.[35]

Figure 4.15b shows the average Raman and luminescence spectrum of erbium mixed commercial SiNCs (Er/Commercial SiNCs) which drop coated from deionized water onto glass coverslip. The Raman feature at 520 cm^{-1} can be assigned to crystalline bulk SiNCs.[32, 33] The peak at 1100 cm^{-1} corresponds to stretching vibration mode of Si-O.[34] The position of these peaks do not change in the presence of erbium ions whereas the crystalline Si peak and Si-O peak become lower in intensity than that of commercial SiNCs due to increasing the intensity of the luminescence signals from SiNCs which located with a maximum at 1968 cm^{-1} (539 nm). There is also a blue shift in the luminescence peak of Er/Commercial SiNCs when it compared with that of commercial SiNCs. The effect of the oxidation on luminescence peak of SiNCs has been discussed previously. Meanwhile, the intensity of this peak (539 nm) has also increased in presence of Er^{3+}. This change in the PL intensity was interpreted previously based on the energy transferred from erbium to silicon as observed also in Er/C_{11}-SiNCs mixture. Consequently, this phenomenon of enhancement the Raman scattering intensity was constant for both mixtures of Er/SiNCs. This phenomenon has been explained as a result of the total energy transferred from erbium ions to silicon nanoparticles. This assumption suggests that the energy level of erbium trichloride i.e. $4F_{7/2}$ absorbs the Raman laser light (the excitation source was 488 nm) and transferred to Si nanoparticles.

The Raman spectrum of erbium trichloride which drops coated from deionized water onto glass coverslip is investigated as shown in figure 4.16. The Raman features at 1334 cm^{-1} (522 nm) and 2143 cm^{-1} (545 nm) can be assigned to $2H_{11/2} \rightarrow 4I_{15/2}$ and $4S_{3/2} \rightarrow 4I_{15/2}$, respectively.[10] The clear peak at 3360 cm^{-1} corresponds to OH vibration mode of water that used as a solvent for erbium trichloride.[37] In addition, the peak at 5154 cm^{-1} (652 nm) is attributed to the electronic transition from $^4F_{9/2}$ to the ground state $^4I_{15/2}$.[10] These peaks do not appear when SiNCs are mixed with aqueous erbium trichloride due to the broad luminescence signal of both types of SiNCs.

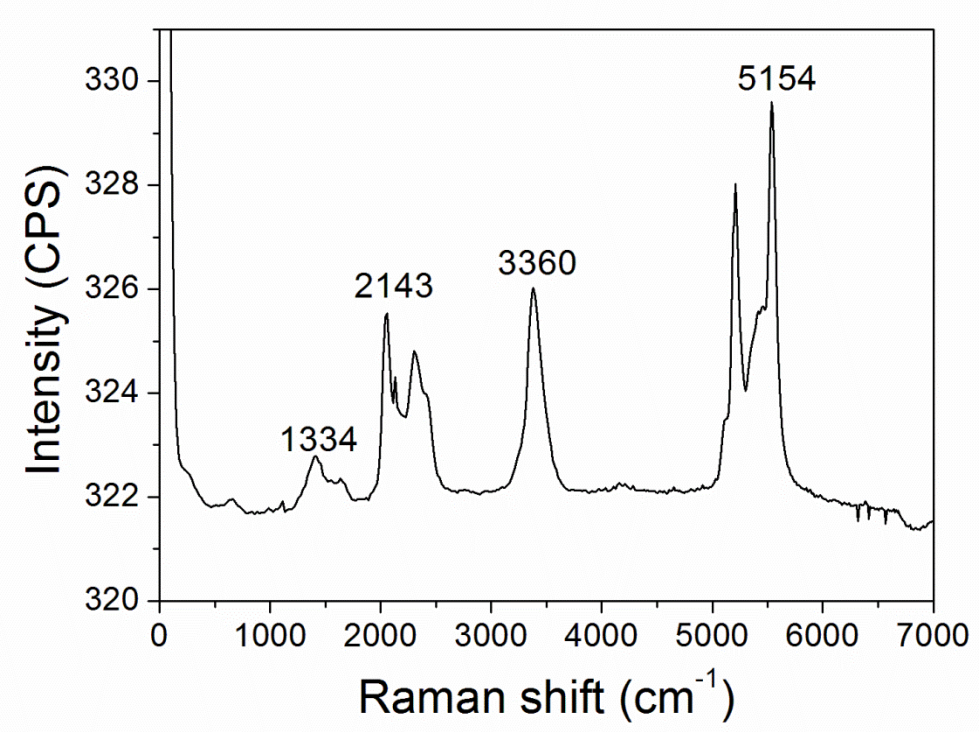

Figure 4.16: Average Raman and luminescence spectra of erbium trichloride drop coated from deionized water onto glass coverslip. The excitation wavelength = 488 nm. The elastically scattered laser light is observed as a higher intensity peak at 0 cm^{-1}.

4.4 Surface enhanced Raman spectroscopy (SERS) effect of synthesised alkylated silicon nanocrystals (C_{11}-SiNCs), commercial silicon nanocrystals (SiNCs) using silver nanoparticles (AgNPs)

To enable surface enhanced Raman spectroscopy (SERS), silver nanoparticles in two different concentrations i.e. 1 mM $AgNO_3$: 5 mM SDS (1:5) and 10 mM $AgNO_3$: 50 mM SDS (10:50) were used in this investigation. Silver nanoparticles were then mixed with SiNCs i.e. alkylated silicon nanocrystals and commercial silicon nanocrystals in order to observe the increasing of Raman scattering from silicon nanocrystals. Thus, the intense SERS effect which observed during this study suggested that AgNPs which synthesized using a green method can be used in SERS substrate. The obtained results from this analysis are reported and discussed below. The experimental details for this investigation are given in (Chapter 2 section 2.3.9).

Confocal spectroscopy investigations were applied to study the surface enhanced Raman and luminescence spectra of silicon nanocrystals with their mixtures with silver nanoparticles. All the samples i.e. AgNPs (1:5)/C_{11}-SiNCs, AgNPs (10:50)/C_{11}-SiNCs, AgNPs (1:5)/Commercial SiNCs and AgNPs (10:50)/Commercial SiNCs were drop-cast on glass coverslips for Raman spectroscopic measurements. Those samples were investigated at an excitation wavelength of 488 nm provided by an Argon ion laser and 150 lines mm^{-1} was also used as a grating in order to disperse the scattered and emitted light of both Raman and luminescence features of interest. The reflected light and confocal luminescence images of all samples which drop coated on a glass coverslip are shown in figure 4.17. The bright regions which determined from the confocal luminescence images of SiNCs with their mixtures with AgNPs using confocal spectroscopy provide clear evidence that SiNCs are aggregates as clusters due to the drying process as have been already obtained in the previous case of SiNCs and their mixture with erbium ions.

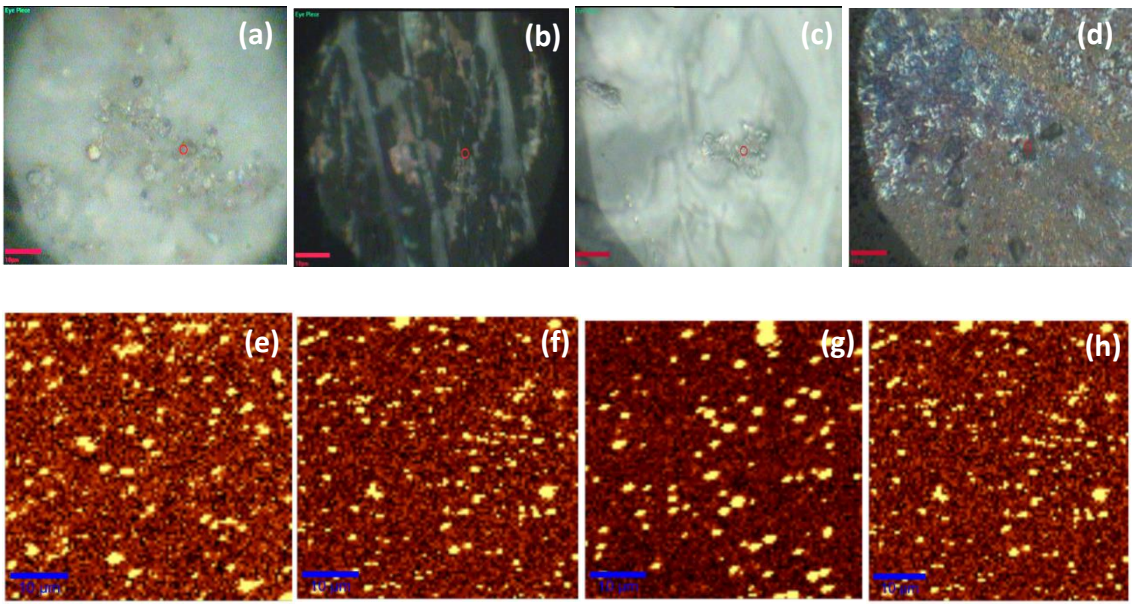

Figure 4.17: Reflected light images of (a) AgNPs (1:5)/C_{11}-SiNCs. (b) AgNPs (10:50)/C_{11}-SiNCs. (c) AgNPs (1:5)/Commercial SiNCs and (d) AgNPs (10:50)/Commercial SiNCs. Confocal luminescence spectrum image of (e) AgNPs (1:5)/C_{11}-SiNCs. (f) AgNPs (10:50)/C_{11}-SiNCs. (g) AgNPs (1:5)/Commercial SiNCs and (h) AgNPs (10:50)/Commercial SiNCs deposited from aqueous solution on the glass coverslips. The laser wavelength was 488 nm and the scale displays the scattered intensity integrated over the Stokes shift range from 200 cm^{-1} to 7000 cm^{-1}, which corresponds to both signals of Raman and luminescence. The scale bar of the reflected light images is 10 µm and the scan size of the luminescence images is 50 X 50 µm.

The bright regions for each sample which observed in figure 4.17 (e-h) were combined together to obtain complete average Raman and luminescence spectra in order to evaluate the SERS and the luminescence enhancement of SiNCs with AgNPs as presented in figure 4.18 and 4.19. Thus, figure 4.18 and 4.19 show the average Raman /luminescence spectra of alkylated SiNCs and commercial SiNCs when they mixed with AgNPs (1:5) and AgNPs (10:50), respectively.

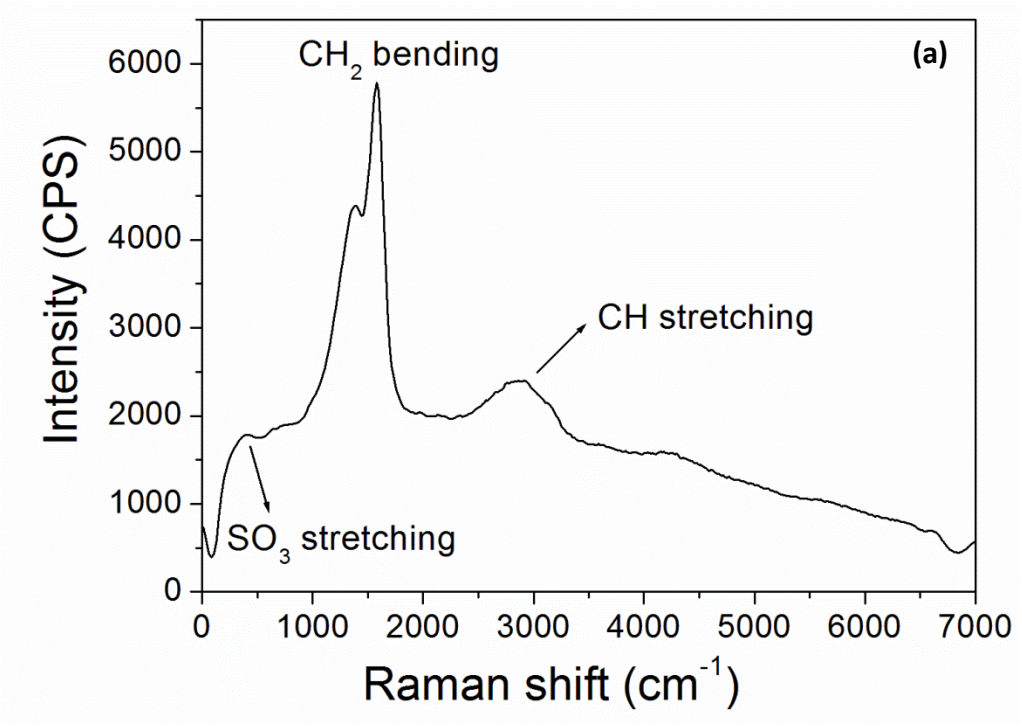

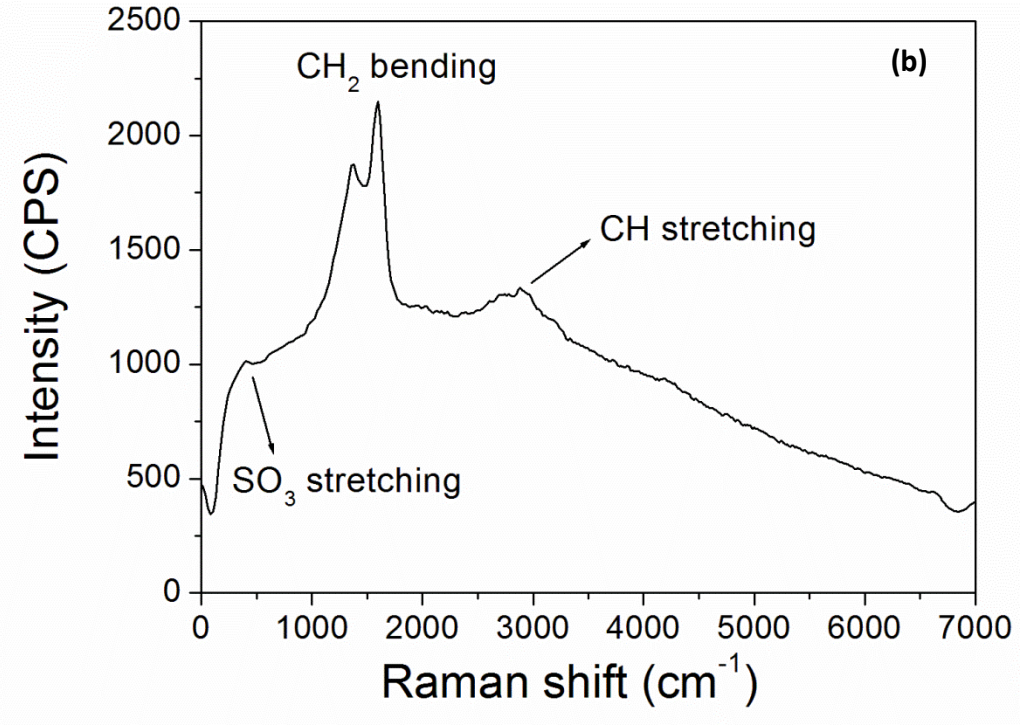

Figure 4.18: Average Raman and luminescence spectra of (a) AgNPs (1:5)/C_{11}-SiNCs (b) AgNPs (10:50)/C_{11}-SiNCs. All samples were drop-coated from aqueous solution on glass coverslips. The excitation wavelength = 488 nm line of an argon ion laser was used to excite the luminescence and the spectra was collected using a grating = 150 lines mm^{-1} which provides collection of both Raman and luminescence from alkylated silicon nanocrystals. The elastically scattered laser light is observed as a higher intensity peak at 0 cm^{-1}.

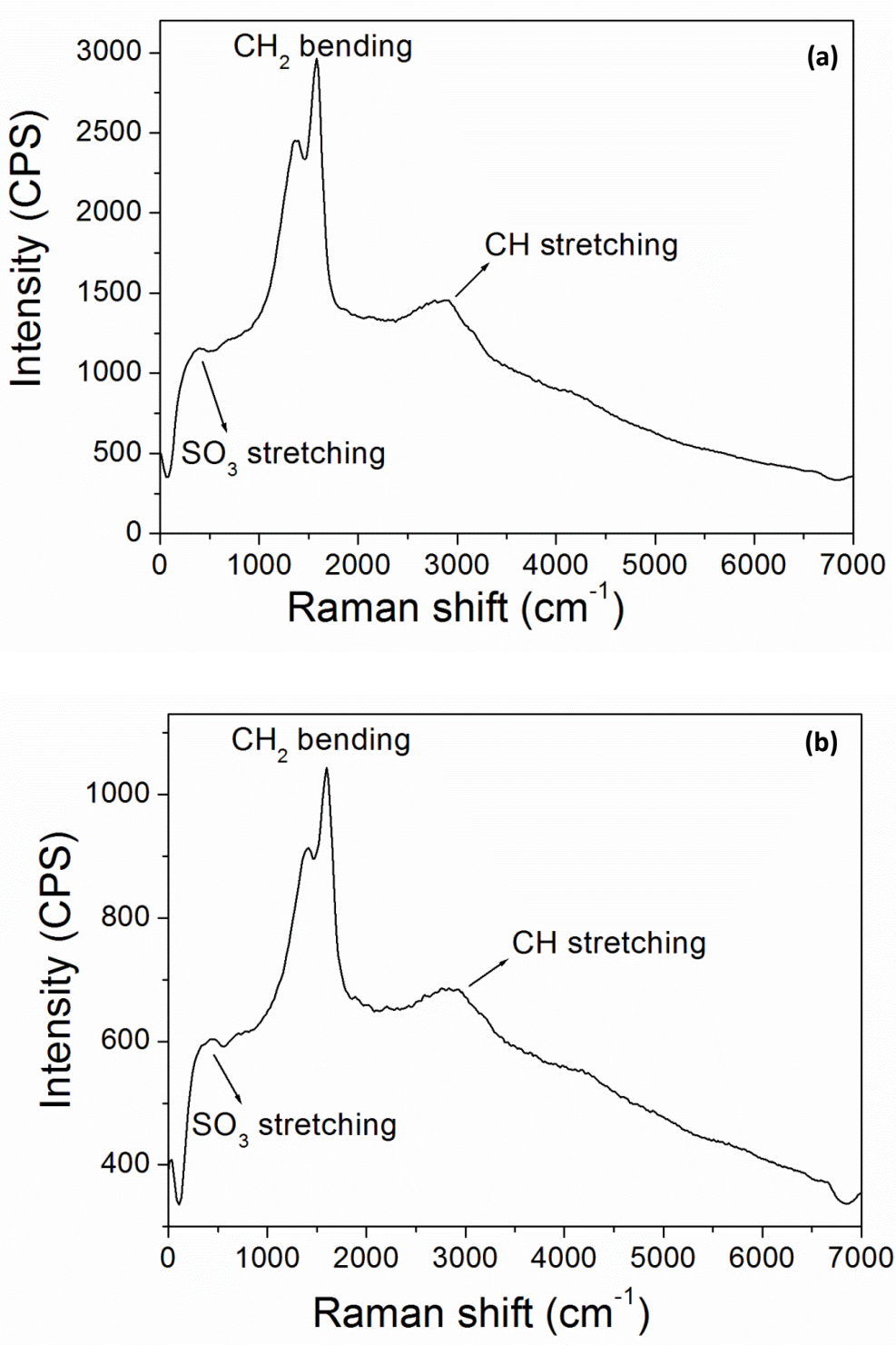

Figure 4.19: Average Raman and luminescence spectra of (a) AgNPs (1:5)/Commercial SiNCs (b) AgNPs (10:50)/Commercial SiNCs. All samples were drop-coated from aqueous solution on glass coverslips. The excitation wavelength = 488 nm line of an argon ion laser was used to excite the luminescence and the spectra was collected using a grating = 150 lines mm^{-1} which provides collection of both Raman and luminescence from silicon nanocrystals.

In general, the SERS features in the region 350 - 630 cm^{-1} can be attributed to SO_3 stretching vibrational modes of SDS which used to synthesis AgNPs.[38] The -CH_2- bending vibrations modes of the carbon chain of the SDS molecule are in the region 1350 - 1580 cm^{-1}.[38] The SERS peaks at around 2900 cm^{-1} can be assigned to C-H stretching vibrations modes of the carbon group of dodecyl sulphate molecule.[38] Table 4.2 listed the assignments of SERS features that observed in figure 4.18 and figure 4.19.

The typical luminescence peak of SiNCs i.e. 642 nm for alkyl capped SiNCs and 550 nm for commercial SiNCs does not disappear but it is dominated by much larger peak at lower wavelength at around 500 – 4000 cm^{-1} (500 – 606 nm) for both types of SiNCs. Thus, the luminescence peak of SiNCs blue shifted in presence of AgNPs (1:5) and (10:50). This blue shift can be explained as a result of the presence of metal nanoparticles i.e. AgNPs. In the presence of metal nanoparticles, the 488 nm light which used as an excitation source mostly does not excite the SiNCs directly, but is absorbed by the plasmon band and the near field of the plasmon couples to the SiNCs and excites it. However, the near field is only strong (near) to the metal, i.e. on the surface of the SiNCs. It is then logical the emission would be blue-shifted because only close to surface states not core states are excited. On the other hand, our group[24] observed that oxide-rich parts of the alkylated silicon quantum dots may have localised states that emit light blue shifted compared to un-oxidized parts of the particle on the surface as already have been discussed previously. Therefore, the effect of trace oxides on the surface of SiNCs is important and known to cause a blue shift in this study. Also, Židek *et al*[39, 40] discuss the effect of the surface on the emitting state as there may be many, slightly different emitting states even in a single particle. The second possible explanation for this blue shift of the luminescence peak of AgNPs/SiNCs compared to the luminescence of SiNCs alone is the coupling of the localized surface plasmon resonance (LSPR) to states near the direct gap of SiNCs, which radiate more efficiently. The reason that LSPR couples efficiently to such states may be simply that the wavelength of the laser i.e. 488 nm and LSPR near 400 nm are very blue compared to the orange luminescence at the indirect gap.

Functional group	λ_{peak} (cm^{-1}) of AgNPs (1:5)/C_{11}SiNCs	λ_{peak} (cm^{-1}) of AgNPs (10:50)/C_{11}SiNCs	λ_{peak} (cm^{-1}) of AgNPs (1:5)/Commercial SiNCs	λ_{peak} (cm^{-1}) of AgNPs (10:50)/Commercial SiNCs
SO_3	396	396	396	396
CH_2	1385 - 1580	1368 - 1580	1370 - 1580	1385 - 1580
CH	2895	2902	2902	2910

Table 4.2: Vibrations modes observed in SERS spectra for AgNPs (1:5)/C_{11}-SiNCs, AgNPs (10:50)/C_{11}-SiNCs, AgNPs (1:5)/Commercial SiNCs and AgNPs (10:50)/Commercial SiNCs.

The mean Raman and luminescence spectra of both SiNCs that mixed with AgNPs (1:5) determined that the SERS intensities were higher than which observed for both SiNCs mixed with AgNPs (10:50) as shown in figure 4.20. A significant enhancement up to 10 times and 4 times in the intensity of the most intense band (CH_2 bending vibration mode) is observed, when C_{11}-SiNCs mixed with AgNPs (1:5) and AgNPs (10:50), respectively as compared to the conventional C_{11}-SiNCs (see figure 4.20a). A similar observation was also reported for the commercial SiNCs when they mixed with AgNPs (1:5) and AgNPs (10:50); where the intensity of the SERS higher 9 times and 3 times, respectively when compared with conventional commercial SiNCs as presented in figure 4.20b. This significant enhancement in SERS intensities may be a consequence of the coupling between the excitation laser light (488 nm) and the plasmon bands of AgNPs; thus this intense field at AgNPs surface couples strongly to SiNCs.

However, this difference in the SERS intensities enhancement can be a result of two reasons i.e. using different sizes of AgNPs through the project and using two different concentrations of AgNPs. It is known that the average particles size of AgNPs (1:5) and AgNPs (10:50) is 100 nm and 30 nm, respectively.[6] Thus, the bigger silver nanoparticles (1:5) exhibit more enhancements in the intensity of Raman signal rather than the smaller silver nanoparticles (10:50) which reflect the strong interaction between the localized surface plasmon resonance of AgNPs and the electric field forming a strong polarization near SiNCs. Our phenomena is in agreement with the

study that reported by Rycenga *et al.*[41] They have found that varying the dimension of AgNPs will influence the scattering and the absorption peak of localised surface plasmon resonance (LSPR). They[41] have suggested that when AgNPs have diameter about 30 nm the absorption is more dominant compared to scattering. Whereas, the AgNPs with size range from 40 nm to 140 nm had a significantly higher scattering intensity compared to the absorption. Thus, based on this assumption[41] our obtained results from UV-Vis and Confocal Raman spectroscopy of all the samples i.e. AgNPs (1:5)/C_{11}-SiNCs, AgNPs (10:50)/C_{11}-SiNCs, AgNPs (1:5)/Commercial SiNCs and AgNPs (10:50)/Commercial SiNCs are constant with above study (see figure 4.3, figure 4.4, figure 4.18 and figure 4.19). The second possible interpretation of this difference enhancement in the Raman signal intensities may be related to the concentration of AgNPs. When the concentration of AgNPs increased from (1:5) to (10:50), AgNPs tend to self-aggregate. Subsequently, these clusters will reduce the luminescence intensity of AgNPs. This explanation is compatible with SEM images of synthesised AgNPs (1:5) and (10:50) which observed further agglomeration for Ag nanoparticles with higher concentration.[6] This observation also is consistent with that observed by Chandra *et al*.[42] They have found that increasing the metallic nanoparticles concentrations will reduce the emission intensity of CdSe/ZnS QDs.

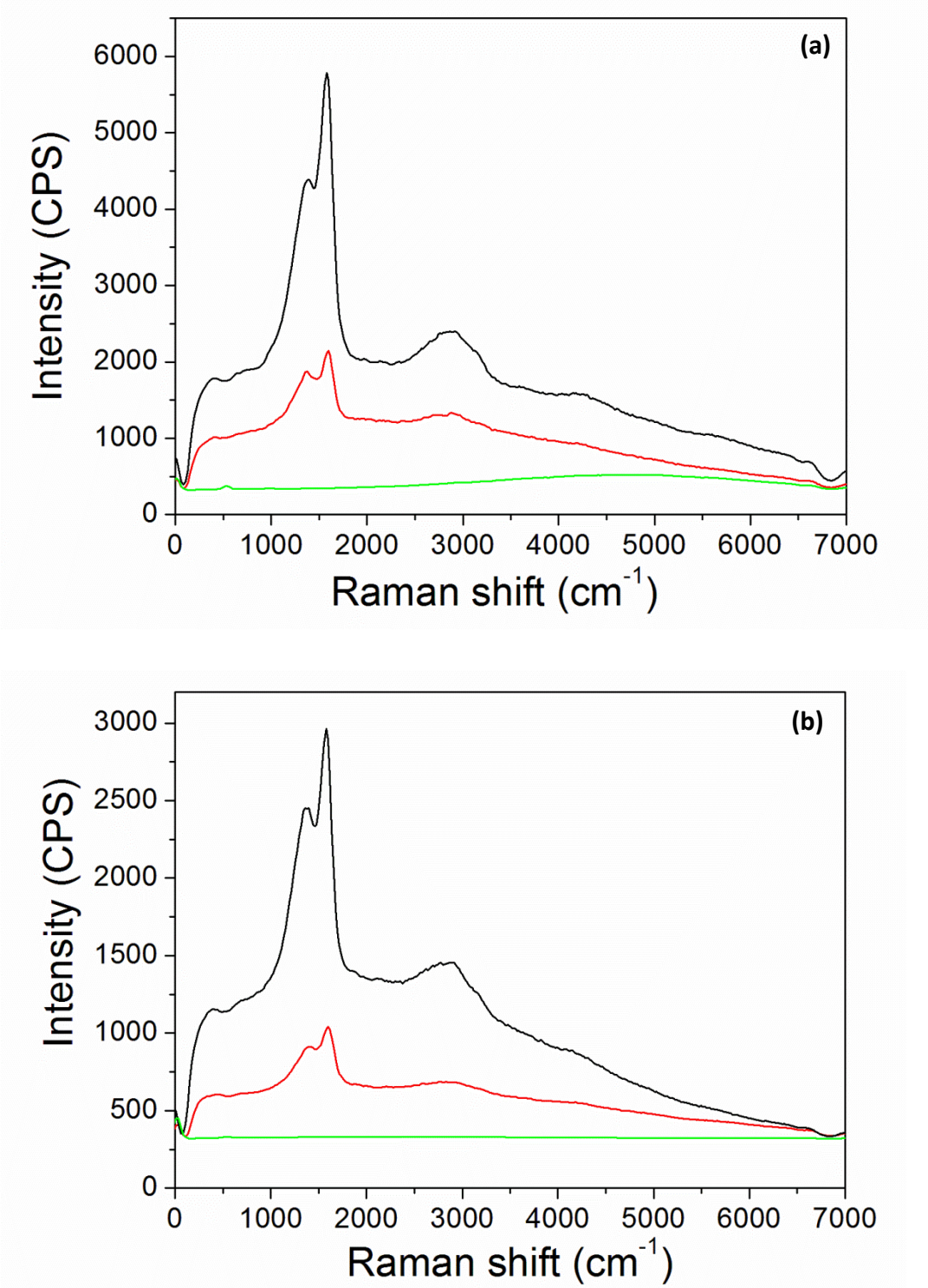

Figure 4.20: Average Raman and luminescence spectra of (a) C_{11}-SiNCs (green line), AgNPs (1:5)/C_{11}-SiNCs (black line) and AgNPs (10:50)/C_{11}-SiNCs (red line). (b) Commercial SiNCs (green line), AgNPs (1:5)/Commercial SiNCs (black line) and AgNPs (10:50)/Commercial SiNCs (red line). All samples were drop-coated from aqueous solution on glass coverslips. The excitation wavelength = 488 nm.

It can be seen that the Raman and luminescence spectra of AgNPs/SiNCs mixtures obtained several peaks which are not presented in Raman spectra of SiNCs (see figure 4.18 & 4.19). Thus, in order to justify these peaks which are presented due to presence of silver, Raman spectrum of AgNPs (1:5) has also performed. Figure 4.21 presents the Raman spectra of AgNPs (1:5) drop coated from aqueous solution onto glass coverslip using 488 nm as an excitation source. The Raman bands in the region 350 – 600 cm^{-1} can be attributed to SO_3 stretching vibration modes of SDS.[38, 43] The Raman peak at around 891 cm^{-1} may be associated to CH_3 rocking vibrations mode of SDS.[38, 43] The Raman feature at 1105 cm^{-1} associated to NO_3 which used in AgNPs preparation.[44] The CH_2 bending modes of the C chain in SDS appear in the region 1300 – 1460 cm^{-1}.[38, 43] While, the sharp Raman peak at 2900 cm^{-1} and the broad peak at 3400 cm^{-1} correspond to CH stretching vibration modes of SDS and O-H, respectively.[37, 38, 43] Thus, all the Raman bands in AgNPs/SiNCs mixtures are generated from Ag nanoparticles as observed in figure 4.18 & 4.19.

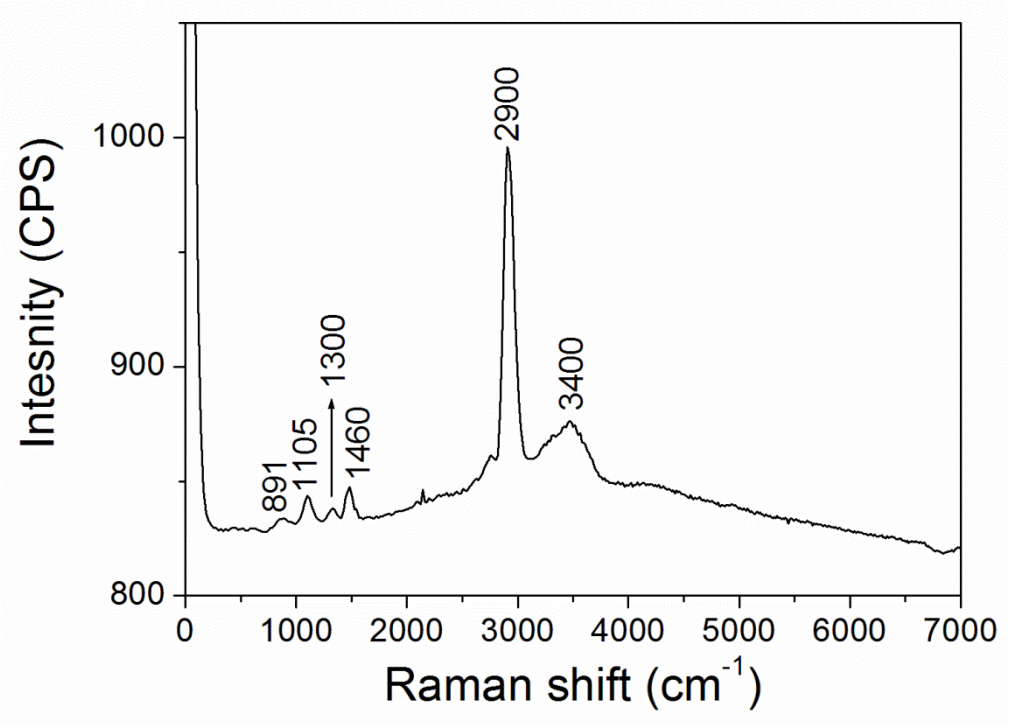

Figure 4.21: Average Raman and luminescence spectrum of AgNPs (1:5) drop coated from aqueous solution onto glass coverslip. The excitation wavelength = 488 nm. The elastically scattered laser light is observed as a higher intensity peak at 0 cm^{-1}.

The SERS effect was carried out also for commercial SiNCs and their mixtures with AgNPs using Lab RAMAN HR 800 with an excitation source of 514.5 nm from an argon ion laser. Using a laser power of 5 mW, the spectra were collected; where the laser has been focused on 1 µm of the sample. It is known that the green laser is more sensitive to detect Raman signals than the blue laser as the intensity of Raman scattering is proportional to the incident light wavelength.[45] However, silver nanoparticles can be readily excited in blue and green regions.[45] Figure 4.22 presents the Raman spectrum of commercial SiNCs drop coated from aqueous solution onto glass cover slip in the region between 200 cm^{-1} and 1800 cm^{-1}. The sharp Raman peak at 520 cm^{-1} can be attributed to the bulk crystalline Si.[33] It can be seen that this Raman peak becomes narrower with increasing the excitation wavelength from 488 nm to 514 nm. This can be due to a resonance of the excitation energy with the electronic state of SiNCs.[46, 47] The feature at 960 cm^{-1} can be attributed to the second order of SiNCs.[24] The broad Raman peak that appeared at 1097 cm^{-1} can be associated to Si-O vibration mode.[34] These peaks were also observed in Raman spectrum of commercial SiNCs using 488 nm as an excitation source (figure 4.15a). The Raman band at 1360 cm^{-1} may be attributed to CH bending vibration mode of commercial SiNCs.[48] Furthermore, there is no luminescence features were captured using Lab RAMAN. This is probably because the excitation source (514.5 nm) in this spectroscopy is not absorbed strongly as in confocal Raman which has excitation source of 488 nm. Thus, the luminescence peak of commercial SiNCs does not appear in this study. However, Raman investigations of commercial SiNCs are in agreement with FTIR study (see figure 3.12) which reflect proper analyses of their chemical composition.

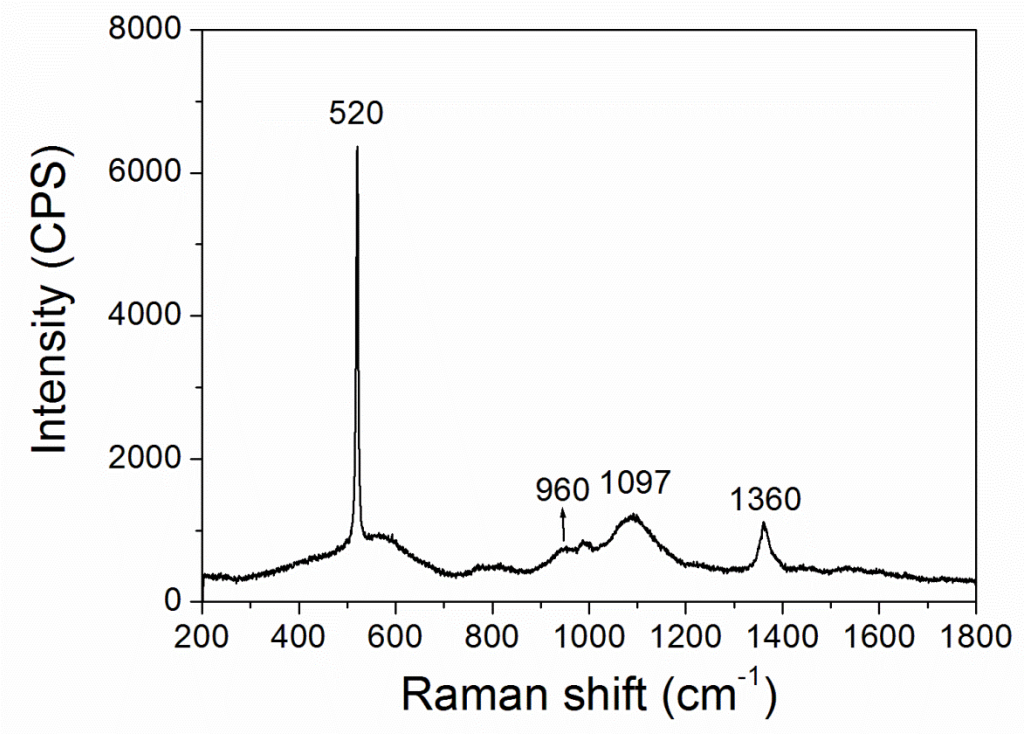

Figure 4.22: Raman spectrum of commercial SiNCs drop coated from aqueous solution onto coverslip. The excitation wavelength = 514.5 nm.

To enable investigate the SERS effect on commercial SiNCs, AgNPs in two different concentration i.e. (1:5) and (10:50) were utilized. Figure 4.23 presents the Raman spectra of commercial SiNCs with their mixtures with AgNPs drop coated from aqueous solution onto glass cover slip in the region between 200 cm^{-1} and 1800 cm^{-1}. Figure 4.23a exhibit the SERS spectrum of AgNPs (1:5) mixed with commercial SiNCs. The sharp Raman peak at 520 cm^{-1} corresponds to bulk crystalline silicon of AgNPs (1:5)/Commercial SiNCs. In addition, the SERS features at around 804 cm^{-1} and 940 cm^{-1} may be assigned to S-OC vibration modes of SDS molecule and to the second order of SiNCs[24,38], respectively. However, the same SERS features have been observed for AgNPs (10:50)/Commercial SiNCs as presented in figure 4.23b; beyond for Si second order which was observed at 955 cm^{-1}. This red shift can be associated to laser induced heating. The heating effect from the laser using Lab RAMAN on the Raman shift was observed also by Astuti.[49]

Taking into account the intensities of SERS, it was found that SERS intensity of AgNPs (1:5)/Commercial SiNCs was higher than that of AgNPs (10:50)/Commercial SiNCs as presented in figure 4.23c. A considerable SERS enhancement up to 7 and 2 times in the intensity of the most intense band (520 cm^{-1}) is observed, when

commercial SiNCs mixed with AgNPs (1:5) and AgNPs (10:50), respectively as compared to the conventional commercial SiNCs. This significant enhancement in the SERS intensities and the difference between the SERS intensities of AgNPs (1:5)/Commercial SiNCs and AgNPs (10:50)/Commercial SiNCs have been already explained in details previously. However, this phenomenon is consistent in the trend with that observed in AgNPs/ Commercial SiNCs mixtures using excitation source = 488 nm; where SERS intensity of AgNPs (1:5)/Commercial SiNCs > AgNPs (10:50)/Commercial SiNCs.

It is noteworthy that the magnitude of the SERS enhancement can be influenced by two factors; localized surface plasmon resonance (LSPR) of silver nanoparticles and the wavelength of the excitation source (λ_{ex}).[50] Consequently, it is eligible to match between the wavelength of LSPR and the laser wavelength. Thus, the enhancement in SERS intensity changes as a function of LSPR of nanoparticles and excitation wavelength. A recent wavelength-scanned SERS study by McFarland *et al*[51] indicates that the maximum SERS enhancement intensity can be achieved by using wavelength excitation source less than the wavelength of LSPR of silver nanoparticles. Thus, our data are expected and present a similar behaviour; as λ_{ex} i.e. 488 nm closer to λ of LSPR i.e. around 400 nm, higher SERS effect can be obtained than that of λ_{ex} = 514.5 nm. Therefore, the use of shorter wavelength (488 nm) was affective to observe significant SERS enhancement in the intensity in commercial SiNCs with their mixtures of AgNPs.

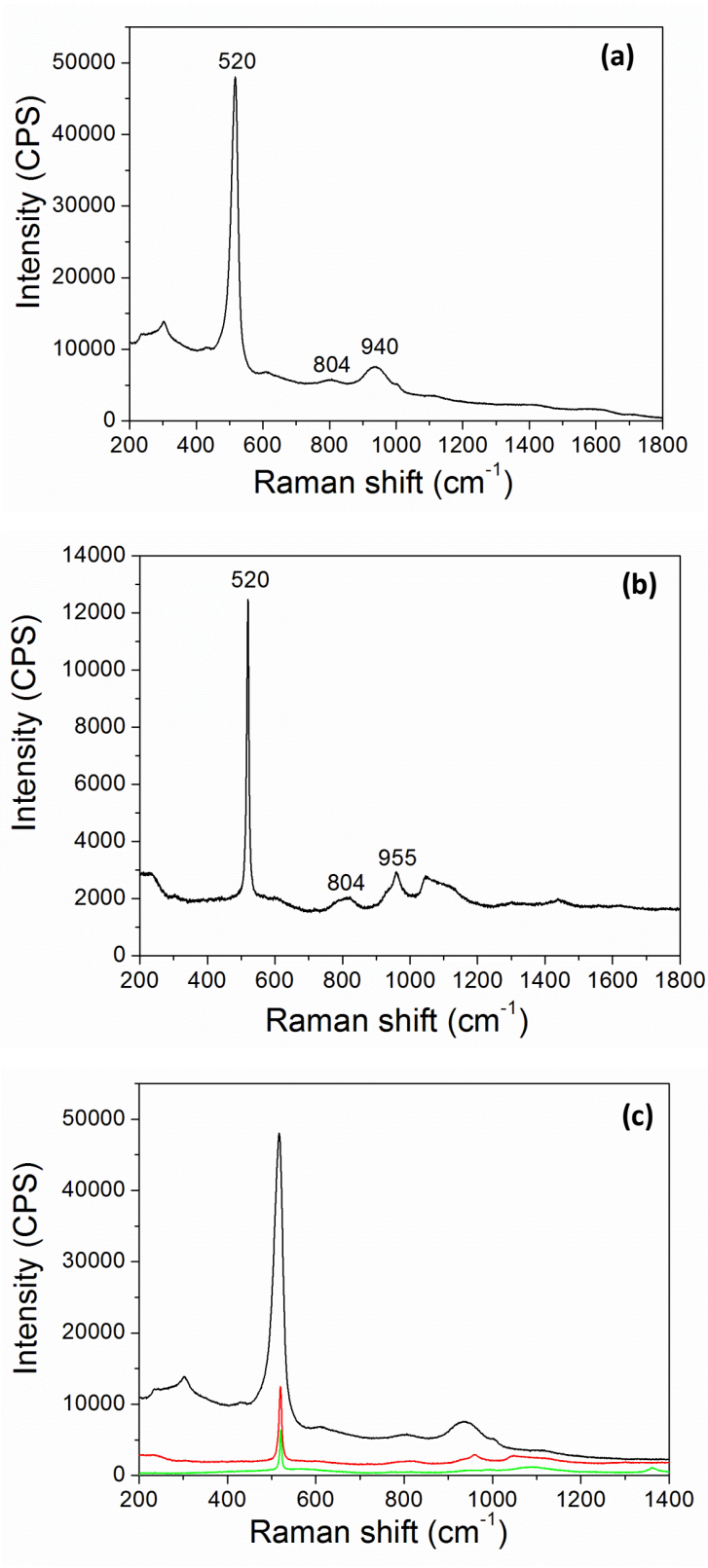

Figure 4.23: SERS spectra of (a) AgNPs (1:5)/Commercial SiNCs. (b) AgNPs (10:50)/Commercial SiNCs and (c) comparison between commercial SiNCs (green line), AgNPs (1:5)/Commercial SiNCs (black line) and AgNPs (10:50)/ Commercial SiNCs (red line). All the samples were drop coated from aqueous solution onto coverslips. The excitation wavelength = 514.5 nm.

4.5 Summary

Alkylated SiNCs, commercial SiNCs and their mixtures with erbium trichloride and silver nanoparticles have been prepared for spectroscopic measurements. The absorption spectra of SiNCs and their mixtures with erbium trichloride are characteristic for an indirect band gap of semiconductor. While, localized surface plasmon resonance (LSPR) peaks are presented as AgNPs mixed with SiNCs.

Both SiNCs either alkylated SiNCs and commercial SiNCs and their mixtures with erbium show an orange PL emission peak at around 595 nm. Er/C_{11}-SiNCs and Er/commercial SiNCs also exhibit weak PL emission peaks at 1536 nm which originate from the intra-4*f* transition in erbium ions (Er^{3+}). The PL peak (595) of Er/C_{11}-SiNCs and Er/Commercial SiNCs are increased in the intensity up to four and three times, respectively as compared to that of C_{11}-SiNCs and commercial SiNCs. Thus, the intensities of PL peaks of SiNCs are found to be influenced by the chemical composition of the films which reflects the energy transfer from erbium to SiNCs.

The luminescence and Raman spectra of both SiNCs and their mixtures with erbium ions were investigated by confocal Raman spectroscopy. The characteristic broad luminescence peak confirmed the presence of SiNCs. The wavelength of this luminescence signal of SiNCs in aqueous medium in presence of trivalent erbium shifts to a lower wavelength due to the formation of oxides which would cause a blue shift to higher energy based on the quantum confinement effect. This suggests that the blue shift arises from states which related to the surface oxide on SiNCs. Thus, the surface chemical composition must play an important role in the blue shift of the luminescence of SiNCs when they mixed with erbium ions. This data suggests that the origin of the luminescence from SiNCs either C_{11}-SiNCs or commercial SiNCs could be attributed to direct band gap transitions in SiNCs and to radiative recombination of excitons through the oxidation surface of SiNCs.

However, this chemical mixing route which used in this work leads to transferring energy from erbium ions to SiNCs not as we expected from excited SiNCs to Er^{3+} as confirmed by PL and Raman investigations. In addition, this simple chemical mixing of SiNCs and erbium ions does not provide efficient PL from erbium ions when they mixed with both types of SiNCs but it has a significant effect on the PL of SiNCs.

Silver nanoparticles in two different concentrations i.e. (1:5) and (10:50) were used as plasmonics metal nanoparticles due to a robust surface enhanced Raman spectroscopy (SERS) effect that observed when they mixed with alkylated SiNCs and commercial SiNCs using an excitation source of 488 nm. A significant enhancement up to 10 and 4 times in the SERS intensity was observed using confocal Raman spectroscopy for AgNPs (1:5)/C_{11}-SiNCs and AgNPs (10:50)/C_{11}-SiNCs, respectively. A similar observation was also reported for the commercial SiNCs when they mixed with AgNPs (1:5) and AgNPs (10:50); where the intensity of the SERS signal increased up to 9 times and 3 times, respectively. Our study suggests that the larger AgNPs (1:5) caused an optimum enhancement in SERS intensity of both types of SiNCs while the smaller particles (10:50) caused a significant lack of the luminescence. However, this enhancement in SERS intensities occurs as a result of the coupling between the excitation laser light (488 nm) and the plasmon bands of AgNPs; thus this intense field at AgNPs surface couples strongly to SiNCs. It was also found that in this work, the luminescence peak of SiNCs blue shifted in presence of AgNPs. This blue shift can be due to (i) strong coupling of LSPR of AgNPs to surface oxides of SiNCs and (ii) LSPR couples strongly to states near the direct gap of SiNCs, which radiative more efficiently.

The SERS effect of AgNPs/Commercial SiNCs mixtures was also investigated using 514.5 nm as an excitation source. Our data suggest that a considerable SERS effect obtained when AgNPs excited using excitation source of 488 nm rather than 514.5 nm. This phenomenon supports the thought that a good match between the wavelength of the laser excitation source and SPR absorption band of silver nanoparticles consider to be an important requirement in SERS experiments. Furthermore, the intense SERS effect which observed during this project where AgNPs mixed with SiNCs suggests that AgNPs which synthesized by a green method can be used in some application such as SERS substrates.

References:

1. L. H. Lie, M. Duerdin, E. M. Tuite, A. Houlton and B. R. Horrocks, *Journal of Electroanalytical Chemistry*, 2002, **538–539**, 183-190.
2. T. Mohanty, N. C. Mishra, A. Pradhan and D. Kanjilal, *Surface and Coatings Technology*, 2005, **196**, 34-38.
3. K. A. Littau, P. J. Szajowski, A. J. Muller, A. R. Kortan and L. E. Brus, *The Journal of Physical Chemistry*, 1993, **97**, 1224-1230.
4. L. Brus, *The Journal of Physical Chemistry*, 1994, **98**, 3575-3581.
5. J. St. John, J. L. Coffer, Y. Chen and R. F. Pinizzotto, *Journal of the American Chemical Society*, 1999, **121**, 1888-1892.
6. G. A. Bhaduri, R. Little, R. B. Khomane, S. U. Lokhande, B. D. Kulkarni, B. G. Mendis and L. Šiller, *Journal of Photochemistry and Photobiology A: Chemistry*, 2013, **258**, 1-9.
7. Y. Chao, A. Houlton, B. R. Horrocks, M. R. C. Hunt, N. R. J. Poolton, J. Yang and L. Siller, *Applied Physics Letters*, 2006, **88**, 263119-263113.
8. P. G. Kik, M. L. Brongersma and A. Polman, *Applied Physics Letters*, 2000, **76**, 2325-2327.
9. C. Strohhöfer and A. Polman, *Optical Materials*, 2003, **21**, 705-712.
10. S. V. J. Lakshman and C. K. Jayasankar, *Spectroc. Acta Pt. A-Molec. Biomolec. Spectr.*, 1984, **40**, 695-704.
11. M. Fujii, M. Yoshida, Y. Kanzawa, S. Hayashi and K. Yamamoto, *Applied Physics Letters*, 1997, **71**, 1198-1200.
12. S. K. Ray, S. Maikap, W. Banerjee and S. Das, *J. Phys. D-Appl. Phys.*, 2013, **46**.
13. M. Fujii, M. Yoshida, S. Hayashi and K. Yamamoto, *Journal of Applied Physics*, 1998, **84**, 4525-4531.
14. L. Jin, D. Li, L. Xiang, F. Wang, D. Yang and D. Que, *Nanoscale Res. Lett.*, 2013, **8**, 1-6.
15. G. Franzo, V. Vinciguerra and F. Priolo, *Appl. Phys. A-Mater. Sci. Process.*, 1999, **69**, 3-12.
16. P. G. Kik and A. Polman, *Journal of Applied Physics*, 2000, **88**, 1992-1998.
17. J. Ji, R. A. Senter, L. R. Tessler, D. Back, C. H. Winter and J. L. Coffer, *Nanotechnology*, 2004, **15**, 643.
18. P. K. Sekhar, A. R. Wilkinson, R. G. Elliman, T. H. Kim and S. Bhansali, *J. Phys. Chem. C*, 2008, **112**, 20109-20113.
19. M. F. Cerqueira, M. Losurdo, T. Monteiro, M. Stepikhova, M. J. Soares, M. Peres, E. Alves and O. Conde, *Journal of Non-Crystalline Solids*, 2006, **352**, 1148-1151.
20. M. F. Cerqueira, M. Losurdo, M. Stepikhova, P. Alpuim, G. Andres, A. Kozanecki, M. J. Soares and M. Peres, *Thin Solid Films*, 2009, **517**, 5808-5812.
21. N. A. Harun, M. J. Benning, B. R. Horrocks and D. A. Fulton, *Nanoscale*, 2013, **5**, 3817-3827.
22. N. A. Harun, B. R. Horrocks and D. A. Fulton, *Nanoscale*, 2011, **3**, 4733-4741.
23. Y. Chao, L. Šiller, S. Krishnamurthy, P. R. Coxon, U. Bangert, M. Gass, L. Kjeldgaard, S. N. Patole, L. H. Lie, N. O'Farrell, T. A. Alsop, A. Houlton and B. R. Horrocks, *Nat Nano*, 2007, **2**, 486-489.
24. F. M. Dickinson, T. A. Alsop, N. Al-Sharif, C. E. M. Berger, H. K. Datta, L. Šiller, Y. Chao, E. M. Tuite, A. Houlton and B. R. Horrocks, *Analyst*, 2008, **133**, 1573-1580.
25. N. A. Harun, Newcastle University, 2013.
26. K. Zídek, F. Trojánek, P. Malý, L. Ondi, I. Pelant, K. Dohnalová, L. Šiller, R. Little and B. R. Horrocks, *Opt. Express*, 2010, **18**, 25241-25249.
27. Y. Chao, S. Krishnamurthy, M. Montalti, L. H. Lie, A. Houlton, B. R. Horrocks, L. Kjeldgaard, V. R. Dhanak, M. R. C. Hunt and L. Šiller, *Journal of Applied Physics*, 2005, **98**, 044316.
28. M. R. Linford and C. E. D. Chidsey, *Journal of the American Chemical Society*, 1993, **115**, 12631-12632.

29. M. R. Linford, P. Fenter, P. M. Eisenberger and C. E. D. Chidsey, *Journal of the American Chemical Society*, 1995, **117**, 3145-3155.
30. G. F. Cerofolini, C. Galati, S. Reina, L. Renna, N. Spinella and G. G. Condorelli, *Physical Review B*, 2006, **74**, 235407.
31. G. Ledoux, J. Gong, F. Huisken, O. Guillois and C. Reynaud, *Applied Physics Letters*, 2002, **80**, 4834-4836.
32. G. Faraci, S. Gibilisco, P. Russo, A. R. Pennisi and S. La Rosa, *Physical Review B*, 2006, **73**, 033307.
33. Y. Duan, J. F. Kong and W. Z. Shen, *Journal of Raman Spectroscopy*, 2012, **43**, 756-760.
34. L. V. Mercaldo, E. M. Esposito, P. D. Veneri, G. Fameli, S. Mirabella and G. Nicotra, *Applied Physics Letters*, 2010, **97**, 153112.
35. S.-W. Lin and D.-H. Chen, *Small*, 2009, **5**, 72-76.
36. N. O'Farrell, A. Houlton and B. R. Horrocks, *Int. J. Nanomed.*, 2006, **1**, 451-472.
37. S. M. Pershin, *Opt. Spectrosc.*, 2005, **98**, 543-554.
38. G. Cazzolli, S. Caponi, A. Defant, C. M. C. Gambi, S. Marchetti, M. Mattarelli, M. Montagna, B. Rossi, F. Rossi and G. Viliani, *Journal of Raman Spectroscopy*, 2012, **43**, 1877-1883.
39. K. Žídek, I. Pelant, F. Trojánek, P. Malý, P. Gilliot, B. Hönerlage, J. Oberlé, L. Šiller, R. Little and B. R. Horrocks, *Physical Review B*, 2011, **84**, 085321.
40. K. Zídek, F. Trojánek, P. Malý, L. Ondi, I. Pelant, K. Dohnalová, L. iller, R. Little and B. R. Horrocks, *Opt. Express*, 2010, **18**, 25241-25249.
41. M. Rycenga, C. M. Cobley, J. Zeng, W. Li, C. H. Moran, Q. Zhang, D. Qin and Y. Xia, *Chemical Reviews*, 2011, **111**, 3669-3712.
42. S. Chandra, J. Doran, S. J. McCormack, M. Kennedy and A. J. Chatten, *Sol. Energy Mater. Sol. Cells*, 2012, **98**, 385-390.
43. M. Picquart, *J. Phys. Chem.*, 1986, **90**, 243-250.
44. G. E. Walrafen and D. E. Irish, *The Journal of Chemical Physics*, 1964, **40**, 911-913.
45. R. A. Álvarez-Puebla, *The Journal of Physical Chemistry Letters*, 2012, **3**, 857-866.
46. S. Guha, P. Steiner and W. Lang, *Journal of Applied Physics*, 1996, **79**, 8664-8668.
47. S. L. Zhang, Y. Hou, K. S. Ho, B. Qian and S. Cai, *Journal of Applied Physics*, 1992, **72**, 4469-4471.
48. D. Lin-Vien, N. B. Colthup, W. G. Fateley and J. G. Grasselli, *The Handbook of Infrared and Raman Characteristic Frequencies of Organic Molecules*, Elsevier Science, 1991.
49. Y. Astuti, Newcastle University, 2014.
50. S. E. Hunyadi and C. J. Murphy, *Journal of Materials Chemistry*, 2006, **16**, 3929-3935.
51. A. D. McFarland, M. A. Young, J. A. Dieringer and R. P. Van Duyne, *The Journal of Physical Chemistry B*, 2005, **109**, 11279-11285.

Chapter 5

Metal-enhanced Luminescence of Silicon Nanocrystals (SiNCs): Effects of Nanoparticles and Molecular Electron Donors & Acceptors on the Photofading Kinetics

In this chapter, we report investigations of the enhanced PL observed in drop-cast films of silicon nanocrystals (i.e. C_{11}-SiNCs or commercial SiNCs) mixed with either noble metal nanoparticles (Ag, Au) or one-electron donors/acceptors (ferrocene/$FeCl_3$). These experiments are designed to test the hypothesis that electron injection into the SiNCs is responsible for the diminution of the photofading and contributes to the overall PL enhancement. First, we describe the model used to analyse the experimental photofading data. Then, we discuss the changes in the initial and steady-state PL spectra under irradiation with the 488 nm line of an argon ion laser. Then, the reversibility of the photofading process is studied. Furthermore, the photofading curves of the luminescence under continuous wave (CW) irradiation have been fitted with distributed kinetics model. The evidence of injection of electrons into SiNCs under irradiation has been provided by a comparison of the photofading curves in the presence and absence of AgNPs and AuNPs or the one-electron donor.

5.1 Model

The photofading of SiNCs under CW irradiation has been treated previously[1] by an amended version of the original random telegraphing model of Efros & Rosen[2]. Here, we briefly describe the model and state those relationships which are of use in analysing the present data on metal-enhanced luminescence.

$$|0\rangle + n\hbar\omega \overset{W}{\leftrightarrow} |1\rangle \overset{k_a}{\rightarrow} |2\rangle \overset{k_{eh}}{\longrightarrow} |1\rangle \qquad 5.1$$

$$|1\rangle \overset{k_{vr}}{\rightarrow} |1'\rangle \overset{k_{rad}}{\longrightarrow} |0\rangle \qquad 5.2$$

SiNCs are excited from their ground state $|0\rangle$ to an excited state$|1\rangle$ by absorption of 1 or more photons i.e. n photons at a rate W. Autoionization of the particles with a rate constant (inverse lifetime) of k_a produces a charged state $|2\rangle$. The particles may then discharge by electron-hole recombination with a rate constant k_{eh}. The excited state $|1\rangle$ may also undergo vibrational relaxation k_{vr} and radiative decay k_{rad} to produce the measured photoluminescence. The excited state $|1\rangle$ is therefore 'bright' whereas the charged state is expected to be 'dark' because of a rapid non-radiative decay pathway for excited states formed upon absorption of photons by state $|2\rangle$. For simplicity, this pathway is not shown explicitly in the model because it is assumed that the internal quantum yield for 'dark' particles in state $|2\rangle$ is zero. The measured radiative lifetime is $k_{rad} \backsimeq$ 20 µs (modal value);[3] the rates of absorption and emissions are therefore much faster than the rate of the ionisation (of order of 100 ms) and recombination processes (minutes) and the applied light field rapidly establishes a quasi-equilibrium between the ground and excited states $|0\rangle$ and $|1\rangle$. The kinetic equations describing the photofading can be written solely in terms of the ionisation ($k_a = T_a^{-1}$) and recombination ($k_{eh} = T_{eh}^{-1}$) rates:

$$\frac{dn_1}{dt} = -\frac{n_1}{T_a} + \frac{n_2}{T_{eh}} \qquad 5.3$$

Where n_1 and n_2 are the populations of the neutral excited state and the dark charged state, respectively. T_a and T_{eh} present the characteristic decay times for autoionization and electron-hole recombination, respectively. In the limit $kt \to \infty$ we showed that[1]:

$$\tau^{-1} = \frac{1}{T_a} + \frac{1}{f[I(\lambda);\lambda]T_{eh}}\ ; or\ k = k_a + \frac{k_{eh}}{f} \qquad 5.4$$

and

$$\frac{T_a}{f[I(\lambda;\lambda]T_{eh}} = \frac{I_\infty}{I_0 - I_\infty} \qquad 5.5$$

$f[I(\lambda;\lambda]$ is the ratio of excited stats $|1\rangle$ to ground states $|0\rangle$ at long times and is an increasing function of intensity, I, and a decreasing function of wavelength, λ, as a result of the absorption spectrum of alkylated SiNCs.[4] In equation 5.5 the initial, I_0, and steady-state, I_∞, intensities are defined as the integrals of the intensity over the

spectrum of the emitted light excluding elastically-scattered light. The quantity f is not easy to measure experimentally because it would require an absolute measure of the light emitted from the focal volume as well as that collected by the objective. However, it is clear from equation 5.4 and 5.5 that the rate constant k extracted from the photofading curves is related to both k_a and k_{eh} and the steady-state PL intensity is proportional to k_{eh}/k_a.

We have previously[1] shown that it is possible to estimate the function f and make a quantitative analysis of k_a and k_{eh} as long as $k_a \gg k_{eh}$. In the case of metal-enhanced PL, we find that k_{eh} increases and therefore a separate determination of k_a and k_{eh} is subject to large uncertainties. Nevertheless, it is clear that the observed rate constant k extracted from the photofading curves increases if k_{eh} increases. It is also clear that the steady-state PL intensity increases as k_{eh} increases and the ratio I_0/I_∞ decreases.

5.2 Fading photoluminescence and luminescence spectra of alkylated SiNCs and their mixtures with metal nanoparticles and molecular electron donors & acceptors

The decay of the luminescence of SiNCs and their mixtures were investigated using a confocal Raman microspectroscopy. When the sample is irritated by 488 nm wavelength light, the intensity of luminescence is detected at each time point and plotted against the time. The spectra were recorded every 1 second for a time period of 300 seconds. The wavenumber range was chosen from 200 to 7000 cm^{-1} in order to exclude the reflected light. The photoluminescence decay of SiNCs was measured first so that the other mixtures of metal nanoparticles or the electron donors/acceptors can be compared. This measurement was repeated for each sample. The preparation method of the films on glass slides by drop-cast technique is given in more details in (Chapter 2, section 2.3.10).

Figure 5.1 exhibits a typical dark field image of C_{11}-SiNCs and C_{11}-SiNCs containing (1:5) AgNPs, (10:50) AgNPs, 0.41 mM AuNPs, 1 mM $FeC_{10}H_{10}$ and 1 mM $FeCl_3$ drop-casted onto a glass coverslip. Figure 5.2 and figure 5.3 show the temporal behaviour of the photoluminescence fading of alkylated SiNCs and their mixtures with metal nanoparticles (Ag, Au) and one-electron donors/acceptors (ferrocene/$FeCl_3$). It was observed that the initial intensity of the luminescence is large (I_0) when the CW

laser light is first incident on the film of C_{11}-SiNCs and their mixtures. As $kt \rightarrow \infty$, the I_0 decays to a steady-state value I_∞. It was observed that the irradiation time of 5 minutes is enough to reach the steady-state. The population of emissive SiNCs decays to a limit due to the ratio of charged particles (dark state) to excited particles (bright state) increases until steady state is achieved where the rates k_a (charging) and k_{eh} (recombination process) are balanced. These observations are similar to those of Rostron *et al*[1].

The time dependence of photoluminescence fading curves have been fitted using double exponential equation (5.7) which presented in section 5.4. However, in order to present the quality of the fitting equation (5.7), figure 5.4 displays the intensity residual of the alkylated silicon nanocrystals with their mixtures of noble metal NPs and the one-electron donors/acceptors. The intensity residuals of C_{11}-SiNCs and their additives show that the equation of the fitting (5.7) matches well with the raw data. This is the main reason of showing the intensity residual in this work.

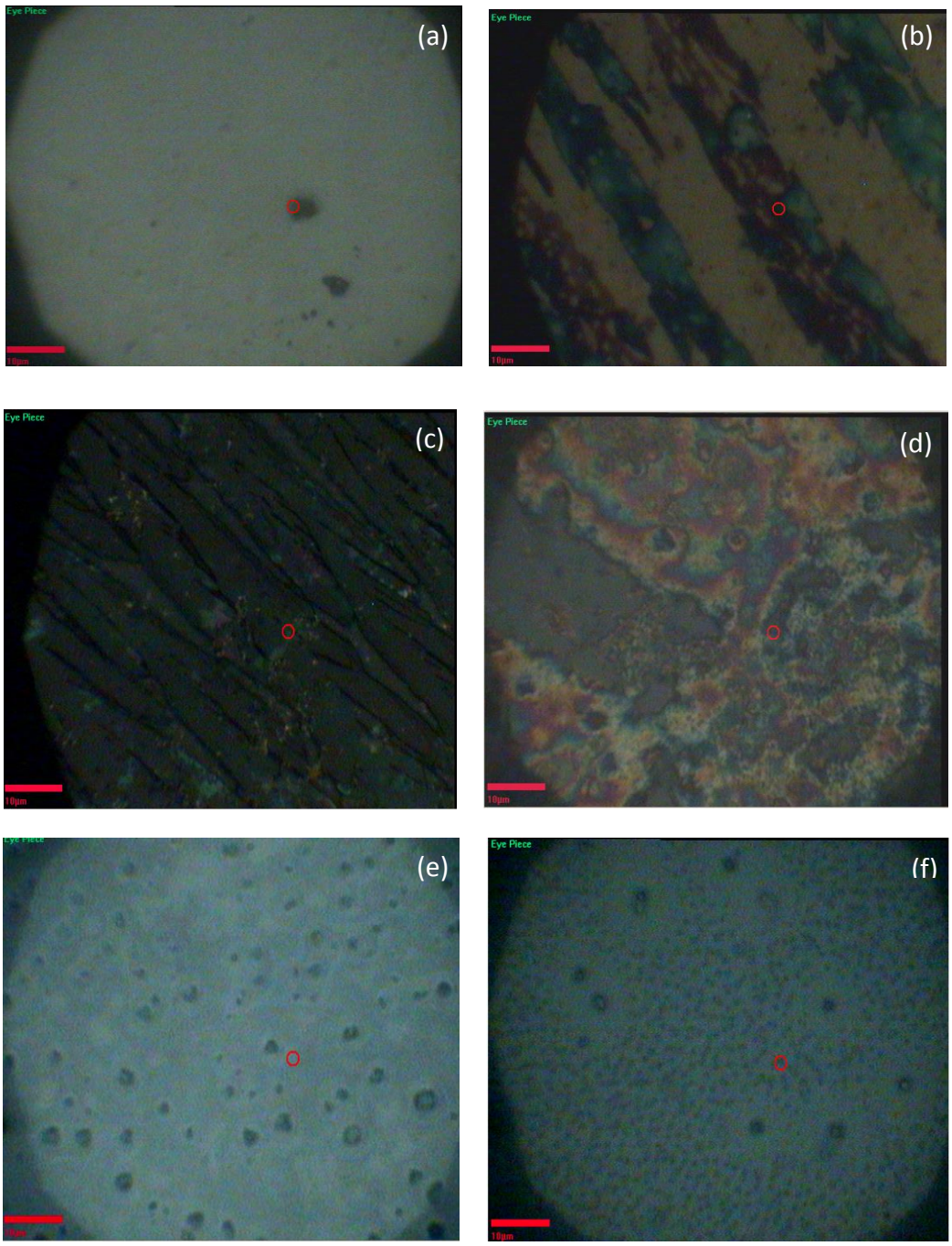

Figure 5.1: Reflected light images of (a) C_{11}-SiNCs, C_{11}-SiNCs containing (b) (1:5) AgNPs, (c) (10:50) AgNPs, (d) 0.41 mM AuNPs, (e) 1 mM $FeC_{10}H_{10}$ and (f) 1 mM $FeCl_3$ drop-cast on glass coverslip. The scale bar = 10 µm.

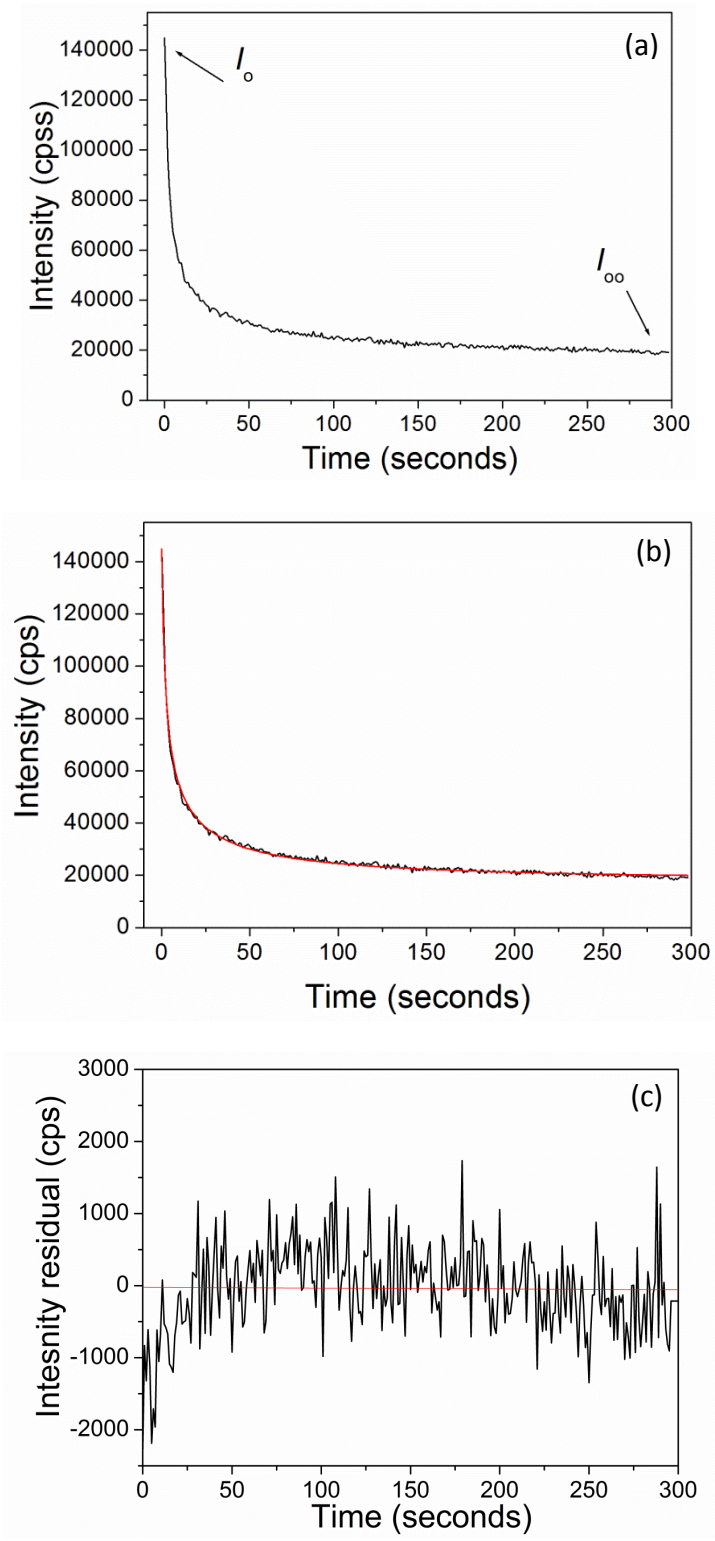

Figure 5.2: (a) Time-dependent photoluminescence of C_{11}-SiNCs presenting the decay of intensity I from initial intensity I_0 to a steady-state value I_∞. The excitation wavelength = 488 nm. (b) Fit of the intensity I over time which recorded at λ = 488 nm to equation (5.7). The black curve is the raw data while the red curve is the fitted data. (c) Plot of the intensity residual $I(t) - I_{fit}(t)$ as a function of time with slope - 0.108 ± 0.399 cps^2.

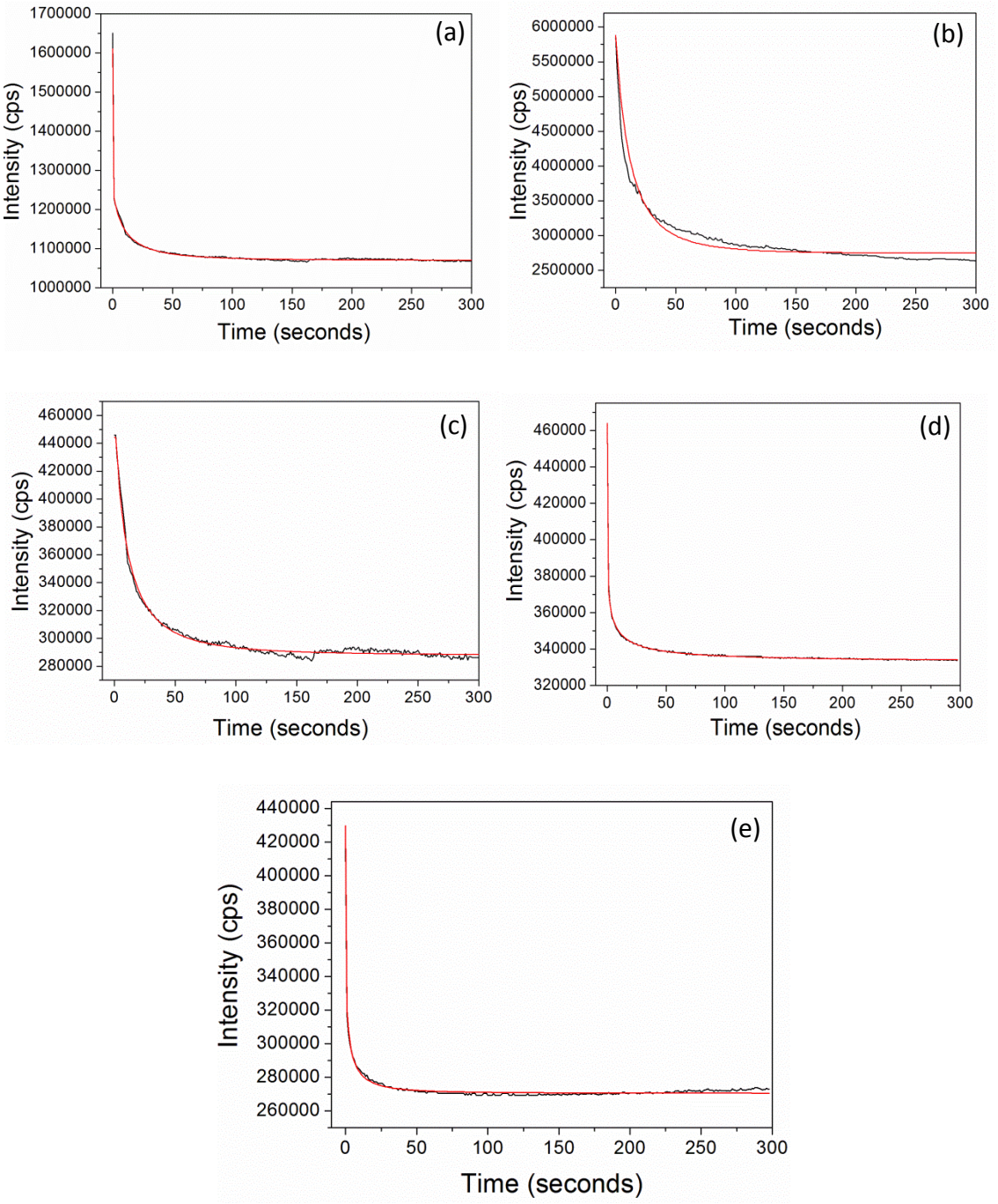

Figure 5.3: Time-dependent photoluminescence of C_{11}-SiNCs containing (a) (1:5) AgNPs, (b) (10:50) AgNPs, (c) 0.41 mM AuNPs, (d) 1 mM $FeC_{10}H_{10}$ and (e) 1 mM $FeCl_3$ showing the decay of intensity I from initial intensity I_0 to a steady-state value I_∞. The excitation wavelength = 488 nm. The black curve is the raw data while the red curve presents the fit of the intensity I over time recorded at λ = 488 nm to equation (5.7).

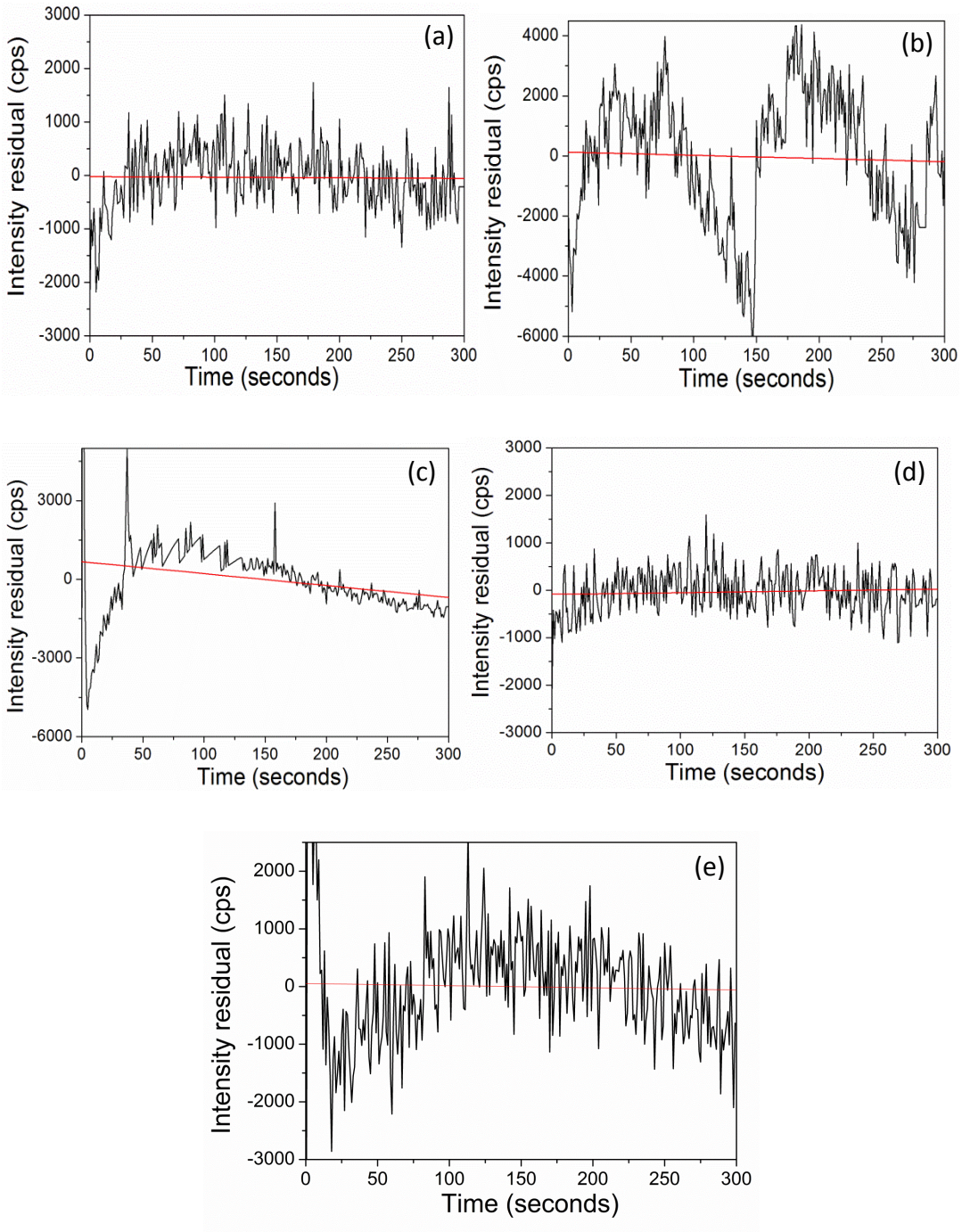

Figure 5.4: Plot of the intensity residual $I(t) - I_{fit}(t)$ as a function of time of C_{11}-SiNCs containing (a) (1:5) AgNPs with slope 0.117 ± 0.489 cps^2, (b) (10:50) AgNPs with slope 0.352 ± 0.317 cps^2, (c) 0.41 mM AuNPs with slope - 1.051 ± 1.459 cps^2, (d) 1 mM $FeC_{10}H_{10}$ with slope - 4.533 ± 1.134 cps^2 and (e) 1 mM $FeCl_3$ with slope 0.370 ± 0.770 cps^2.

An investigation of PL spectra at different times during the decay period shows clear evidence that the PL fading is originated by a physical process rather than any chemical reaction. Figure 5.5 and figure 5.6 show PL spectra of C_{11}-SiNCs and their

mixtures with metal nanoparticles and molecular electron donors & acceptors which shown in figure 5.2 and figure 5.3 at the commencement of irradiation, after 100 s and after 300 s, when the intensity I has nearly reached its steady state limit. Table 5.1 shows the scale factor and the offset when the time = 100 seconds and time = 300 seconds in order to facilitate comparison for each investigated samples. After normalization, it is clear that the PL spectra are identical with respect to shape and position. In addition, it is not expected that the chemical reaction occurs when the laser light exposed to the SiNCs and their mixtures with nanoparticles and molecules. This is because the PL spectra should change if any chemical process happens. Subsequently, figure 5.5 and figure 5.6 are showing that each spectrum at different time points has the same shape, so no chemical reaction is occurring, only the intensities change; except for $FeCl_3/C_{11}$-SiNCs mixture which has a red shift after 100 seconds and 300 seconds.

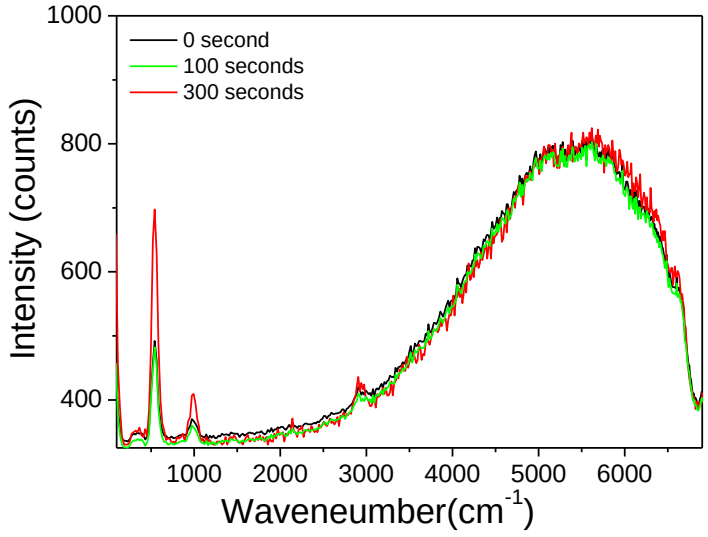

Figure 5.5: PL spectra of C_{11}-SiNCs recorded at 0 s (black curve), 100 s (green curve) and 300 s (red curve). The laser light λ = 488 nm. The spectra recorded at t = 100 and 300 s have been shifted higher by 300 and 335 counts and multiplied by 2.2 and 2.4 respectively to simplify comparison.

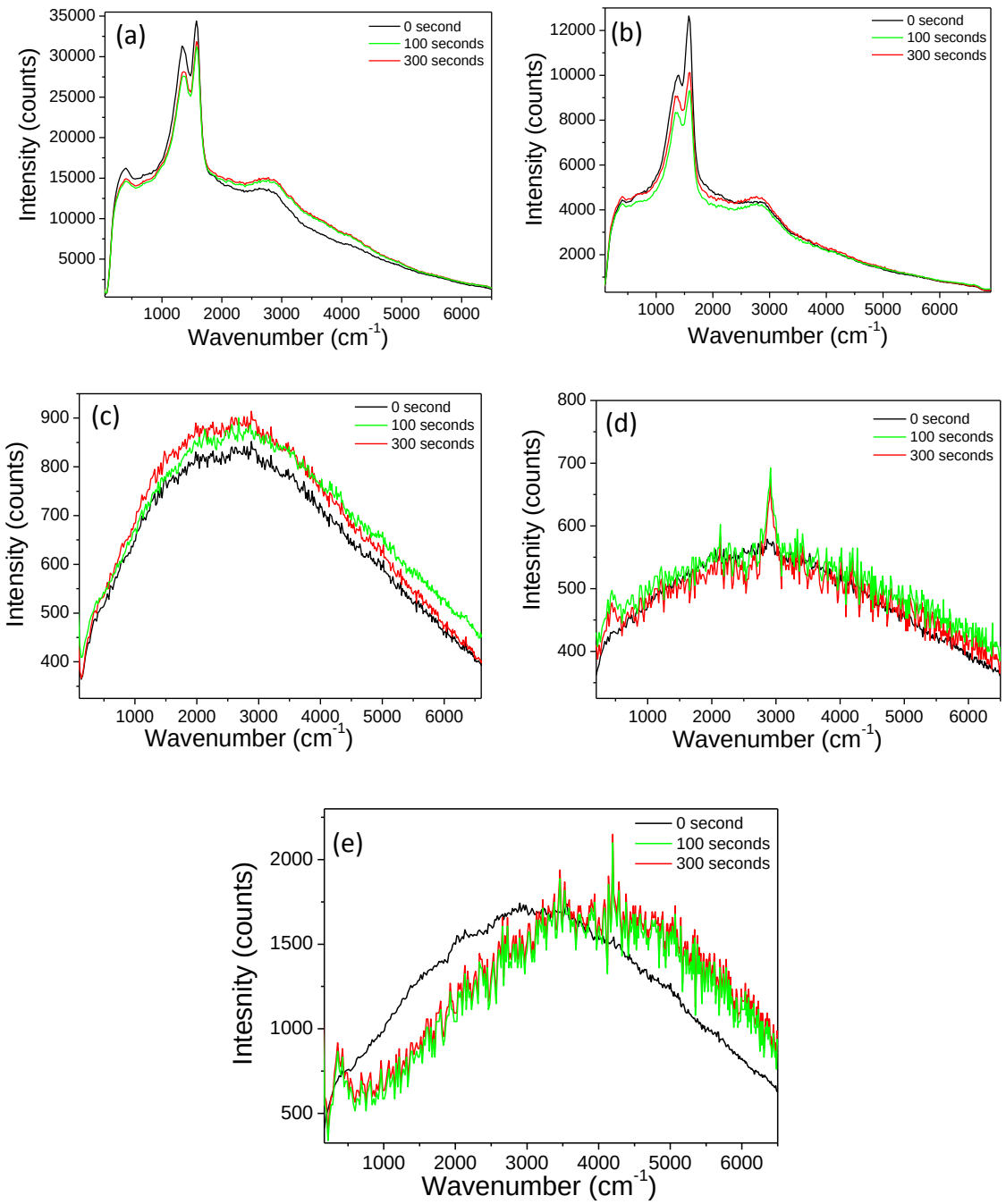

Figure 5.6: PL spectra of C_{11}-SiNCs containing (a) (1:5) AgNPs, (b) (10:50) AgNPs, (c) 0.41 mM AuNPs, (d) 1 mM $FeC_{10}H_{10}$ and (e) 1 mM $FeCl_3$. The spectra recorded at 0 s (black curve), 100 s (green curve) and 300 s (red curve). The laser light λ = 488 nm.

Investigated Samples	Scale factor Time = 100 s	Offset Time = 100 s	Scale factor Time = 300 s	Offset Time = 300 s
(1:5) AgNPs/C_{11}-SiNCs	1	300	1.02	335
(10:50) AgNPs/C_{11}-SiNCs	1.12	300	1.32	335
0.41 mM AuNPs/C_{11}-SiNCs	1	300	1.89	350
1 mM $FeC_{10}H_{10}$/C_{11}-SiNCs	7.5	320	7.8	330
1 mM $FeCl_3$/C_{11}-SiNCs	3.5	300	3.9	320

Table 5.1: The scale factor and the offset values of normalization PL spectra of the investigated samples when time= 100 seconds and time= 300 seconds.

As mentioned above that figure 5.5 and figure 5.6 show the luminescence spectra at various times irradiation for SiNCs films and films containing mixtures of SiNCs and Ag or Au NPs and (ferrocene/$FeCl_3$). The spectra for drop-cast films of SiNCs alone show the characteristic feature of SiNCs PL – a large Stokes' shift between the excitation line at 488 nm and the emission peak at a Raman shift ≃ 5000 cm^{-1} or 650 nm in terms of wavelength. The Raman band of the Si core is clearly visible at ≃ 515 cm^{-1} and the second order feature at ≃ 960 cm^{-1}.[4] The C-H stretching modes of the C_{11} alkyl capping are present as a weak band just under 3000 cm^{-1}.[5] In bulk Si, the first order Raman band is at 520.7 cm^{-1} and the blue shift in the SiNCs is a known effect of size quantisation on the optical phonons.[6] Together, these Raman & PL features confirm the current samples are consistent with our previous reports.[4, 7-9]

It is clear that there is a substantial increase in overall spectral intensity in the presence of metal NPs, however the AgNPs/C_{11}-SiNCs samples (see figure 5.6a-b) also show intense sharp features due to Raman scattering at 1358 cm^{-1} and 1585 cm^{-1}. These two bands are assigned to bending vibration modes of the CH_2 originating from the carbon chain of SDS molecule used to prepare AgNPs and of the undecyl capping of the SiNCs.[10, 11] Other Raman bands from molecular species employed in the preparation are also visible in figure 5.6a-b; the band at 400 cm^{-1} is assigned to SO_3^-; while the Raman band at around 2850 cm^{-1} associated to C-H stretching vibrations modes of the carbon group of dodecyl sulphate molecule.[11] In addition, the band at ≃ 3000 cm^{-1} in figure 5.6d is assigned to the sp^2C-H stretching mode of ferrocene.[12]

In order to estimate the PL enhancement, we compared the integrated intensity of the spectra between 200 and 7000 cm^{-1} and also integrated over a time of 300s of irradiation. The values in table 5.2 show the ratios of integrated intensity of the various mixtures against the pure alkylated SiNCs spectra, but with the intensity of CH_2 Raman bands subtracted from the integral for the samples containing AgNPs. The CH_2 bending/deformation Raman bands are sufficiently large to account for 20% of the integral intensity in those spectra, but the enhancement are still very substantial up to a factor of ×30 in the case of (10:50) AgNPs sample. This is comparable with enhancements ratios of ×60 and ×50 in other AgNPs/SiNCs systems.[13, 14] However, an effect which we have not accounted for in table 5.2 is the SERS background.[15] This has typically not been accounted for in other estimates of large enhancement factors in the AgNPs/SiNCs system,[13] but it may be significant. A crude estimate was obtained from control experiments in which samples of nanocrystalline commercial silicon powder (SiNCs: mean particle diameter ≃ 65 nm) were mixed with AgNPs (1:5) and AgNPs (10:50) in the same manner as for alkylated SiNCs. The PL spectra of commercial SiNCs in these mixtures were similar in appearance to those of AgNPs/C_{11}-SiNCs (see section 5.7), but with an integrated intensity of ≃ 30% of the AgNPs (1:5)/C_{11}-SiNCs sample and ≃ 18% of the AgNPs (10:50)/C_{11}-SiNCs sample respectively. We interpret these spectra as being dominated by the SERS background – they do not show the same photofading ($I_o/I_\infty \simeq 1.1 \pm 0.3; n = 10$) as commercial SiNCs– and assume that the contribution of the SERS background to the enhancement factors in table 5.2 is approximately 30% of the AgNPs (1:5)/C_{11}-SiNCs sample and 18% of the AgNPs (10 mM)/C_{11}-SiNCs sample. The PL enhancement in the presence of AuNPs of similar size (the average diameter = 20 nm)[16] is an order of magnitude lower. We attribute this to the unfavourable longer wavelength of the plasmon band in AuNPs i.e. 520 nm compared to AgNPs i.e. 400 nm; the optimal situation for SERS, and likely for metal-enhanced PL also, is that for which the wavelength of the incident light is to the low energy side of the plasmon resonance.[17]

	C_{11}-SiNCs	+ (1:5) AgNPs	+ (10:50) AgNPs	+ 0.41 mM AuNPs	+ 1 mM Ferrocene	+ 1 mM $FeCl_3$
Replicates:	(n = 12)	(n = 17)	(n = 15)	(n = 9)	(n = 10)	(n = 11)
PL enhancement	1.0	14 ± 2	39 ± 8	3.4 ± 0.4	5.1 ± 0.5	0.7 ± 0.2

Table 5.2: Photoluminescence intensity for alkylated SiNCs under irradiation at 488 nm from an argon ion laser and in the presence of noble metal nanoparticles and one-electron donors/acceptors. The intensity reported is $\int_0^{300} I\,(t)dt$, i.e., the spectral intensity I integrated over the full range of the wavenumbers (excluding elastically scattered light) and over a period of 5 min of irradiation. The enhancement factors have been corrected to exclude the SERS bands, but as discussed in the text, may overestimate the real enhancement because of the presence of the SERS background.

However, the most obvious difference between the spectra in the presence of AgNPs and their absence is the very large blue shift around 3500 cm^{-1} of the emission maximum (see figure 5.6a-b). The coupling of the plasmon resonance to excited states of the alkylated SiNCs will be more effective for those states near the laser energy, therefore we suggest that the observed PL corresponds to emission from states at energies higher than those responsible for the usual 658 nm emission band of the pure alkylated SiNCs. For both AgNPs/C_{11}-SiNCs and AgNPs/commercial SiNCs samples, the position and shape of the spectral features are dominated by the optical properties of the AgNPs and difficult to distinguish for SERS background effects. The blue shift is less for the AuNPs (although still large $\backsimeq$ 2500 cm^{-1}), because the plasmon resonance is at lower energy (λ = 520 nm) than the laser (λ = 488 nm) as shown in figure 5.6c. Nevertheless, it is clear that simple mixtures of alkylated SiNCs with noble metal nanoparticles yield substantial increases in the intensity of emitted/scattered light. In the following sections, we observe in more detail the effects of these metal nanoparticles on the photofading kinetics and discuss their role as electron donors. In addition, we have obtained spectra for two molecular species (ferrocene and $FeCl_3$) which can act as an electron donor and acceptor respectively, but do not possess the

plasmon resonance typical of metals. Interestingly, there is also blue shift (≃ 2000 cm^{-1}) in the PL spectrum of alkylated SiNCs in the presence of the one-electron donor ferrocene as well as a substantial ×5 enhancement of the PL. Ferrocene is stable in the Fe(II) and Fe(III) states; ferrocene, the Fe(II) state is orange in colour with only a very weak absorption tail in the blue region of the visible spectrum, but ferrocenium, the Fe(III) state formed upon electron loss, has a substantial absorption in the red at about 620 nm (ε ≃ 350 M^{-1} cm^{-1}).[18] It is therefore possible that the apparent blue shift is simply a result of self-absorption of the long wavelength emitted light in the sample film. Neither ferrocene itself nor $FeCl_3$was not observed to show any PL.

5.3 Reversibility of the photofading of alkylated SiNCs

Figure 5.5 and 5.6 also illustrate the evolution of the PL spectra with irradiation time. In each sample, the spectra are scaled so that the maximum intensity is 1.0 irrespective of the time; this facilities comparison of the shape of the spectra at different times of irradiation. In figure 5.5 the 3 curves corresponding to the initial, $t = 100s$ and $t = 300s$ spectra superimpose closely, except for the Raman bands previously discussed at 515, 960 and ≃ 3000 cm^{-1} which are time-independent and therefore are enhanced at $t = 300s$ by the scaling applied to the PL. The lack of any changes in spectrum has reported previously[1] and is simply interpreted in terms of the model if state $|2\rangle$ is entirely dark and the PL is entirely due to state $|1\rangle$ via the sequence of equation 5.2. In other words, all that changes during the photofading experiment is the population of state $|1\rangle$.

Figure 5.7 shows also that the PL recovers after a period in which the irradiation is interrupted; the reversibility of the photofading and the lack of changes in the spectra support our interpretation that the fading is a physical rather than a chemical process. Therefore, no chemical reaction occurs to SiNCs during the irradiation time, such a reaction would be an irreversible at room temperature and would also change the PL spectrum through introduction of defect states or a reduction in the size of Si core. The model we apply instead interprets these effects as a reversible charging of the alkylated SiNCs and this possibility is supported by previous observations of reversible charging/discharging in X-ray photoemission experiments.[19]

The laser was switched on for 300 seconds then turned off for 60 seconds and then was repeated twice for a similar time. It was observed that the second initial intensity is less than the previous initial luminescence due to that all the particles do not recover while the laser switches off as also observed by Rostron *et al*[1]. It is known that the majority of alkylated SiNCs become charged at the focal point when the photoluminescence reached the steady-state where the SiNCs under CW irradiation. In contrast, the electron-hole recombination dominates when the CW laser light is switched off.

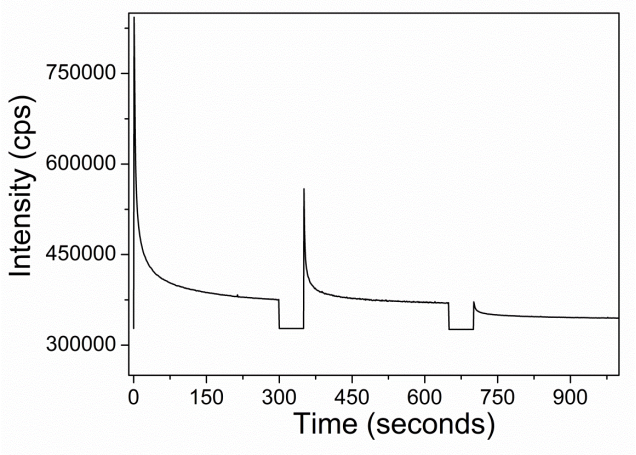

Figure 5.7: Intensity against time for photofading of C_{11}-SiNCs under irradiation with the 488 nm line of an argon ion laser. The intensity plotted is the integral of the spectrum at each time point over the wavenumber range 200-7000 cm^{-1}. At $t = 300s$ the irradiation was interrupted for 60s by closing the shutter (the intensity in this period is simply the integral of the dark counts on the CCD which has not been subtracted). When the shutter was reopened at 360s some of the initial intensity was regained.

In mixtures of C_{11}-SiNCs with AuNPs (figure 5.6c) or C_{11}-SiNCs with ferrocene (figure 5.6d) we also find PL spectra which are independent of irradiation after scaling, although a small tail appears on the low energy side of the $t = 300s$ spectrum for AuNPs/C_{11}-SiNCs. The interpretation of the AgNPs/C_{11}-SiNCs spectra (figure 5.6a-b) is less clear-cut because of the substantial contribution from SERS bands; however these spectra are still consistent with the simple model. The case of $FeCl_3$/C_{11}-SiNCs sample is different; there is a substantial redshift ($\simeq$ 1000 cm^{-1}) under irradiation and this sample clearly has a more complex behaviour than the model of equation 5.1 and 5.2.

5.4 Dispersed kinetics of photofading

Figure 5.2 and figure 5.3 show typical examples of photofading experiments; under CW irradiation the PL intensity decays with time. The connection between the photofading of ensembles of QDs and the statistics of the blinking phenomenon has been explored in the case of (CdSe)ZnS core-shell particles.[20] We prefer to fit the photofading curves directly to extract the rate constant k which describes the fading using a distributed kinetics model which generalises the simple first order kinetics of the random telegraphing model of NCs blinking described above (section 5.1). In previous work, we have shown that a simple long-normal distribution of k, i.e., a Gaussian distribution of activation energies, provides a satisfactory regression model.[1] In this project, we show that the same model also can be fitted to the photofading curves in the presence of metal NPs (Ag, Au) and iron-based electron donors and acceptors (ferrocene, $FeCl_3$).

The dispersed kinetics treatment is preferred over multiexponential or stretched-exponential models for the reasons discussed in[1, 21]. In brief, it is natural to expect a distribution of rates for heterogeneous system such as NCs and the parameters obtained in the regression analysis have a clearer physical meaning than the rate constant or lifetimes extracted from multiexponential fits or the parameter β from a stretched exponential expression such as $e^{-\left(\frac{t}{\tau}\right)^{\beta}}$. In addition, the dispersed kinetics treatment has fewer floating parameters (amplitude, mode and width of the distribution) than even a double exponential fit (two amplitudes and two lifetimes).

According to the model on which we base the analysis, each SiNCs may be either bright or dark according to whether it is uncharged or has undergone photoionization[1] and the concentrations of bright particles is proportional to the intensity of the luminescence, I. A first check that the model is consistent with the experimental data can be made by comparing the spectra obtained upon initial radiation and at longer times. Figure 5.5 and figure 5.6 show that, as expected, the spectra change in the intensity, but do not change shape with extended times of irradiation. It is therefore consistent to interpret them in terms of the population of bright ($|1\rangle$) and dark ($|2\rangle$) states described in the theoretical model.

If I_0 is the luminescence intensity at the commencement of irradiation and I_∞ is the steady-state intensity, the decay of I_0 to I_∞ is modelled by a lognormal distribution of rate constant k which represents the heterogeneity in the sample. The parameter $\langle k \rangle$ is the most probable value of the rate constant for the first order photofading and γ is the spread of the Gaussian distribution of Gibbs energies for the reaction in units of RT:

$$\Delta G = \Delta G - \gamma RT\, x \quad and\ P(x) = \frac{1}{\sqrt{x}}\, e^{-x^2} \qquad 5.6$$

The distribution of the rate constant is obtained from: $k = \langle k \rangle\, e^{\gamma x}$ and the regression model which was employed to analyse the data is the first order decay of bright states averaged over the Gaussian distribution:

$$I = \frac{(I_0 - I_\infty)}{\sqrt{\pi}} \int_{-\infty}^{\infty} e^{-x^2}\, e^{-kte^{\gamma x}} dx + I_\infty \qquad 5.7$$

The model was fitted to the data using the Levenberg-Marquardt method and an extended Simpson's rule using 100 integration points was used to evaluate the integral on the range $u\,[-1, 1]$ after making the transformations $lnu = x$ and splitting the original range into $[-\infty, 0]$ and $[0, \infty]$. Four parameters were extracted from the fitting of equation 5.7 to the photofading curves: I_0 , I_∞ , $\langle k \rangle$ and γ. Tables 5.3 and 5.4 show the values of these parameters for six types of sample and their means and standard deviation over a number of replicate experiments. In addition, we report the time-integrated intensity over a period of 300 seconds irradiation $\int_0^{300} I dt$ and the ratio of the initial and steady-state intensities, I_0/I_∞.

The curves in figures 5.2b and 5.3 have been normalised by I_∞ in order to display all the data together. The residual is shown on each trace and for most of the samples, we found a good fit of equation 5.7 to the data, as judged by a small residual ($\simeq$ 1%) which showed no systematic deviations from zero (see figure 5.2c and 5.4). The exceptions to this were photofading curves for the AgNPs (10 mM)/C_{11}-SiNCs samples (5.3b) in which systematic deviations were typically observed. We suggest that these are related to heating effects in the confocal volume. This is due to that AgNPs (10 mM)/C_{11}-SiNCs sample has a biggest enhancement comparing with other sample (see figure 5.6). Thus, the heating effect is generated as a result of the enhancement in the

SERS intensity of AgNPs (10 mM)/C_{11}-SiNCs sample as observed by Liang *et al*.[22] They assigned the heating effects in the confocal volume to the significant enhancement in the Raman intensity caused by AgNPs.

5.5 Effect of metal nanoparticles on the photofading kinetics of alkylated SiNCs

The presence of either AgNPs or AuNPs in a simple mixture with alkylated SiNCs produces a substantial enhancement of the integrated intensity, up to ×30 in the case of alkylated SiNCs mixed with 10 mM $AgNO_3$ preparation (mean particle size ≃ 30 nm). It is also noteworthy that the extent of photofading, measured by the ratio I_0/I_∞ is substantial less in the presence of metal NPs. The normal explanation for the PL enhancement by metal NPs is in terms of the efficient coupling of the excitation light to the SiNCs via the surface plasmon resonance of the metal NPs and of the coupling of the emissive states to the NPs. SiNCs have a relatively low absorbance at 488 nm, but the absorption coefficient of metal NPs near the plasmon resonance is known to be very large and so long as the SiNCs are within the range of the near-field at the metal surface, the rate of absorption can be much greater. However, such an effect does not account for the observation of a smaller I_0/I_∞ ratio in the presence of NPs; in fact, this ratio might be expected to increase because the rate of photoionization depends on the number of SiNCs in an electronic excited state. If the rate of recombination does not increase proportionally, then the steady-state PL intensity will decrease and the ratio I_0/I_∞ will increase. The decrease in the ratio I_0/I_∞ by a factor of 3-5 in the presence of Ag or Au NPs therefore provides evidence that there is a second mechanism for the enhancement of the PL; we suggest that the metal NPs act as a source/sink for electrons that are transferred to the SiNCs and neutralize the positive charged particle which formed under irradiation and increase the rate of recombination ($k_{eh}\ |2\rangle$). This effect increases the PL because state $|2\rangle$ is dark and only state $|1\rangle$ is emissive.

The metal NPs also have a substantial effect on the kinetics of the photofading; the most probable rate constant describing the decay of the initial intensity towards the steady-state increases and the width of the distribution of rates decreases. The increase in the modal value of the rate constant is quite expected on the basis of the reaction scheme (equations 5.1 and 5.2). In an analogues manner to the well-known

behaviour of chemical reactions near equilibrium, the observed rate constant is the sum of the forward and backward rate constants. In the present case, the system is not at equilibrium, but rather tends towards a steady-state at long times, nevertheless the steady-state is reached more quickly if either the rate of ionization or of recombination increases (equation 5.4). The AgNPs and, to a lesser extent the AuNPs act as sources of electrons and can quench the charge developing on the alkylated SiNCs in the focal volume.

	C_{11}-SiNCs	+ (1:5) AgNPs	+ (10:50) AgNPs	+ 0.41 AuNPs
Replicates:	$n = 12$	$n = 17$	$n = 15$	$n = 9$
10^{-7} x $\int_0^{300} Idt$ / counts	1.96 ± 0.17	34.2 ± 0.50	94.9 ± 7.0	6.62 ± 0.30
10^{-5} x I_0 / cps	1.44 ± 0.21	16.1 ± 0.30	58.6 ± 6.2	4.44 ± 0.28
10^{-5} x I_∞ / cps	0.208 ± 0.044	10.7 ± 0.20	26.9 ± 2.6	2.88 ± 0.10
$\langle k \rangle / s^{-1}$	0.125 ± 0.007	0.368 ± 0.004	0.461 ± 0.004	0.146 ± 0.014
γ	3.60 ± 0.45	2.35 ± 0.55	1.00 ± 0.42	2.47 ± 0.40
I_0/I_∞	6.93 ± 0.64	1.45 ± 0.03	2.16 ± 0.08	2.14 ± 0.14

Table 5.3: Kinetic data from photofading experiments on alkylated SiNCs in the presence of AgNPs and AuNPs.

However, the decrease in the width of the distribution of rates does not follow naturally from the reaction scheme in the same way. Excitation of only localized oxide-relate states at the alkylated SiNCs surface is quite likely to result in a narrower distribution of rates, especially considering that such stats are less sensitive to particle size. The narrowing distribution of the γ could be explained in the following way. Židek *et al*[23, 24] discuss the effect of the surface on the emitting state as there may be many, slightly different emitting states even in a single particle. Also, our group was observed that oxide-rich parts of the C_{11}-SiNCs may have localised states that emit light blue shifted compared to un-oxidized parts of the particle on the surface.[7] This explains why the γ is big for the pure C_{11}-SiNCs because 488 nm light penetrates very

far into SiNCs because the absorbance is rather weak at 488 nm then all the different possible excited states will be excited and emit and so big spread is likely to occur. In the presence of metal nanoparticles i.e. AgNPs and AuNPs, the 488 nm light mostly does not excite the SiNCs directly, but is absorbed by the plasmon band and the near field of the plasmon couples to the SiNCs and excites it. However, the near-field is only strong "near" to the metal particle surface and so maybe can only excite states in the SiNCs near to the metal, i.e. on the surface of the SiNCs. It is then logical that the emission would be has a narrow distribution because only close to surface states, not core states are excited and small spread is likely to happen.

5.6 Effect of one-electron donors and acceptors on the photofading kinetics of alkylated SiNCs

	C_{11}-SiNCs	+ 1 mM ferrocene	+ 1 mM $FeCl_3$
Replicates:	$n = 12$	$n = 10$	$n = 11$
10^{-7} x $\int_0^{300} Idt$ / counts	1.96 ± 0.17	10.0 ± 0.20	1.4 ± 0.18
10^{-5} x I_0 / cps	1.44 ± 0.21	4.64 ± 0.45	4.26 ± 0.17
10^{-5} x I_∞ / cps	0.208 ± 0.044	3.33 ± 0.06	2.17 ± 0.13
$\langle k \rangle / s^{-1}$	0.125 ± 0.007	0.240 ± 0.015	0.150 ± 0.048
γ	3.60 ± 0.45	2.82 ± 0.11	3.17 ± 0.13
I_0/I_∞	6.93 ± 0.64	1.12 ± 0.11	2.15 ± 0.22

Table 5.4: Kinetic data from photofading of alkylated SiNCs in the presence of electron donor or an electron acceptor.

In order to explain the decrease in the ratio I_o/I_∞ by factors of 3-5 in the presence of Ag or Au NPs, we suggest that exchange of electrons occurs between the metal NPs and alkylated SiNCs. This is also an important factor contributing towards the PL enhancement, but cannot easily be distinguished from the usual plasmon-related effects. To test this hypothesis, we prepared mixtures of alkylated SiNCs with molecular donors (ferrocene) and acceptors (ferric chloride). It is important to note

that the concentration of ferrocene and ferric chloride which used during this study is 1 mM. This is because this concentration is sufficient to surround SiNCs with electron donor and acceptor. Thus, the charge transfer process will achieve. Another reason is neither ferrocene itself nor $FeCl_3$was not observed to show any PL. However, ferrocene is a well-known one-electron redox mediator which has rapid self-exchange kinetics and is known to be stable in both Fe(II) and Fe(III) oxidation states. It can therefore act as a source/sink of electrons in the same manner as metal NPs, but without the confounding effects related to the surface plasmon of metal NPs. Table 5.4 shows that ferrocene has a large effect on the ratio I_o/I_∞ which is reduced by a factor of more than 6 compared to the pure C_{11}-SiNCs sample. Another redox species, $FeCl_3$ also reduces this ratio, but as described in section 5.3 has a complicated effect on the PL spectrum. Ferrocene also reduces the spread of the rates γ to similar extent as do large AgNPs (1:5) (mean particle diameter 100 nm) and AuNPs. We suggest that this is because the rate of electron injection into alkylated SiNCs is also a distributed kinetic process and that those particles for which the injection is rapid do not contribute to the photofading.

5.7 Fading photoluminescence and luminescence spectra of commercial SiNCs and their mixtures with metal nanoparticles and molecular electron donors & acceptors

The decay of the luminescence of commercial SiNCs and their mixtures were investigated using a confocal Raman microspectroscopy. When the sample is irritated by CW 488 nm wavelength light, the intensity of luminescence is detected at each time point and plotted against the time. The spectra were recorded every 1 second for a time period of 300 seconds. The wavenumber was chosen from 200 to 7000 cm^{-1} in order to avoid the reflected light. The photoluminescence decay of commercial SiNCs was measured first so that the other mixtures of metal nanoparticles or the electron donors/acceptors can be compared. This measurement was repeated for each sample. The preparation method of the films on glass slides by drop-cast technique is given in more details in (Chapter 2, section 2.3.10).

Figure 5.8 presents a typical dark field image of commercial SiNCs and commercial SiNCs containing (1:5) AgNPs, (10:50) AgNPs, 0.41 mM AuNPs, 1 mM $FeC_{10}H_{10}$ and 1 mM $FeCl_3$ drop-casted onto a glass coverslip. Figure 5.9 and figure 5.10 present the temporal behaviour of the photoluminescence fading of commercial SiNCs

and their mixtures with metal nanoparticles (Ag, Au) and one-electron donors/acceptors (ferrocene/$FeCl_3$). It is observed that the luminescence intermittency of commercial SiNCs follow the similar behaviour of alkylated SiNCs. The time dependence of photoluminescence fading curves have also been fitted using single exponential equation (5.7) in section 5.4. However, in order to display the quality of the fitting equation (5.7), figure 5.11 displays the intensity residual of the commercial SiNCs with their mixtures of noble metal NPs and the one-electron donors/acceptors. The intensity residuals of commercial SiNCs and their additives show that the equation of the fitting matches well with the data. This is the main reason to present the intensity residual in this work.

It can be seen that the ratio of the initial and steady-state intensities (I_0/I_∞) of commercial SiNCs is $\backsimeq$ 1 (table 5.7); while this ratio I_0/I_∞ is up to $\backsimeq$ 7 (table 5.4) for alkyl-capped SiNCs. This significant difference between these two types of SiNCs suggests that the commercial SiNCs are not easy to ionize as the extent of the photofading is very small. This can be explained as a result of the different sizes of SiNCs that used in this work i.e. the average diameter of commercial SiNCs and alkyl-capped SiNCs is 65 nm and 2.5 nm, respectively.

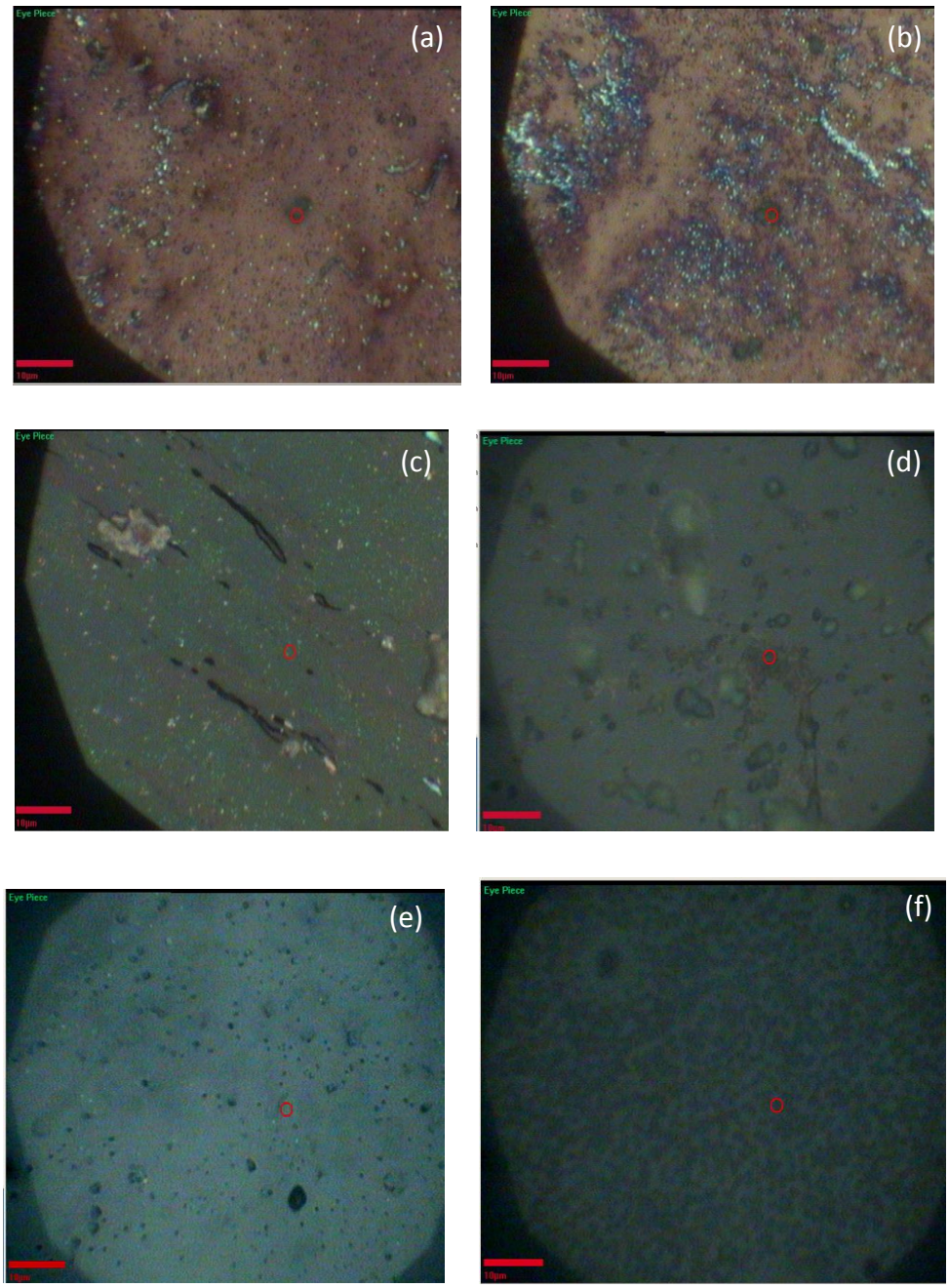

Figure 5.8: Reflected light images of (a) Commercial SiNCs, commercial SiNCs containing (b) (1:5) AgNPs, (c) (10:50) AgNPs, (d) 0.41 mM AuNPs, (e) 1 mM $FeC_{10}H_{10}$ and (f) 1 mM $FeCl_3$ drop-cast on glass coverslip. The scale bar = 10 µm.

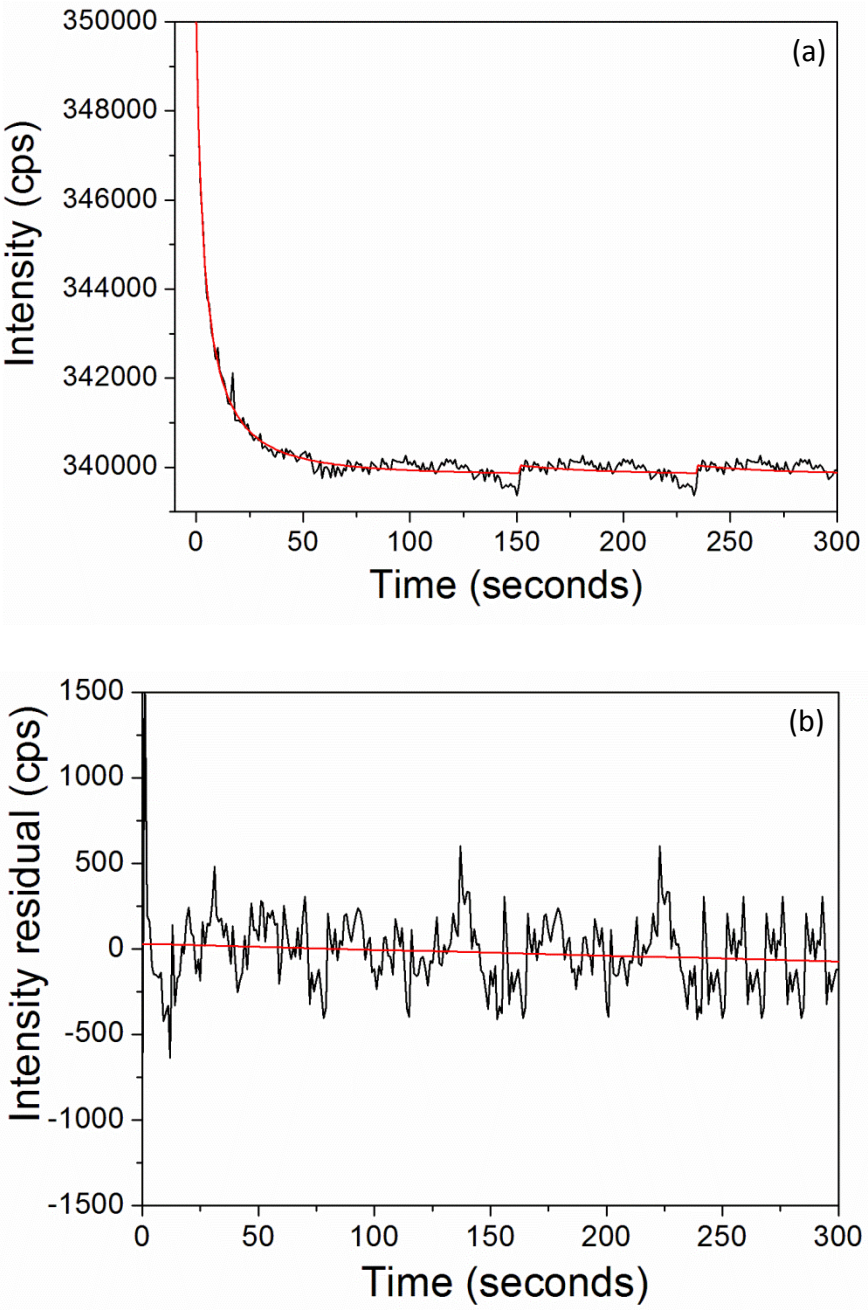

Figure 5.9: (a) Time-dependent photoluminescence of commercial SiNCs presenting the decay of intensity I from initial intensity I_0 to a steady-state value I_∞. The excitation wavelength = 488 nm. The black curve is the raw data while the red curve presents the fit of the intensity I over time recorded at λ = 488 nm to equation (5.7). (b) Plot of the intensity residual $I(t) - I_{fit}(t)$ as a function of time with slope - 0.341 ± 0.148 cps^2.

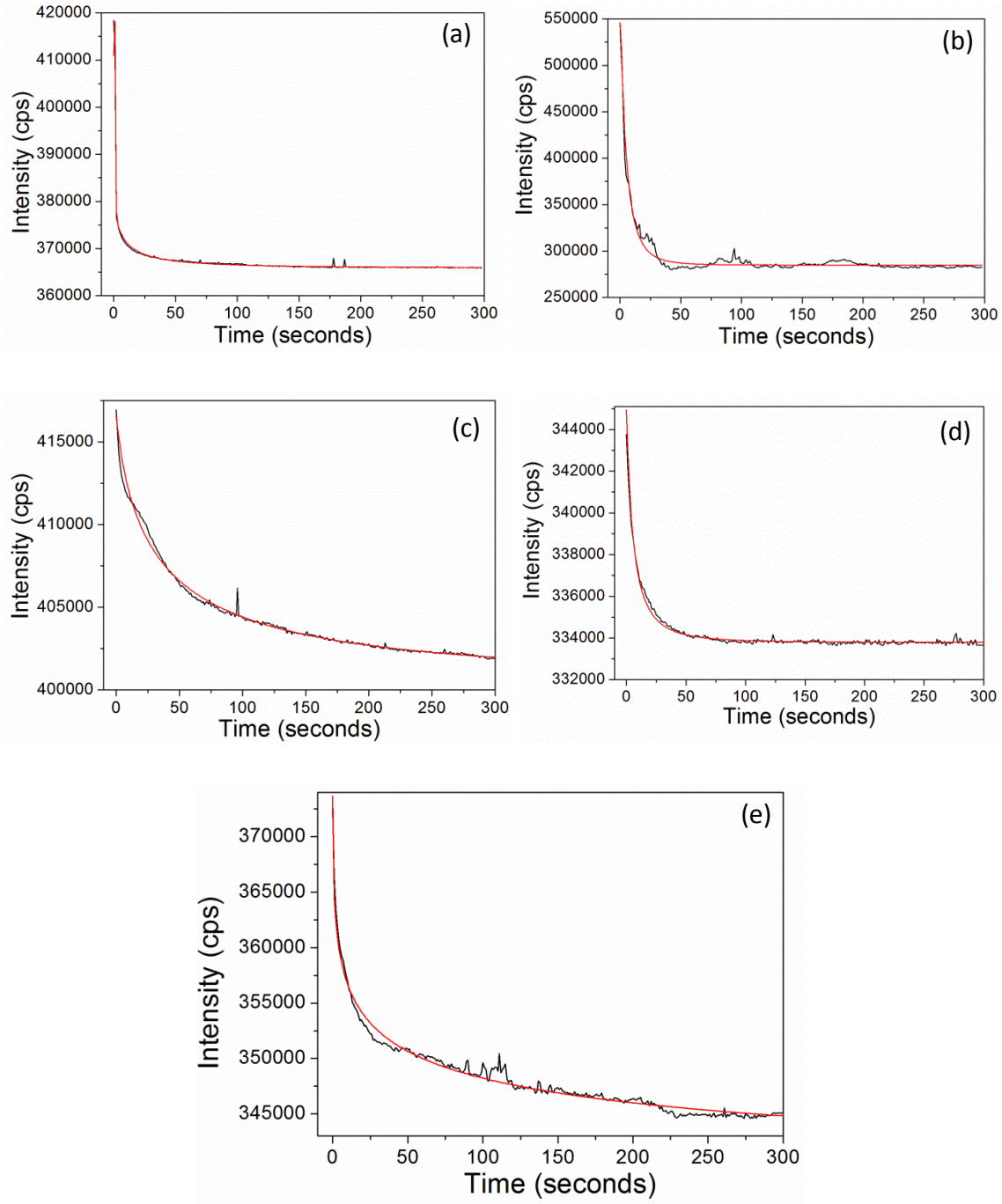

Figure 5.10: Time-dependent photoluminescence of commercial SiNCs containing (a) (1:5) AgNPs, (b) (10:50) AgNPs, (c) 0.41 mM AuNPs, (d) 1 mM $FeC_{10}H_{10}$ and (e) 1 mM $FeCl_3$ presenting the decay of intensity I from initial intensity I_0 to a steady-state value I_∞. The excitation wavelength = 488 nm. The black curve is the raw data while the red curve presents the fit of the intensity I over time recorded at λ = 488 nm to equation (5.7).

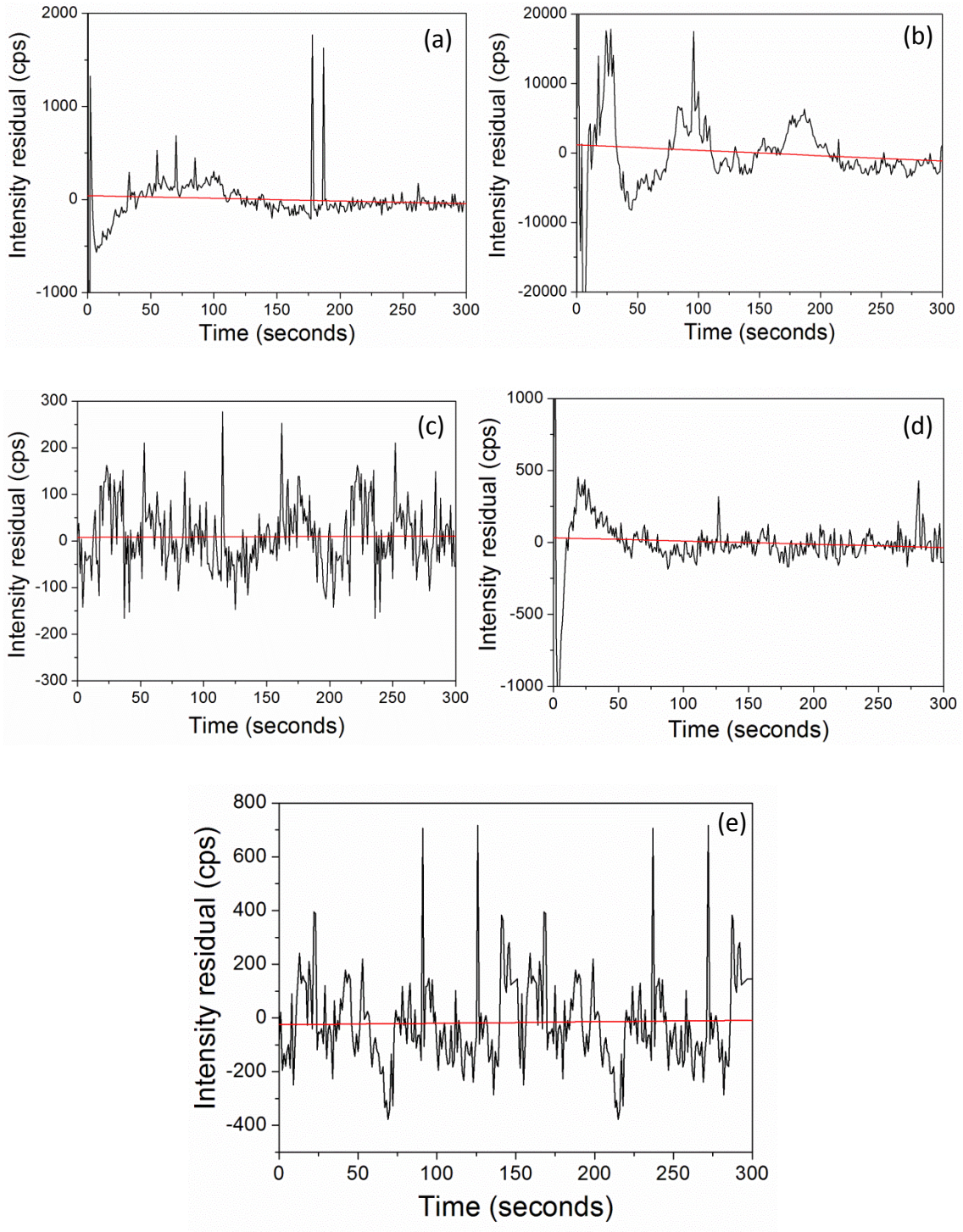

Figure 5.11: Plot of the intensity residual $I(t) - I_{fit}(t)$ as a function of time of commercial SiNCs contain (a) (1:5) AgNPs with slope -7.704 ± 4.769 cps^2, (b) (10:50) AgNPs with slope 0.866 ± 1.212 cps^2, (c) 0.41 mM AuNPs with slope 0.009 ± 0.048 cps^2, (d) 1 mM $FeC_{10}H_{10}$ with - 0.223 ± 0.170 cps^2 and (e) 1 mM $FeCl_3$ with slope 0.056 ± 0.113 cps^2.

Figure 5.12 exhibits the PL spectra at various times after irradiation for commercial SiNCs and films containing mixtures of commercial SiNCs and AgNPs or AuNPs and ferrocene or $FeCl_3$. In this work, it is clear that the PL fading is originated by a physical process rather than any chemical reaction following the same behaviour of C_{11}-SiNCs and their mixtures. Table 5.5 shows the scale factor and the offset when the time = 100 seconds and time = 300 seconds, in order to facilitate comparison for each sample. After normalization, it can be seen that the PL spectra are identical as observed for alkylated SiNCs and their mixtures; with respect to intensities of the peaks. However, it is not expected that the chemical reaction occurs when the laser light exposed to commercial SiNCs and their mixtures with metal nanoparticles and molecules. This is because the PL spectra should change if any chemical process happens. Subsequently, figure 5.12 indicates that each spectrum at different time points has the same shape, so no chemical reaction is occurring, only the intensities change.

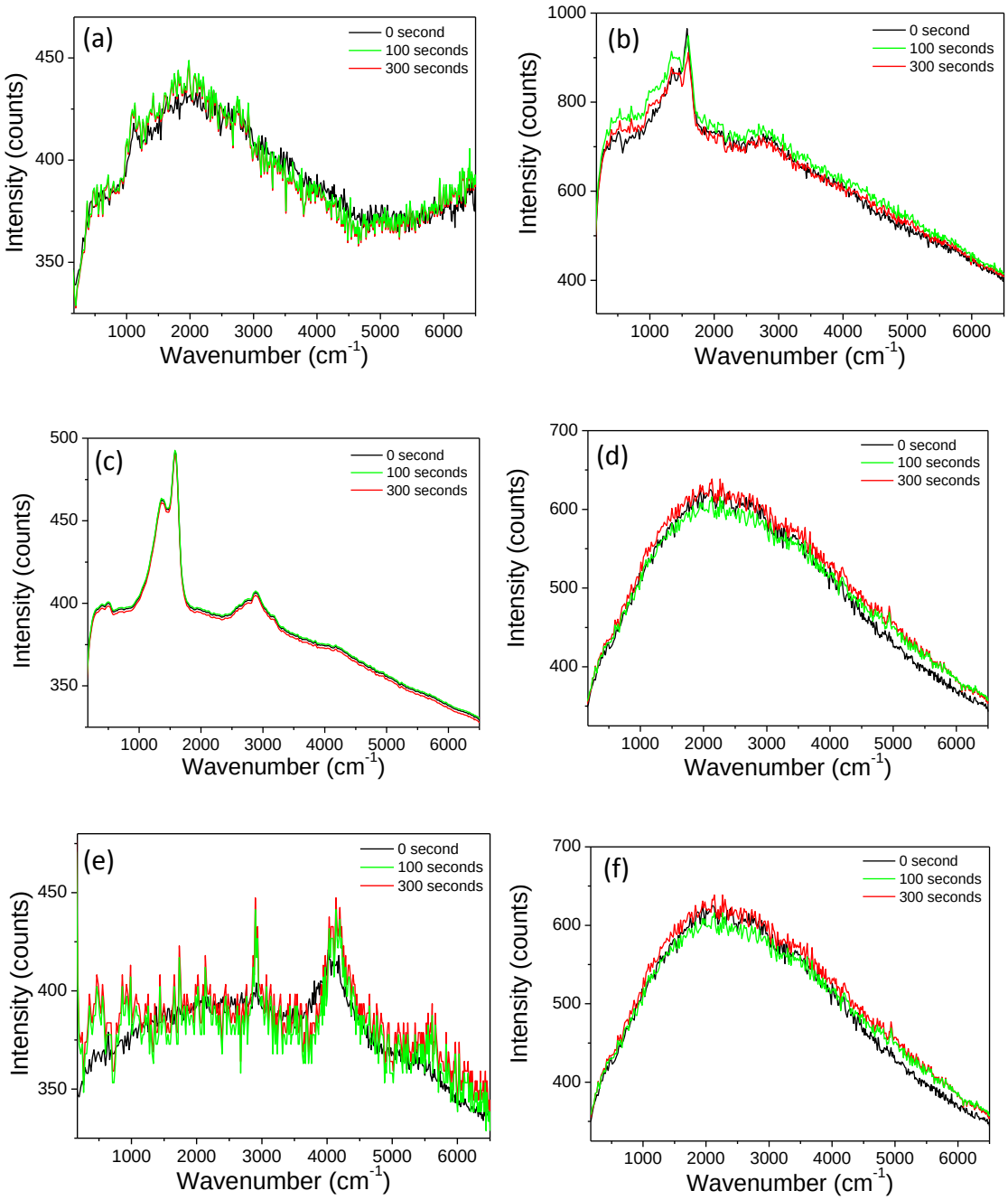

Figure 5.12: PL spectra of (a) Commercial SiNCs, commercial SiNCs containing (b) (1:5) AgNPs, (c) (10:50) AgNPs, (d) 0.41 mM AuNPs, (e) 1 mM $FeC_{10}H_{10}$ and (f) 1 mM $FeCl_3$. The spectra recorded at 0 s (black curve), 100 s (green curve) and 300 s (red curve). The laser light λ = 488 nm.

Investigated Samples	Scale factor Time=100 s	Offset Time=100 s	Scale factor Time=300 s	Offset Time=300 s
Commercial SiNCs	1.6	300	1.9	350
(1:5) AgNPs/SiNCs	1.5	350	1.7	355
(10:50) AgNPs/ SiNCs	1.0	320	1.9	350
0.41 mM AuNPs/ SiNCs	1.0	390	1.1	395
1 mM $FeC_{10}H_{10}$/ SiNCs	5.0	320	5.9	350
1 mM $FeCl_3$/ SiNCs	2.2	315	2.4	320

Table 5.5: The scale factor and the offset values of normalization PL spectra of the investigated samples when time= 100 seconds and time= 300 seconds.

The PL spectrum of commercial SiNCs exhibits peak at 520 cm^{-1} which attributed to bulk Si.[25] The Raman feature at 1100 cm^{-1} can be assigned to Si-O vibration mode.[26] In addition, this Raman peak can be also associated to second order of SiNCs.[7] The large and broad Raman peak which detected at 2330 cm^{-1} (550 nm) refers to the luminescence signals from commercial SiNCs.

It is clear that there is a small increase in overall spectral intensity in the presence of metal NPs, however the AgNPs/SiNCs samples (see figure 5.12b-c) also show intense sharp features due to Raman scattering at 1350 cm^{-1} and 1580 cm^{-1}. These two bands are attributed to bending vibration modes of the CH_2 of SDS molecule.[10, 11] The Raman band at 400 cm^{-1} is attributed to SO_3^-; whereas the Raman peak at about 2850 cm^{-1} assigned to C-H stretching vibrations modes of SDS.[11]

The integrated intensity of the spectra between 200 and 7000 cm^{-1} have been reported in order to measure the PL enhancement. Table 5.6 shows the ratios values of integrated intensity of the various mixtures against the pure commercial SiNCs, but with the intensity of CH_2 Raman bands subtracted from the integral for the samples containing AgNPs. The enhancement is up to a factor of 1.6 in the case of (10:50) AgNPs while the enhancement in the presence of AuNPs of similar size i.e. 20 nm[16] is less. As mentioned previously this is due to the unfavourable longer wavelength of the plasmon band in AuNPs i.e. 520 nm compared to AgNPs i.e. 400 nm; the optimal

situation for SERS, and likely for metal-enhanced PL also, is that for which the wavelength of the incident light is to low energy side of the plasmon resonance.[17]

	Commercial SiNCs	+ (1:5) AgNPs	+ (10:50) AgNPs	+ 0.41 mM AuNPs	+ 1 mM Ferrocene	+ 1 mM $FeCl_3$
Replicates:	(n = 13)	(n = 10)	(n = 9)	(n = 5)	(n = 7)	(n = 6)
PL enhancement	1.0	1.3 ± 0.2	1.6 ± 0.5	1.2 ± 0.4	1.0 ± 0.5	1.0 ± 0.2

Table 5.6: Photoluminescence intensity for commercial SiNCs under irradiation at 488 nm from an argon ion laser and in the presence of noble metal nanoparticles and one-electron donors/acceptors. The intensity reported is $\int_0^{300} I\,(t)dt$, i.e., the spectral intensity I integrated over the full range of the wavenumbers (excluding elastically scattered light) and over a period of 5 min of irradiation. The enhancement factors have been corrected to exclude the SERS bands, but as discussed in the text, may overestimate the real enhancement because of the presence of the SERS background.

Figure 5.12b-c present a large blue shift around 830 cm^{-1} of the emission maximum which indicates the difference between the spectra in the presence of Ag nanoparticles and their absence. As mentioned previously this is due to the coupling of the plasmon resonance to excited states of the commercial SiNCs which will be more effective for those states near the laser energy. Therefore, we suggest that the observed PL corresponds to emission from states at energies higher than those responsible for the usual 550 nm emission band of the pure commercial SiNCs. In addition, this shift is much lower for the AuNPs (around 130 cm^{-1}), because the plasmon resonance is at lower energy (λ = 520 nm) than the laser (λ = 488 nm) as shown in figure 5.12d. Another interpretation of the blue shift is that it corresponds to an enhanced SERS background. However, bearing in mind the recent theoretical description of the SERS background in terms of coupling of the plasmon resonance to virtual states in the scatterer[27] these two explanations are very similar and the precise nature of the transitions responsible cannot be determined from steady-state measurements. Nevertheless, it is clear that simple mixture of commercial SiNCs with noble metal nanoparticles yield substantial increases in the intensity of

emitted/scattered light. However, this phenomenon is constant for alkylated SiNCs when they mixed with metal NPs. In the following sections, we observe in more details the effects of those metal nanoparticles on the photofading kinetics and discuss their roles as electron donors.

We have also detected the PL spectra for ferrocene and $FeCl_3$ which can act as an electron donor and acceptor respectively, but do not possess the typical plasmon resonance of metals (see figure 5.12e-f). Figure 5.12e shows Raman peak at 4032 cm^{-1} which attributed to C-H stretching mode of ferrocene.[12] However, there is a red shift ≃ 590 cm^{-1} in the PL spectrum of commercial SiNCs in the presence of the one-electron donor (ferrocene), while there is a blue shift ≃ 100 cm^{-1} in the PL spectrum of the sample contains one-electron acceptor ($FeCl_3$) as presented in figure 512e-f. As discussed previously in the case of alkylated SiNCs mixtures with ferrocene and $FeCl_3$, this shift can be explained as a result of self-absorption of the long wavelength emitted light in the samples.[18] In addition, it also should be noted that ferrocene itself and $FeCl_3$ were not observed to show any PL.

5.8 Reversibility of the photofading of commercial SiNCs

As mentioned above that there is no any chemical reaction occurs to commercial SiNCs during the irradiation time, subsequently SiNCs will not be oxidised. Therefore, this would be reversible at room temperature. Figure 5.13 presents the reversibility luminescence of commercial SiNCs. The laser was switched on for 300 seconds then turned off for 60 seconds and then was repeated twice for a similar time. It was observed that the second initial intensity is less than the previous initial luminescence due to that all the particles do not recover while the laser switches off[1] as also observed in the case of alkylated SiNCs. In addition, the majority of SiNCs become in charged state at the focal point of the Raman microspectroscopy when the photoluminescence reached the steady-state where the SiNCs under CW irradiation. In contrast, the electron-hole recombination process solely takes a place when the CW laser light switches off.

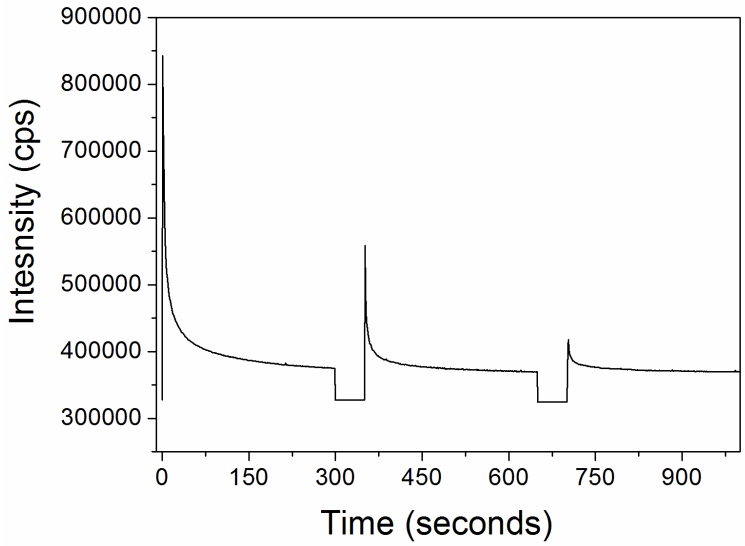

Figure 5.13: Intensity against time for the photofading of commercial SiNCs under irradiation with the 488 nm line of an argon ion laser. The intensity plotted is the integral of the spectrum at each time point over the wavenumber range 200-7000 cm^{-1}. At $t = 300s$ the irradiation was interrupted for 60s by closing the shutter (the intensity in this period is simply the integral of the dark counts on the CCD which has not been subtracted). When the shutter was reopened at 360s some of the initial intensity was regained.

5.9 Effect of metal nanoparticles on the photofading kinetics of commercial SiNCs

As discussed previously that the luminescence intermittency process is expected to be first order according to the random telegraphing model of NCs blinking, figure 5.9 and figure 5.10 present typical examples of photofading experiments; under CW irradiation. The curves in figure 5.9a and 5.10 have been normalised by I_∞ in order to display all the data together. It is clear that there is a slight enhancement in the integrated intensity in presence of either AgNPs or AuNPs as presented in table 5.6. Therefore, there is no remarkable change in the extent of photofading, measured by the ratio I_0/I_∞ in presence of metal NPs. Thus, this small enhancement in the integrated intensity provides also an evidence that the metal NPs act as a source for electrons; therefore there is increase in the rate of recombination ($k_{eh}\,|2\rangle$).

Four parameters were extracted from the fitting of equation 5.7 to the photofading curves: I_0 , I_∞ , $\langle k \rangle$ and γ . Table 5.7 shows the values of these parameters for four types of sample and their means and standard deviation over a

number of replicate experiments. Furthermore, we report the integrated intensity over a period of 300 seconds irradiation $\int_0^{300} Idt$ and the ratio of the initial and steady-state intensities, I_0/I_∞.

	Commercial-SiNCs	+ (1:5) AgNPs	+ (10:50) AgNPs	+ 0.41 AuNPs
Replicates:	$n = 13$	$n = 10$	$n = 9$	$n = 5$
10^{-8} x $\int_0^{300} Idt$ / counts	1.03 ± 0.04	1.30 ± 0.12	1.68 ± 0.99	1.21 ± 0.20
10^{-5} x I_0 / cps	3.51 ± 0. 18	4.24 ± 0.17	5.46 ± 0.21	4.11 ± 0.73
10^{-5} x I_∞ / cps	3.41 ± 0.11	3.66 ± 0.55	2.85 ± 0.23	4.02 ± 0.62
$\langle k \rangle / s^{-1}$	0.036 ± 0.010	0.087 ± 0.021	0.130 ± 0.019	0.140 ± 0.010
γ	2.16 ± 0.48	1.03 ± 0.10	1. 13 ± 0.01	1.31 ± 0.01
I_0/I_∞	1.03 ± 0.01	1.13 ± 0.30	1.92 ± 0.27	1.02 ± 0.02

Table 5.7: Kinetic data from photofading experiments on commercial SiNCs in the presence of AgNPs and AuNPs.

The metal NPs also have an effect on the kinetics of the photofading; the most probable rate constant which is describing the decay of the initial intensity towards the steady-state increases and the width of the distribution of rates decreases. The increase in the modal value of the rate constant is quite expected on the basis of the reaction scheme (equation 5.1 and 5.2). In an analogues manner to the well-known behaviour of systems near equilibrium, the observed rate constant is the sum of the forward and backward rate constants. As mentioned previously, the present system is not at equilibrium, but rather tends towards a steady-state at long times, however the steady-state is reached more quickly if either the rate of ionization or of recombination increases (equation 5.4). The AgNPs and, to a lesser extent the AuNPs act as sources of electrons and can quench the charge developing on the commercial SiNCs in the focal volume. However, this observation is similar to alkylated SiNCs with their mixtures with metal nanoparticles.

5.10 Effect of one-electron donors and acceptors on the photofading kinetics of commercial SiNCs

It is clear that the presence of either one electron donors/acceptors (ferrocene/$FeCl_3$) does not present any significant effective at enhancing the PL as presented in table 5.6. Table 5.8 exhibits the kinetic data from photofading of commercial SiNCs in the presence of ferrocene as an electron donor or $FeCl_3$ as an electron acceptor. This table indicates that in the presence of ferrocene and $FeCl_3$ the rate constant $\langle k \rangle$ increased slightly, a slight decrease in the γ values were observed and there is no remarkable change in the ratio I_0/I_∞.

	Commercial-SiNCs	+ 1 mM ferrocene	+ 1 mM $FeCl_3$
Replicates:	$n = 13$	$n = 7$	$n = 6$
10^{-8} x $\int_0^{300} Idt$ / counts	1.03 ± 0.04	1.05 ± 0.16	1.04 ± 0.02
10^{-5} x I_0 / cps	3.51 ± 0. 18	3.44 ± 0.15	3.71 ± 0.64
10^{-5} x I_∞ / cps	3.41 ± 0.11	3.38 ± 0.04	3.45 ± 0.10
$\langle k \rangle / s^{-1}$	0.036 ± 0.010	0.182 ± 0.002	0.181 ± 0.008
γ	2.16 ± 0.48	1.36 ± 0.01	1.85 ± 0.01
I_0/I_∞	1.03 ± 0.01	1.02 ± 0.05	1.07 ± 0.16

Table 5.8: Kinetic data from photofading of commercial SiNCs in the presence of electron donor or an electron acceptor.

5.11 Summary

Under CW irradiation in a confocal microscope, alkyl-capped SiNCs and commercial SiNCs show reversible photoluminescence fading behaviour. This can be interpreted by the same model originally proposed to describe luminescence intermittency, i.e., 'blinking'.[2] Particles in an excited state may undergo either photoionization or radiative decay; the charged particles produced by a photoionization are dark because there is an efficient non-radiative decay pathway in which energy transferred from the exciton to the hole. When single particles are studied, this leads to the well-known blinking phenomenon as particles ionize and later discharge by electron-hole recombination. In an ensemble, the result is a reversible photofading as the initial photoluminescence I_0 decays to a steady-state I_∞ controlled by the relative rates of photoionization k_a and recombination k_{eh}. Evidence for this interpretation comes from three observations: (i) upon cessation of the irradiation, electron-hole recombination occurs in the dark and the photoluminescence is regained when irradiation recommences; (ii) we have previously detected the photocurrent produced under CW irradiation of the SiNCs[1] and (iii) the initial and steady-state spectra are identical except for a scale factor. The photofading data can be modelled as a simple first order decay with a lognormal distribution of rate constants and therefore characterized by three parameters; $\langle k \rangle$ the modal rate constant, γ which measurs the spread of activiation free energies in units of RT and I_o/I_∞.

Alkyl-capped SiNCs and commercial SiNCs show enhanced luminescence when drop cast as films on glass slides in mixtures with Ag or Au nanoparticles. Such metal-enhanced luminescence is generally explained in terms of the large electric field near the metal surface upon excitation of the plasmon resonance and an increase in the radiative decay rate owing to the effect of the plasmon on the optical density of sates.

In this work, we find evidence for a third effect: the metal nanoparticles can act as a source of electrons and increase the time integrated luminescence intensity by increasing the rate of electron-hole recombination. In the presence of Ag and Au nanoparticles with alkyl-capped SiNCs, the modal rate constants $\langle k \rangle$ increase by factors of up to 4-fold and the ratios I_o/I_∞ decrease by factors up to 5-fold; this is consistent with an increase in the rate of electron-hole recombination facilitated by the metal

nanoparticles acting as a source of electrons. It is also should be noted that the presence of either Ag or Au NPs with commercial SiNCs are less effective at enhancing the PL than alkyl-capped SiNCs due to the large average size of commercial SiNCs i.e. 65 nm. Further support for this interpretation comes from the enhancement in the photoluminescence observed in photofading experiments with films of alkyl-capped SiNCs mixed with ferrocene; this compound is insulating and shows no plasmon band but is a well-known one-electron donor.

It is clear that the ratio I_0/I_∞ of commercial SiNCs is $\backsimeq 1$; while this ratio I_0/I_∞ is up to $\backsimeq 7$ for alkyl-capped SiNCs. This significant difference between these two types of SiNCs suggests that the commercial SiNCs are not easy to ionize as the extent of the photofading is very small. This is due to the different sizes of SiNCs that used in this work i.e. the diameter of commercial SiNCs and alkyl-capped SiNCs is 65 nm and 2.5 nm, respectively.

References

1. R. J. Rostron, Y. Chao, G. Roberts and B. R. Horrocks, *Journal of Physics Condensed Matter*, 2009, **21**, 235301.
2. A. L. Efros and M. Rosen, *Physical Review Letters*, 1997, **78**, 1110-1113.
3. R. J. Rostron, B. R. Horrocks and G. Roberts, *Journal of Applied Physics*, 2009, **105**, 094302-094308.
4. L. H. Lie, M. Duerdin, E. M. Tuite, A. Houlton and B. R. Horrocks, *Journal of Electroanalytical Chemistry*, 2002, **538–539**, 183-190.
5. N. A. Harun, B. R. Horrocks and D. A. Fulton, *Nanoscale*, 2011, **3**, 4733-4741.
6. Y. Duan, J. F. Kong and W. Z. Shen, *Journal of Raman Spectroscopy*, 2012, **43**, 756-760.
7. F. M. Dickinson, T. A. Alsop, N. Al-Sharif, C. E. M. Berger, H. K. Datta, L. Šiller, Y. Chao, E. M. Tuite, A. Houlton and B. R. Horrocks, *Analyst*, 2008, **133**, 1573-1580.
8. Y. Chao, A. Houlton, B. R. Horrocks, M. R. C. Hunt, N. R. J. Poolton, J. Yang and L. Siller, *Applied Physics Letters*, 2006, **88**, 263119-263113.
9. K. Zídek, F. Trojánek, P. Malý, L. Ondi, I. Pelant, K. Dohnalová, L. Šiller, R. Little and B. R. Horrocks, *Opt. Express*, 2010, **18**, 25241-25249.
10. M. Picquart, *The Journal of Physical Chemistry*, 1986, **90**, 243-250.
11. G. Cazzolli, S. Caponi, A. Defant, C. M. C. Gambi, S. Marchetti, M. Mattarelli, M. Montagna, B. Rossi, F. Rossi and G. Viliani, *Journal of Raman Spectroscopy*, 2012, **43**, 1877-1883.
12. J. S. Hager, J. Zahardis, R. M. Pagni, R. N. Compton and J. Li, *The Journal of Chemical Physics*, 2004, **120**, 2708-2718.
13. T. Nychyporuk, Y. Zakharko, T. Serdiuk, O. Marty, M. Lemiti and V. Lysenko, *Nanoscale*, 2011, **3**, 2472-2475.
14. H. K. Subramanian, 2013.
15. S. M. Barnett, N. Harris and J. J. Baumberg, *Physical Chemistry Chemical Physics*, 2014, **16**, 6544-6549.
16. N. A. Harun, M. J. Benning, B. R. Horrocks and D. A. Fulton, *Nanoscale*, 2013, **5**, 3817-3827.
17. A. D. McFarland, M. A. Young, J. A. Dieringer and R. P. Van Duyne, *The Journal of Physical Chemistry B*, 2005, **109**, 11279-11285.
18. A. Trojanek, J. Langmaier, J. Sebera, S. Zalis, J.-M. Barbe, H. H. Girault and Z. Samec, *Chemical Communications*, 2011, **47**, 5446-5448.
19. Y. Chao, S. Krishnamurthy, M. Montalti, L. H. Lie, A. Houlton, B. R. Horrocks, L. Kjeldgaard, V. R. Dhanak, M. R. C. Hunt and L. Šiller, *Journal of Applied Physics*, 2005, **98**, 044316.
20. I. Chung and M. G. Bawendi, *Physical Review B*, 2004, **70**, 165304.
21. A. F. van Driel, I. S. Nikolaev, P. Vergeer, P. Lodahl, D. Vanmaekelbergh and W. L. Vos, *Physical Review B*, 2007, **75**, 035329.
22. H. Liang, Z. Li, W. Wang, Y. Wu and H. Xu, *Advanced Materials*, 2009, **21**, 4614-4618.
23. K. Žídek, I. Pelant, F. Trojánek, P. Malý, P. Gilliot, B. Hönerlage, J. Oberlé, L. Šiller, R. Little and B. R. Horrocks, *Physical Review B*, 2011, **84**, 085321.
24. K. Zídek, F. Trojánek, P. Malý, L. Ondi, I. Pelant, K. Dohnalová, L. iller, R. Little and B. R. Horrocks, *Opt. Express*, 2010, **18**, 25241-25249.
25. G. Faraci, S. Gibilisco, P. Russo, A. R. Pennisi and S. La Rosa, *Physical Review B*, 2006, **73**, 033307.
26. L. V. Mercaldo, E. M. Esposito, P. D. Veneri, G. Fameli, S. Mirabella and G. Nicotra, *Applied Physics Letters*, 2010, **97**, 153112.
27. N. M. B. Perney, J. J. Baumberg, M. E. Zoorob, M. D. B. Charlton, S. Mahnkopf and C. M. Netti, *Opt. Express*, 2006, **14**, 847-857.

Chapter 6

Conclusions and Future Work

In this chapter, a brief explanation of what was concluded throughout this thesis is presented. Lastly, the proposed future work will be explained.

6.1 Conclusions and future work

Due to the significant growing interest on SiNCs to be used in different applications including photonic devices and biological labels, it is desirable to synthesis these unique structures and investigate their optical properties. Furthermore, the recent studies[1-9] attempted to enhance the emitted light from SiNCs by using metallic nanoparticles and rare earth ions.

This thesis has focused on the characterization of two types of SiNCs i.e. C_{11}-SiNCs and commercial SiNCs using different spectroscopic techniques. The data presented in this research show that the optical properties of SiNCs can be manipulated by rare earth ions and metal nanoparticles.

Porous silicon was prepared successfully by a galvanostatic etching method of p-Si(100) wafers followed by a thermal hydrosilation reaction of 1-undecene in refluxing toluene in order to extract the C_{11}-SiNCs from porous silicon. The chemical characterization of C_{11}-SiNCs was carried out using XPS; they are known to be crystalline and of diameter about 5 nm from previous work[10]. The commercial SiNCs have been characterized using SEM, TEM, HRTEM, AFM, XRD, XPS and FTIR. It was found that the average diameter of commercial SiNCs is 65 nm and are crystalline with an FCC lattice.

Erbium trichloride was added to both types of SiNCs using a simple mixing chemical route. To the best of our knowledge, this is a first investigation on mixing SiNCs with erbium ions (III) by this chemical method. However, the main goal of mixing SiNCs with erbium ions is to observe the energy transfer from the excited state of SiNCs to erbium. Erbium is useful because it has a narrow emission spectrum centred at $\sim$ 1500 nm which is a range of interest in optical fiber technology. The erbium trichloride hydrolysis to erbium sesquioxide (Er_2O_3) in Er/C_{11}-SiNCs film which

coat the surface of alkylated SiNCs. The presence of Er_2O_3 on the surface of C_{11}-SiNCs affects the oxidation state of alkylated SiNCs on the surface as observed by XPS measurement.

Both SiNCs either C_{11}-SiNCs or commercial SiNCs and their mixtures with Er^{3+} were investigated using Raman spectroscopy and photoluminescence (PL). The characteristic broad luminescence peak confirmed the presence of SiNCs. The wavelength of this luminescence signal of SiNCs in aqueous medium in presence of trivalent erbium shifts to a lower wavelength due to the formation of oxides which would cause a blue shift to higher energy based on the quantum confinement effect. This suggests that the blue shift arises from states which related to the surface oxide on SiNCs. Thus, the surface chemical composition must play an important role in the blue shift of the luminescence of SiNCs when they mixed with erbium ions. This data suggests that the origin of the luminescence from SiNCs either C_{11}-SiNCs or commercial SiNCs could be attributed to direct band gap transitions in SiNCs and to radiative recombination of excitons through the oxidation surface of SiNCs. In addition, the samples show an orange PL emission peak at around 595 nm originates from Si. Er/SiNCs mixtures also exhibit a weak PL emission peak at 1536 nm which originates from the intra-4*f* transition in erbium ions (Er^{3+}). The PL peak of Si in Er/C_{11}-SiNCs and Er/Commercial SiNCs mixtures are increased in the intensity up to four and three times, respectively as compared to pure C_{11}-SiNCs and commercial SiNCs. The collected data suggest that this chemical mixing route leads instead to a transfer of energy from erbium ions to SiNCs.

Metal-enhanced luminescence has been studied for mixtures of SiNCs (either C_{11}-SiNCs or commercial SiNCs) with silver nanoparticles (AgNPs). AgNPs of two different sizes were synthesised using photochemical reduction of $AgNO_3$ with sodium dodecyl sulphate (SDS). The synthesized AgNPs (1:5) and (10:50) have a polycrystalline structure with an average particle diameter of 100 nm and 30 nm, respectively.[11] A significant enhancement up to 10 and 4 times in the PL intensity was observed for AgNPs (1:5)/C_{11}-SiNCs and AgNPs (10:50)/C_{11}-SiNCs, respectively using an excitation source of 488 nm. A similar observation was also reported for AgNPs (1:5)/Commercial SiNCs and AgNPs (10:50)/Commercial SiNCs; where the intensity of the PL signal increased up to 9 and 3 times respectively, using 488 nm; whereas the intensity of the

PL signal increased up to 7 and 2 times respectively, using 514.5 nm excitation source. The enhancement in PL intensities occurs as a result of the coupling between the excitation laser light and the plasmon bands of AgNPs; thus this intense field at AgNPs surface couples strongly to SiNCs. The results show that the closer wavelength of the laser excitation source to the surface plasmon resonance absorption bands of silver nanoparticles the greater the emission intensity. Our study also suggests that the larger AgNPs (1:5) caused an optimum enhancement in PL intensity of both types of SiNCs. It was also found that in this work, the luminescence peak of SiNCs blue shifted in presence of AgNPs. This blue shift can be due to (i) strong coupling of LSPR of AgNPs to surface oxides of SiNCs and (ii) LSPR couples strongly to states near the direct gap of SiNCs, which radiative more efficiently. Furthermore, the intense SERS effect which observed during this project where AgNPs mixed with SiNCs suggests that AgNPs which synthesized by a green method can be used in some application such as SERS substrates.

Under continuous wave (CW) irradiation in a confocal microscope, both types of SiNCs show reversible photoluminescence fading behaviour. This can be interpreted by the same model originally proposed to describe luminescence intermittency, i.e., 'blinking'. When single particles are studied, this leads to the well-known blinking phenomenon as particles ionize and later discharge by electron-hole recombination. In an ensemble, the result is a reversible photofading as the initial photoluminescence I_0 decays to a steady-state I_∞ controlled by the relative rates of photoionization k_a and recombination k_{eh}. Evidence for this interpretation comes from two observations: (i) upon cessation of the irradiation, electron-hole recombination occurs in the dark and the photoluminescence is regained when irradiation recommences and (ii) the initial and steady-state spectra are identical except for a scale factor. The photofading data can be modelled as a simple first order decay with a lognormal distribution of rate constants and therefore characterized by three parameters; $\langle k \rangle$ the modal rate constant, γ which measurs the spread of activiation free energies in units of RT and I_o/I_∞.

C_{11}-SiNCs and commercial SiNCs show enhanced luminescence when drop cast as films on glass slides in mixtures with Ag or Au nanoparticles. Such metal-enhanced luminescence is generally explained in terms of the large electric field near the metal

surface upon excitation of the plasmon resonance and an increase in the radiative decay rate owing to the effect of the plasmon on the optical density of sates. In this work, we find evidence for a third effect: the metal nanoparticles can act as a source of electrons and increase the time integrated luminescence intensity by increasing the rate of electron-hole recombination. In the presence of Ag and Au nanoparticles with alkyl-capped SiNCs, the modal rate constants $\langle k \rangle$ increase by factors of up to 4-fold and the ratios I_o/I_∞ decrease by factors up to 5-fold; this is consistent with an increase in the rate of electron-hole recombination facilitated by the metal nanoparticles acting as a source of electrons. It is also should be noted that the presence of either Ag or Au NPs with commercial SiNCs are less effective at enhancing the PL than alkyl-capped SiNCs due to the large average particle size of commercial SiNCs. Further support for this interpretation comes from the enhancement in the photoluminescence observed in photofading experiments with films of alkyl-capped SiNCs mixed with ferrocene; this compound is insulating and shows no plasmon band but is a well-known one-electron donor.

It is clear that the ratio I_0/I_∞ of commercial SiNCs is $\backsimeq 1$; while this ratio I_0/I_∞ is up to $\backsimeq 7$ for alkyl-capped SiNCs. This significant difference between these two types of SiNCs suggests that the commercial SiNCs are not easy to ionize as the extent of the photofading is very small. This is due to the different sizes of SiNCs that used in this work i.e. the diameter of commercial SiNCs and alkyl-capped SiNCs is 65 nm and 2.5 nm, respectively.

In terms of developing this research, another technique; for example, ion implantation should be used to incorporate and to produce optically active erbium ions into silicon nanocrystals instead of chemical mixing method that used during this study in order to avoid the oxidation of erbium ion and allow the energy transfer from Si nanocrystals to erbium. Kik *et al*[12] and Ji *et al*[13] prepared erbium doped SiNCs by ion implantation. They[12, 13] observed that the efficient enhancement in the PL band of erbium at $\sim$ 1530 nm occur when the Er^{3+} are spaced closely enough to SiNCs in order to allow the energy transfer process which achieved by ion implantation. Also, changing the concentration of erbium and SiNCs is required to investigate the effect of this factor in the PL band of Er. Fujii *et al*[14] and Cerqueira *et al*[15, 16] prepared erbium

doped SiNCs by sputtering. They[14-16] found that the PL intensity of erbium ions increases as the concentration of erbium decreased within the SiNCs.

However, it is valuable also to find out a way to prepare mixtures of SiNCs with metal NPs with high degree in controlling the spacing between the SiNCs and metal nanoparticles and different shapes of Ag nanoparticles in order to detect the maximum metal-enhanced luminescence of SiNCs. Rezaee *et al*[17] controlled the space between the Au nanoparticles and silicon by using focused ion beam technique. Rycenga *et al*[18] reported that the shape of silver nanoparticles affect deeply the plasmonics properties of metallic nanoparticles. Furthermore, AgNPs with sharp structures are promising candidate for surface enhanced Raman scattering (SERS).[18]

References:

1. S. K. Ray, S. Maikap, W. Banerjee and S. Das, *J. Phys. D-Appl. Phys.*, 2013, **46**.
2. M. G. Panthani and B. A. Korgel, *Annu. Rev. Chem. Biomol. Eng.*, 2012, **3**, 287-311.
3. N. A. Harun, M. J. Benning, B. R. Horrocks and D. A. Fulton, *Nanoscale*, 2013, **5**, 3817-3827.
4. I. Abdulhalim, *Small*, 2014, **10**, 3499-3514.
5. J. Goffard, D. Gerard, P. Miska, A. L. Baudrion, R. Deturche and J. Plain, *Sci Rep*, 2013, **3**.
6. R. Lu, J. Sha, W. Xia, Y. Fang, L. Gu and Y. Wang, *CrystEngComm*, 2013, **15**, 6207-6212.
7. L. Zeiri, K. Rechav, Z. Porat and Y. Zeiri, *Appl. Spectrosc.*, 2012, **66**, 294-299.
8. R. J. Kashtiban, U. Bangert, I. F. Crowe, M. Halsall, A. J. Harvey and M. Gass, in *Electron Microscopy and Analysis Group Conference 2009*, ed. R. T. Baker, Iop Publishing Ltd, Bristol, 2010, vol. 241.
9. L. B. Xu, D. S. Li, L. Jin, L. L. Xiang, F. Wang, D. R. Yang and D. L. Que, *Nanoscale Res. Lett.*, 2014, **9**.
10. Y. Chao, L. Šiller, S. Krishnamurthy, P. R. Coxon, U. Bangert, M. Gass, L. Kjeldgaard, S. N. Patole, L. H. Lie, N. O'Farrell, T. A. Alsop, A. Houlton and B. R. Horrocks, *Nat Nano*, 2007, **2**, 486-489.
11. G. A. Bhaduri, R. Little, R. B. Khomane, S. U. Lokhande, B. D. Kulkarni, B. G. Mendis and L. Šiller, *Journal of Photochemistry and Photobiology A: Chemistry*, 2013, **258**, 1-9.
12. P. G. Kik and A. Polman, *Journal of Applied Physics*, 2000, **88**, 1992-1998.
13. J. Ji, R. A. Senter, L. R. Tessler, D. Back, C. H. Winter and J. L. Coffer, *Nanotechnology*, 2004, **15**, 643.
14. M. Fujii, M. Yoshida, S. Hayashi and K. Yamamoto, *Journal of Applied Physics*, 1998, **84**, 4525-4531.
15. M. F. Cerqueira, M. Losurdo, T. Monteiro, M. Stepikhova, M. J. Soares, M. Peres, E. Alves and O. Conde, *Journal of Non-Crystalline Solids*, 2006, **352**, 1148-1151.
16. M. F. Cerqueira, M. Losurdo, M. Stepikhova, P. Alpuim, G. Andres, A. Kozanecki, M. J. Soares and M. Peres, *Thin Solid Films*, 2009, **517**, 5808-5812.
17. A. Rezaee, A. K. A. Aliganga, L. C. Pavelka and S. Mittler, *Physical Chemistry Chemical Physics*, 2010, **12**, 4104-4111.
18. M. Rycenga, C. M. Cobley, J. Zeng, W. Li, C. H. Moran, Q. Zhang, D. Qin and Y. Xia, *Chemical Reviews*, 2011, **111**, 3669-3712.